DESIGN AND MODELLING OF NANOPHOTONIC DEVICES

A Thesis Submitted
in Partial Fulfillment of the Requirements
for the Degree of

DOCTOR OF PHILOSOPHY

in

Electronics and Communication Engineering

by

Kirti Dalal
(Roll No. 2K20/PHDEC/03)

Under the Supervision of

Dr. Yashna Sharma
Assistant Professor, ECE, DTU

Department of Electronics and Communication Engineering

DELHI TECHNOLOGICAL UNIVERSITY
(Formerly Delhi College of Engineering)
Shahbad Daulatpur, Main Bawana Road, Delhi–110042, India

October, 2025

DELHI TECHNOLOGICAL UNIVERSITY
(Formerly Delhi College of Engineering)
Shahbad Daulatpur, Main Bawana Road, Delhi-110042, India

CANDIDATE'S DECLARATION

I, **Kirti Dalal**, hereby certify that the work which is being presented in the thesis entitled **"Design and modelling of nanophotonic devices"** in partial fulfillment of the requirements for the award of the Degree of **Doctor of Philosophy**, submitted in the Department of Electronics and Communication Engineering, Delhi Technological University, India, is an authentic record of my own work carried out during the period from **25th August 2020** to **31st October 2025** under the supervision of **Dr. Yashna Sharma**.

The matter presented in the thesis has not been submitted by me for the award of any other degree of this or any other Institute.

Date: 31st October 2025 **Kirti Dalal**

Place: Delhi, India **(2K20/PHDEC/03)**

This is to certify that the student has incorporated all the corrections suggested by the examiners in the thesis and the statement made by the candidate is correct to the best of our knowledge.

Signature of Supervisor **Signature of External Examiner**

DELHI TECHNOLOGICAL UNIVERSITY
(Formerly Delhi College of Engineering)
Shahbad Daulatpur, Main Bawana Road, Delhi-110042, India

CERTIFICATE BY THE SUPERVISOR

Certified that **Kirti Dalal (2K20/PHDEC/03)** has carried the research work presented in this thesis entitled **"Design and modelling of nanophotonic devices"** for the award of the Degree of **Doctor of Philosophy** from the Department of Electronics and Communication Engineering, Delhi Technological University, India, under my supervision. The thesis embodies results of original work, and studies are carried out by the student herself and the contents of the thesis do not form the basis for the award of any other degree to the candidate or to anybody else from this or any other University/Institution.

Dr. Yashna Sharma
Assistant Professor,
Department of Electronics and Communication Engineering,
Delhi Technological University, Delhi

Date: 31st October 2025
Place: Delhi, India

ABSTRACT

This thesis presents a brief overview of the research work carried out on the design and modelling of nanophotonic devices, especially plasmonic switches based on vanadium dioxide (VO_2) – a promising phase change material (PCM). Plasmonic switches, which modulate light propagation at the nanoscale, have gained significant attention for applications in integrated photonics, plasmonic logic circuits, and optical communication networks. These devices utilize the tunable plasmonic properties of PCM covered nanostructures under external stimuli — thermal, electrical, or optical — offering ultra-fast switching speeds, wide spectral tunability, compact sizes, and low losses. The thesis also explains the rationale for selecting VO_2 and presents an extensive review of VO_2 based plasmonic switches developed over the past few decades.

Plasmonic switch designs proposed in this thesis are analyzed using Finite Difference Time Domain (FDTD) simulations. Firstly, active broadband plasmonic switches are designed using periodic arrays of metallic nanodisc-dimers with increasing diameters on a gold-coated silicon dioxide (SiO_2) substrate, separated by a thin VO_2 spacer layer. It is well known that — for a periodic array of circular metallic discs on a substrate, the applied optical field is efficiently coupled into the plasmonic modes of the nanostructure at specific plasmon resonance wavelengths, thus resulting in narrow and strong dips in the reflection spectrum of the nanostructure. Further, there is a red-shift in the plasmon resonance wavelength due to the retardation of the depolarization field when the diameter of the nanodiscs is increased. It can therefore be inferred that by employing an array of dimers of metallic nanodiscs with progressively increasing diameters, multiple wavelengths can be coupled into the plasmonic modes of the nanostructure such that each nanodisc-dimer with a specific value of diameter results in the coupling of incident electromagnetic radiation into the plasmonic modes of the nanostructure at a specific plasmon resonance wavelength. This coupling of incident radiation to plasmonic modes at multiple wavelengths results in an overall broadband resonance dip in the reflection spectrum of the nanostructure, enabling broadband response across the C, L, and U optical communication bands. The proposed designs achieve a broadband extinction ratio (ER) of 5 dB over 650 nm (from 1460 nm to 2110 nm wavelength) and 4 dB over 702 nm (from 1432 nm to 2134 nm wavelength) for a periodic array of five sets of nanodisc-dimers. The trade-off between ER and bandwidth is also explored for design optimization.

Next, polarization-independent dual-wavelength switches are proposed using a periodic combination of U and C shaped gold nanostructures on a gold coated SiO_2 substrate with a thin VO_2 film spacer between the nanostructures and the underlying plasmonic substrate. The U and C shaped nanopillars are placed on the underlying substrate such that there is a spatial offset between them. It is well known that when three nanopillars are arranged in a U shaped nanostructure, two plasmonic modes — a short wavelength mode and a long wavelength mode — are generated when the incident light is X-polarized, whereas a single plasmonic mode is generated when the incident light is Y-polarized. For the C shaped nanostructure, this situation becomes inverted, with two plasmonic modes being excited for Y-polarized light and

one plasmonic mode being excited for X-polarized light. However, when both U and C shaped nanostructures are placed together to form a U-C type plasmonic switch, two plasmonic modes — a short wavelength mode and a long wavelength mode — are generated for both X- and Y-polarized incident light. Due to the excitation of two plasmonic modes at both polarization angles of incident light, these U-C type plasmonic nanostructures are employed in this work to realize an efficient polarization-independent multi-wavelength switch by placing them on a VO_2 coated plasmonic substrate. The proposed U-C type plasmonic switches exhibit an ER of ~20 dB simultaneously at two wavelengths — at ~1560 nm and at ~2130 nm — for a linearly polarized incident light with any polarization angle from 0° to 90°.

Further, periodic arrays of identical V-shaped gold nanostructures and variable V-shaped gold nanostructures are designed on top of a gold-coated SiO_2 substrate with a thin spacer layer of VO_2 to realize multi-wavelength and broadband plasmonic switches, respectively. The periodic array of identical V-shaped nanostructures (IVNSs) with small inter-particle separation leads to coupled interactions of the elementary plasmons of a V-shaped nanostructure (VNS), resulting in a hybridized plasmon response with two longitudinal plasmonic modes in the reflectance spectra of the proposed switches when the incident light is polarized in the x-direction. FDTD modelling is employed to demonstrate that an ER > 12 dB at two wavelengths can be achieved by employing the proposed switches. Further, plasmonic switches based on variable V-shaped nanostructures (VVNSs) — i.e., multiple VNSs with variable arm lengths in one unit cell of a periodic array — are proposed for broadband switching. In the broadband operation mode, an ER > 5 dB over an operational wavelength range > 1400 nm in the near-IR spectral range spanning over all optical communication bands, i.e., the O, E, S, C, L and U bands, is reported. Further, it is also demonstrated that the operational wavelength of these switches can be tuned by adjusting the geometrical parameters of the proposed design.

Additionally, the thesis investigates near-field plasmonic switching using pentagon shaped fractal plasmonic nanoantennas placed on a VO_2 thin film overlaying a gold-coated SiO_2 substrate. These fractal geometries are designed to confine electromagnetic fields to deep sub-wavelength volumes, generating intense field enhancements at the nanogap between the antenna arms. Upon phase transition of the VO_2 layer, a significant change in local field distribution is observed, leading to an intensity switching ratio (ISR) exceeding ~2300 for higher fractal orders. The spectral response is shown to be tunable via geometric parameters. These near-field designs hold promise for utilization in areas like surface enhanced Raman spectroscopy (SERS), nonlinear optical phenomena, and nanoscale sensing.

In summary, this thesis offers a detailed exploration of VO_2 based plasmonic switches, emphasizing their potential for broadband, multi-wavelength, polarization-independent, and near-field switching applications. The proposed designs, supported by rigorous simulations, contribute significantly toward the development of compact and high-performance plasmonic devices for next-generation optical communication and photonic integration.

ACKNOWLEDGEMENTS

I would like to express my sincere gratitude to all those who have supported me throughout the journey of my Ph.D. research.

First and foremost, I am deeply indebted to my supervisor, Dr. Yashna Sharma, for being the cornerstone of my academic journey. Her invaluable guidance, unwavering support, constant encouragement, deep subject expertise, critical insights, and constructive feedback have been instrumental in shaping the direction and depth of my research. More than just a mentor, she has been a constant source of inspiration, always approachable, patient, and generous with her time and knowledge. Her ability to balance academic rigor with empathy and encouragement has had a profound impact on both my work and personal growth. I will always be grateful for her constructive criticism, motivating words during challenging times, and her unwavering belief in my potential. It has been a privilege and an honor to work under the guidance of such a dedicated and compassionate mentor.

I am thankful to the faculty and staff of Delhi Technological University (DTU) for providing a conducive research environment and access to essential resources. I extend my heartfelt thanks to the former HODs of ECE, Prof. N. S. Raghava and Prof. O. P. Verma, and the current HOD of ECE, Prof. Neeta Pandey, for the constant support, cooperation, and encouragement during the course of my research. I also thank my Student Research Committee (SRC) and Doctoral Research Committee (DRC) members for their valuable suggestions and feedback during various stages of my research work. I gratefully acknowledge the institute fellowship support from DTU, which provided the necessary financial assistance for carrying out this research.

I am also thankful to my colleagues and fellow researchers, especially – Mrs. Asbah Masih, Mr. Ankit Kumar Sonkar, Mr. Vishal Chaudhary, Mrs. Yogita Chopra, Mrs. Puja Priya, Mr. Merbin John, Mr. Vaibhav Chaturvedi, Dr. Kamal Kumar, and Mr. Mohd Asif – for their support, collaboration, and the many stimulating discussions that enriched my knowledge.

On a personal note, I am forever grateful to my family. Their unconditional love, patience, and encouragement gave me the strength to persevere. To my parents, who have been my pillar of support, and to my siblings, thank you for your understanding and sacrifices during this long academic pursuit.

Lastly, I thank the Almighty for granting me the health, strength, and wisdom to complete this thesis.

Kirti Dalal

LIST OF PUBLICATIONS

SCIE-Indexed Journal Papers:

1. **Dalal, K.**, and Sharma, Y. "VO_2 based polarization-independent dual-wavelength plasmonic switches using U and C shaped nanostructures", *Scientific Reports*, 15, 4020, 2025. https://doi.org/10.1038/s41598-025-85349-9
2. **Dalal, K.**, and Sharma, Y. "Multi-wavelength and broadband plasmonic switching with V-shaped plasmonic nanostructures on a VO_2 coated plasmonic substrate", *Nanotechnology*, 35(39), 395203, 2024. https://doi.org/10.1088/1361-6528/ad5dc2
3. **Dalal, K.**, and Sharma, Y. "Plasmonic switches based on VO_2 as the phase change material", *Nanotechnology*, 35(14), 142001, 2024. https://doi.org/10.1088/1361-6528/ad1642
4. **Dalal, K.**, and Sharma, Y. "Broadband plasmonic switches based on nanodisc-dimers with progressively increasing diameters on a plasmonic film with a VO_2 spacer", Optics Communications, 530, 129121, 2023. https://doi.org/10.1016/j.optcom.2022.129121

SCOPUS-Indexed International Conference Papers:

1. **Dalal, K.**, and Sharma, Y. "Vanadium dioxide based plasmonic switching in V shape nanostructures", *2024 4th International Conference on Advancement in Electronics & Communication Engineering (AECE)*, Ghaziabad, Uttar Pradesh, India (pp. 1341-1344), 2024. https://doi.org/10.1109/AECE62803.2024.10911425
2. **Dalal, K.**, and Sharma, Y. "Broadband plasmonic switching based on asymmetric metallic nanostructures on a VO_2 coated metallic film", Proceedings SPIE 12575, *Integrated Optics: Design, Devices, Systems and Applications VII*, SPIE Optics + Optoelectronics 2023, Prague, Czech Republic (article no. 125750K, pp. 108-115), 2023. https://doi.org/10.1117/12.2665503
3. **Dalal, K.**, and Sharma, Y. "Tunable LSPR in asymmetric plasmonic bowtie nanostructures", *2023 10th International Conference on Signal Processing and Integrated Networks (SPIN)*, Noida, Uttar Pradesh, India (pp. 36-39), 2023. https://doi.org/10.1109/SPIN57001.2023.10116564
4. **Dalal, K.**, and Sharma, Y. "Tunable plasmon resonance in asymmetric plasmonic cross-bowtie nanostructures", *2022 IEEE International Conference on Nanoelectronics, Nanophotonics, Nanomaterials, Nanobioscience & Nanotechnology (5NANO)*, Kottayam, Kerala, India (pp. 1-3), 2022. https://doi.org/10.1109/5NANO53044.2022.9828941

Manuscript in process:

1. **Dalal, K.**, and Sharma, Y. "Fractalization of pentagon shaped plasmonic nanoantennas for VO_2 based near-field switching application", 2025.

TABLE OF CONTENTS

LIST OF TABLES

LIST OF FIGURES

LIST OF SYMBOLS, ABBREVIATIONS AND NOMENCLATURE

Ag	Silver
AgInSbTe or AIST	Silver indium antimony tellurium
Al	Aluminium
Al_2O_3	Aluminium oxide
ALD	Atomic layer deposition
AT	Asymmetric transmission
ATR	Attenuated total reflection
Au	Gold
CaF_2	Calcium fluoride
CD	Circular dichroism
CMOS	Complementary metal-oxide-semiconductor
Cu	Copper
DFT	Density functional theory
DMFT	Dynamical mean field theory
DWDM	Dense wavelength division multiplexing
EBL	Electron beam lithography
EFIE	Electric field intensity enhancement
E	Electric field
EM	Electromagnetic
ER	Extinction ratio
FDTD	Finite difference time domain
Fe	Iron
FSO	Free space optics
FWHM	Full width at half maxima
Ge	Germanium
GeSbSeTe or GSST	Germanium antimony selenium tellurium
GeSbTe or GST	Germanium antimony tellurium
H	Magnetic field
He	Helium
HfO_2	Hafnium dioxide
HIM	Helium ion milling
IMT	Insulator-to-metal transition
InSbTe or IST	Indium antimony tellurium
IR	Infrared
ISR	Intensity switching ratio
ITO	Indium tin oxide
LCP	Left circular polarization
LSPR	Localized surface plasmon resonance
LW	Long wavelength
MIT	Metal-to-insulator transition
Mo	Molybdenum
MPEBL	Massively parallel electron beam lithography
Nb	Niobium
NIR	Near infrared

PCM	Phase change material
PDMS	Polydimethylsiloxane
PLD	Pulsed laser deposition
PML	Perfectly matched layer
PMMA	Polymethylmethacrylate
PON	Passive optical network
PTEE	Polytetrafluoroethylene
RCP	Right circular polarization
RM	Reflection mode
SEM	Scanning electron microscope
Si	Silicon
SiO_2	Silicon dioxide
SMT	Semiconductor-to-metal transition
SPP	Surface plasmon polariton
SPR	Surface plasmon resonance
SW	Short wavelength
Ta	Tantalum
TDFA	Thulium doped fiber amplifiers
TFSF	Total field scattered field
THz	Terahertz
TIR	Total internal reflection
TM	Transmission mode
V_2O_3	Vanadium trioxide
V_2O_5	Vanadium pentoxide
VO_2	Vanadium dioxide
W	Tungsten
WDM	Wavelength division multiplexing
WS_2	Tungsten disulfide
XAS	X-ray absorption spectroscopy
XPS	X-ray photoelectron spectroscopy

CHAPTER 1

INTRODUCTION

1.0 Chapter Overview

This chapter presents the foundational background of nanophotonics, emphasizing the increasing significance of nanophotonic devices in diverse applications ranging from biomedical imaging to high-speed optical communication systems. Traditional photonic devices face limitations, particularly in terms of size constraints imposed by the diffraction limit. To overcome these challenges, plasmonic devices have emerged as a promising alternative, offering the ability to confine light beyond the diffraction limit and thereby enabling the development of compact and high-performance optical components. Among these, plasmonic switches are recognized as essential elements for dynamic control of light in optical communication and computing networks. The discussion further focuses on the integration of phase change materials, which facilitate active switchability in plasmonic nanostructures. Specifically, vanadium dioxide (VO_2) is identified as a highly suitable phase change material owing to its near-room temperature phase transition, high switching speeds, and compatibility with standard fabrication processes.

Accordingly, this chapter articulates the problem statement and motivation underlying the research work carried out in this thesis. It also outlines the key research objectives formulated for the design and modelling of nanophotonic devices. Finally, the organization of the subsequent chapters of the thesis is briefly described.

1.1 Background

Nanophotonics or nano-optics is the study of light at the nanoscale and its interactions with nanometer-sized structures [1]. These interactions occur at a wavelength or sub-wavelength scale, where the physical and structural characteristics of nanostructured materials govern the behavior. Nanophotonics impacts numerous real-world applications, including: biomedical imaging for disease diagnosis and treatment [2], new imaging systems in cameras [3], sensors and sensor systems for chemicals or bio-analytes [4], and nanophotonic devices such as switches and modulators for communications [5]. Over the past few decades, photonic devices have increasingly supplanted electronic components in contemporary communication systems due to their significantly higher operational speeds [6]. However, despite this advantage, photonic devices are fundamentally constrained by the diffraction limit of light, which results in comparatively larger device dimensions than their electronic counterparts [7]. Consequently, achieving miniaturization and high-density on-chip integration of photonic devices remains a persistent challenge.

Plasmonics, with its ability to confine light at the nanoscale, has enabled the emergence of nanophotonic devices that integrate the benefits of both photonic and electronic systems — ultra-high speed and ultra-compactness. By overcoming the

limitations imposed by the diffraction limit, plasmonics facilitates the realization of ultra-compact photonic components [8, 9]. Plasmonics allows the coupling of light to the free electrons in metals (such as gold and silver), leading to the generation of surface plasmon resonances [10]. These resonant oscillations can either propagate along the metal-dielectric interface as surface plasmon polaritons (SPPs) [11] or can be confined to the metallic nanostructures as localized surface plasmons [12]. As the surface plasmons can be constricted to sub-wavelength volumes, the overall size of optical devices based on plasmonics can be decreased below the diffraction limit which subsequently leads to a higher integration density and an ultrasmall footprint of such devices [13]. For integrated photonic systems and computing networks, various ultra-small plasmonic devices such as nanophotonic lasers [14], waveguides [15], amplifiers [16], filters [17], splitters [18], polarizers [19], absorbers [20], modulators [21], switches [22] and photodetectors [23] have been proposed in the past with combined advantages of a smaller footprint, high-speed and low power consumption. One of the most critical issues in a photonic system is to control the optical signals through processes like routing [24] and switching [25]. Therefore, the primary focus of this thesis is on plasmonic switches which can be utilized in high-speed communication networks, integrated photonic circuits, and various other applications [26, 27].

A plasmonic switch is a nanoscale plasmonic device which performs transition or switching (i.e., ON to OFF state and OFF to ON state) in terms of light and can block or divert, i.e., modify the propagation of radiation through a system [28]. Plasmonic switches are widely employed as switching elements for telecommunication applications and other optical communication applications [29, 30]. In the past, plasmonic switches have been developed based on multiple physical effects, such as thermo-optical effect [31], free carrier dispersion effect [32], acousto-optic effect [33], Pockels effect [34], electro-optic effect [35], all-optical effect [36] and phase change effect [37]. Moreover, plasmonic switching can also be achieved by exploiting the non-linearity of the materials or by employing tunable gaps in the plasmonic nanostructures [38]. Additionally, active plasmonic switches on the basis of nanostructures coated with electro-optic films of liquid crystals molecules [39], polymer layers doped with photochromic molecules [40], electromechanically controlled conductive polymer layers [41], electrically-controlled materials like graphene [42] or plasmonic nanoparticles incorporated into freestanding stimulus-responsive hydrogels [43] have also been designed in the past.

In the last few decades, plasmonic switches based on the phase transition of various phase change materials (PCMs) have been widely employed owing to numerous advantages such as ultrafast switching speed, high latent heat values, low power consumption, dynamic tuning, high degree of scalability, and low cost [44, 45]. PCMs are the materials that go through collective structural and/or electronic transitions across the bulk of the material along with massive changes in their optical, dielectric, and electrical properties [46]. PCMs mainly incorporate correlated oxides showing metal-insulator transitions [47] and chalcogenide (such as selenium and tellurium) alloys showing crystalline-amorphous transitions [48]. Examples of PCMs include, but are not limited to, vanadium dioxide (VO_2) [49], germanium-antimony-tellurium (GeSbTe or GST) [50], germanium-antimony-selenium-tellurium

(GeSbSeTe or GSST) [51], silver-indium-antimony-tellurium (AgInSbTe or AIST) [52], indium-antimony-tellurium (InSbTe or IST) [53], and many more. As PCMs can be efficiently switched from one phase (e.g., crystalline phase) to another phase (e.g., amorphous phase), they offer versatility in plasmonic applications and extraordinary capabilities to manipulate light while providing high switching speed, tunability, reconfigurability, and minimal losses [54, 55].

Vanadium dioxide (VO_2) is a phase change material with a bandgap energy of ~0.6 - 0.7 eV at room temperature, which undergoes transition from a semiconducting or insulating phase to a metallic phase at a transition temperature of ~68°C when triggered thermally [56], at a critical electric field of ~10^7 Vm^{-1} when triggered electrically [57], and at a picosecond to femtosecond timescales when triggered optically [58]. In the last two decades, VO_2 has been extensively employed as the PCM in various plasmonic switches due to multiple advantages such as the potential for a near-room temperature transition and ultra-fast switching speed, exhibiting minimal thermal hysteresis, and the ability to sustain millions of switching cycles without any deterioration in performance [59, 60]. VO_2 is generally preferred over other PCMs because its transition temperature is near room temperature and when triggered by optical radiation, the phase transition happens on a picosecond to a femtosecond timescale [61, 62]. The phase transition temperature can also be modulated by doping VO_2 with dopants such as tungsten (W), molybdenum (Mo), tantalum (Ta), and niobium (Nb) [63]. In addition, the state-of-the-art fabrication processes such as the sol-gel method, sputtering, pulsed laser deposition and others are widely available for the growth of VO_2 films [64]. It must be noted that although many oxides of vanadium such as vanadium trioxide (V_2O_3) and vanadium pentoxide (V_2O_5) are also capable of being used as switching materials at different wavelengths, higher order vanadium oxides tend to be inhomogeneous as well as porous which leads to degradation of the switching properties, thus making VO_2 the most commonly used vanadium oxide for switching applications [65, 66]. Plasmonic switches based on VO_2 can be utilized in telecommunication networks [67] and high-speed optical communication networks such as — wavelength division multiplexing (WDM) networks [68] and free space optical (FSO) networks [69]. They can also be employed in plasmonic logic circuits [70] and integrated photonic circuits [71]. Other futuristic applications of such plasmonic switches include, but are not limited to, super-resolution imaging [72], sensing [73], quantum computing [74], and neural networking [75].

1.2 Problem Statement and Motivation

The advancement of integrated photonic systems necessitates nanoscale optical components that are compact, high-speed, and energy-efficient. Plasmonic devices, by virtue of their ability to confine light beyond the diffraction limit, offer a viable route toward miniaturization and dense photonic integration. Among these, plasmonic switches are essential for enabling dynamic light manipulation in applications such as high-speed communication networks, optical computing, and signal routing. Phase change materials, particularly vanadium dioxide (VO_2), have gained prominence in active plasmonic switching due to their abrupt and reversible insulator-to-metal transition near room temperature, fast response times, and

compatibility with standard fabrication techniques. However, despite the demonstrated advantages of VO_2, several critical challenges remain unaddressed. Existing designs often rely on complex geometries or limited functional bandwidths, and do not fully exploit the potential of VO_2 for broadband, multi-wavelength, or near-field switching.

This research is driven by the need to develop simplified, high-performance plasmonic switch designs that leverage the phase transition properties of VO_2 for tunable, efficient, and scalable operation. The work aims to bridge current limitations by exploring nanostructures that enhance optical field confinement and switching contrast, while maintaining design simplicity and fabrication feasibility. Emphasis is placed on achieving broadband operation across communication bands, dual-wavelength switching, polarization-independent response, and strong near-field enhancement. By addressing these aspects, the thesis contributes toward the realization of practical, reconfigurable, and multi-functional nanophotonic devices, positioning VO_2-based plasmonic switches as key components for next-generation photonic platforms.

1.3 Research Objectives

This thesis addresses the research gaps through the design and modelling of VO_2-based plasmonic switches that combine simplified nanostructures with broadband and multi-wavelength operation. It further explores asymmetric nanostructures to enhance switching efficiency and investigates near-field switching dynamics, aiming to expand the functional capabilities of VO_2 in active nanophotonics. Hence, the following four research objectives had been formulated:

Objective 1: Design and modelling of broadband switches based on VO_2.

Objective 2: Design and modelling of multi-wavelength switches (C, L, U bands of communication) with high extinction ratios based on VO_2.

Objective 3: Electromagnetic modelling of near-field plasmonic switches by employing VO_2.

Objective 4: Exploration of asymmetric plasmonic nanostructures (geometric and multi-material) to achieve high electromagnetic enhancement for nanophotonic applications.

1.4 Thesis Organization

The thesis entitled “Design and modelling of nanophotonic devices” is divided into eight chapters, with each chapter dedicated to a particular component of the study. The first chapter provided an overview of the emerging field of nanophotonics, key concepts in plasmonics, the role of phase change materials — particularly vanadium dioxide (VO_2) — and the motivation behind using VO_2 for plasmonic switching. A brief overview of the subsequent chapters is provided below:

Chapter 2: Literature Review

This chapter presents a detailed review of the basics of plasmonics and phase change materials, as well as prior research on VO_2 based plasmonic switches. It examines various device configurations, switching mechanisms, and performance parameters reported over the past decades. The critical analysis helps identify existing gaps and challenges in current designs, thereby motivating the new designs proposed in the thesis.

Chapter 3: Finite Difference Time Domain Modelling

This chapter presents the numerical simulation methodology employed to investigate the optical behavior of the proposed plasmonic switches. The Finite Difference Time Domain (FDTD) technique, implemented using Ansys Lumerical FDTD Solver, is used to analyze light-matter interactions at the nanoscale. Additionally, the chapter outlines the preliminary structural designs and simulation setups used for modeling the nanophotonic devices.

Chapter 4: Broadband plasmonic switches based on nanodisc-dimers with progressively increasing diameters on a plasmonic film with a VO_2 spacer

This chapter presents the design and modelling of broadband plasmonic switches employing VO_2. The study investigates nanodisc-dimer arrays with progressively increasing diameters, which are designed to achieve wide spectral coverage of ~650 nm across the C, L, and U bands with extinction ratio up to 5 dB.

Chapter 5: VO_2 based polarization-independent dual-wavelength plasmonic switches using U and C shaped nanostructures

This chapter focuses on the design of plasmonic switches using arrays of U and C shaped gold nanostructures that operate simultaneously at dual wavelengths for all polarization angles of incident light. These structures demonstrate strong spectral selectivity and high extinction ratios of ~20 dB at 1560 nm and 2130 nm.

Chapter 6: Multi-wavelength and broadband plasmonic switching with V-shaped plasmonic nanostructures on a VO_2 coated plasmonic substrate

This chapter investigates the performance of arrays of identical V-shaped nanostructures (IVNSs) and variable V-shaped nanostructures (VVNSs) to realize multi-wavelength and broadband plasmonic switches, respectively. These configurations are shown to produce an extinction ratio of >12 dB at two wavelengths – 1320 nm and 2800 nm – using IVNSs and extinction ratio of >5 dB over an operational wavelength range >1400 nm in the near-IR spectral range spanning over all optical communication bands, i.e. the O, E, S, C, L and U bands, using VVNs.

Chapter 7: Electromagnetic modelling of near-field plasmonic switches based on fractal nanoantennas

This chapter explores the application of VO_2 in near-field plasmonic switches. Emphasis is placed on understanding the localized electromagnetic field distributions and the switching behavior induced by the phase transition in VO_2 to achieve high intensity switching ratio (ISR) >2200 by using the fractals of pentagon-shaped nanoantennas.

Chapter 8: Conclusions, Future scope, and Social impact

The final chapter presents a summary of the key findings of the research, highlighting the advantages of VO_2 based plasmonic designs in achieving broadband, multi-wavelength, polarization-independent, and near-field switching. It also outlines the limitations of the current work and proposes future directions, including experimental validation and exploration of other phase-change materials for dynamic nanophotonic applications.

1.5 References

[1] Novotny, L., and Hecht, B. *Principles of Nano-Optics*. Cambridge University Press, 2012. ISBN: 9780511794193. https://doi.org/10.1017/CBO9780511794193

[2] Zhang, S., *et al.* "Metasurfaces for biomedical applications: imaging and sensing from a nanophotonics perspective", *Nanophotonics*, 10(1), 259-293, 2020. https://doi.org/10.1515/nanoph-2020-0373

[3] Sajedi, S., Sabet, H., and Choi, H. S. "Intraoperative biophotonic imaging systems for image-guided interventions", *Nanophotonics*, 8(1), 99-116, 2018. https://doi.org/10.1515/nanoph-2018-0134

[4] Xiang, W., and Lee, C. "Nanophotonics sensor based on microcantilever for chemical analysis", *IEEE Journal of Selected Topics in Quantum Electronics*, 15(5), 1323-1326, 2009. https://doi.org/10.1109/JSTQE.2009.2016578

[5] Alexander, K., *et al.* "Nanophotonic Pockels modulators on a silicon nitride platform", *Nature Communications*, 9, 3444, 2018. https://doi.org/10.1038/s41467-018-05846-6

[6] Yariv, A., and Yeh, P. *Photonics: Optical electronics in modern communications*. Oxford University Press, 2007. ISBN: 9780195179460.

[7] Pshenichnyuk, I. A., Kosolobov, S. S., and Drachev, V. P. "Towards deep integration of electronics and photonics", *Applied Sciences*, 9(22), 4834, 2019. https://doi.org/10.3390/app9224834

[8] Maier, S. A. *Plasmonics: Fundamentals and Applications*. Springer, New York, USA, 2007. ISBN: 9780387331508. https://doi.org/10.1007/0-387-37825-1

[9] Ozbay, E. "Plasmonics: Merging photonics and electronics at nanoscale dimensions", *Science*, 311(5758), 189-193, 2006. https://doi.org/10.1126/science.1114849

[10] Maier, S. A., and Atwater, H. A. "Plasmonics: Localization and guiding of electromagnetic energy in metal/dielectric structures", *Journal of Applied Physics*, 98(1), 011101, 2005. https://doi.org/10.1063/1.1951057

[11] Pitarke, J. M., Silkin, V. M., Chulkov, E. V., and Echenique, P. M. "Theory of surface plasmons and surface-plasmon polaritons", *Reports on Progress in Physics*, 70(1), 1, 2006. https://doi.org/10.1088/0034-4885/70/1/R01

[12] Hutter E., and Fendler, J. H. “Exploitation of localized surface plasmon resonance”, *Advanced Materials*, 16(19), 1685-1706, 2004. https://doi.org/10.1002/adma.200400271

[13] Gramotnev, D. K., and Bozhevolnyi, S. I. “Plasmonics beyond the diffraction limit”, *Nature Photonics*, 4(2), 83-91, 2010. https://doi.org/10.1038/nphoton.2009.282

[14] Oulton, R. F., *et al.* “Plasmon lasers at deep subwavelength scale”, *Nature*, 461(7264), 629-632, 2009. https://doi.org/10.1038/nature08364

[15] Oulton, R. F., Sorger, V. J., Genov, D. A., Pile, D. F. P., and Zhang, X. “A hybrid plasmonic waveguide for subwavelength confinement and long-range propagation”, *Nature Photonics*, 2(8), 496-500, 2008. https://doi.org/10.1038/nphoton.2008.131

[16] Chen, A., *et al.* “Plasmonic amplifiers: Engineering giant light enhancements by tuning resonances in multiscale plasmonic nanostructures”, *Small*, 9(11), 1939-1946, 2013. https://doi.org/10.1002/smll.201202216

[17] Lu, H., Liu, X., Wang, G., and Mao, D. “Tunable high-channel-count bandpass plasmonic filters based on an analogue of electromagnetically induced transparency”, *Nanotechnology*, 23(44), 444003, 2012. https://doi.org/10.1088/0957-4484/23/44/444003

[18] Guo, Y., *et al.* “A plasmonic splitter based on slot cavity”, *Optics Express*, 19(15), 13831-13838, 2011. https://doi.org/10.1364/OE.19.013831

[19] Ellenbogen, T., Seo, K., and Crozier, K. B. “Chromatic plasmonic polarizers for active visible color filtering and polarimetry”, *Nano Letters*, 12(2), 1026-1031, 2012. https://doi.org/10.1021/nl204257g

[20] Ullah, H., Khan, A. D., Noman, M., and Rehman, A. U. “Novel multi-broadband plasmonic absorber based on a metal-dielectric-metal square ring array”, *Plasmonics*, 13, 591-597, 2018. https://doi.org/10.1007/s11468-017-0549-6

[21] Wang, Y., Li, T., and Zhu, S. “Graphene-based plasmonic modulator on a groove-structured metasurface”, *Optics Letters*, 42(12), 2247-2250, 2017. https://doi.org/10.1364/OL.42.002247

[22] Haghighi, S. B., Ghayour, R., and Sheikhi, M. H. “All-optical cross-bar switch based on a low-loss suspended graphene plasmonic coupler”, *Plasmonics*, 14, 447-456, 2018. https://doi.org/10.1007/s11468-018-0823-2

[23] Shackleford, J. A., Grote, R., Currie, M., Spanier, J. E., and Nabet, B. “Integrated plasmonic lens photodetector”, *Applied Physics Letters*, 94(8), 083501, 2009. https://doi.org/10.1063/1.3086898

[24] Sridarshini, T., and Gandhi, S. I. “Compact 3×3 wavelength routing for photonic integrated circuits”, *Photonic Network Communications*, 36, 68-81, 2018. https://doi.org/10.1007/s11107-018-0757-9

[25] Djavid, M., *et al.* “Photonic crystal-based permutation switch for optical networks”, *Photonic Network Communications*, 35, 90-96, 2018. https://doi.org/10.1007/s11107-017-0719-7

[26] Merlo, J. M., *et al.* “Wireless communication system via nanoscale plasmonic antennas”, *Scientific Reports*, 6, 31710, 2016. https://doi.org/10.1038/srep31710

[27] Wang, F., *et al.* “Nanoscale on-chip all-optical logic parity checker in integrated plasmonic circuits in optical communication range”, *Scientific Reports*, 6, 24433, 2016. https://doi.org/10.1038/srep24433

[28] Li, B., and Chua, S. J. *Optical Switches*. Woodhead Publishing, 2010. ISBN: 9781845695798.

[29] Carvalho, W. O. F., and Salazar, J. R. M. “Plasmonics for telecommunications applications”, *Sensors*, 20(9), 2488, 2020. https://doi.org/10.3390/s20092488

[30] Mynbaev, D. K., and Sukharenko, V. "Plasmonic-based devices for optical communications", *International Journal of High Speed Electronics and Systems*, 21(1), 1250006, 2012. https://doi.org/10.1142/S0129156412500061

[31] Nielsen, M. G., Bernardin, T., Hassan, K., Kriezis, E. E., and Weeber, J. "Silicon-loaded surface plasmon polariton waveguides for nanosecond thermo-optical switching", *Optics Letters*, 39(8), 2282-2285, 2014. https://doi.org/10.1364/OL.39.002282

[32] Sun, D. "A proposal for digital electro-optic switches with free-carrier dispersion effect and Goos-Hanchen shift in silicon-on-insulator waveguide corner mirror", *Journal of Applied Physics*, 114, 104502, 2013. https://doi.org/10.1063/1.4820378

[33] Smith, D. A., *et al.* "Evolution of the acousto-optic wavelength routing switch", *Journal of Lightwave Technology*, 14(6), 1005-1019, 1996. https://doi.org/10.1109/50.511601

[34] Bishop, A. I., and Barker, P. F. "Subnanosecond Pockels cell switching using avalanche transistors", *Review of Scientific Instruments*, 77, 044701, 2006. https://doi.org/10.1063/1.2194472

[35] Wang, Q., and Yao, J. "A high speed 2×2 electro-optic switch using a polarization modulator", *Optics Express*, 15(25), 16500-16505, 2007. https://doi.org/10.1364/OE.15.016500

[36] Khani, S., Danaie, M., and Rezaei, P. "All-optical plasmonic switches based on asymmetric directional couplers incorporating Bragg gratings", *Plasmonics*, 15, 869-879, 2020. https://doi.org/10.1007/s11468-019-01106-5

[37] Heidari, S., and Nozhat, N. "Wideband polarization-independent plasmonic switch based on GST phase-change material", *Applied Optics*, 61(14), 4068-4073, 2022. https://doi.org/10.1364/AO.456423

[38] Wurtz, G. A., *et al.* "Designed ultrafast optical nonlinearity in a plasmonic nanorod metamaterial enhanced by nonlocality", *Nature Nanotechnology*, 6, 107-111, 2011. https://doi.org/10.1038/nnano.2010.278

[39] Dickson, W., Wurtz, G. A., Evans, P. R., Pollard, R. J., and Zayats, A. V. "Electronically controlled surface plasmon dispersion and optical transmission through metallic hole arrays using liquid crystal", *Nano Letters*, 8(1), 281-286, 2008. https://doi.org/10.1021/nl072613g

[40] Pala, R. A., Shimizu, K. T., Melosh, N. A., and Brongersma, M. L. "A nonvolatile plasmonic switch employing photochromic molecules", *Nano Letters*, 8(5), 1506-1510, 2008. https://doi.org/10.1021/nl0808839

[41] Leroux, Y. R., *et al.* "Conducting polymer electrochemical switching as an easy means for designing active plasmonic devices", *Journal of the American Chemical Society*, 127(46), 16022-16023, 2005. https://doi.org/10.1021/ja054915v

[42] Farmani, A., Yavarian, M., Alighanbari, A., Miri, M., and Sheikhi, M. H. "Tunable graphene plasmonic Y-branch switch in the terahertz region using hexagonal boron nitride with electric and magnetic biasing", *Applied Optics*, 56(32), 8931-8940, 2017. https://doi.org/10.1364/AO.56.008931

[43] Thoniyot, P., Tan, M. J., Karim, A. A., Young, D. J. and Loh, X. J. "Nanoparticle–hydrogel composites: Concept, design, and applications of these promising, multi-functional materials", *Advanced Science*, 2, 1400010, 2015. https://doi.org/10.1002/advs.201400010

[44] Farmakidis, N., *et al.* "Electronically reconfigurable photonic switches incorporating plasmonic structures and phase change materials", *Advanced Science*, 9(20), 2200383, 2022. https://doi.org/10.1002/advs.202200383

[45] Gholipour, B., *et al.* "Phase-change-driven dielectric-plasmonic transitions in chalcogenide metasurfaces", *NPG Asia Materials*, 10, 533-539, 2018. https://doi.org/10.1038/s41427-018-0043-4

[46] Raoux, S., and Wuttig, M. *Phase Change Materials*. Springer, USA, 2009. ISBN: 9780387848730. https://doi.org/10.1007/978-0-387-84874-7

[47] Pergament, A. L., Boriskov, P. P., Velichko, A. A., and Kuldin, N. A. "Switching effect and the metal-insulator transition in electric field", *Journal of Physics and Chemistry of Solids*, 71(6), 874-879, 2010. https://doi.org/10.1016/j.jpcs.2010.03.032

[48] Siegrist, T., *et al.* "Disorder-induced localization in crystalline phase-change materials", *Nature Materials*, 10, 202-208, 2011. https://doi.org/10.1038/nmat2934

[49] Sanchez, L., Lechago, S., Gutierrez, A., and Sanchis, P. "Analysis and design optimization of a hybrid VO_2/Silicon 2×2 microring switch", *IEEE Photonics Journal*, 8(2), 1-9, 2016. https://doi.org/10.1109/JPHOT.2016.2551463

[50] Zareizadeh, A., and Nozhat, N. "GST plasmonic gap structure investigation as a switch and sensor", *Applied Optics*, 62(23), 6156-6162, 2023. https://doi.org/10.1364/AO.497742

[51] Jiang, W. "Nonvolatile and ultra-low-loss reconfigurable mode (De) multiplexer/switch using triple-waveguide coupler with $Ge_2Sb_2Se_4Te_1$ phase change material", *Scientific Reports*, 8, 15946, 2018. https://doi.org/10.1038/s41598-018-34419-2

[52] Xiao, Z. F., *et al.* "Bipolar resistive switching effect in laser-induced crystallization AgInSbTe films", *Optik*, 180, 271-275, 2019. https://doi.org/10.1016/j.ijleo.2018.11.100

[53] Hebler, A., Conrads, L., Wirth, K. G., Wuttig, M., and Taubner, T. "Reconfiguring magnetic infrared resonances with the plasmonic phase-change material In_3SbTe_2", *ACS Photonics*, 9(5), 1821-1828, 2022. https://doi.org/10.1021/acsphotonics.2c00432

[54] Li, P., *et al.* "Reversible optical switching of highly confined phonon–polaritons with an ultrathin phase-change material", *Nature Materials*, 15, 870-875, 2016. https://doi.org/10.1038/nmat4649

[55] Zhang, Y., *et al.* "Broadband transparent optical phase change materials for high-performance nonvolatile photonics", *Nature Communications*, 10, 4279, 2019. https://doi.org/10.1038/s41467-019-12196-4

[56] Huang, Y., *et al.* "Phase transition analysis of thermochromic VO_2 thin films by temperature-dependent Raman scattering and ellipsometry", *Applied Surface Science*, 456(31), 545-551, 2018. https://doi.org/10.1016/j.apsusc.2018.06.125

[57] Wu, B., *et al.* "Electric-field-driven phase transition in vanadium dioxide", *Physical Review B*, 84(24), 241410(R), 2011. https://doi.org/10.1103/PhysRevB.84.241410

[58] Becker, M. F., Buckman, A. B., and Walser, R. M. "Femtosecond laser excitation of the semiconductor-metal phase transition in VO_2", *Applied Physics Letters*, 65(12), 1507, 1994. https://doi.org/10.1063/1.112974

[59] Gurunatha, K. L., *et al.* "Combined effect of temperature induced strain and oxygen vacancy on metal-insulator transition of VO_2 colloidal particles", *Advanced Functional Materials*, 30(49), 2005311, 2020. https://doi.org/10.1002/adfm.202005311

[60] Rincon, J. A. R., *et al.* "Thermal hysteresis measurement of the VO_2 dielectric function for its metal-insulator transition by visible-IR ellipsometry", *Journal of Applied Physics*, 124(19), 195102, 2018. https://doi.org/10.1063/1.5049747

[61] Messaoud, T. B., *et al.* "High contrast optical switching in vanadium dioxide thin films", *Optics Communications*, 281(24), 6024-6027, 2008. https://doi.org/10.1016/j.optcom.2008.09.027

[62] Donges, S. A., *et al.* "Ultrafast nanoimaging of the photoinduced phase transition dynamics in VO_2", *Nano Letters*, 16(5), 3029-3035, 2016. https://doi.org/10.1021/acs.nanolett.5b05313

[63] Jorgenson, G. V., and Lee, J. C. "Doped vanadium oxide for optical switching films", *Solar Energy Materials*, 14(3-5), 205-214, 1986. https://doi.org/10.1016/0165-1633(86)90047-X

[64] Wang, H., Yi, X., Chen, S., and Fua, X. “Fabrication of vanadium oxide micro-optical switches”, *Sensors and Actuators A: Physical*, 122(1), 108-112, 2005. https://doi.org/10.1016/j.sna.2005.03.063

[65] Lamsal, C., and Ravindra, N. M. “Optical properties of vanadium oxides - An analysis”, *Journal of Materials Science*, 48, 6341-6351, 2013. https://doi.org/10.1007/s10853-013-7433-3

[66] Huang, T., *et al.* “Study of the phase evolution, metal-insulator transition, and optical properties of vanadium oxide thin films”, *Optical Materials Express*, 6(11), 3609-3621, 2016. https://doi.org/10.1364/OME.6.003609

[67] Karimi, Y., Kaatuzian, H., Tooghi, A., and Danaie, M. “All-optical plasmonic switches based on Fano resonance in an X-shaped resonator coupled to parallel stubs for telecommunication applications”, *Optik*, 243, 167424, 2021. https://doi.org/10.1016/j.ijleo.2021.167424

[68] Papaioannou, S., *et al.* “Active plasmonics in WDM traffic switching applications”, *Scientific Reports*, 2, 652, 2012. https://doi.org/10.1038/srep00652

[69] Jamali, V., *et al.* “Intelligent reflecting surface assisted free-space optical communications”, *IEEE Communications Magazine*, 59(10), 57-63, 2021. https://doi.org/10.1109/MCOM.001.2100406

[70] Ghosh, R. R., and Dhawan, A. “Integrated non-volatile plasmonic switches based on phase-change-materials and their application to plasmonic logic circuits”, *Scientific Reports*, 11, 18811, 2021. https://doi.org/10.1038/s41598-021-98418-6

[71] Nisar, M. S., Yang, X., Lu, L., Chen, J., and Zhou, L. “On-chip integrated photonic devices based on phase change materials”, *Photonics*, 8(6), 205, 2021. https://doi.org/10.3390/photonics8060205

[72] Wu, H. Y., *et al.* “Ultrasmall all-optical plasmonic switch and its application to superresolution imaging”, *Scientific Reports*, 6, 24293, 2016. https://doi.org/10.1038/srep24293

[73] Nejat, M., and Nozhat, N. “Analytical methods of equivalent circuit model and transmission matrix for a plasmonic switch with sensing capability in near-infrared region”, *Plasmonics*, 15, 1459-1470, 2020. https://doi.org/10.1007/s11468-020-01167-x

[74] Hatef, A., Zamani, N., and Johnston, W. “Coherent control of optical absorption and the energy transfer pathway of an infrared quantum dot hybridized with a VO_2 nanoparticle”, *Journal of Physics: Condensed Matter*, 29(15), 155305, 2017. https://doi.org/10.1088/1361-648X/aa61ee

[75] Zhou, X., *et al.* “Phase-transition-induced VO_2 thin film IR photodetector and threshold switching selector for optical neural network applications”, *Advanced Electronic Materials*, 7(5), 2001254, 2021. https://doi.org/10.1002/aelm.202001254

CHAPTER 2

LITERATURE REVIEW

2.0 Chapter Overview

This chapter provides a detailed overview of the fundamentals and advancements in plasmonics and vanadium dioxide (VO_2)-based plasmonic switches. It begins with the basic principles of plasmonics, discussing the excitation of surface plasmon polaritons (SPPs) and localized surface plasmon resonances (LSPRs), their dispersion relations, and field enhancement effects at metal-dielectric interfaces. These concepts form the basis for understanding light confinement and manipulation at the nanoscale. The discussion then focuses on different phase change materials available in literature to achieve optical switching and the underlying mechanism of the phase transition. In particular, a comprehensive review of the recent advancements in the design and development of plasmonic switches based on VO_2 is presented. These switches are employed in applications such as integrated photonics, plasmonic logic circuits and computing networks for light routing and switching, and are based on the switching of the plasmonic properties under the effect of an external stimulus. In the last few decades, VO_2 based plasmonic switches have seen a significant growth because of their ultra-fast switching speed, wide spectral tunability, ultra-compact size, and low losses. Subsequently, an exhaustive review and comparison of the current state-of-the-art plasmonic switches based on VO_2 proposed in the last decades is carried out. As the phase transition in VO_2 can be activated by application of temperature, voltage or optical light pulses, the literature review has been categorized into thermally-activated, electrically-activated, and optically-activated plasmonic switches based on VO_2 operating in the visible, near-infrared, infrared and terahertz frequency regions.

2.1 Introduction to Plasmonics

Plasmonics [1-4] is a rapidly growing branch of nanophotonics that examines how electromagnetic waves interact with free electrons in metallic nanostructures. The field is rooted in the fundamental concept of plasmons — collective oscillations of conduction electrons induced by an external electromagnetic field. When light interacts with metallic structures smaller than or comparable to its wavelength, the oscillations of these free electrons can couple to the electromagnetic wave, giving rise to a range of phenomena that enable strong localization and manipulation of light at subwavelength scales. This property forms the foundation of plasmonics, bridging the gap between electronics and photonics and enabling optical functionalities beyond the diffraction limit.

2.1.1 Electromagnetic foundations of plasmonics

The optical behavior of metals can be understood using Maxwell's equations and the constitutive relation between the electric field E, the displacement

field D, and the material's permittivity $\varepsilon(\omega)$. For metals, the permittivity is complex and frequency-dependent:

$$\varepsilon(\omega) = \varepsilon'(\omega) + i\varepsilon''(\omega) \tag{2.1}$$

where the real part, $\varepsilon'(\omega)$, governs dispersion and the imaginary part, $\varepsilon''(\omega)$, represents absorption losses. The Drude model [5], which describes the free electron response in metals, expresses this relation as

$$\varepsilon(\omega) = \varepsilon_\infty - \frac{\omega_p^2}{\omega^2 + i\gamma\omega} \tag{2.2}$$

where ω_p is the plasma frequency, γ the electron collision rate, and ε_∞ accounts for interband transitions.

When $\varepsilon'(\omega)$ becomes negative at optical frequencies (typically below ω_p), electromagnetic waves cannot propagate freely in the bulk metal but can instead exist as bound surface modes at the interface between the metal and a dielectric. This phenomenon underpins the formation of surface plasmons.

2.1.2 Classification of plasmons

Plasmons represent quantized modes of electron oscillations and can be broadly categorized based on their spatial confinement:

- Bulk plasmons correspond to longitudinal oscillations of conduction electrons within the metallic volume. Their characteristic plasma frequency, $\omega_p = \sqrt{ne^2/(\varepsilon_0 m_e)}$, depends on the free electron density n.
- Surface plasmons, in contrast, arise at metal–dielectric interfaces, where collective electron oscillations couple with the transverse electromagnetic field. When these surface modes interact with photons, they generate surface plasmon polaritons (SPPs) — electromagnetic waves confined to and propagating along the interface.

2.1.3 Surface plasmon polaritons (SPPs)

Surface Plasmon Polaritons (SPPs) [1, 3, 6-8] are transverse magnetic (TM) polarized electromagnetic modes bound to the metal–dielectric interface (See Fig. 2.1(a)). They propagate along the surface while decaying exponentially perpendicular to it, both in the dielectric and in the metal [9]. Their dispersion relation is obtained by solving Maxwell's equations subject to the appropriate boundary conditions at the interface, yielding:

$$k_{SPP} = k_0 \sqrt{\frac{\varepsilon_m(\omega)\varepsilon_d(\omega)}{\varepsilon_m(\omega) + \varepsilon_d(\omega)}} \tag{2.3}$$

where $k_0 = \omega/c$ is the free-space wave number, and ε_m and ε_d are the permittivities of the metal and dielectric, respectively.

Because $k_{SPP} > k_0 n_d$, the in-plane wave vector of the SPP is greater than that of a freely propagating photon in the dielectric medium. This mismatch prevents direct coupling between incident light and the surface plasmon mode in free space, necessitating specialized excitation schemes such as prism or grating coupling (discussed later in section 2.1.4).

The dispersion relation characterizes how the angular frequency ω of an electromagnetic mode varies with its propagation constant k_x (See Fig. 2.1(b)). For dispersive systems like plasmonic interfaces, this relationship reveals crucial information about the wave's group velocity, phase velocity, and confinement properties [6, 10, 11].

Using Eq. 2.3, the general form of the dispersion relation for a surface plasmon polariton can be expressed as:

$$k_x = k_0 \sqrt{\frac{\varepsilon_1(\omega)\varepsilon_2(\omega)}{\varepsilon_1(\omega) + \varepsilon_2(\omega)}} \tag{2.4}$$

where ε_1 and ε_2 denote the dielectric constants of the dielectric medium and the metallic substrate, respectively.

To model the metal (medium 2), the Drude formulation [5] can be applied:

$$\varepsilon_2(\omega) = 1 - \frac{\omega_p^2}{\omega^2} \tag{2.5}$$

where ω_p is the bulk plasma frequency. Substituting this into the dispersion equation provides insight into how k_x evolves with frequency.

At low frequencies, where $\varepsilon_2 \to -\infty$, the dispersion relation approaches:

$$k_x \approx \frac{\omega}{c}\sqrt{\varepsilon_1} \tag{2.6}$$

which corresponds to the light line in the dielectric medium (denoted as curve "A" in Fig. 2.1(b)). In this regime, the SPP mode behaves similarly to a freely propagating light wave in the dielectric.

As the frequency increases toward the surface plasmon resonance frequency (ω_{SP}), the condition for resonance can be derived by setting $\varepsilon_2(\omega) = -\varepsilon_1$.

Using the Drude expression, this leads to:

$$1 - \frac{\omega_p^2}{\omega_{SP}^2} = -\varepsilon_1 \tag{2.7}$$

which simplifies to:

$$\omega_{SP} = \frac{\omega_p}{\sqrt{1 + \varepsilon_1}} \tag{2.8}$$

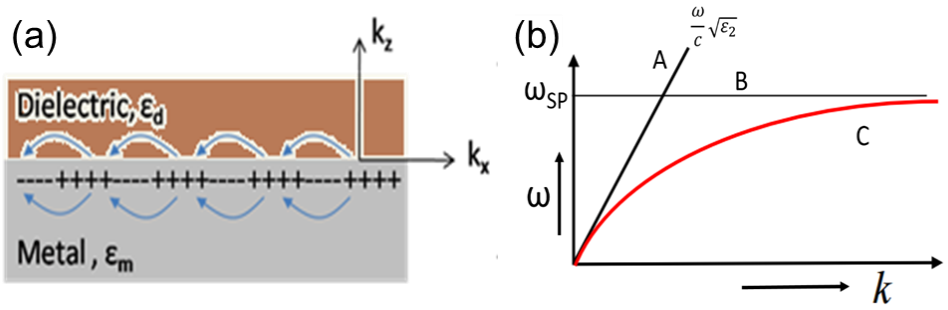

Fig. 2.1 (a) Excitation of surface plasmons at the metal-dielectric interface. **(b)** Dispersion relation curve for a surface plasmon polariton [6].

This frequency defines the asymptotic limit of the SPP dispersion relation, beyond which the SPP mode cannot propagate. The resulting dispersion curve (curve "C" in Fig. 2.1(b)) thus begins near the light line at low frequencies and gradually bends, asymptotically approaching ω_{SP} at high wave numbers.

This characteristic flattening of the curve signifies increasing field confinement and reduced group velocity, both hallmarks of SPP behavior near resonance. The group velocity $v_g = d\omega/dk$ tends toward zero as $\omega \rightarrow \omega_{SP}$, indicating that the plasmon mode becomes highly localized at the interface.

2.1.4 Excitation of surface plasmons

The direct excitation of surface plasmons by free-space light is fundamentally restricted due to the momentum mismatch between photons and surface plasmon polaritons (SPPs). As described earlier, the propagation constant of SPPs (k_{SPP}) is always greater than that of light in the adjacent dielectric medium ($k_0 n_d$), i.e., $k_{SPP} > k_0 n_d$. Therefore, a photon in free space does not naturally possess sufficient in-plane momentum to couple with the surface plasmon mode [3, 6]. To overcome this mismatch, prism coupling schemes are employed, where the incident light is passed through a high-refractive-index medium to enhance its in-plane wavevector component, thereby matching the SPP dispersion curve. Two such commonly used prism-based excitation arrangements are the Otto and Kretschmann configurations.

2.1.4.1 Otto configuration

The Otto configuration [12], proposed by Otto in 1968, utilizes an optical prism of high refractive index separated from the metallic surface by a narrow dielectric gap (typically an air gap of around 80-100 nm) as shown in Fig. 2.2(a). When light is incident from within the prism at an angle exceeding the critical angle for total internal reflection (TIR), an evanescent field is generated at the prism-air interface. This evanescent wave, though non-propagating, penetrates slightly beyond the interface and can tunnel across the thin air gap to reach the metal surface. If the in-plane component of this evanescent wave matches the propagation constant of the SPP mode at the metal-air interface, resonance coupling occurs, leading to efficient excitation of surface plasmons.

The Otto configuration effectively uses the evanescent field as a momentum-matching mechanism, enabling the conversion of incident photons into surface plasmon modes. However, the practical realization of this setup is limited by the mechanical difficulty in maintaining a uniform and sub-100 nm air gap between the prism and metal, which is critical for stable and reproducible coupling.

2.1.4.2 Kretschmann configuration

To address the mechanical constraints of the Otto setup, Kretschmann in 1968 proposed a modified configuration in which the thin metallic film is directly deposited on the base of the high-refractive-index prism as shown in Fig. 2.2(b). In this Kretschmann configuration [13], the light is incident from within the prism onto the metal film at an angle greater than the critical angle, ensuring TIR at the prism-metal interface. The resulting evanescent wave penetrates through the thin metal layer and excites surface plasmons at the outer metal-air interface.

This arrangement eliminates the need for an air gap, simplifying the experimental geometry and enhancing reproducibility. The thickness of the metallic layer is typically optimized (≈ 40-60 nm) to balance between sufficient transmission of the evanescent field and minimal propagation losses within the metal. When resonance is achieved, a sharp dip appears in the reflectance spectrum, corresponding to the surface plasmon resonance (SPR) condition.

Mathematically, for an incident beam at an angle θ to the normal, the in-plane component of the wavevector parallel to the metal surface can be expressed as:

$$k_x = \sqrt{\varepsilon_d}\,\frac{\omega}{c}\,sin\theta \tag{2.9}$$

where ε_d is the dielectric constant of the prism medium.

The resonance condition for coupling to SPPs is therefore given by:

$$k_x = k_{SPP}; \qquad \sqrt{\varepsilon_d}\,\frac{\omega}{c}\,sin\theta = \frac{\omega}{c}\sqrt{\frac{\varepsilon_m \varepsilon_a}{\varepsilon_m + \varepsilon_a}} \tag{2.10}$$

where ε_m and ε_a are the dielectric constants of the metal and the adjacent medium (air), respectively.

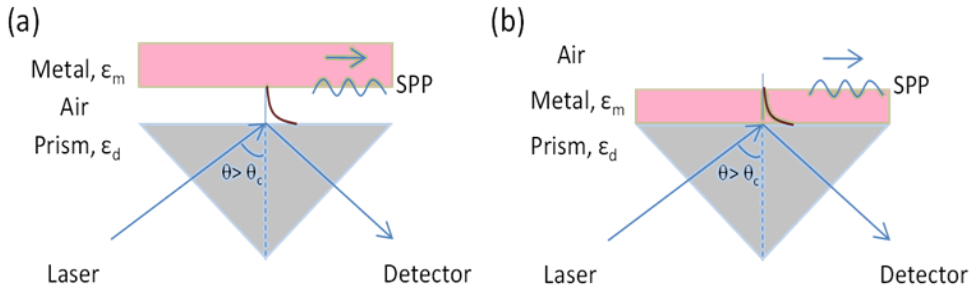

Fig. 2.2 Excitation of surface plasmons with **(a)** Otto configuration [12] and **(b)** Kretschmann configuration [13].

During experimentation, the surface plasmon resonance can be identified either by wavelength interrogation [14], where the wavelength of the incident light is varied at a fixed angle; or by angular interrogation [15], where the incident angle is varied for a fixed wavelength. In both methods, a distinct minimum in the reflected intensity corresponds to the excitation of SPPs, representing the SPR resonance condition.

2.1.5 Localized surface plasmon resonance (LSPR)

While surface plasmon polaritons (SPPs) correspond to propagating electromagnetic surface waves traveling along a metal-dielectric interface, localized surface plasmons (LSPs) represent non-propagating oscillations of the conduction electron cloud confined within metal nanoparticles or nanostructures [16-19]. These oscillations occur when incident electromagnetic radiation interacts with the conduction electrons of the nanoparticle, driving them collectively against the positive ion background [1, 3]. The restoring force experienced by these displaced electrons, arising from the nanoparticle's curved geometry, gives rise to a resonance condition known as Localized Surface Plasmon Resonance (LSPR). This resonance results in significant amplification of the local electromagnetic field near the nanoparticle surface [20].

Unlike SPPs — which require specialized coupling schemes such as prism or grating coupling to overcome momentum mismatch — LSPs can be excited directly by light incident at virtually any angle. The curvature of the nanoparticle surface inherently provides the necessary momentum matching conditions, allowing for strong light-matter interaction even under normal incidence. Fig. 2.3(a) conceptually illustrates the oscillation of the free electron cloud relative to the fixed ionic background within a metallic nanoparticle under illumination.

When a metallic nanoparticle is exposed to an oscillating electric field, a dipole moment is induced within the particle, producing an enhanced electric field both inside and around it. The quasi-static approximation [21] is generally invoked to describe this interaction, assuming that the nanoparticle dimensions are much smaller

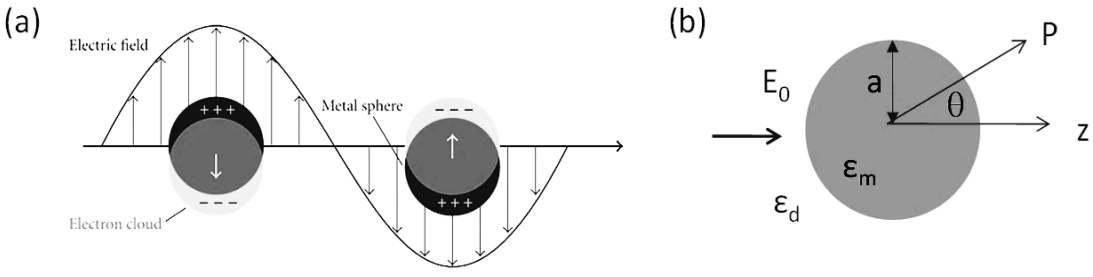

Fig. 2.3 (a) Illustration showing the collective oscillation of the conduction electron cloud within a metallic nanoparticle under localized surface plasmon resonance (LSPR). **(b)** A schematic representation of a metallic nanoparticle of radius a and dielectric constant ε_m, embedded in a surrounding dielectric medium of dielectric constant ε_d. An external electric field of magnitude E_0 is applied as indicated, where P denotes the position vector corresponding to a point of observation [1].

than the wavelength of the incident light in the surrounding medium. Under this assumption, the incident field is approximately uniform across the particle, and the phase variation of the electromagnetic wave over the nanoparticle volume can be neglected. Consequently, the problem can be analyzed electrostatically by solving Laplace's equation ($\nabla^2\Phi = 0$) with appropriate boundary conditions at the metal-dielectric interface.

Consider a spherical metallic nanoparticle of radius a and dielectric constant ε_m, embedded in a homogeneous dielectric environment of dielectric constant ε_d, as illustrated in Fig. 2.3(b). When an external electric field E_0 is applied along the z-axis, the scalar potential Φ satisfies Laplace's equation both inside (Φ_{in}) and outside (Φ_{out}) the particle. The general solutions, obtained using Legendre polynomials [22], are as follows:

$$\Phi_{in} = -\frac{3\varepsilon_d}{\varepsilon_m + 2\varepsilon_d} E_0 r\cos\theta \tag{2.11}$$

$$\Phi_{out} = -E_0 r\cos\theta + \frac{\varepsilon_m - \varepsilon_d}{\varepsilon_m + 2\varepsilon_d} E_0 \frac{a^3\cos\theta}{r^2} \tag{2.12}$$

where ε_m and ε_d denote the complex dielectric functions of the metal and surrounding medium, respectively; r is the distance from the nanoparticle center, and θ is the angle between r and the applied field direction. The second term in Eq. (2.12) represents the scattered or induced dipole field outside the nanoparticle, which contributes to local field enhancement.

The resonance condition for the localized surface plasmon is achieved when the denominator of the enhancement term, ($\varepsilon_m + 2\varepsilon_d$), approaches zero. At this point, the induced dipole moment and local field reach their maximum amplitude. This yields the Fröhlich condition [23] for LSPR:

$$Re\{\varepsilon_m(\omega)\} = -2\varepsilon_d \tag{2.13}$$

Here, $\varepsilon_m(\omega)$ is the frequency-dependent complex dielectric function of the metal. The condition implies that resonance occurs when the real part of the metal's permittivity equals minus twice that of the surrounding medium. Metals such as gold (Au), silver (Ag), and aluminum (Al) exhibit this condition in the visible to near-infrared spectral range. The dielectric response of these metals can be described using dispersion models like the Drude, Lorentz, or Drude-Lorentz formulations, which incorporate parameters such as the plasma frequency (ω_p) and damping constant (γ).

From the electrostatic potential expressions, the corresponding electric fields can be derived using $E = -\nabla\Phi$. Thus, the internal and external electric fields are given as [1, 3]:

$$E_{in} = \frac{3\varepsilon_d}{\varepsilon_m + 2\varepsilon_d} E_0 \tag{2.14}$$

$$E_{out} = E_0 + \frac{1}{4\pi\varepsilon_0\varepsilon_d}\frac{3(n.p)n - p}{r^3} \tag{2.15}$$

where n is the unit vector from the nanoparticle center to the observation point, and p is the induced dipole moment given by:

$$p = 4\pi\varepsilon_0\varepsilon_d a^3 \frac{\varepsilon_m - \varepsilon_d}{\varepsilon_m + 2\varepsilon_d} E_0 \tag{2.16}$$

At resonance, when the Fröhlich condition is satisfied, the denominator of the polarizability term approaches zero, leading to a sharp increase in $|p|$ and consequently a substantial amplification of the local electric field around the nanoparticle. This enhanced near-field region is often referred to as an "electromagnetic hotspot", where the electric field intensity can exceed that of the incident field by several orders of magnitude.

Numerical simulations and experimental studies reveal that for a gold nanosphere of diameter ~20 nm, the strongest field enhancement occurs around a wavelength of approximately 520-530 nm [24]. These local enhancements are directionally dependent and align with the polarization axis of the incident field. Variations in particle geometry — such as transitioning from spherical to rod-shaped, cubic, or polygonal structures — lead to distinct LSPR spectral signatures [25]. Such structural diversity enables tuning of the resonance wavelength across the visible and near-infrared regimes by controlling nanoparticle shape, size, aspect ratio, and dielectric environment.

Furthermore, when multiple nanoparticles are brought into close proximity [26], their localized fields can interact through dipole–dipole coupling, giving rise to coupled plasmonic modes. These interactions generate intense hotspots within interparticle gaps, often only a few nanometers wide, greatly amplifying the electromagnetic field in those regions. Such coupled resonances are the foundation of many advanced plasmonic devices, including plasmonic switches and nanoscale optical antennas.

2.2 Phase Change Materials

Phase Change Materials (PCMs) constitute a unique class of functional materials capable of exhibiting reversible transitions between distinct structural phases, often accompanied by dramatic variations in their optical, electrical, and thermal properties [27, 28]. These phase transitions can be triggered thermally, optically, or electrically, and are typically characterized by a significant change in refractive index and electrical conductivity. The reversible and repeatable nature of such transformations makes PCMs highly attractive for use in non-volatile memory, reconfigurable photonic devices, and tunable plasmonic systems [29, 30].

PCMs are broadly categorized based on the nature of their phase transition. The two most widely investigated families are vanadium oxides, particularly vanadium dioxide (VO_2), and chalcogenide alloys, such as germanium–antimony–telluride

($Ge_2Sb_2Te_5$, commonly known as GST), GeTe, and many more. Each of these materials exhibits distinct mechanisms governing their phase change behavior, thereby offering different advantages for specific device applications [30].

A comparative analysis of different PCMs is presented in Table 2.1. In summary, phase change materials — particularly VO_2 and chalcogenide alloys like GST — serve as a versatile foundation for the development of reconfigurable photonic and plasmonic systems. Their ability to undergo rapid, reversible, and controllable phase transitions provides an effective means to achieve dynamic modulation of optical properties, positioning them as key enablers for next-generation photonic computing, optical communication, and integrated nanophotonic technologies. Chalcogenide alloys based PCMs are particularly employed for designing optical storage devices. However, the focus of this thesis is to design plasmonic switches so VO_2 is chosen as the preferred PCM.

Table 2.1 Comparison of VO_2 with other phase change materials

Property	**VO_2**	**GST (GeSbTe)**	**GSST (GeSbSeTe)**	**AIST (AgInSbTe)**	**IST (InSbTe)**
Transition Type	Metal – Insulator	Amorphous – Crystalline	Amorphous – Crystalline	Amorphous – Crystalline	Amorphous – Crystalline
Transition Temperature	~68 °C [31] (Flexible with doping)	~160 °C [32]	~320 °C [32]	~165 °C [33]	~300 °C [34]
Switching timescale	Femtoseconds [35]	Nanoseconds [36]	Milliseconds [37]	Microseconds [33]	Nanoseconds [38]
Fabrication Complexity / Techniques	Requires epitaxial control; typically grown by Pulsed Laser Deposition (PLD), RF sputtering, or MOCVD on lattice-matched substrates (e.g., TiO_2, sapphire)	RF/DC sputtering or thermal evaporation on Si/SiO_2; CMOS-compatible; annealing ~200 °C	Co-sputtering or PLD with Se-target; precise stoichiometry control needed to minimize Se volatility	RF co-sputtering with multi-target calibration; low deposition temperature (~150 °C); post-anneal for crystallization	Sputtering or MBE; single-phase uniformity easier than AIST; compatible with Si wafers; annealing ~180 °C
Applications	Smart windows, ultrafast optical switches, THz modulators	PCM/PRAM, optical data storage, neuromorphic computing	Infrared photonics, low-loss tunable waveguides, metasurfaces	Fast non-volatile memory, reconfigurable photonics	Logic-memory integration, on-chip memory arrays

2.2.1 Vanadium dioxide (VO_2)

Ever since the discovery of vanadium dioxide (VO_2) in 1959, where Morin [39] demonstrated the metal to insulator transition (MIT) in the oxides of vanadium at Neel temperature, VO_2 has been of immense interest to researchers due to its intriguing properties. In 1967, Mitsuishi [40] further studied the phase transformation of VO_2 by optical microscopy and X-ray diffraction. In 1975, Zylbersztejn and Mott [41] described the properties of VO_2 phase transition in terms of magnetic susceptibility by using the band structure approach. In 1981, the critical behavior of the plasmon resonance at the MIT of VO_2 was studied by Bianconi *et al.* [42] with the help of thermo-reflectance spectra, where they observed a large red-shift of plasmon resonance in VO_2. In 1996, Dachuan *et al.* [43] demonstrated a novel method for fabrication of VO_2 films which could exhibit good switching properties in terms of resistivity change of 4-5 orders of magnitude at ~60°C. Since VO_2 was emerging out to be a promising switching material and the field of plasmonics was growing with it in parallel in the late 20th century and early 21st century, VO_2 began to be employed for plasmonic switching. Some of the initial reports of plasmonic switching employing VO_2 as the phase change material included the use of VO_2 nanoparticles by Lopez *et al.* [44], Au-VO_2 nano-composites by Maaza *et al.* [45], nanograin-VO_2 by Gentle *et al.* [46], and many others [47-49].

2.2.2 Phase transition in VO_2

Over the years, the first order phase transition in VO_2 from its low-temperature semiconducting state to its high-temperature metallic state has been explained as a structure-distortion-driven Peierls transition [50, 51], an electron-correlation-driven Mott transition [52, 53], or as a combination of the two mechanisms [54, 55]. The exact mechanism of phase transition is still controversial but has been studied intricately during the last two decades by employing spatial, spectral, thermal and time-resolved techniques along with theoretical analysis of the transition. It has been broadly concluded that the transition is characterized by an interplay of lattice distortion and electronic correlation.

The fundamental crystal structures of VO_2 [56] in its tetragonal and monoclinic phases are shown in Fig. 2.4(a). The tetragonal phase of VO_2 has a symmetric rutile crystal structure with $P4_2/mnm$ space-group symmetry whereas the monoclinic phase of VO_2 has $P2_1/c$ space-group symmetry [57, 58]. In its high temperature rutile phase, the crystal structure is composed of vanadium atoms evenly spaced at the center of edge-sharing oxygen octahedra. The vanadium atoms are separated by a finite distance of 2.85 $\dot{A}$ from each other and form linear chains along the c_R axis (depicted as x-axis in Fig. 2.4(a)). The phase transition of VO_2 from the tetragonal to the monoclinic phase was initially explained as a Peierls transition by Goodenough [59] in 1971. He suggested that the octahedral crystal field in the tetragonal (R) phase splits the V_{3d} orbital into two higher e_g and three lower t_{2g} levels. Therefore, in the oxidation state V^{4+}, the valence electron of vanadium can occupy any of the three t_{2g} levels. The t_{2g} orbitals are further differentiated into a singlet $d_{||}$ and a doublet π^* with bonding and antibonding nature along the c_R axis. It can be observed

from the band structure shown in Fig. 2.4(b) that the Fermi level lies between the π^* band and the $d_{||}$ band in case of the tetragonal phase and thus depicts the electric conductivity of the metallic state. During the phase transition from the tetragonal (R) to the monoclinic phase (M_1), the V^{4+} ions tend to move away from the interstitial position because of a dimerization along the (001) direction in combination with a ferroelectric distortion along the (110) and $(1\bar{1}0)$ directions of the tetragonal unit cell [60, 61]. This orthorhombic distortion of the octahedra causes the formation of different axial and equatorial V-O bonds. The vanadium ions (V^{4+} ions) form pairs along the c_R axis which leads to alternative short and long V-V distances of 2.65 $\dot{A}$ and 3.12 $\dot{A}$. Thus, each of the interpenetrating chain of V-V zig-zag pairs get surrounded by six oxygen atoms in an octahedral arrangement when VO_2 is in its monoclinic phase [62, 63]. Goodenough proposed that the basal-plane component of the ferroelectric distortion raises the energy of the π^* with respect to the $d_{||}$ band. The c_R component of distortion leads to the splitting of the $d_{||}$ band into two energy bands ($d_{||}$ band and $d_{||}^*$ band), thus opening a hybridization gap in the band structure. It can be seen from Fig. 2.4(b), that a forbidden band is formed between the $d_{||}$ band and the π^* band, thus explaining the semiconducting nature of the monoclinic phase (M_1). Goodenough's claims of the transition being a Peierls transition were also confirmed by Wentzcovitch *et al.* [64], Liebsch *et al.* [65], Budai *et al.* [66] and many others [67].

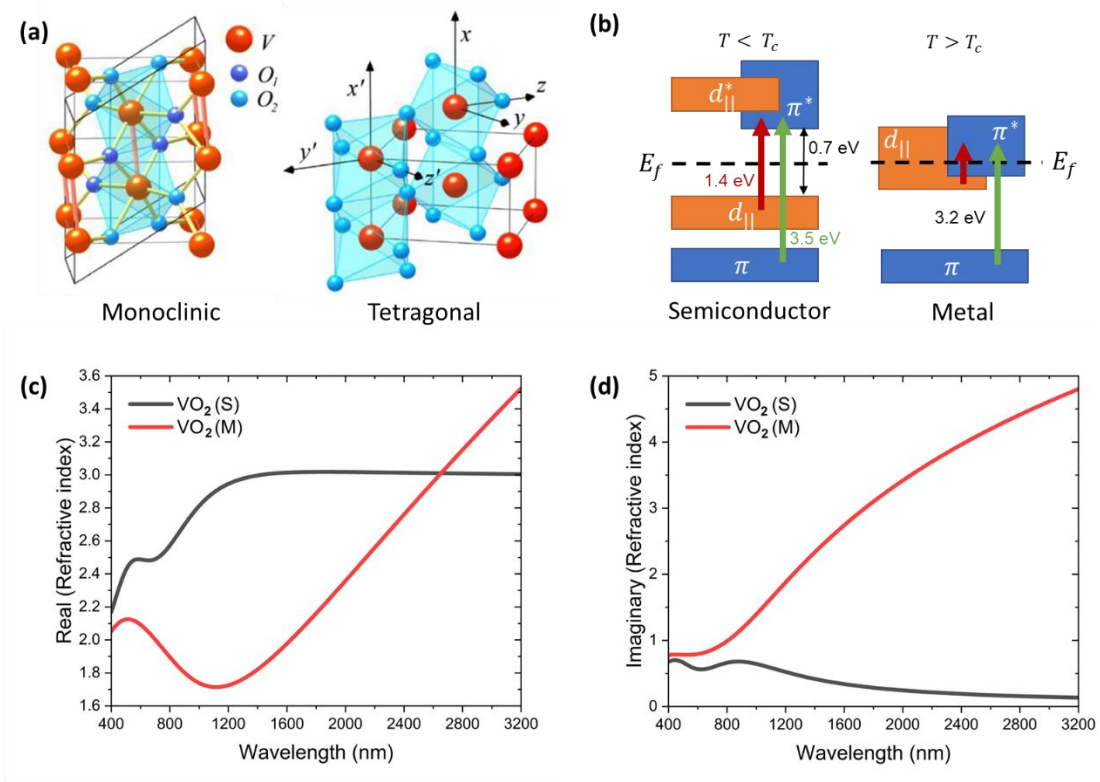

Fig. 2.4 (a) Crystal structures of VO_2 when it is in its monoclinic semiconducting phase and tetragonal metallic phase [68]. **(b)** Band structure for the monoclinic semiconducting phase and tetragonal metallic phase of VO_2. **(c, d)** Real and imaginary parts of the complex refractive index of VO_2 in its monoclinic semiconducting phase (VO_2(S)) and tetragonal metallic phase (VO_2(M)), respectively.

Although the opening of the gap between the $d_{||}$ band and the π^* band due to the strong V-V dimerization in the monoclinic phase (M_1) is suggestive of the fact that the VO_2 transition is a Peierls transition, additional analysis by means of density functional theory (DFT) calculations showed that the large experimental bandgap of 0.6 eV in the M_1 phase cannot be explained by the structural distortions alone [64, 68]. In addition, it was also found that under uniaxial stress, hydrostatic pressure or when VO_2 is doped with chromium, aluminium and other dopants, another metastable monoclinic phase (M_2) appears [69, 70]. In the M_2 phase, half of the vanadium atoms are paired along the c_R axis, and the others undergo a zig-zag distortion along the c_R axis. The existence of this metastable phase with localized electrons in zig-zag chains cannot be explained by the Peierls transition and is suggestive of the fact that electron correlations (Mott-transition) also play a role in the metal-to-insulator transition (MIT) of VO_2 [67].

To settle the controversy between a lattice distortion driven, or an electron correlation driven transition, it was suggested that the introduction of an additional Hubbard energy (Mott-Hubbard mechanism) would help in explaining the role of electron correlation in the phase transition of VO_2 [64, 71]. In the last two decades, a lot of theoretical work employing density functional theory (DFT) [60, 72] and dynamical mean field theory (DMFT) [73, 74]; and experimental work based on spatially resolved and energy-resolved probing of the crystal and electronic structure has been carried out to find the nature of the transition [75, 76]. Most of the research points to an interplay of the Mott and Peierls transitions in understanding the complete behavior of the MIT of VO_2, suggesting that the transition can be understood as a Peierls-assisted Mott transition or a Mott-assisted Peierls transition.

Further, Lee *et al.* [55] carried out in-situ X-ray photoelectron spectroscopy (XPS) and X-ray absorption spectroscopy (XAS) to understand the contribution of the Peierls and Mott transitions to the MIT of the epitaxial VO_2 films at different temperatures. They found that the VO_2 films deposited at lower temperatures (500-550°C), intermediate temperatures (600-650°C) and high temperatures (700-720°C) exhibited Mott-like, Mott-Peierls, and Peierls-like transitions, respectively. Brito *et al.* [73] employed a DMFT model to prove that the phase transition in VO_2 is adiabatically linked to a Peierls-type transition but is actually a Mott-transition when intersite exchange is present. Chen *et al.* [77] employed DFT-based calculations to analyze the nature of transitions and found that the MIT is a staged electron-correlation driven Mott transition followed by a structure driven Peierls transition. More recently, Grandi *et al.* [74] modelled the transition using a dynamical mean field theory and suggested that the transition is a two-step process. They suggested that with an increase in the temperature, there is melting of the dimerization component of the antiferrodistortive displacement, leading to a phase change from the monoclinic insulator to an intermediate monoclinic metal phase. This is followed by the disappearance of the tilting component turning the monoclinic metal into a rutile metal phase. They suggested that the role of the electron-electron interaction is to strengthen the coupling to the lattice, thereby stabilizing a distorted structural phase which would have been otherwise metastable in the absence of electron-electron interaction. Therefore, it could be concluded that the phase transition

is caused by a delicate interplay of the interactions between the lattice structure, electron correlations and orbitals.

The phase transition in VO_2 is accompanied by variations in its electrical and optical properties like resistivity, conductivity, transmittance, and reflectance [78-81]. However, because the focus of this thesis is only plasmonic switching, emphasis is only on the change in optical properties that VO_2 undergoes due to the underlying changes in the refractive index (See Figs. 2.4(c, d)). The optical constants of VO_2 can be described by using the classical dispersion model [82-84] which is based on the sum of the Lorentz and Drude oscillators as shown in Eq. 2.17. The dispersion models are discussed in detail in Appendix-I (See Appendix-I, Dispersion Models).

$$\varepsilon(\omega) = \big(n(\omega) + i\kappa(\omega)\big)^2 = \varepsilon_\infty + \left(\sum_{i=1}^{n} \frac{s_i}{1 - \omega^2/\omega_i^2 - i\Gamma_i\,\omega/\omega_i}\right) - \left(\frac{\omega_n^2}{\omega^2 + i\omega_c\omega}\right) \qquad (2.17)$$

where, $\omega_n = \sqrt{4\pi n_c e^2/m^*}$

Here, $\varepsilon(\omega)$ is the frequency-dependent complex dielectric constant of the material, n and κ are the real and imaginary parts of the frequency-dependent refractive index of the material, ω_n is the carrier density parameter which is related to the plasma frequency, n_c is the number of conduction electrons, e is the charge of an electron, m^* is the optical mass of the electrons, and ω_c is the collision frequency. The strength, frequency, and linewidth of the i^{th} oscillator are denoted by s_i, ω_i, and Γ_i, respectively. The first term in the equation, ε_∞, is a constant contributing to the real part of the dielectric constant due to high-frequency electronic transitions. The second term, based on the sum of Lorentz oscillators, represents the sum of the non-constant contributions — such as those due to lattice vibrations or the inter-band transitions of bound electrons — to the dielectric constant. The third term, which exists only for metallic VO_2, is based on the Drude model and represents the contribution of free-electrons to the dielectric constant. In the semiconductor state, the dielectric constant of VO_2 is modeled using the first two terms corresponding to the Lorentz model. However, in the metallic state, VO_2 behaves as a Drude metal with strong absorption. Hence, for the metallic state, a third term based on the Drude model is added to the dielectric function.

2.3 Plasmonic Switches Based on VO_2

In the last decade, many plasmonic switches based on the phase transition of VO_2 from its semiconducting to metallic state have been proposed. The phase transition of VO_2 from the semiconducting state to the metallic state can be achieved thermally, electrically, or optically. Therefore, in this chapter, the advances in the design and development of plasmonic switches under three categories based on the type of the activation mechanism for the phase transition have been reviewed. Further, most of the VO_2 based plasmonic switches proposed in the literature have been specifically designed for particular wavelength regions with specific applications.

Therefore, the plasmonic switches discussed in each section are sub-categorized according to their operating spectral regions, i.e., visible, near-infrared, infrared and terahertz regions. Some of the major developments in plasmonic switches which have happened over the last few years are shown in Fig. 2.5. The performance of each of the VO_2 based plasmonic switch discussed in the subsequent sections has been reviewed and compared with their counterparts based on figure of merits or an index of their switching efficiency.

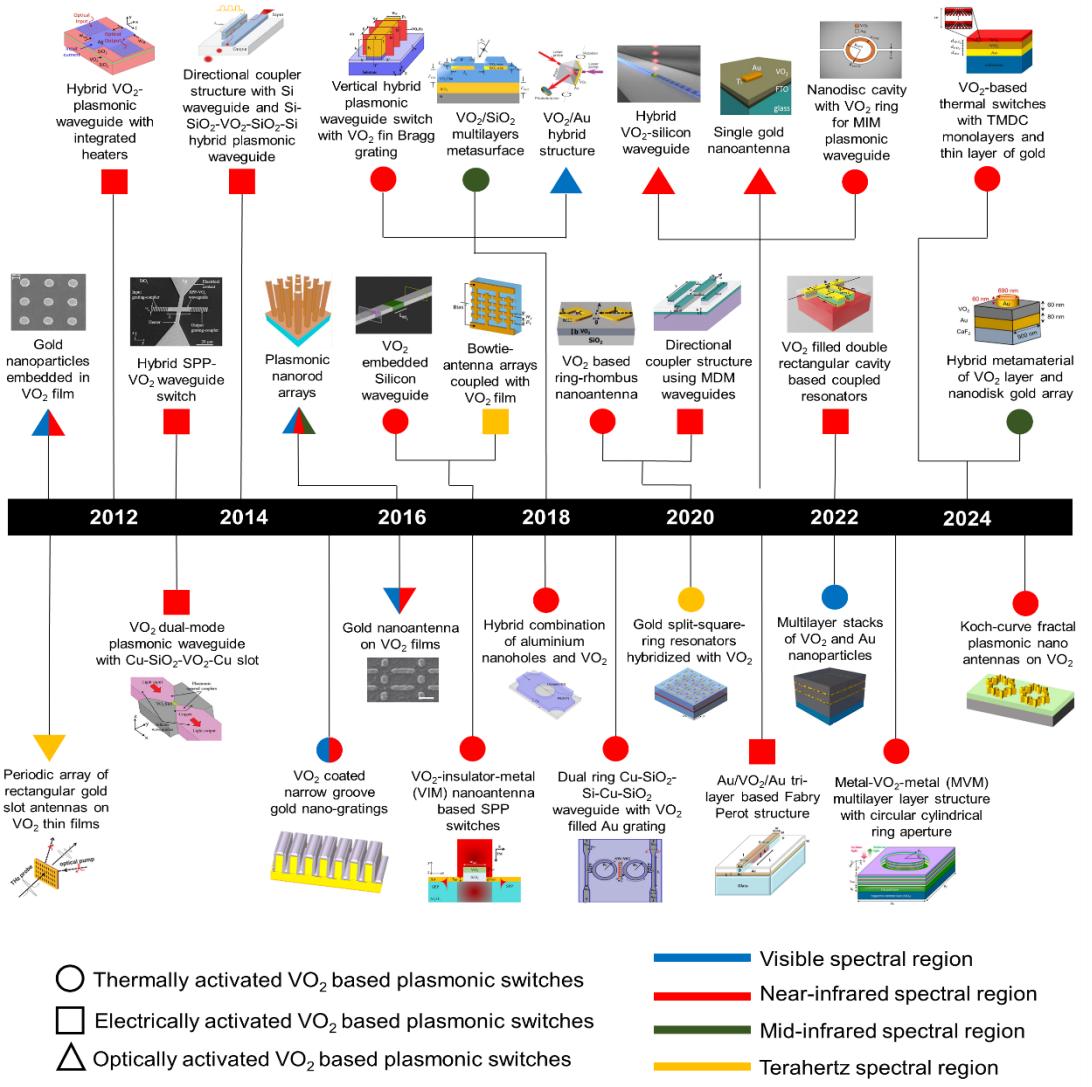

Fig. 2.2 Classification of VO_2 based plasmonic switches proposed in the last decade according to the type of activation mechanism for the phase transition in different spectral regions. The type of the activation mechanism is captured with the help of geometrical pointers, where circle represents the thermally activated VO_2 based plasmonic switch, square represents the electrically activated VO_2 based plasmonic switch, and triangle represents the optically activated VO_2 based plasmonic switch. The color scheme specifies the operating wavelength region of VO_2 based plasmonic switch, where blue represents the visible spectral region, red represents the near-infrared spectral region, green represents the mid-infrared spectral region, and yellow represents the terahertz spectral region. The snapshots of the structural design of plasmonic switches are also placed for the convenience.

2.3.1 Thermally activated switches

Thermally activated VO_2 switches are the plasmonic switches which undergo transition from a monoclinic semiconducting phase to a tetragonal metallic phase on heating at a transition temperature, i.e., near 68°C. This phase transition temperature can be modulated by using doped-VO_2. For instance, the transition temperature reported is ~25°C for tungsten-doped VO_2 [85], ~28°C for niobium-doped VO_2 [86], ~28°C for boron-doped VO_2 [87], ~35°C for fluorine-doped VO_2 [88], ~42°C for molybdenum-doped VO_2 [89], and ~45°C for aluminium-doped VO_2 [90]. In addition, the phase transition temperature can also be increased by using doped-VO_2 such as ~95°C for germanium-doped VO_2 [91] and ~134°C for iron-doped VO_2 [92].

In this section, a review of thermally activated VO_2 switches is presented. These switches have been sub-categorized based on their operating spectral range, i.e., visible, near-infrared, C-band, mid-infrared and terahertz regions. Thermally-activated plasmonic switches based on combination of VO_2 with plasmonic nanoparticles, plasmonic nanostructures, plasmonic nanoantenna, plasmonic waveguides, silicon waveguides and other structures have been discussed. In addition, this section also discusses the thermally-activated VO_2-based plasmonic switches exhibiting circular dichroism and polarization conversion.

Thermally activated VO_2-based switches operating in the visible spectrum have been developed using various nanostructures, including nanoparticles [93], narrow-groove nano-gratings [94], and nanodiscs [95]. Agrawal *et al.* [93] demonstrated plasmonic switches comprising gold nanoparticles (NPs) embedded between VO_2 film layers deposited on a sapphire substrate. These were implemented in both single-layer and double-layer gold NP configurations, as illustrated in Fig. 2.6(a). The plasmonic switches fabricated using pulsed laser deposition (PLD) were designed such that all VO_2 layers, along with the gold nanoparticles in both the single and double gold NP layer configurations, were deposited within the same PLD chamber without breaking the vacuum. The switching between the low-temperature phase at 25°C (OFF state) and the high-temperature phase at 90°C (ON state) was demonstrated in the visible spectral region (650 nm to 1000 nm). The maximum switchability and the tunability of the switching wavelength were measured by varying various geometrical parameters like the number of VO_2 and gold NP layers, gold NP size, and the thickness of the middle VO_2 layer. The proposed plasmonic switch could achieve an extinction ratio ≈ 3.3 dB for spectral regions below 1000 nm as shown in the graph of Fig. 2.6(a). Sharma *et al.* [94] presented one dimensional plasmonic narrow groove nano-gratings (NGs) of gold as plasmonic switch coated with a VO_2 film as illustrated in Fig. 2.6(b). The differential reflectance between the semiconducting and metallic phases of VO_2 was optimized by adjusting the nano-grating (NG) parameters like the groove depth, the groove width, the overall NG width, and the thickness of the VO_2 layer. Moreover, the tunable plasmonic switch could be tuned to different wavelengths by varying the NG parameters. The maximum differential reflectance of 41.18% was obtained at a wavelength value of 1544 nm as shown in the graph of Fig. 2.6(b). Kepic *et al.* [95] fabricated VO_2 nano-discs (NDs)

to study the nature of Mie resonances in the visible region as shown in Fig. 2.6(c). Using the multipole decomposition analysis, it was demonstrated that both the low-temperature (30°C) and high temperature (90°C) phases of VO_2 behaved like lossy dielectrics in the visible range and the Mie resonances red-shifted as the diameter of the NDs was increased. These Mie resonances got sharper and more prominent when the single VO_2 ND nanostructures were arranged in a composite periodic lattice. The tunable Mie resonances in VO_2 NDs offered scattering and extinction modulation depths of 5 to 8 dB and 1 to 3 dB, respectively. Moreover, the potential use of these VO_2 NDs in optically tunable metasurfaces was also explored by using a continuous-wave visible laser.

Thermally activated near-field VO_2 switches operating in the near-infrared range have been developed using various nanoantenna geometries, including nanorod-dipole, bowtie, and rod-disk configurations [96]; ring-bowtie and ring-rhombus structures [97]; Sierpinski-fractal contour-bowtie designs [98]; and Koch-curve fractal geometries [99]. Savaliya *et al.* [96] proposed switchable plasmonic nanoantennas (SPNs) for near-field optical switching in the near-infrared region using VO_2 filled gold (Au) nanoantenna structures. The switching of electric-field intensity enhancement (EFIE) between two phases of VO_2 (i.e., metallic phase and semiconducting phase) was demonstrated for four different types of SPN geometries, i.e., nanorod-dipole, bowtie, rod-disk, and planar trapezoidal toothed log-periodic, as shown in Fig. 2.7(a). Further, a comparison of EFIE of non-inverted SPN structures (i.e., the VO_2 thin film layer inside the gold nanoantenna structure) with EFIE of inverted SPN structures (i.e., the gold nanoantenna structure surrounded by the VO_2 thin film layer on their outer surface) was also carried out. The switching performance

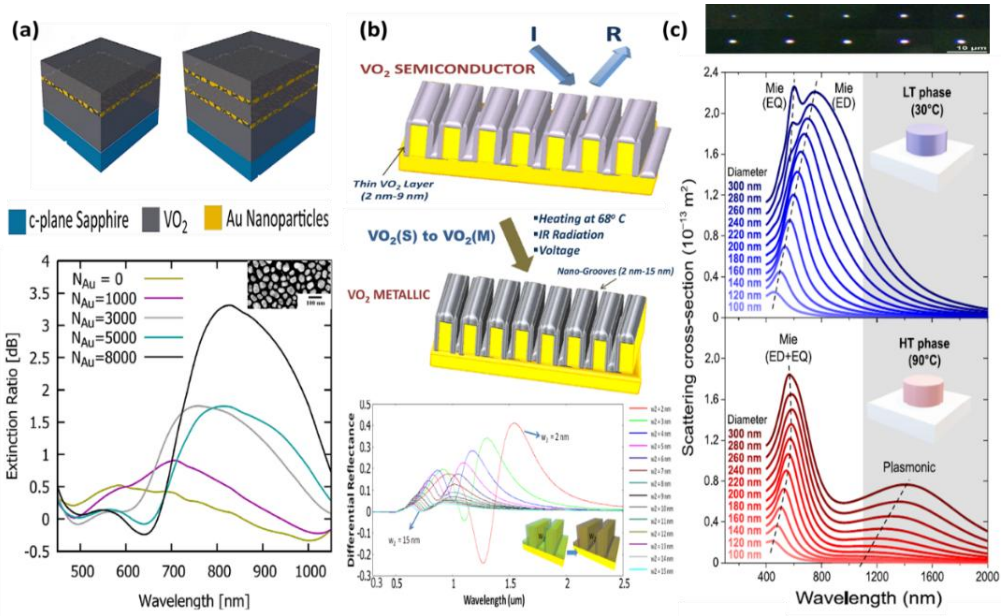

Fig. 2.6 Thermally activated VO_2 based plasmonic switches in the visible range. **(a)** Schematic and extinction ratio spectra of a fabricated single gold NP layer stack and double gold NP layer stack [93]. **(b)** Schematic and differential reflectance spectra for a gold NG covered with a VO_2 film [94]. **(c)** Scattering cross-section spectra for single VO_2 ND on fused silica substrate in the low-temperature (LT) and high-temperature (HT) VO_2 phases [95].

of the near-field plasmonic switches was evaluated using the intensity switching ratio (ISR), defined as ISR = I_{ON}/I_{OFF}, i.e., where I_{ON} and I_{OFF} represent the intensities in the ON state (VO_2 in the metallic phase) and OFF state (VO_2 in the semiconducting phase), respectively. Among the geometries studied, the non-inverted nanorod-dipole SPNs exhibited the highest ISR of approximately 7 dB at a wavelength of around 950 nm, whereas the ISR values for the non-inverted bowtie and rod-disk SPNs were approximately 4.5 dB and 4 dB, respectively. Further, ISR values for the inverted SPNs were lower (~1.4) than that of the non-inverted SPNs. Gupta *et al.* [97] presented two near-field plasmonic switches, i.e., ring-bowtie nanoantenna (RBN) switch and ring-rhombus nanoantenna (RRN) switch, by using ring-shaped plasmonic nanoantennas on a VO_2 thin film. The geometric parameters such as ring thickness and VO_2 film thickness, were optimized to maximize the ISR. The maximum ISR of ~59.5 was reported for the RBN switch at a wavelength of 1100 nm, whereas the RRN switch reported the maximum ISR of ~80.85 at a wavelength of 1140 nm as shown in Fig. 2.7(b). Sharma and Dhawan [98] proposed Sierpinski-fractal contour-bowtie plasmonic nanoantennas placed on a VO_2 coated silicon dioxide (SiO_2) substrate to demonstrate active near-field plasmonic switches as shown in the inset of Fig. 2.7(c). When the fractal order of the plasmonic nanoantenna was increased, the ON state intensity of the switch got enhanced while the OFF state intensity of the switch got reduced. For fractal order of 2, an ISR of ~900 was reported for the proposed switch as shown in the graph of Fig. 2.7(c). It was also demonstrated that the spectral response and the ISR of the plasmonic switch can be controlled by varying its geometrical parameters like the contour thickness, the length of the nanoantenna arm, and the thickness of VO_2 layer. For an optimized nanoantenna arm length of 325 nm, the maximum ISR of ~2600 was reported. Moreover, the wavelength of maximum ISR was red-shifted by over 350 nm when the thickness of VO_2 layer was increased from 10 nm to 100 nm. Masih and Sharma [99] proposed fractal plasmonic gold nanoantennas based on the Koch-curve fractal geometry, fabricated on a VO_2-coated SiO_2 substrate, for near-field plasmonic switching, as illustrated in the inset of Fig. 2.7(d). Their study demonstrated that increasing the number of iterations in the Koch-curve fractal structure led to a significant enhancement in the ISR, rising from ~22 at iteration 0 to ~2500 at iteration 2, as shown in Fig. 2.7(d). Furthermore, spectral tunability of the switching behavior was achieved by modifying geometrical parameters like the length of the Koch-curve fractal nanoantenna and the thickness of the VO_2 layer.

As high-speed optical communication is one of the primary applications of the VO_2 based plasmonic switches, many thermally activated VO_2 switches have been proposed in literature specifically for the 1550 nm communication band. For this band, multiple VO_2-based switches using waveguides have been proposed and are discussed in this section. Miller *et al.* [100] designed a broadband, non-resonant, and compact hybrid Si-PCM integrated optical waveguide switch by utilizing the semiconductor-metal transition (SMT) of thermally induced VO_2 at 68°C. The structure comprised a Si ridge waveguide on a SiO_2 substrate where a VO_2 patch having the same dimensions as that of the Si ridge was embedded within the silicon waveguide as illustrated in Fig. 2.8(a). The length of the VO_2 patch (L_{VO_2}) in the direction of propagation was varied and transmission as a function of L_{VO_2} was plotted

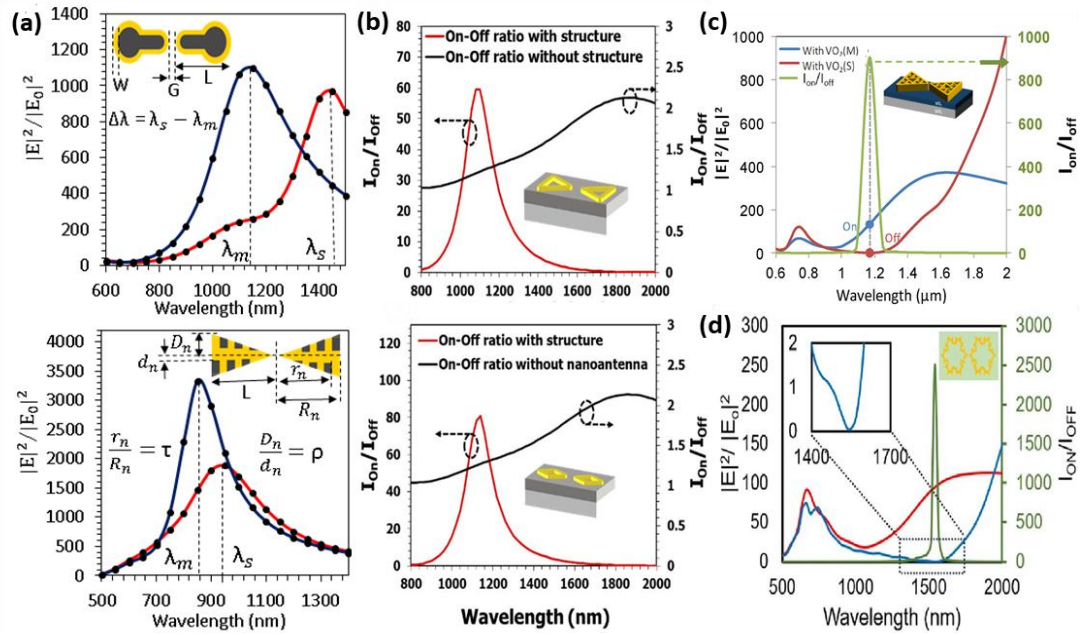

Fig. 2.7 Thermally activated VO_2 based near-field plasmonic switches in the near infrared range. **(a)** Electric-field enhancement plots for the semiconducting state and the metallic state of a non-inverted rod-disk SPN and a planar trapezoidal toothed log-periodic SPN [96]. **(b)** Intensity switching ratio curves for a RBN switch and a RRN switch [97]. **(c)** Intensity enhancement curve for a Sierpinski-fractal contour-bowtie plasmonic nanoantenna based switch [98]. **(d)** Intensity enhancement curve for a Koch-curve fractal plasmonic nanoantenna based switch [99].

for both the semiconducting phase and the metallic phase of VO_2. For L_{VO_2} of 200 nm, an extinction ratio of ~14 dB (as shown in the graph of Fig. 2.8(a)) with ~2 dB insertion loss and ~10 dB modulation was achieved at 1550 nm wavelength. Singh and Datta [101] proposed a three-dimensional narrowband plasmonic switch in a vertical silicon hybrid plasmonic waveguide (HPWG) with a frequency selective element (Bragg grating) as shown in Fig. 2.8(b). The Bragg grating was realized by periodic arrangement of VO_2 fins within the silicon waveguide, which responded via heat-induced metal-insulator-transition (MIT). The switching response was assessed by tailoring the parameters such as the number of VO_2 fins, width of the silicon waveguide, height of the silicon waveguide, and oxide spacer dimension. The narrow bandwidth (30 nm) switch achieved an extinction ratio of ~11.14 dB and figure-of-merit of 1.57 at 1.55 μm wavelength with 933.4 nm device length and three VO_2 fins as seen from the graph of Fig. 2.8(b). Moshfeghifar *et al.* [102] presented a cavity structure comprising of a VO_2 ring within a nanodisk to develop a reconfigurable active switch for the metal-insulator-metal (MIM) plasmonic waveguides as shown in Fig. 2.8(c). The designed structure could achieve an extinction ratio of 23.3 dB at 1550 nm as shown in the graph of Fig. 2.8(c). It was also demonstrated that the central wavelength of the transmission band of the nanostructure can be tuned by varying the geometrical parameters of the VO_2 ring. Singh [103] proposed a 1X2 Metal-Insulator-Silicon-Insulator-Metal (MISIM) waveguide switch-cum-splitter as shown in Fig. 2.8(d). The switch was operated in the telecommunication C-band at 1.505 μm – 1.584 μm. The switch offered 14.36 dB extinction ratio by selective tuning of VO_2 through

localized heating as well as -8.05 dB power splitting at room temperature as seen from the scattering parameter plots shown in Fig. 2.8(d). Singh [104] also designed a nanophotonic dual ring Cu-SiO_2-Si-Cu-SiO_2 waveguide plasmonic switch with VO_2 filled subwavelength metal gratings (SW-MG) of gold as switching element as shown in Fig. 2.8(e). The switch was operated in the optical C-band at 1.53 µm – 1.57 µm. The effect of the geometrical parameters of ring and SW-MG on the switching performance was also demonstrated. The switch offered 4.14 dB extinction ratio along with free spectral range (FSR) of 129 nm and 173 nm in the ON state and OFF state, respectively, as seen from the port transmission plots shown in Fig. 2.8(e). The figure of merit (Q) was found to be 68.03 in the ON state and 96.12 nm in the OFF state of the plasmonic switch.

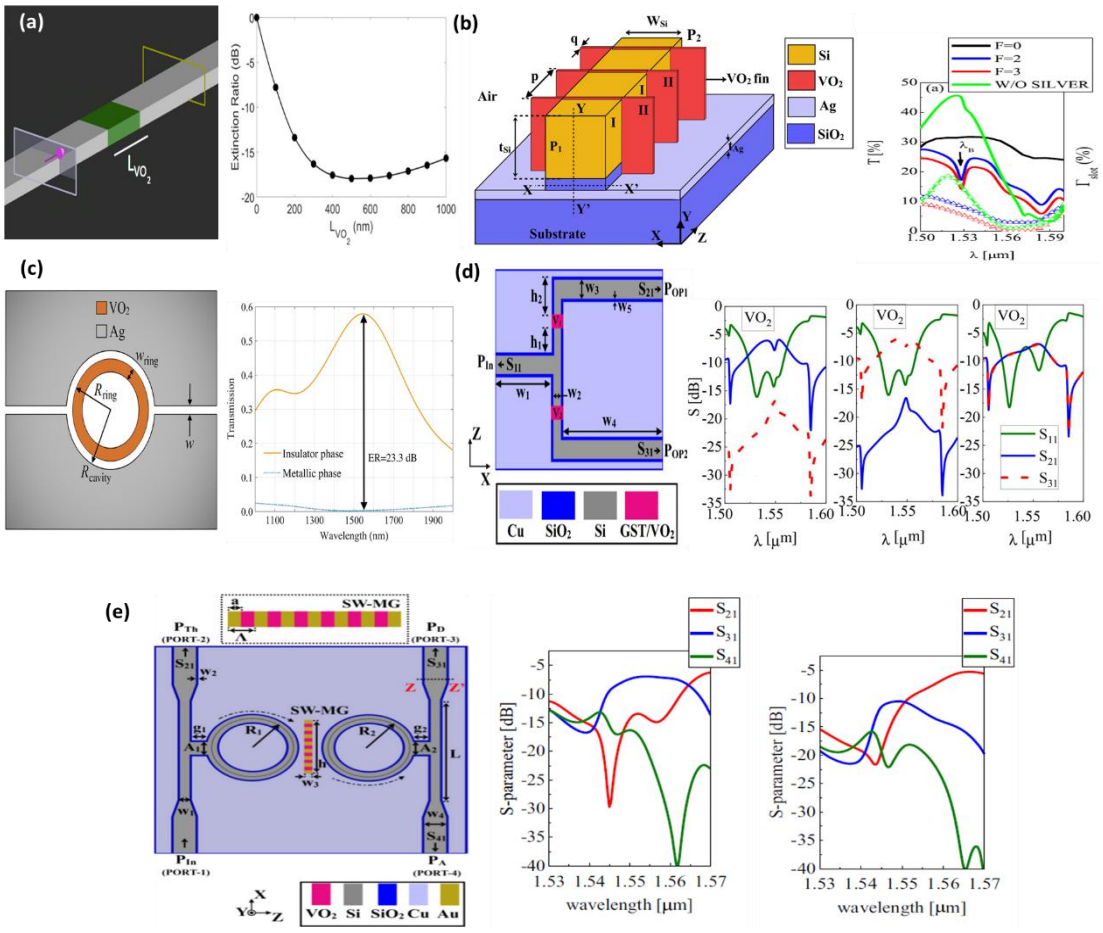

Fig. 2.8 Thermally activated VO_2 based plasmonic waveguide switches for the 1550 nm communication band. **(a)** Schematic and extinction ratio plot for a VO_2 embedded Si waveguide switch [100]. **(b)** Schematic and transmittance plot of a vertical Si HPWG switch with three thin VO_2 fins [101]. **(c)** Transmission spectra of a nanodisc cavity with a VO_2 ring controlling the propagation of light through an MIM plasmonic waveguide [102]. **(d)** Schematic of a 1X2 switch-cum splitter along with the simulated scattering parameters for V1: Insulator and V2: Metal, V1: Metal and V2: Insulator, and V1: Insulator and V2: Insulator, respectively [103]. **(e)** Schematic of a hybrid MISIM ring resonator plasmonic switch incorporating SW-MG as the switching element, accompanied by port transmission plots corresponding to the ON state and OFF state, respectively [104].

Thermally activated far-field VO_2 switches in the near-infrared range have also been specifically designed for important optical communication bands like C, L, and U bands. Kim *et al.* [105] demonstrated two novel reversible thermo-optical surface plasmon polariton (SPP) switches, i.e., a symmetric VO_2-insulator-metal (VIM) nanoantenna and an asymmetric VIM nanoantenna as shown in Fig. 2.9(a). The symmetric VIM nanoantenna consisted of a compound structure of VO_2-SiO_2-Au slabs, whereas the asymmetric VIM nanoantenna had an extra nano-slit in it for tuning the directional launching of SPPs between the gold layer and the sapphire substrate. The directional power distinction ratio of SPPs was switched in accordance with the device temperature at telecom wavelengths (i.e., 1300 nm and 1550 nm). The directional power distinction ratio changed from 3.725:1 to 1:3.132 when the VIM metagratings were heated up to 90°C. Petronijevic *et al.* [106] investigated a magnetic dipole resonant nanostructure that comprises of a gold nanoantenna and a multi-layer structure, which consists of a thin VO_2 layer placed on a SiO_2 substrate and coated with a thin spacer layer of luminescent ions (i.e., Er^{3+} ions) doped silica, as shown in Fig. 2.9(b). A single gold nanoantenna based VO_2 plasmonic switch provided high magnetic field in the emission layer when VO_2 was in its metallic or hot phase thus giving rise to high emission of magnetic dipoles. This emission was reduced when VO_2 was switched back to its semiconducting or cold phase as can be seen from the magnetic field intensity profiles shown in Fig. 2.9(b). The contrast ratio of the proposed nanostructure was also investigated by considering different orientations, distributions, and types of dipoles (i.e., magnetic dipole or electric dipole). The nanostructure with periodicity of 850 nm could achieve the maximum modulation depth of ~69 dB and highest contrast ratio of ~5.5 at 1540 nm wavelength. Sun *et al.* [107] designed a broadband plasmonic switch based on aluminium (Al) nanohole hexagonal arrays on quartz substrate by utilizing the SMT of VO_2 as shown in Fig. 2.9(c). The fabricated plasmonic switch could achieve 21%, 23%, and 26.5% transmission change in switching with extinction ratio of 4.3 dB, 4.9 dB, and 5.3 dB in C, L, and U-band, respectively, over a broad operating range of 650 nm as seen from the transmission spectra shown in Fig. 2.9(c). Mandal [108] proposed metal–VO_2–metal (MVM) multilayer metasurface with circular cylindrical ring aperture as shown in Fig. 2.9(d). On excitation with left circularly polarized light, the phase change of VO_2 in the metasurface showed a high reflection switching, i.e., ΔR ~80%, in the range of 1.5 μm to 3.5 μm with large full width at half maximum (FWHM) bandwidth of >500 nm as shown in the graph of Fig. 2.9(d). Hashemi *et al.* [109] proposed VO_2-based photothermal switch as shown in Fig. 2.9(e), incorporating tungsten disulfide (WS_2) monolayers and a thin gold layer on a silica substrate to enable tunable reflection-mode switching. The switch demonstrated that optimizing WS_2 layer count and Au layer thickness significantly enhanced the switching performance, achieving 17% reflection change and a switching bandwidth of 0.62 μm as shown in the graph of Fig. 2.9(e).

Thermally activated VO_2 switches have also been developed for the mid-infrared range using various structural configurations such as square array of Y-shaped gold nanoantennas [110], VO_2/SiO_2 multilayers [111], aluminium nano-disk arrays [112], and hybrid metamaterial of VO_2 layer and a nanodisk gold array [113]. Kats *et al.* [110] demonstrated a square array of Y-shaped gold nanoantennas by depositing a

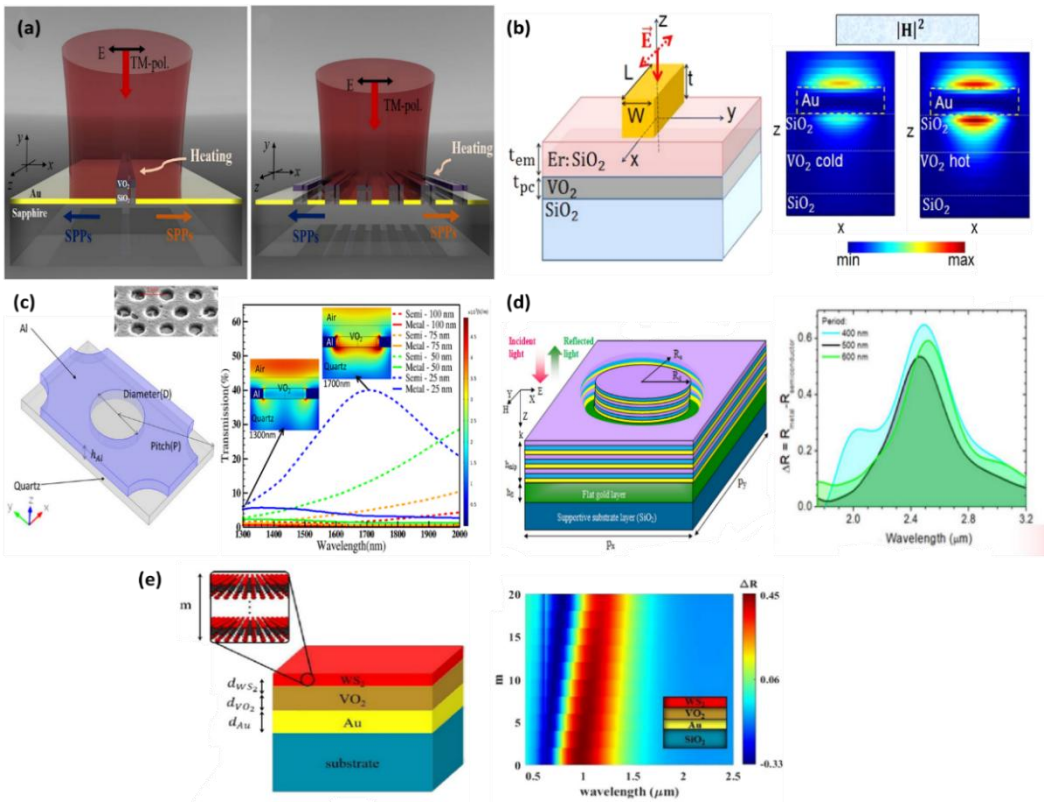

Fig. 2.9 Thermally activated VO_2 based far-field plasmonic switches in the near-infrared range. **(a)** Schematic illustration of an asymmetric VIM nanoantenna and a periodic VIM metagrating [105]. **(b)** Schematic of a hybrid nanostructure of gold nanoantenna-Er:SiO_2-VO_2-SiO_2 along with magnetic field intensity profiles at wavelength of 1540 nm [106]. **(c)** Simulation model and transmission spectra of a photonic switch using Al/VO_2 hexagonal nanohole array [107]. **(d)** Schematic and thermal reflection switching spectra of MVM multilayer metasurface [108]. **(e)** Schematic of VO_2-based photothermal switch and reflection change spectra as a function of number of WS_2 layers [109].

thin film of VO_2 on a sapphire substrate as shown in Fig. 2.10(a). The switching was achieved through a thermally driven insulator-to-metal transition (IMT) in VO_2 above ~67°C. The change in the reflectivity as a function of wavelength for different temperatures was used for measuring the switching efficiency as shown in the graph of Fig. 2.10(a). When VO_2 was in the dielectric state (e.g., T=28°C), the reflectivity peak was observed around 9.3 µm wavelength, which was red-shifted to 10.5 µm when the temperature was increased to 69°C. Hence, the tunability/switchability of the resonance wavelength achieved was ~10%. Wu *et al.* [111] presented a tunable VO_2 based mid-infrared metasurface for temperature control. The metasurface structure composed of a VO_2/SiO_2 multilayer which supported a thermally switchable Fabry-Perot like resonance mode from 8 µm to 13 µm wavelength range. The bottom to top layer configuration of the structure consisted of a silicon substrate, silicon dioxide film, VO_2 film, silicon dioxide wire, and VO_2 wire as illlustrated in Fig 2.10(b). As observed from the graphs given in Fig. 2.10(b), the absorption at the transparency window (8 µm to 13 µm) changed from ~0.6 to ~0.95 as the insulating phase VO_2 changed to a metallic phase VO_2. Wang *et al.* [112] demonstrated a tunable mid-infrared wavelength-selective plasmonic switch based on a plasmonic nanostructure

comprising of aluminium nano-disk arrays on VO_2 thin film as shown in Fig. 2.10(c). The plasmonic nanostructure consisted of a periodic four-layer structure: a silicon dioxide substrate, an aluminium metal layer, a VO_2 thin film layer, and an aluminium nano-disk array surrounded by naturally grown aluminium oxide (Al_2O_3) film that can protect it from oxidation. For the ON state, a reflectivity of ~0.8 was achieved at a resonant frequency of 4410 nm while a reflectivity of ~0.002 was achieved for the OFF state as seen from the graph shown in Fig. 2.10(c). The plasmon resonance wavelength could be tuned in the mid-infrared region by varying the structural parameters like the radii of the aluminium nano-disks. A modulation depth of ~99.4% and an extinction ratio >22.16 dB was reported for the proposed plasmonic switch. Petronijevic *et al.* [113] presented a metal-insulator-metal (MIM) hybrid metamaterial consisting a thin film of VO_2 spacer between a flat gold layer and a 2D array of golf nanodisks on a calcium fluoride (CaF_2) substrate as shown in Fig. 2.10(d). The switch exhibited reversible and monotonic thermal tuning of the absorption resonance with a wavelength shift of ~0.6 µm and absorption contrast controlled via the VO_2 phase transition in the mid-wave infrared range from 4.72 µm to 5.34 µm as shown in the graph of Fig. 2.10(d).

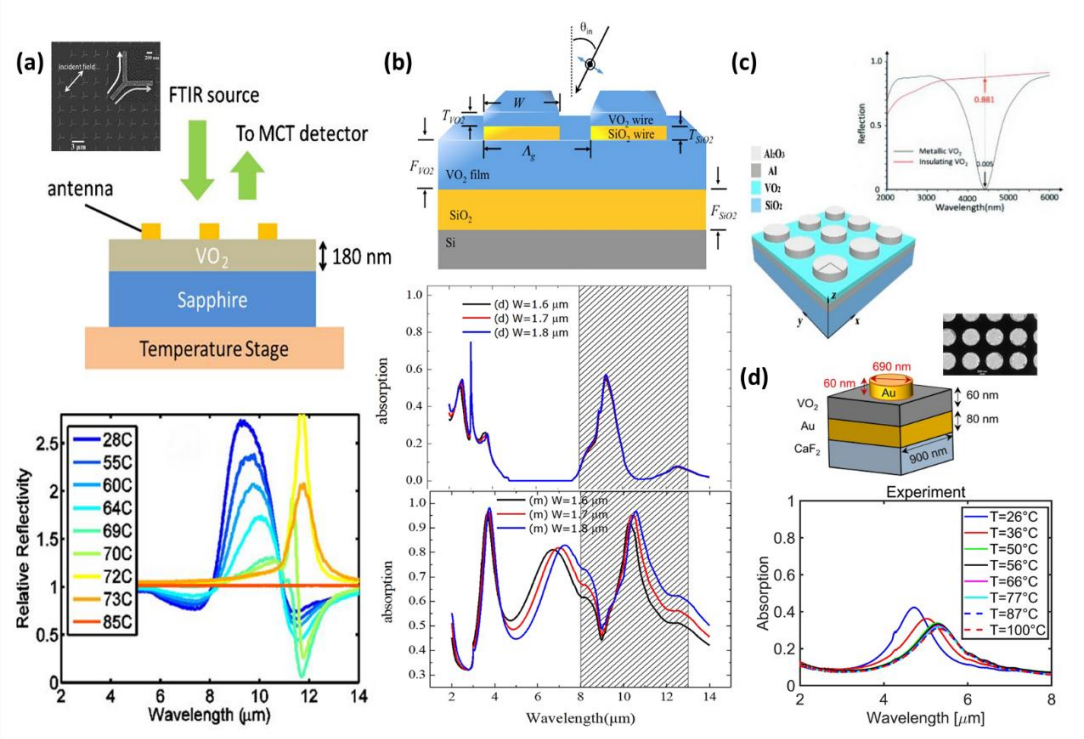

Fig. 2.10 Thermally activated VO_2 based plasmonic switches in the mid-infrared range. **(a)** Schematic and reflectivity spectra of a square array of Y-shaped gold nanoantennas on a VO_2 thin film deposited on a sapphire wafer [110]. **(b)** Side view diagram of a SiO_2/VO_2 multilayer metasurface along with the absorption spectrum for semiconducting and metallic state of VO_2 [111]. **(c)** Schematic and the spectral reflectance characteristics of a wavelength-selective plasmonic switch based on aluminium nano-disk arrays on VO_2 thin film [112]. **(d)** 3D schematic of the unit cell and SEM image of the metamaterial fabricated on a CaF_2 substrate, along with experimental spectra illustrating temperature-dependent resonance tuning of the metamaterial [113].

Terahertz metasurfaces hybridized with VO_2 have also been employed for switching in the terahertz region. Li *et al.* [114] designed a switchable metasurface employing VO_2 for variety of applications in the terahertz (THz) frequency region. The VO_2 integrated terahertz metasurface consisted of six functional layers, i.e., periodic VO_2 brick-shaped nanoantennas, a polyimide spacer layer, double chromium square ring resonators, a continuous VO_2 layer, a second polyimide layer, and a bottom chromium substrate as shown in Fig. 2.11(a). The proposed metasurface could be tuned from a broadband absorber to a reflecting surface due to IMT of VO_2 by altering the working temperature. The metasurface could efficiently absorb ~97.2% of the normally incident THz wave when VO_2 was in its insulating phase, whereas the metasurface exhibited broadband reflection of >80% when VO_2 was heated and switched to its metallic phase over the frequency range from 0.5 to 1.3 THz as seen from the graphs shown in Fig. 2.11(a). Wang *et al.* [115] demonstrated a phase-change metasurface employing metallic resonators hybridized with VO_2 for the terahertz applications as shown in Fig. 2.11(b). The metasurface consisted of a VO_2 nanofilm sandwiched between a quartz substrate and a quartz spacer. The gold split-square-ring resonators were arranged on top of the quartz spacer as a square lattice with VO_2 nanopads placed into the three splits. The metasurface could be switched from a state of broadband electromagnetically induced transparency (EIT) when VO_2 was in its insulating phase to a state of broadband nearly perfect absorption when VO_2 was in its metallic phase. It can be seen from the transmittance spectra shown in Fig. 2.11(b) that when VO_2 was in its insulating phase, the metasurface achieved a maximum of 83% transmittance with a bandwidth of 0.27 THz, and whenVO_2 was in its metallic phase, the metasurface achieved absorptance >93% and a bandwidth of 0.5 THz.

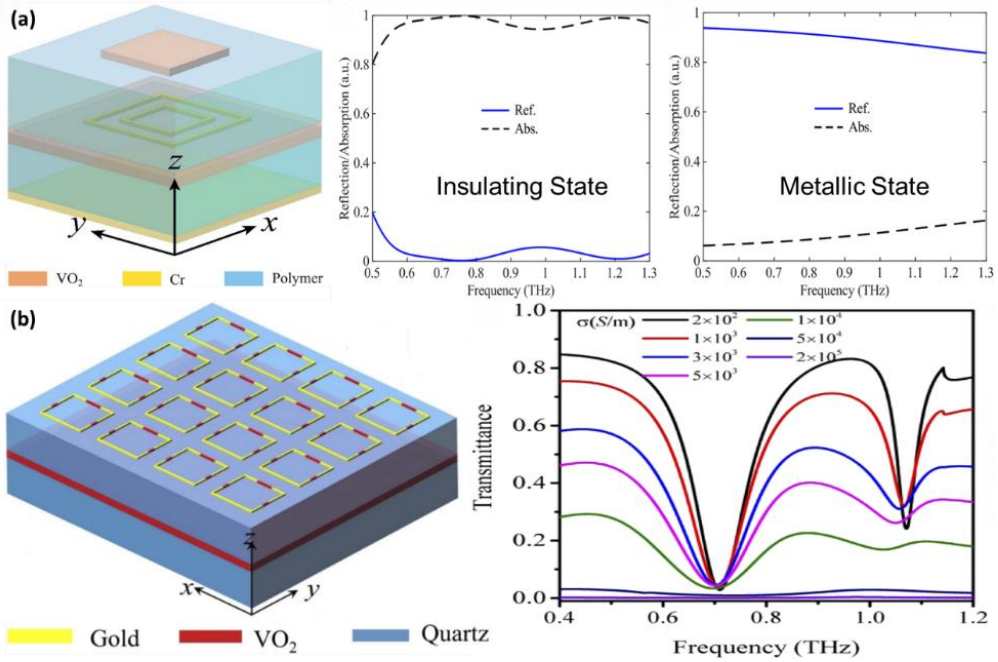

Fig. 2.11 Thermally activated VO_2 based plasmonic switches in the terahertz region. **(a)** Schematic and simulated absorption and reflection spectra of a switchable multifunctional THz metasurfaces employing VO_2 [114]. **(b)** 3D schematic view and transmittance spectra of metasurfaces employing gold split-square-ring resonators hybridized with VO_2 [115].

In addition, thermally activated VO_2 switches exhibiting the circular dichroism (CD) have also been designed in the recent past. Ren *et al.* [116] presented a bi-functional switchable metamaterial device using a hybrid nanostructure of gold and VO_2. The proposed nanostructure composed of a VO_2 substrate, a SiO_2 dielectric layer, and two equal thickness gold arcs as shown in Fig. 2.12(a). The proposed VO_2-based metamaterial could thermally switch between the perfect absorption and asymmetric transmission (AT) for circularly polarized lights in the near-IR region. For an operating frequency range from 0.8 μm to 1.5 μm, the proposed metamaterial device behaved as a chiral-selective perfect plasmonic absorber, which resulted in an optical circular dichroism (CD) response with peak value of ~0.7, when VO_2 was in the metallic phase; whereas it exhibited a dual-band AT effect with maximum value of ~0.19, when VO_2 was in the insulating phase. Mandal *et al.* [117] proposed a hybrid metal-VO_2 hybrid dagger-like plasmonic structure to achieve multi-resonant broadband circular dichroism (CD) in both the visible and near-infrared spectral regions, as depicted in Fig. 2.12(b). Asymmetry was intentionally introduced between the two arms of the dagger structure to break in-plane rotational symmetry, thereby rendering the structure in-plane chiral. In the case of a purely asymmetric metallic dagger-like structure (MDLS) composed of gold, two narrowband resonant CD peaks were observed. In contrast, the asymmetric metal-VO_2 hybrid dagger-like structure (MVHDLS) exhibited multiple broadband resonant CD peaks, as shown in Fig. 2.12(b). The MVHDLS structure enabled active control of CD through externally applied thermal stimuli, demonstrating a switching behavior wherein a low-chirality OFF state corresponded to the VO_2 metallic phase, and a high-chirality ON state corresponded to its semiconductor phase. Additionally, the study examined various CD-related properties — including transmission, reflection, absorption spectra, and CD spectra — under left circularly polarized (LCP) and right circularly polarized (RCP) light excitation for both MDLS and MVHDLS configurations.

Thermally activated VO_2 switches based on the polarization conversion have also been explored recently. Jia *et al.* [118] designed a composite anisotropic plasmonic nanostructure to dynamically tune the polarization state of the reflected light via thermally induced SMT of VO_2. The nanostructure consisted of four layers: a gold film at the bottom, a SiO_2 layer on its top, followed by two types of periodic gold particles in the shapes of the letters L and I, and finally a VO_2 layer covering the whole sample as shown in Fig. 2.13(a). The nanostructure exhibited distinct reflections under x-polarized and y-polarized incident lights at room temperature and high temperature states as seen from the graphs shown in Fig. 2.13(a). For instance, the polarization of the incident light was 135° at 3 μm wavelength and the polarization of the reflected light was 165° at 20°C which was switched back to 135° at 80°C. Lv *et al.* [119] proposed a controllable switch-type chiral metamaterial (SCMM) to achieve asymmetric transmission (AT) polarization conversion. The structure consisted of three layers where the top and bottom resonators comprised of asymmetric split copper ring and VO_2, and the dielectric substrate used polytetrafluoroethylene (PTEE) as shown in Fig. 2.13(b). The switching of the AT polarization conversion function was controlled by the conductivity of VO_2. When VO_2 was in its insulating state, the SCMM realized AT polarization conversion from linear polarization to cross polarization. It was found from the surface current distribution that the main cause of

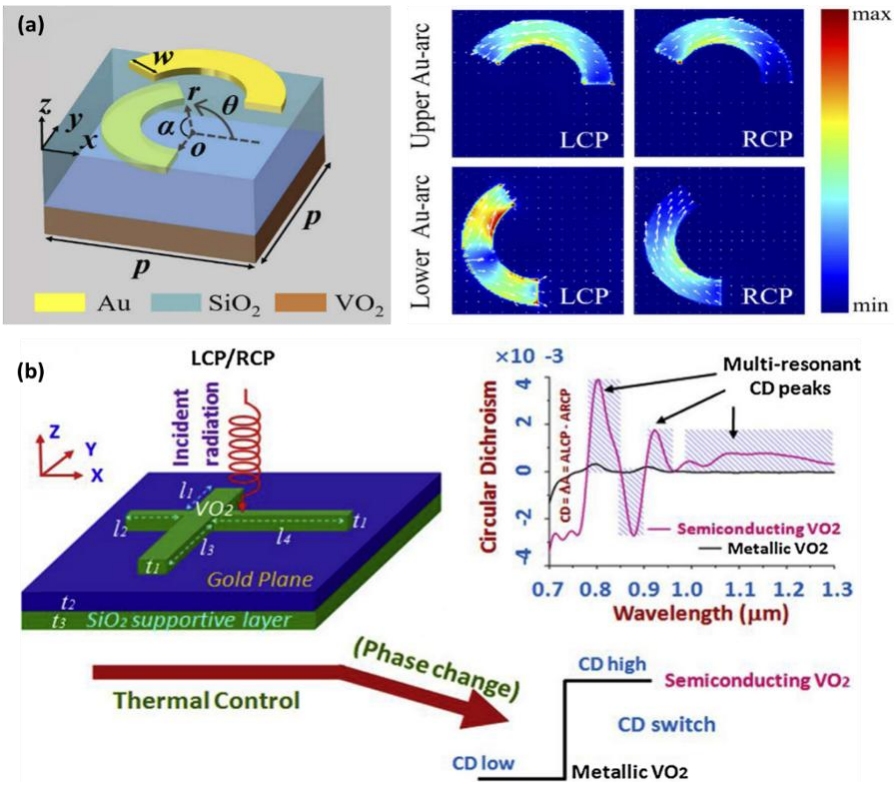

Fig. 2.12 Thermally activated VO_2 based plasmonic switches exhibiting circular dichroism. **(a)** Schematic of a unit cell of the VO_2 based metamaterial with gold arcs along with combined distributions of E-field and current vectors in the upper and lower gold arcs under LCP and RCP incident light at a wavelength of 1120 nm [116]. **(b)** Schematic and circular dichroism spectra of a thermally controlled planar chiral dagger-like structure [117].

AT polarization conversion was the cross-coupling between the induced magnetic field generated by the magnetic dipole and the incident electric field. Further, when VO_2 was in its metallic state, the AT polarization conversion function was turned off because the surface current was symmetrical and the chiral parameter was zero. In the frequency bands of 1.67 THz - 1.74 THz and 1.86 THz - 2.05 THz, 90° polarization azimuth, extremely low ellipticity, and >90% polarization conversion rate (PCR) was achieved. Moreover, the AT parameter $|\Delta|$ was as high as 0.87 in the frequency band of 1.67 THz - 2.05 THz. Zhao *et al.* [120] proposed a terahertz dual-mode polarization conversion metasurface consisting of dual-layer graphene grating, metal resonator, gold-VO_2 alternative grating, and SiO_2 dielectric spacer as shown in Fig. 2.13(c). The graphene-VO_2 integrated metasurface achieved active switching of polarization between transmission mode (TM) and reflection mode (RM). For VO_2 in its insulating phase, linear polarization conversion in TM was achieved in the range of 0.52 THz ~ 1.74 THz with a relative bandwidth of ~107.9% by increasing the Fermi level of the dual-layer graphene. For VO_2 in its metallic phase, linear polarization conversion in RM was achieved in the range of 0.62 THz ~ 1.70 THz with a relative bandwidth of ~93.1% because the Fermi level of graphene was 0 eV. Further, when VO_2 was switched from insulating phase to metallic phase, the lowest value of PCR increased from 30% to 85% (as shown in the graph of Fig. 2.13(c)) and thus, a modulation depth of about 64.7% was achieved.

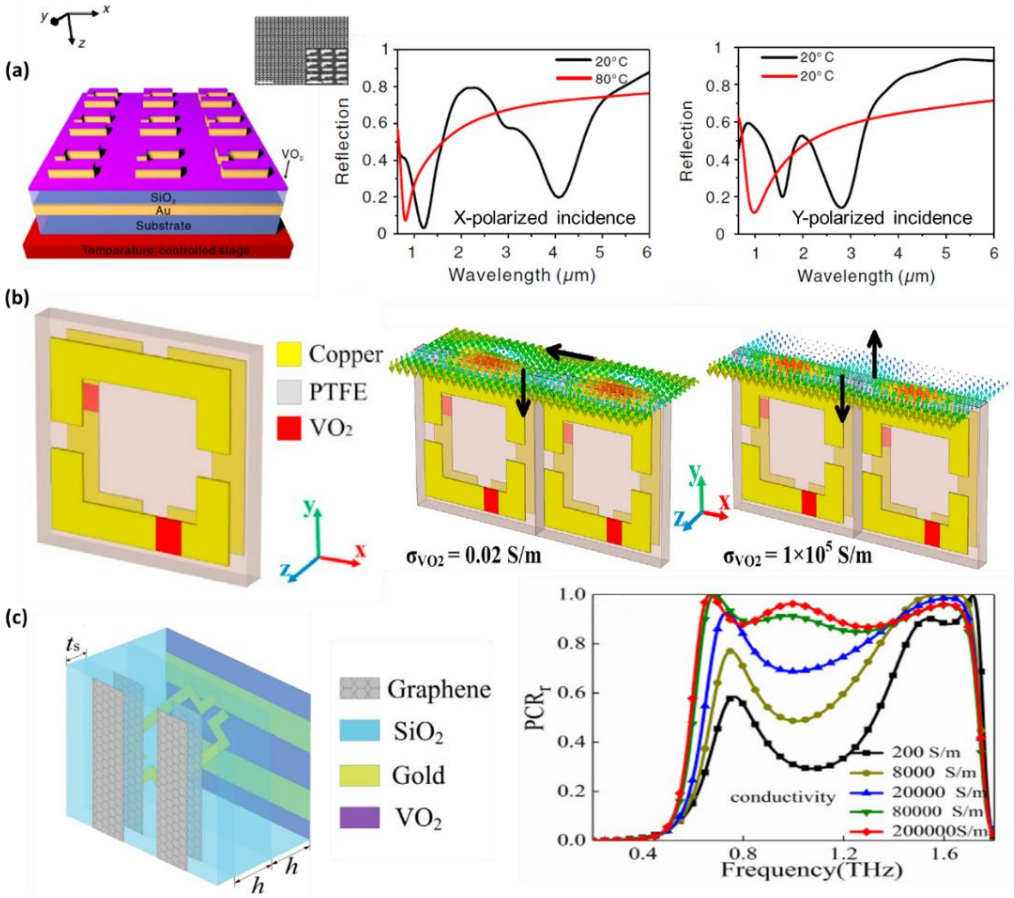

Fig. 2.13 Thermally activated VO_2 based plasmonic switches using polarization conversion. **(a)** Schematic of a switchable polarizer consisting of a periodic array of Au particles in the L and I shapes along with the reflection spectra under the x-polarized incidence and y-polarized incidence [118]. **(b)** Unit structure model of a switch-type chiral metamaterial (SCMM) along with the electric field distribution in the insulating and metallic states of VO_2 at 2.01 THz [119]. **(c)** Schematic diagrams of a graphene-VO_2 integrated metasurface along with the spectra of polarization conversion rate for metasurface working in reflection mode with different conductivities of VO_2 [120].

The summary of the review of thermally activated VO_2 based plasmonic switches discussed in this section is presented in Table 2.2.

Table 2.2 Review of thermally activated VO_2 based plasmonic switches

Ref. No.	Description of switch	Figure of merit (FOM)	Index of FOM	Operating wavelength range
Agrawal *et al.*, 2022 [93]	Multilayer stacks of VO_2 and gold nanoparticles	Extinction ratio	Extinction ratio ≈ 3.3 dB	650 nm – 1000 nm
Sharma *et al.*, 2015 [94]	VO_2 coated narrow groove gold nano-grating switch	Differential reflectance	Differential reflectance = 41.18%	0.3 μm – 2.5 μm

Kepic *et al.*, 2021 [95]	VO_2 nanodiscs on fused silica substrate	Scattering modulation depth and extinction modulation depth	Scattering modulation depth = 5 dB to 8 dB and extinction modulation depth = 1dB to 3 dB	400 nm – 2000 nm
Savaliya *et al.*, 2017 [96]	Switchable plasmonic nanoantenna (SPN) switches in nanorod-dipole, bow-tie, rod-disk, and trapezoidal toothed log-periodic configuration	Intensity switching ratio	Intensity switching ratio for (i) non-inverted nanorod-dipole SPN ~7 dB (ii) non-inverted bowtie SPN ~4.5 (iii) non-inverted rod-disk SPN ~4 (iv) inverted SPNs ~1.4	600 nm – 1400 nm
Gupta *et al.*, 2020 [97]	VO_2 based ring-bowtie nanoantenna (RBN) and ring-rhombus nanoantenna (RRN) switches	Intensity switching ratio	For the RBN switch, intensity switching ratio ~59.5 For the RRN switch, intensity switching ratio ~80.85	800 nm – 2000 nm
Sharma and Dhawan, 2022 [98]	Sierpinski-fractal contour-bowtie nanoantennas on VO_2 thin film	Intensity switching ratio (ISR)	ISR of ~900	0.6 μm – 2 μm
Masih and Sharma, 2025 [99]	Koch-curve fractal nanoantennas on VO_2 coated SiO_2 substrate	Intensity switching ratio (ISR)	ISR of ~2500	600 nm – 2000 nm
Miller *et al.*, 2017 [100]	VO_2 embedded Silicon waveguide switch	Extinction ratio, insertion loss, and modulation	Extinction ratio ~14 dB, insertion loss ~2 dB, and modulation ~10 dB	1550 nm
Singh and Datta, 2018 [101]	Plasmonic waveguide switch with VO_2 fin Bragg grating	Extinction ratio and figure-of-merit	Extinction ratio ~11.14 dB and figure-of-merit = 1.57	1.55 μm
Moshfeghifar *et al.*, 2021 [102]	Nanodisc cavity structure with VO_2 ring for MIM plasmonic waveguide	Extinction ratio	Extinction ratio = 23.3 dB	1550 nm
Singh, 2019 [103]	MISIM waveguide switch-cum-splitter	Extinction ratio	Extinction ratio = 14.36 dB	1.544 μm

Singh, 2019 [104]	Dual ring Cu-SiO_2-Si-Cu-SiO_2 waveguide with VO_2 filled gold grating	Extinction ratio	Extinction ratio = 4.14 dB	1.544 μm
Kim *et al.*, 2017 [105]	Symmetric VO_2-insulator-metal (VIM) nanoantenna and asymmetric VIM nanoantenna based SPP switches	Directional power distinction ratio	Directional power distinction ratio changed from 3.725:1 to 1:3.132 on IMT of VO_2	1650 nm
Petronijevic *et al.*, 2019 [106]	Hybrid nanostructure of Au nanoantenna-Er:SiO_2-VO_2-SiO_2	Modulation depth and contrast ratio	Modulation depth ~69 dB and contrast ratio of emission efficiency ~5.5	800 nm – 2000 nm
Sun *et al.*, 2018 [107]	Hybrid combination of aluminium nanoholes and VO_2	Transmission and extinction ratio	21%, 23%, and 26.5% transmission change in switching with extinction ratio of 4.3 dB, 4.9 dB, and 5.3 dB in C, L, and U-band, respectively	1300 nm – 2000 nm
Mandal 2023 [108]	Metal-VO_2-metal multilayered metasurface	Reflection switching	Reflection switching ~80%	0.5 μm – 3.5 μm
Kats *et al.*, 2013 [110]	Array of gold Y-shaped nanoantennas on VO_2 film deposited on sapphire substrate	Tunability of resonance wavelength	Tunability of resonance wavelength ~10%	4 μm – 14 μm
Wang *et al.*, 2021 [112]	Aluminium nano-disk arrays with VO_2 thin film	Modulation depth and extinction ratio	Modulation depth ~99.4% and extinction ratio ~22.16 dB	2000 nm - 6000 nm
Li *et al.*, 2019 [114]	Switchable terahertz metasurfaces employing VO_2	Absorption and reflection intensity	Average absorption ~97.2% in OFF state and reflection >80% in ON state	0.535 THz – 1.3 THz
Wang *et al.*, 2020 [115]	Metasurfaces employing gold split-square-ring resonators with VO_2	Transmittance and absorptance	Transmittance = 83% in insulting phase and absorptance = 93% in metallic phase	0.4 THz – 1.2 THz

Ren *et al.*, 2021 [116]	VO_2 based metamaterial with Au-arcs	Circular dichroism (CD) response and asymmetric transmission (AT) effect	CD response ~0.7 and AT effect ~0.19	800 nm – 1500 nm
Jia *et al.*, 2018 [118]	Periodic array of Au particles in the shapes of letters L and I coated with VO_2	Polarization state of light	Polarization of the reflected light was switched from 165° direction at 20°C to 135° direction at 80°C	0.5 μm – 6 μm
Lv *et al.*, 2021 [119]	Switch-type chiral metamaterial based on VO_2	Asymmetric transmission (AT) parameter	AT parameter ~0.87	1.6 THz – 2.1 THz
Zhao *et al.*, 2022 [120]	Metasurface with integrated graphene-VO_2	Modulation depth	Modulation depth ~64.7%	0.2 THz – 1.8 THz

2.3.2 Electrically activated switches

Electrically activated VO_2 switches are the plasmonic switches which undergo transition from a monoclinic semiconducting or insulating phase to a tetragonal metallic phase on the application of electric field ~10^7 Vm^{-1} [121] or switching voltage ~1.3 V [122] to ~6 V [123]. Electrically activated VO_2 switches based on different designs have been proposed and are discussed below.

In the near infrared range (especially for telecommunication wavelength of 1550 nm), many electrically activated VO_2 based plasmonic switches have been designed by using waveguides. Chauhan *et al.* [124] presented a plasmonic switch based on metal-dielectric-metal (MDM) waveguide in a directional coupler structure as shown in Fig. 2.14(a). The directional coupler structure consisted of two parallel side arms (WG2 and WG3 with VO_2 as dielectric) and one main waveguide (WG1 with active elasto-optic material). The driving voltage used was 5 V. The first state of the plasmonic switch (i.e., OFF state) was obtained when voltage was applied only across WG2 and WG3. The dielectric of both these side arms acted as metal and absorbed all the light that pass through these side arms; thus, no power was transferred to the output of the main waveguide. The second state of the plasmonic switch (i.e., ON state) was obtained when voltage was applied across WG1. The dielectric of the main waveguide was compressed to 50% of its value due to the elasto-optic effect. However, the side arms remained in the insulating state of VO_2 as no voltage was applied to them. This resulted in maximum power transfer to the output of the main waveguide. The plasmonic switch was optimized by varying the device specifications, such as length of the device, separation distance, thickness of the dielectric of waveguide, and length of gap. The graph of Fig. 2.14(a) shows the transmittance spectra for the OFF and ON states of the plasmonic switch. The plasmonic switch achieved a modulation depth of 19.44 dB, loss of -2.55 dB, and a figure of merit of

7.62 at a wavelength of 1.58 µm. Chauhan *et al.* [125] then proposed a nano-plasmonic compact waveguide-based switch with a gold-VO_2-gold tri-layer based Fabry Perot structure as shown in Fig. 2.14(b). The designed switch was based on the electrically-driven phase transition in the VO_2 layer, which behaved as insulator in its ON-state and as metal in its OFF-state when a switching voltage of 2.7 V was applied across the VO_2 layer. The effect of device parameters, such as width, length, and height, on the device performance was also shown. The graph of Fig. 2.14(b) shows the transmittance spectra for the OFF state and the ON state of the plasmonic switch. A modulation depth of 44.77 dB, insertion loss of 1.43 dB, quality factor of 146, and figure-of-merit of 3.31 were obtained by the nano-plasmonic waveguide switch for the near-infrared wavelength region from 1 µm to 2 µm. Chauhan *et al.* [126] also proposed an active compact plasmonic waveguide switch by using two VO_2 filled rectangular cavities (or two Metal-Insulator-Metal, i.e., MIM rectangular resonators) and placed perpendicularly to the main waveguide at a finite coupling distance as shown in Fig. 2.14(c). The main waveguide comprised of gold/electro-optic/gold layers, where polymethylmethacrylate (PMMA) was used as an electro-optic material. The effect on the device performance by varying the different geometrical parameters such as the length of the rectangular cavities, gap in the main waveguide, gap between the rectangular cavities, distance between the main waveguide and the two rectangular cavities, and width of the rectangular cavities was demonstrated. The graph of Fig. 2.14(c) shows the transmittance spectra for the OFF and ON states of the plasmonic switch. The switch achieved a modulation depth of 26.40 dB, a quality factor of 156, and a figure of merit of 12. Moreover, the switch exhibited a large wavelength tunability of ~280 nm around the resonant wavelength of 1.56 µm as the applied voltage was varied from 0 V and 2.7 V.

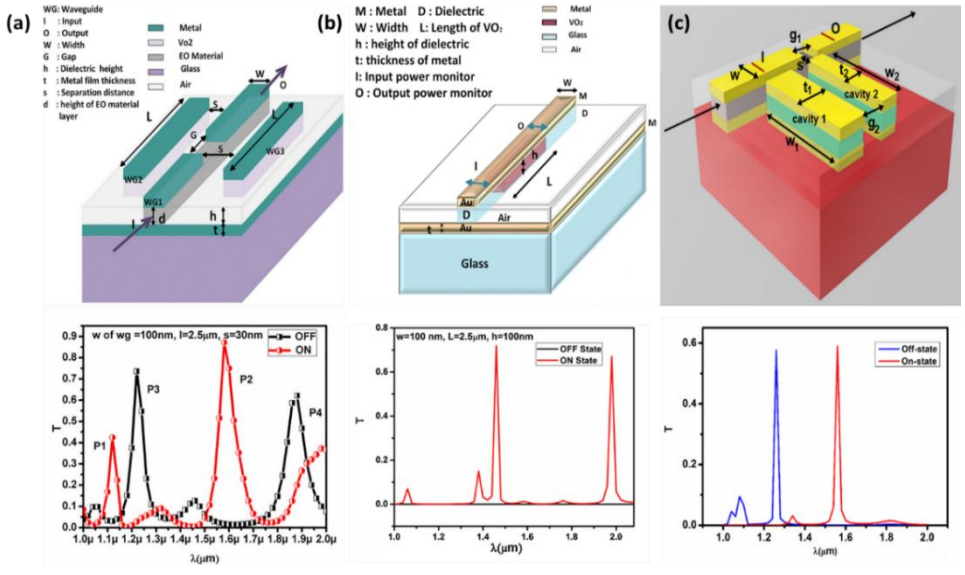

Fig. 2.14 Electrically activated VO_2 based plasmonic waveguide switches in the near-infrared range. **(a)** 3D view and transmission spectra of a plasmonic switch based on MDM waveguide in a directional coupler structure [124] **(b)** 3D schematic and transmission spectra of a plasmonic switch based on Au/VO_2/Au tri-layer based Fabry Perot structure [125] **(c)** 3D schematic view and transmission spectra of a VO_2 filled dual rectangular cavity based coupled resonators for plasmonic switching applications [126].

Joushaghani *et al.* [127] demonstrated an electrically-controlled, low voltage, broadband and compact plasmonic switch as shown in Fig. 2.15(a). Surface plasmon polaritons (SPPs) at strongly confined low-loss transverse magnetic polarized mode were used in high-index-contrast silicon waveguide to form an efficient and compact hybrid SPP-VO_2 electro-optic plasmonic waveguide switch. The hybrid SPP-VO_2 plasmonic switch consisted of a thick silver layer, thick SiO_2 spacer, thin VO_2 layer, thin Si layer, very thick buried oxide (BOX) layer, and thick Si layer from top to bottom. The insulator-to-metal transition (IMT) of VO_2 was initiated with switching voltage near 400 mV as seen from the graph of Fig. 2.15(a). The plasmonic switch recorded high extinction ratio (ER) of 16.4 dB at an operating wavelength of 1550 nm. Kim [128] proposed a complementary metal-oxide-semiconductor (CMOS)-compatible hybrid plasmonic modulator on the basis of a directional coupler that comprised of a Si waveguide and a Si-SiO_2-VO_2-SiO_2-Si hybrid plasmonic waveguide (HPWG) as illustrated in Fig. 2.15(b). When the VO_2 phase transition was electrically triggered by a driving voltage of 2 V, the propagation loss of the HPWG was switched and thus, the output optical power was modulated. The graphs for electric field distribution, insertion losses, and on/off extinction ratio of the HPWG modulator were also plotted and discussed. For a gap of 360 nm, the HPWG switch achieved an extinction ratio of 6.56 dB with 2 dB insertion loss at a wavelength of 1.55 μm as seen from the graph shown in Fig. 2.15(b). Kruger *et al.* [129] presented an electrically controlled hybrid VO_2-plasmonic waveguide switch as shown in Fig. 2.15(c). The hybrid VO_2-plasmonic switch coupled light to and from free-space via grating couplers. The hybrid VO_2-plasmonic switch was consisted of a single thin metallic layer of silver separated from the VO_2 film by a SiO_2 buffer layer. The VO_2 film was deposited on an optically thick SiO_2 layer. The hybrid VO_2-plasmonic switch required a switching voltage of ~60 mV and a switching power of ~9 mW over the operating wavelength of 1.55 μm. The plasmonic switch was designed for two operational regions, i.e., strongly-hybridized region and weakly-hybridized region. The strongly-hybridized device switched between two strongly hybridized modes; whereas, the weakly-hybridized device switched between a strongly and weakly hybridized mode as seen from the electric field intensity graphs shown in Fig. 2.15(c). The strongly-hybridized device achieved 13.4 dB insertion loss and 32.1 dB extinction ratio in an active region of 5 μm. On the other hand, the weakly-hybridized device achieved 17.0 dB insertion loss of and 22.7 dB extinction ratio in the 5 μm active region.

Electrically activated VO_2 switches have also been designed by using different kinds of nanostructured substrates. Ooi *et al.* [130] proposed the design of an ultracompact planar VO_2 based plasmonic dual-mode waveguide modulator by using a metal-insulator-VO_2-insulator-metal (MIVIM) waveguide structure as shown in Fig. 2.16(a). The VO_2 slot was placed between two copper layers to form a MIM waveguide by interfacing the VO_2 slot's front and back ends with copper-silicon-copper tapered couplers. The VO_2 slot and the silicon plasmonic tapered couplers were covered with a thin film of loss-less dielectric before being surrounded with the copper layers to form a MIVIM waveguide. At a driving voltage of ~4.6 V, the proposed modulator could exhibit switching of transmission modes from a low-loss hybrid plasmonic mode to a high-loss MIM mode for the ON state and OFF state, respectively, due to the huge refractive index contrast between the insulating phase and metallic phase of VO_2.

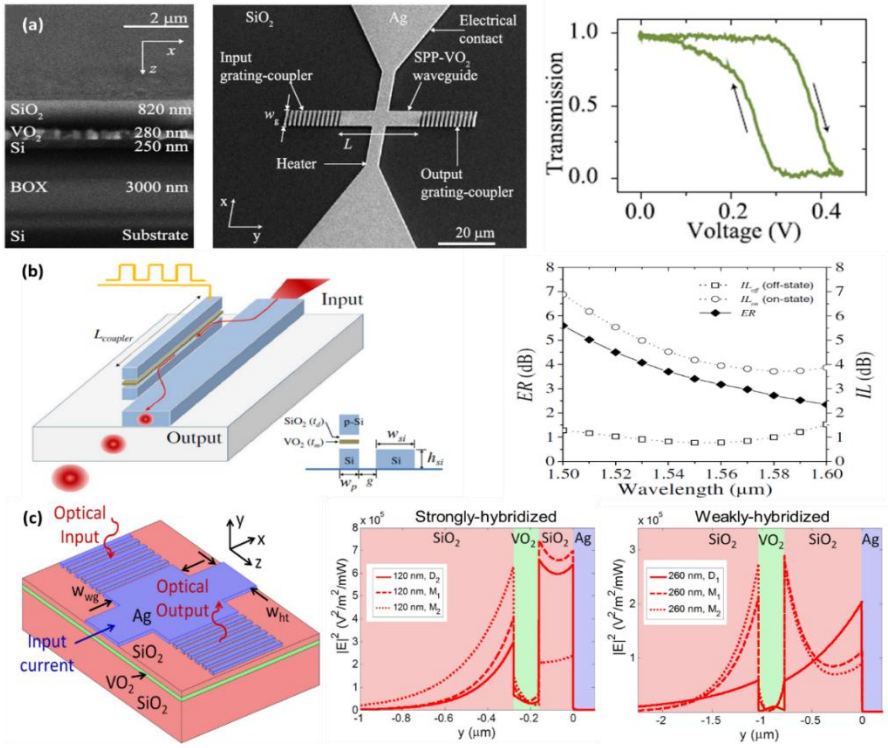

Fig. 2.15 Electrically activated VO_2 based plasmonic waveguide switches for the 1550 nm communication band. **(a)** SEM image and transmission-voltage hysteresis of a hybrid SPP-VO_2 waveguide switch [127]. **(b)** Schematic view and ON/OFF extinction ratio and insertion losses spectra of a hybrid plasmonic switch based on VO_2 [128]. **(c)** Schematic of a hybrid VO_2-plasmonic waveguide switch including integrated heaters along with the electric field intensity spectra for the strongly-hybridized device and the weakly-hybridized device [129].

Moreover, a large modulation depth of ~10 dB was achieved along with a significantly low insertion loss of ~1 dB as seen from the graphs shown in Fig. 2.136(a). Joushaghani *et al.* [131] investigated the voltage-controlled VO_2 switching based on lateral nano-gap junctions with different gap lengths and contact metals (e.g., palladium (Pd), gold (Au), silver (Ag), copper (Cu)) to compute the E-field at the initiation of the VO_2 phase transition at various heat dissipation rates as shown in Fig. 2.16(b). A switching voltage of 3 V could establish an average electric field of 75 kV/cm across a 300 nm VO_2 nano-gap junction. For low current, the electric-field at the initiation of IMT was non-dependent on the work function and thermal conductivity of the contact metals, but the reverse MIT and width of hysteresis strongly depended on the contact metals as shown in the graph of Fig. 2.16(b). Han *et al.* [132] proposed sharp switching, low voltage and broadband multifunctional terahertz modulation devices based on metallic bowtie-antenna arrays coupled with VO_2 films/wires on sapphire substrate as shown in Fig. 2.16(c). The IMT of VO_2 was electrically driven by applying an external voltage of ~4 V. This phase transition was found to be dependent on the size of VO_2 area such that smaller VO_2 patterns led to higher modulation speed and lower phase transition voltage. A broadband modulation depth response of 0.9 and minimum amplitude transmission of 0.06 was achieved over the spectral range from 0.3 THz to 2.5 THz as seen from the graphs shown in Fig. 2.16(c).

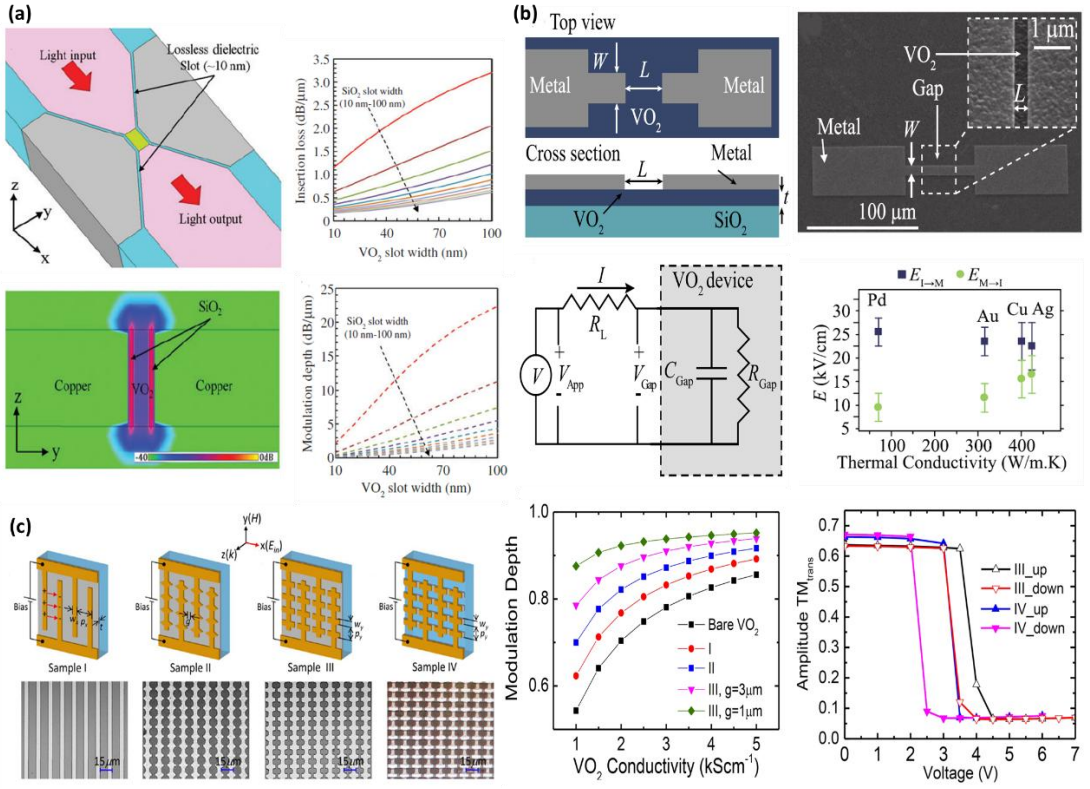

Fig. 2.16 Electrically activated VO_2 based plasmonic switches. **(a)** 3D view of a VO_2 based plasmonic dual-mode waveguide electroabsorption modulator, E-field mapping of surface plasmons in the Cu-SiO_2-VO_2-Cu slot during the ON state, and variations in insertion loss and modulation depth with respect to VO_2 and SiO_2 slot widths [130]. **(b)** Top and cross-section view of a VO_2 based lateral nano-junction, SEM image of the device, simplified circuit model of the device, and electric field distribution at the onset of phase transitions as a function of thermal conductivity of the contact metals [131]. **(c)** Design of the electrically driven hybrid bowtie antenna-VO_2 devices; modulation depth characterization at 1 THz for bare VO_2, sample I, sample II and sample III; and electrical characterizations at 1 THz for sample III and sample IV [132].

The summary of the review of electrically activated VO_2 based plasmonic switches discussed in this section is presented in Table 2.3.

Table 2.3 Review of electrically activated VO_2 based plasmonic switches

Ref. No.	Description of switch	Phase transition voltage	Figure of merit (FOM)	Index of FOM	Operating wavelength range
Chauhan *et al.*, 2020 [124]	Directional coupler structure using MDM waveguides	5 V	Modulation depth, loss, and figure of merit	Modulation depth = 19.44 dB, loss = -2.55 dB, and figure of merit = 7.62	1 μm – 2 μm

Chauhan *et al.*, 2021 [125]	Gold-VO_2-gold tri-layer based Fabry Perot structure	2.7 V	Modulation depth, insertion loss, quality factor, and figure-of-merit	Modulation depth = 44.77 dB, insertion loss = 1.43 dB, quality factor = 146, and figure-of-merit = 3.31	1 μm – 2 μm
Chauhan *et al.*, 2022 [126]	VO_2 filled dual rectangular cavity based coupled resonators	2.7 V	Modulation depth, quality factor, tunability, and figure of merit	Modulation depth = 26.40 dB, quality factor = 156, tunability = 280 nm, and figure of merit = 12	1 μm – 2 μm
Joushaghani *et al.*, 2013 [127]	Hybrid SPP-VO_2 waveguide switch	0.4 V	Extinction ratio	Extinction ratio = 16.4 dB	1550 nm
Kim, 2014 [128]	Directional coupler structure with Si waveguide and Si-SiO_2-VO_2-SiO_2-Si hybrid plasmonic waveguide	2 V	Extinction ratio and insertion loss	Extinction ratio = 6.56 dB and insertion loss = 2 dB	1.55 μm
Kruger *et al.*, 2012 [129]	Hybrid VO_2-plasmonic waveguide with integrated heaters	0.06 V	Extinction ratio and insertion loss	For strongly-hybridized device: Extinction ratio = 32.1 dB and insertion loss = 13.4 dB For weakly-hybridized device: Extinction ratio = 22.7 dB and insertion loss = 17.0 dB	1.55 μm
Ooi *et al.*, 2013 [130]	VO_2 based plasmonic dual-mode waveguide modulator with Cu-SiO_2-VO_2-Cu slot	~4.6 V	Modulation depth and insertion loss	Modulation depth ~10 dB and insertion loss ~1 dB	1.55 μm
Han *et al.*, 2017 [132]	Bowtie-antenna arrays coupled with VO_2 film	~4 V	Modulation depth	Modulation depth = 0.9	0.3 THz – 2.5 THz

2.3.3 Optically activated switches

Optically activated VO_2 switches are the plasmonic switches which undergo transition from a monoclinic semiconducting or insulating phase to a tetragonal metallic phase on the application of optical pulses. Optically activated VO_2 based plasmonic switches are of special interest as they are capable of an ultrafast switching owing to the ultrafast phase transition that can be achieved by irradiating VO_2 with optical pulses.

Over the years, the nature of insulator-to-metal transition (IMT) in VO_2, when excited optically by femtosecond laser pulses has continued to be controversial and has been explained either by a Peierls structural distortion [51], or by a Mott-like electron correlation [53] or a combination of both [55]. The initial studies on the photo excitation of VO_2 by Becker *et al.* [133] employing pump-probe optical measurements, and by Cavalleri *et al.* [134] employing X-ray measurements revealed that the phase transition happens at a picosecond time scale. In 2004, Cavalleri *et al.* [135] employed hole photo-doping in the valence band of the insulating VO_2 to induce the IMT. They found a structural bottleneck timescale of ~80 fs for the transition, associated with the phonon connecting the two crystal phases, and thus suggested the presence of a Peierls like behavior for the phase transition in VO_2. However, in 2014, Wegkamp *et al.* [136] employed femtosecond time-resolved photoelectron spectroscopy and demonstrated that VO_2 transforms quasi-instantaneously from its monoclinic to metallic state. They suggested that the IMT is a fully electronically-driven isostructural transition and reported switching speeds less than 60 fs. Wall *et al.* [137] also measured switching timescales <60 fs by employing transient reflectivity measurements. They suggested that at high pump fluences, the timescales of the switching process are no more controlled by the phonon period of the monoclinic phase. In fact, there is a complete loss of coherent motion associated with the monoclinic phase, thus leading to a change in the symmetry of the crystal potential that is driven by the laser pulse. Thus, the system melts on a subphonon-period timescale, with complex changes happening in multiple phonons to result in a final state that is an ordered solid. In other words, they suggested the existence of a non-equilibrium pathway between the two crystalline equilibrium states of VO_2. Further, in 2015, O'Callahan *et al.* [138] demonstrated timescales of ~40±8 fs much shorter than the phonon bottleneck, in single crystal microrods. More recently, Jager *et al.* [35] employed few-femtosecond extreme UV transient absorption spectroscopy and found that the IMT occurs on a timescale of 26±6 fs. The ultrafast switching times were explained by Mott-Hubbard-like mechanism driving the IMT, and were explained based on electronic screening effects along with lattice dynamics. Hence, optically-activated VO_2 based plasmonic switches can potentially allow ultrafast switching [139-141], and some of the optically-activated VO_2 based switches are discussed in this section.

Optically activated VO_2 switches designed only for the visible wavelength range are discussed first. As discussed earlier, Kepic *et al.* [95] fabricated VO_2 nanodiscs to study the nature of Mie resonances in the visible region. The VO_2 nanodiscs were also tested for optical switching and tunability by using a 633 nm continuous-wave visible laser. Modulation depth of 1.5 dB was reported for laser-

triggered phase transition of VO_2 nanodiscs. Kumar *et al.* [142] investigated a photorefractive VO_2/Au hybrid structure as shown in Fig. 2.17(a). The light-induced ultrafast plasmonic switching due to IMT of VO_2 was induced by femtosecond pulse (130 fs duration with central wavelength of 800 nm). The photo-induced modulation of surface plasmon resonance in the VO_2-gold bilayer was demonstrated by using time-resolved optical techniques, such as attenuated total reflection (ATR). The surface plasmon polariton (SPP) scattering was controlled by SPP enhancement, surface roughness, SPP propagation length at VO_2-gold interface, and by varying the optical constants of VO_2. There was 40% relative change of reflectance (i.e., change in VO_2-gold reflectivity due to IMT) for 639 nm wavelength and more than 10% change for 801 nm wavelength as seen from the graph shown in Fig. 2.17(a).

Optically activated VO_2 based plasmonic switches have also been designed for the near-infrared regions. Ferrara *et al.* [143] proposed an array of gold nanoparticles (NPs) embedded in a VO_2 thin film as shown in Fig. 2.14(b). The square arrays of gold NPs were fabricated on an indium-tin-oxide (ITO) covered glass substrate with the help of conventional electron-beam lithography (EBL) techniques by using a poly(methyl methacrylate) resist. The VO_2 thin film was deposited on the array of gold NPs by pulsed laser ablation. The SMT of VO_2 was introduced by a shuttered 785 nm pump laser. The peak of the localized surface plasmon resonance (LSPR) in the extinction spectra was red-shifted by ~250 nm during the SMT of VO_2 as shown in the graph of Fig. 2.17(b). Muskens *et al.* [144] fabricated arrays of crossed gold nanoantennas on top of a VO_2 film as shown in Fig. 2.17(c). Picosecond pulsed excitation with pump wavelength of 1060 nm was used to drive a highly localized phase-transition in plasmonic nanoantenna-VO_2 hybrids over the visible and near-infrared spectral region from 750 nm to 2250 nm. The hybrid nanostructures resulted in twenty times reduction in switching energy and five times improvement in recovery time as compared to a VO_2 film without nanoantennas. Thus, fully reversible switching was enabled in the hybrid nanostructures at over 2 million cycles per second and picojoule switching energies.

Optically activated VO_2 based plasmonic switches have also been specifically designed for the 1550 nm optical communication band. Bergamini *et al.* [145] fabricated single gold nanoantenna on top of a VO_2 film as shown in Fig. 2.17(d). The picosecond IMT in VO_2 was derived by using a laser-induced pumping with 1060 nm pump wavelength. The correlation of the geometry of the single nanoantenna with the size and permittivity of the nanoscale VO_2 regions was analyzed in the spectral range between 1100 nm to 1900 nm which showed a plasmon resonance wavelength around 1550 nm as depicted in the graph of Fig. 2.17(d). Hallman *et al.* [146] proposed a photo-induced hybrid VO_2-silicon waveguide sub-picosecond switch as depicted in Fig. 2.17(e). The reversible and ultra-fast phase transition in VO_2 was driven by a temporally synchronized 130 fs pulse at a pump wavelength of 1670 nm. A 105 fs probe beam at 1550 nm launched in a transverse electric waveguide mode was switched with an ON to OFF time of less than 1 ps. The switching energies reported above threshold were of order 600 fJ per switch.

Some optically activated VO_2 based plasmonic switches have been designed for visible, near-infrared, as well as mid-infrared ranges. Guo *et al.* [147]

composed a hybrid platform of plasmonic ITO nanorod array (ITO-NRA) conformally coated with an ultra-thin layer of VO_2 grown by atomic layer deposition (ALD) as shown in Fig. 2.17(f). The ITO-NRA supported transverse LSPR in the near-infrared, long-LSPR in the mid-infrared, and dielectric resonances in the visible spectral range. The coating of VO_2 on ITO-NRA reduced the overall transmittance owing to the imaginary part of the refractive index of VO_2 in the visible range. In comparison to the 1450 nm and 2000 nm OFF-resonance pump conditions, the 1850 nm ON-resonance pump gave stronger ΔOD (change of optical density) amplitude of 0.2 due to a plasmonic hotspot effect as shown in the graph of Fig. 2.17(f).

Terahertz metasurfaces hybridized with VO_2 have also been employed for optical switching in the terahertz region. Choi *et al.* [148] presented a patterned nanoresonator, i.e., a periodic array of rectangular gold slot antennas, fabricated on VO_2 thin films as shown in Fig. 2.17(g). Ultrafast (i.e., sub-picosecond time scale) control of terahertz transmission with moderate optical pumping power was enabled

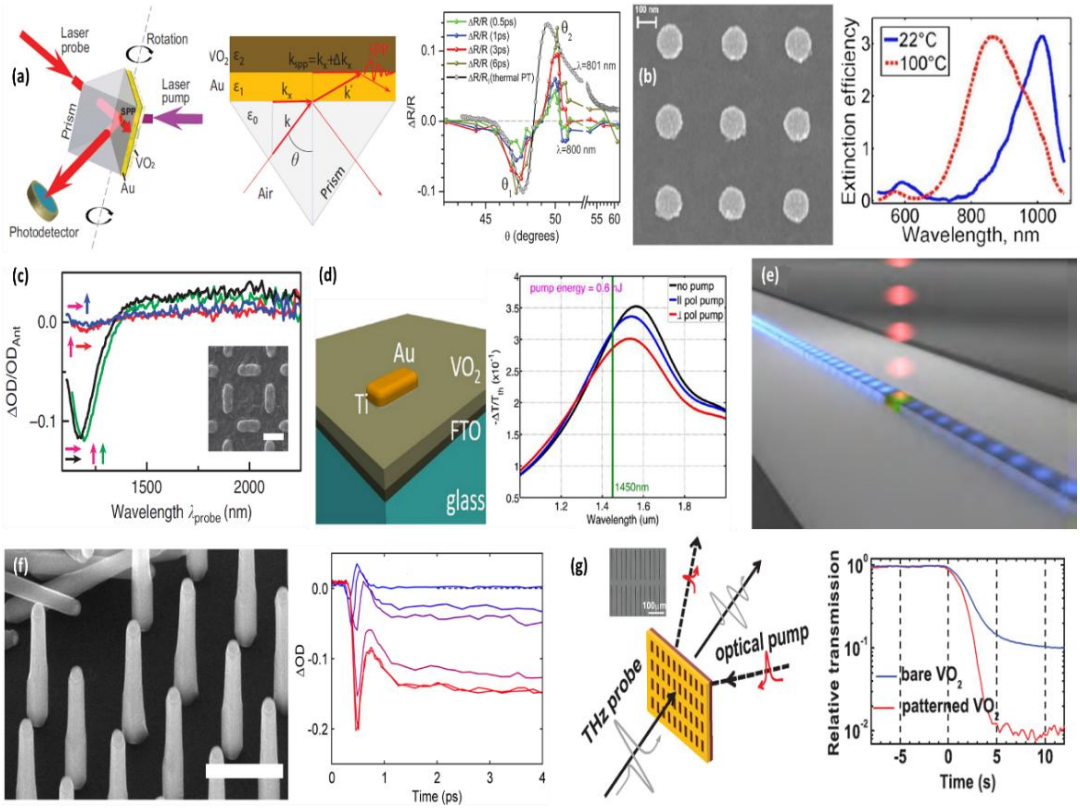

Fig. 2.17 Optically activated VO_2 based plasmonic switches. **(a)** Experimental geometry and SPPs excitation at VO_2-gold interface by attenuated total reflection (ATR) procedure using Kretschmann-Raether configuration along with relative change of the reflectivity plots for various probe delays as a function of incident angle [142]. **(b)** SEM image and extinction spectra of the 140 nm gold nanoparticles array [143]. **(c)** Differential nonlinear response spectrum for a gold nanoantenna array on VO_2 film [144]. **(d)** 3D sketch and response spectra of a single Au antenna-VO_2 system [145]. **(e)** Schematic view of a photo-induced hybrid VO_2-silicon waveguide switch [146]. **(f)** SEM image and transmission spectra of ITO-NRA sample coated with VO_2 [147]. **(g)** Schematic diagram and THz switching time measurements of sample array of nanoresonator-patterned gold rectangular holes deposited on VO_2 film [148].

in the patterned nanoresonator due to the phase transition in VO_2 from its insulating state to metallic state, while no modulation was observed with bare films as shown in the graph of Fig. 2.17(g). Moreover, a sharp resonance was obtained in the transmittance spectra at a specific frequency determined by the nanoresonator length, the refractive index of substrates, and the periodicities of the hole arrays. In insulating state of VO_2, near perfect transmission of >90% was achieved at the 0.5 THz resonant frequency with only 1.2% aperture-coverage ratio of the patterned nanoresonator.

The summary of the review of optically activated VO_2 based plasmonic switches discussed in this section is presented in Table 2.4. Table 2.5 provides a comparative analysis of the important performance parameters, advantages, and potential limitations of the VO_2 based plasmonic switches with different activation mechanisms as discussed in this review.

Table 2.4 Review of optically activated VO_2 based plasmonic switches

Ref. No.	Description of switch	Optical pulse characteristic	Figure of merit (FOM)	Index of FOM	Operating wavelength range
Kepic *et al.*, 2021 [95]	VO_2 nanodiscs on fused silica substrate	Continuous-wave visible laser at 633 nm wavelength	Modulation depth	Modulation depth = 1.5 dB	400 nm – 900 nm
Kumar *et al.*, 2018 [142]	VO_2/Au hybrid structure	Femtosecond pulse at 800 nm wavelength	Relative change of reflectance	Relative change of reflectance = 40% and >10% for wavelengths at 639 nm and 801 nm	639 nm and 801 nm
Ferrara *et al.*, 2011 [143]	Gold nanoparticles embedded in VO_2 thin film	Pump laser at 785 nm wavelength	Shift in extinction spectra	~250 nm shift during the VO_2 SMT	500 nm – 1100 nm
Muskens *et al.*, 2016 [144]	Arrays of crossed gold nanoantennas on VO_2 film	Picosecond pulse at 1060 nm wavelength	Modulation contrast	Modulation contrast ~20%	750 nm – 2250 nm
Hallman *et al.*, 2021 [146]	Hybrid VO_2-silicon waveguide	Femtosecond laser pulse at 1670 nm wavelength	Transmission contrast	Transmission contrast ~22%	1550 nm
Choi *et al.*, 2011 [148]	Periodic array of rectangular gold slot antennas on VO_2 thin films	Pulse laser at 730 nm wavelength	Transmission spectra	90% transmission at resonance frequency	0.2 THz – 3 THz

Table 2.5 Comparative analysis of VO_2 based plasmonic switches with different activation mechanisms

Activation Mechanism	Performance Parameters	Advantages	Limitations
Thermally activated switches	• Extinction ratio as high as ~23 dB [102] • Modulation depth as high as ~69 dB [106] • Insertion loss as low as ~2 dB [100] • Intensity switching ratio as high as ~2500 for near-field switching [99]	• Low-cost operation • No requirement for sophisticated equipment such as femtosecond lasers	• Lower switching speeds than electrically and optically activated plasmonic switches [149] • High power consumption • Requirement of an external heating arrangement or an integrated heater to induce the phase transition • Micro-heaters may need to be fabricated to heat switches with smaller area [150]
Electrically activated switches	• Extinction ratio as high as ~32 dB [129] • Modulation depth as high as ~44 dB [125] • Insertion loss as low as ~1 dB [130]	• Moderate switching speed with IMT timescales of the order of nanoseconds [151] • Phase transition voltages <0.5 V [127, 129] • Low power consumption (~mW) [127] • Can be integrated with electrical circuits [125]	• Switching speeds less than optically-activated VO_2 based plasmonic switches [149, 151] • Heat generated due to the flow of current needs to be dissipated [131]
Optically activated switches	• Relative change of reflectance ~40% [142] • Potential switching timescales of the order of picoseconds to femtoseconds [139]	• Higher switching speeds than thermally or electrically activated switches [138, 146, 149] • Lower power consumption than thermally-activated and electrically-activated VO_2 based switches	• Requirement of expensive ultrafast spectroscopy set-ups such as time-resolved photoelectron spectroscopy (TR-PES) or few-femtosecond extreme UV transient absorption spectroscopy (FXTAS) [138, 142] • Requirement of precise optical alignment [138, 142]

2.4 Chapter Summary

In this chapter, the recent advancements in the development of plasmonic switches based on vanadium dioxide (VO_2) as the phase change material have been comprehensively reviewed. The VO_2 based plasmonic switches were reviewed under three categories, i.e., thermally-activated, electrically-activated and optically-activated switches, along with a discussion of the underlying physical phenomenon that leads to high switching efficiencies in these switches. Moreover, the switches in each category were further classified according to the wavelength range for which they are proposed. The review concludes that with the recent developments in the area of VO_2 based plasmonic switches, higher extinction ratios have been reported with smaller footprints, simpler fabrication, and lower losses. For thermally activated VO_2 switches, extinction ratios >20 dB have been reported by employing various designs of the switches. These switches have been proposed for the visible, near-infrared, infrared and the terahertz wavelength range. Further, near-field switching using VO_2 based plasmonic nanoantenna structures has been reported with intensity switching ratios >900. However, it should be noted that the extinction ratios of thermally-activated VO_2 based plasmonic switches are limited to ~5 dB for broadband operations. Hence, the future designs of such switches are expected to demonstrate an increase in the extinction ratio for broadband switching. In addition, multiwavelength operation of such switches will be promising for multiple switching applications. For electrically driven VO_2 based switches, recent developments have led to the design of switches with higher extinction ratios >30 dB and phase transition voltages <0.5 V at switching timescales of the order of a few nanoseconds. In the near future, electrically-driven VO_2 based plasmonic switches can allow large scale integration of electrodes with VO_2. Additionally, the future designs for the devices proposed for electrically-driven VO_2 based switching can cover a critical analysis for the effect of electrodes on the performance of the switch. For optically-activated VO_2 based plasmonic switches, the switching has been demonstrated with both continuous wave and pulsed lasers, but there is further scope for the development of switches with higher switching efficiencies and lower switching energies. Although, switching timescales <50 fs for the photo-excited phase transition in VO_2 have been reported by employing sophisticated processes such as few-femtosecond extreme UV transient absorption spectroscopy (FXTAS), achievement of femto-second switching speeds for VO_2 based plasmonic switches in integrated devices can be explored in the near future. Optically-activated VO_2 based switches can be integrated with Photonic Integrated Circuits (PICs) where optical waveguides could be employed for carrying the pump and probe light. Further, in addition to the well-known semiconducting and metallic states, future work could include exploiting the intermediate states of VO_2 for plasmonic switching. In conclusion, there has been a significant progress in the development of ultrafast, low-loss, high efficiency plasmonic switches based on VO_2 over the last decade. However, in the near future, there is a huge potential to develop such switches with even higher switching efficiencies, lower losses and higher switching speeds for integrated photonics, plasmonic logic circuits, optical communication, computing network applications, superresolution imaging, quantum computing, and neural networking.

2.5 References

[1] Maier, S. A. *Plasmonics: Fundamentals and applications*. Springer, New York, USA, 2007. ISBN: 9780387331508. https://doi.org/10.1007/0-387-37825-1

[2] Maier, S. A., and Atwater, H. A. "Plasmonics: Localization and guiding of electromagnetic energy in metal/dielectric structures", *Journal of Applied Physics*, 98(1), 011101, 2005. https://doi.org/10.1063/1.1951057

[3] Novotny, L., and Hecht, B. *Principles of nano-optics*. Cambridge University Press, 2008. ISBN: 9780511794193. https://doi.org/10.1017/CBO9780511794193

[4] Ozbay, E. "Plasmonics: Merging photonics and electronics at nanoscale dimensions", *Science*, 311(5758), 189-193, 2006. https://doi.org/10.1126/science.1114849

[5] Drude, P. "Zur elektronentheorie der metalle", *Annalen der Physik*, 306(3), 566-613, 1900. https://doi.org/10.1002/andp.19003060312

[6] Raether, H. *Surface plasmons on smooth and rough surfaces and on gratings*. Springer, Berlin, Germany, 1988. https://doi.org/10.1007/BFb0048317

[7] Zayats, A. V., Smolyaninov, I. I., and Maradudin, A. A. "Nano-optics of surface plasmon polaritons", *Physics Reports*, 408(3), 131-314, 2005. https://doi.org/10.1016/j.physrep.2004.11.001

[8] Barnes, W. L., Dereux, A., and Ebbesen, T. W. "Surface plasmon subwavelength optics", *Nature*, 424(6950), 824-830, 2003. https://doi.org/10.1038/nature01937

[9] Pitarke, J. M., Silkin, V. M., Chulkov, E. V., and Echenique, P. M. "Theory of surface plasmons and surface-plasmon polaritons", *Reports on Progress in Physics*, 70(1), 1, 2006. https://doi.org/10.1088/0034-4885/70/1/R01

[10] Maier, S. A., Kik, P. G., and Atwater, H. A. "Optical pulse propagation in metal nanoparticle chain waveguides", *Physical Review B*, 67(20), 205402, 2003. https://doi.org/10.1103/PhysRevB.67.205402

[11] Agranovich, V. M. *Surface Polaritons*. Elsevier, 2012. ISBN: 9780444598691

[12] Akowuah, E. K., Gorman, T., and Haxha, S. "Design and optimization of a novel surface plasmon resonance biosensor based on Otto configuration", *Optics Express*, 17(26), 23511-23521, 2009. https://doi.org/10.1364/OE.17.023511

[13] Gwon, H. R., and Lee, S. H. "Spectral and angular responses of surface plasmon resonance based on the Kretschmann prism configuration", *Materials Transactions*, 51(6), 1150-1155, 2010. https://doi.org/10.2320/matertrans.M2010003

[14] Homola, J. "On the sensitivity of surface plasmon resonance sensors with spectral interrogation", *Sensors and Actuators B: Chemical*, 41(1), 207-211, 1997. https://doi.org/10.1016/S0925-4005(97)80297-3

[15] Guo, J., Keathley, P. D., and Hastings, J. T. "Dual-mode surface-plasmon-resonance sensors using angular interrogation", *Optics Letters*, 33(5), 512-514, 2008. https://doi.org/10.1364/OL.33.000512

[16] Willets, K. A., and Duyne, R. P. V. "Localized surface plasmon resonance spectroscopy and sensing", *Annual Reviews on Physical Chemistry*, 58, 267-297, 2007. https://doi.org/10.1146/annurev.physchem.58.032806.104607

[17] Hutter E., and Fendler, J. H. "Exploitation of localized surface plasmon resonance", *Advanced Materials*, 16(19), 1685-1706, 2004. https://doi.org/10.1002/adma.200400271

[18] Mayer, K. M., and Hafner, J. H. "Localized surface plasmon resonance sensors", *Chemical Reviews*, 111(6), 3828-3857, 2011. https://doi.org/10.1021/cr100313v

[19] Sherry, L. J., *et al.* "Localized surface plasmon resonance spectroscopy of single silver nanocubes", *Nano Letters*, 5(10), 2034-2038, 2005. https://doi.org/10.1021/nl0515753

[20] Brolo, A. G., Gordon, R., Leathem, B., and Kavanagh, K. L. “Surface plasmon sensor based on the enhanced light transmission through arrays of nanoholes in gold films”, *Langmuir*, 20(12), 4813-4815, 2004. https://doi.org/10.1021/la0493621

[21] Long, Y. T., and Jing, C. *Localized Surface Plasmon Resonance Based Nanobiosensors*. Springer, Berlin, Germany, 2014. https://doi.org/10.1007/978-3-642-54795-9

[22] Nordlander, P., and Prodan, E. “Plasmon hybridization in nanoparticles near metallic surfaces”, *Nano Letters*, 4(11), 2209-2213, 2004. https://doi.org/10.1021/nl0486160

[23] Fan, X., Zheng, W., and Singh, D. J. “Light scattering and surface plasmons on small spherical particles”, *Light: Science & Applications*, 3(6), e179, 2014. https://doi.org/10.1038/lsa.2014.60

[24] Klar, T., *et al.* “Surface-plasmon resonances in single metallic nanoparticles”, *Physical Review Letters*, 80(19), 4249, 1998. https://doi.org/10.1103/PhysRevLett.80.4249

[25] Nehl, C. L., and Hafner, J. H. “Shape-dependent plasmon resonances of gold nanoparticles”, *Journal of Material Chemistry*, 18(21), 2415-2419, 2008. https://doi.org/10.1039/B714950F

[26] Marzan, L. M. L. “Tailoring surface plasmons through the morphology and assembly of metal nanoparticles”, *Langmuir*, 22(1), 32-41, 2006. https://doi.org/10.1021/la0513353

[27] Yang, Z., and Ramanathan, S. “Breakthroughs in photonics 2014: Phase change materials for photonics”, *IEEE Photonics Journal*, 7(3), 0700305, 2015. https://doi.org/10.1109/JPHOT.2015.2413594

[28] Prabhathan, P., *et al.* “Roadmap for phase change materials in photonics and beyond”, *iScience*, 26(10), 107946, 2023. https://doi.org/10.1016/j.isci.2023.107946

[29] Wang, J., Wang, L., and Liu, J. “Overview of phase-change materials based photonic devices”, *IEEE Access*, 8, 121211-121245, 2020. https://doi.org/10.1109/ACCESS.2020.3006899

[30] Tripathi, D., Vyas, H. S., Kumar, S., Panda, S. S., and Hegde, R. “Recent developments in chalcogenide phase change material-based nanophotonics”, *Nanotechnology*, 34(50), 502001, 2023. https://doi.org/10.1088/1361-6528/acf1a7

[31] Huang, Y., *et al.* “Phase transition analysis of thermochromic VO_2 thin films by temperature-dependent Raman scattering and ellipsometry”, *Applied Surface Science*, 456(31), 545-551, 2018. https://doi.org/10.1016/j.apsusc.2018.06.125

[32] Burtsev, A. A., *et al.* “Physical properties’ temperature dynamics of GeTe, $Ge_2Sb_2Te_5$ and $Ge_2Sb_2Se_4Te_1$ phase change materials”, *Materials Science in Semiconductor Processing*, 150, 106907, 2022. https://doi.org/10.1016/j.mssp.2022.106907

[33] Ziegler, S., and Wuttig, M. “Nucleation of AgInSbTe films employed in phase-change media”, *Journal of Applied Physics*, 99(6), 064907, 2006. https://doi.org/10.1063/1.2184428

[34] Pandey, S. K., and Manivannan, A. “Direct evidence for structural transformation and higher thermal stability of amorphous insbte phase change material”, *Scripta Materialia*, 192, 73-77, 2021. https://doi.org/10.1016/j.scriptamat.2020.10.014

[35] Jager, M. F. *et al.* “Tracking the insulator-to-metal phase transition in VO_2 with few-femtosecond extreme UV transient absorption spectroscopy”, *Proceedings of the National Academy of Sciences*, 114(36), 9558-9563, 2017. https://doi.org/10.1073/pnas.170760211

[36] Bai, K., Tan, T. L., Branicio, P. S., and Sullivan, M. B. “Time-temperature-transformation and continuous-heating-transformation diagrams of $GeSb_2Te_4$ from nanosecond-long ab initio molecular dynamics simulations”, *Acta Materialia*, 121, 257-265, 2016. https://doi.org/10.1016/j.actamat.2016.09.011

[37] Mikheeva, E., *et al.* “Space and time modulations of light with metasurfaces: Recent progress and future prospects”, *ACS Photonics*, 9(5), 1458-1482, 2022. https://doi.org/10.1021/acsphotonics.1c01833

[38] Pandey, S. K., and Manivannan A. "Sub-nanosecond threshold-switching dynamics and set process of In_3SbTe_2 phase-change memory devices", *Applied Physics Letters*, 108, 233501, 2016. https://doi.org/10.1063/1.4953196

[39] Morin, F. J. "Oxides which show a metal-to-insulator transition at the Neel temperature", *Physical Review Letters*, 3(1), 34, 1959. https://doi.org/10.1103/PhysRevLett.3.34

[40] Mitsuishi, T. "On the phase transformation of VO_2", *Japanese Journal of Applied Physics*, 6(9), 1060, 1967. https://doi.org/10.1143/JJAP.6.1060

[41] Zylbersztejn, A. and Mott, N. F. "Metal-insulator transition in vanadium dioxide", *Physical Review B*, 11(11), 4383, 1975. https://doi.org/10.1103/PhysRevB.11.4383

[42] Bianconi, A., Stizza, S., and Bernardini, R. "Critical behavior of the plasmon resonance at the metal-insulator transition in VO_2", *Physical Review B*, 24(8), 4406, 1981. https://doi.org/10.1103/PhysRevB.24.4406

[43] Dachuan, Y., Niankan, X., Jingyu, Z., and Xiulin, Z. "Vanadium dioxide films with good electrical switching property", *Journal of Physics D: Applied Physics*, 29(4), 1051, 1996. https://doi.org/10.1088/0022-3727/29/4/017

[44] Lopez, R., Feldman, L. C., and Haglund Jr, R. F. "Size-dependent optical properties of VO_2 nanoparticle arrays", *Physical Review Letters*, 93(17), 177403, 2004. https://doi.org/10.1103/PhysRevLett.93.177403

[45] Maaza, M., Nemraoui, O., Sella, C., Beye, A. C., and Barak, B. B. "Thermal induced tunability of surface plasmon resonance in Au-VO_2 nano-photonics", *Optics Communications*, 254(1-3), 188-195, 2005. https://doi.org/10.1016/j.optcom.2004.08.056

[46] Gentle, A., Maaroof, A. I., and Smith, G. B. "Nanograin VO_2 in the metal phase: a plasmonic system with falling dc resistivity as temperature rises", *Nanotechnology*, 18(2), 025202, 2007. https://doi.org/10.1088/0957-4484/18/2/025202

[47] Suh, J. Y., Donev, E. U., Lopez, R., Feldman, L. C., and Haglund Jr, R. F. "Modulated optical transmission of subwavelength hole arrays in metal-VO_2 films", *Applied Physics Letters*, 88(13), 133115, 2006. https://doi.org/10.1063/1.2190463

[48] Suh, J. Y. *et al.* "Modulation of the gold particle-plasmon resonance by the metal-semiconductor transition of vanadium dioxide", *Journal of Optics A: Pure and Applied Optics*, 10(5), 055202, 2008. https://doi.org/10.1088/1464-4258/10/5/055202

[49] Nag, J. *et al.* "Ultrafast compact silicon-based ring resonator modulators using metal-insulator switching of vanadium dioxide", Proceedings SPIE 7597, *Physics and Simulation of Optoelectronic Devices XVIII*, 759710, 2010. https://doi.org/10.1117/12.843866

[50] Semenov, A. L. "Dynamics of a Peierls system in a light field", *Journal of Experimental and Theoretical Physics*, 89, 1168-1179, 1999. https://doi.org/10.1134/1.559068

[51] Biermann, S., Poteryaev, A., Lichtenstein, A. I., and Georges, A. "Dynamical singlets and correlation-assisted Peierls transition in VO_2", *Physical Review Letters*, 94(2), 026404, 2005. https://doi.org/10.1103/PhysRevLett.94.026404

[52] Mott, N. F. "Metal-insulator transition", *Reviews of Modern Physics*, 40(4), 677, 1968. https://doi.org/10.1103/RevModPhys.40.677

[53] Stefanovich, G., Pergament, A., and Stefanovich, D. "Electrical switching and Mott transition in VO_2", *Journal of Physics: Condensed Matter*, 12(41), 8837, 2000. https://doi.org/10.1088/0953-8984/12/41/310

[54] Weber, C. *et al.* "Vanadium dioxide: A Peierls-Mott insulator stable against disorder", *Physical Review Letters*, 108(25), 256402, 2012. https://doi.org/10.1103/PhysRevLett.108.256402

[55] Lee, D. *et al.* "Deposition-temperature-mediated selective phase transition mechanism of VO_2 films", *The Journal of Physical Chemistry C*, 124(31), 17282-17289, 2020. https://doi.org/10.1021/acs.jpcc.0c03038

[56] Haglund Jr, R. F., Weiss, S. M., and Appavoo, K. "Photonic and plasmonic modulators based on optical switching in VO_2", Proceedings SPIE 9370, *Quantum Sensing and Nanophotonic Devices XII*, 93701C, 2015. https://doi.org/10.1117/12.2083422

[57] Oka, Y., Yao, T., and Yamamoto, N. "Powder X-ray crystal structure of VO_2(A)", *Journal of Solid State Chemistry*, 86(1), 116-124, 1990. https://doi.org/10.1016/0022-4596(90)90121-D

[58] Oka, Y., Yao, T., Yamamoto, N., Ueda, Y., and Hayashi, A. "Phase transition and V^{4+}-V^{4+} pairing in VO_2(B)", *Journal of Solid State Chemistry*, 105(1), 271-278, 1993. https://doi.org/10.1006/jssc.1993.1215

[59] Goodenough, J. B. "The two components of the crystallographic transition in VO_2", *Journal of Solid State Chemistry*, 3(4), 490-500, 1971. https://doi.org/10.1016/0022-4596(71)90091-0

[60] Mellan, T. A., and Crespo, R. G. "Density functional theory study of rutile VO_2 surfaces", *The Journal of Chemical Physics*, 137(15), 154706, 2012. https://doi.org/10.1063/1.4758319

[61] Tao, Z. *et al.* "Decoupling of structural and electronic phase transitions in VO_2", *Physical Review Letters*, 109(16), 166406, 2012. https://doi.org/10.1103/PhysRevLett.109.166406

[62] Oka, Y., Sato, S., Yao, T., and Yamamoto, N. "Crystal structures and transition mechanism of VO_2(A)", *Journal of Solid State Chemistry*, 141(2), 594-598, 1998. https://doi.org/10.1006/jssc.1998.8025

[63] Moatti, A., Sachan, R., Prater, J., and Narayan, J. "Control of structural and electrical transitions of VO_2 thin films", *ACS Applied Materials & Interfaces*, 9(28), 24298-24307, 2017. https://doi.org/10.1021/acsami.7b05620

[64] Wentzcovitch, R. M., Schulz, W. W., and Allen, P. B. "VO_2: Peierls or Mott-Hubbard? A view from band theory", *Physical Review Letters*, 72(21), 3389, 1994. https://doi.org/10.1103/PhysRevLett.72.3389

[65] Liebsch, A., Ishida, H., and Bihlmayer, G. "Coulomb correlations and orbital polarization in the metal-insulator transition of VO_2", *Physical Review B*, 71, 085109, 2005. https://doi.org/10.1103/PhysRevB.71.085109

[66] Budai, J. D. *et al.* "Metallization of vanadium dioxide driven by large phonon entropy", *Nature*, 515, 535-539, 2014. https://doi.org/10.1038/nature13865

[67] Shao, Z., Cao, X., Luo, H., and Jin, P. "Recent progress in the phase-transition mechanism and modulation of vanadium dioxide materials", *NPG Asia Materials*, 10, 581-605, 2018. https://doi.org/10.1038/s41427-018-0061-2

[68] Eyert, V. "The metal-insulator transitions of VO_2: A band theoretical approach", *Annalen Der Physik*, 514(9), 650-704, 2002. https://doi.org/10.1002/andp.20025140902

[69] Pouget, J. P., Launois, H., D'Haenens, J. P., Merenda, P., and Rice, T. M. "Electron localization induced by uniaxial stress in pure VO_2", *Physical Review Letters*, 35(13), 873, 1975. https://doi.org/10.1103/PhysRevLett.35.873

[70] Strelcov, E. *et al.* "Doping-based stabilization of the M_2 phase in free-standing VO_2 nanostructures at room temperature", *Nano Letters*, 12(12), 6198-6205, 2012. https://doi.org/10.1021/nl303065h

[71] Huffman, T. J. *et al.* "Insulating phases of vanadium dioxide are Mott-Hubbard insulators", *Physical Review B*, 95(7), 075125, 2017. https://doi.org/10.1103/PhysRevB.95.075125

[72] Sun, C., Yan, L., Yue, B., Liu, H., and Gao, Y. "The modulation of metal-insulator transition temperature of vanadium dioxide: a density functional theory study", *Journal of Materials Chemistry C*, 2(43), 9283-9293, 2014. https://doi.org/10.1039/C4TC00778F

[73] Brito, W. H., Aguiar, M. C. O., Haule, K., and Kotliar, G. "Metal-insulator transition in VO_2: A DFT+DMFT perspective", *Physical Review Letters*, 117(5), 056402, 2016. https://doi.org/10.1103/PhysRevLett.117.056402

[74] Grandi, F., Amaricci, A., and Fabrizio, M. "Unraveling the Mott-Peierls intrigue in vanadium dioxide", *Physical Review Research*, 2(1), 013298, 2020. https://doi.org/10.1103/PhysRevResearch.2.013298

[75] Yao, T. *et al.* "Understanding the nature of the kinetic process in a VO_2 metal-insulator transition", *Physical Review Letters*, 105(22), 226405, 2010. https://doi.org/10.1103/PhysRevLett.105.226405

[76] Laverock, J. *et al.* "Direct observation of decoupled structural and electronic transitions and an ambient pressure monocliniclike metallic phase of VO_2", P*hysical Review Letters*, 113(21), 216402, 2014. https://doi.org/10.1103/PhysRevLett.113.216402

[77] Chen, S., Liu, J., Luo, H., and Gao, Y. "Calculation evidence of staged Mott and Peierls transitions in VO_2 revealed by mapping reduced-dimension potential energy surface", *The Journal of Physical Chemistry Letters*, 6(18), 3650-3656, 2015. https://doi.org/10.1021/acs.jpclett.5b01376

[78] Peterseim, T., Dressel, M., Dietrich, M., and Polity, A. "Optical properties of VO_2 films at the phase transition: Influence of substrate and electronic correlations", *Journal of Applied Physics*, 120(7), 075102, 2016. https://doi.org/10.1063/1.4961406

[79] Lu, S., Hou, L., and Gan, F. "Preparation and optical properties of phase-change VO_2 thin films", *Journal of Materials Science*, 28(8), 2169-2177, 1993. https://doi.org/10.1007/BF00367579

[80] Liu, H., Vasquez, O., Santiago, V. R., Diaz, L., and Fernandez, F. E. "Excited state dynamics and semiconductor-to-metallic phase transition of VO_2 thin film", *Journal of Luminescence*, 108(1-4), 233-238, 2004. https://doi.org/10.1016/j.jlumin.2004.01.050

[81] Lu, S., Hou, L., and Gan, F. "Structure and optical property changes of sol-gel derived VO_2 thin films", *Advanced Materials*, 9(3), 244-246, 2004. https://doi.org/10.1002/adma.19970090313

[82] Verleur, H. W., Barker Jr, A. S., and Berglund, C. N. "Optical properties of VO_2 between 0.25 and 5 eV", *Physical Review Journals Archive*, 172(3), 788, 1968. https://doi.org/10.1103/PhysRev.172.788

[83] Kana, J. B. K., Ndjaka, J. M., Vignaud, G., Gibaud, A., and Maaza, M. "Thermally tunable optical constants of vanadium dioxide thin films measured by spectroscopic ellipsometry", *Optics Communications*, 284(3), 807-812, 2011. https://doi.org/10.1016/j.optcom.2010.10.009

[84] Mahdieh, M. H., and Sohrabi, M. "Precise design of VO_2 thin films for smart windows by employing thickness-dependent refractive index", *Physica Status Solidi A*, 220(2), 2200553, 2023. https://doi.org/10.1002/pssa.202200553

[85] Peng, Z., Wang, Y., Du, Y., Lu, D., and Sun, D. "Phase transition and IR properties of tungsten-doped vanadium dioxide nanopowders", *Journal of Alloys and Compounds*, 480(2), 537-540, 2009. https://doi.org/10.1016/j.jallcom.2009.01.092

[86] Li, Y., Liu, Y., Liu, J., and Ren, L. "The effects of niobium on the structure and properties of VO_2 films", *Journal of Materials Science: Materials in Electronics*, 27, 4981-4987, 2016. https://doi.org/10.1007/s10854-016-4384-x

[87] Zhou, Q. *et al.* "Boron doped M-phase VO_2 nanoparticles with low metal-insulator phase transition temperature for smart windows", *Ceramics International*, 46(4), 4786-4794, 2020. https://doi.org/10.1016/j.ceramint.2019.10.211

[88] Dai, L. *et al.* "F-doped VO_2 nanoparticles for thermochromic energy-saving foils with modified color and enhanced solar-heat shielding ability", *Physical Chemistry Chemical Physics*, 15(28), 11723-11729, 2013. https://doi.org/10.1039/C3CP51359A

[89] Mai, L. Q., Hu, B., Hu, T., Chen, W., and Gu, E. D. "Electrical property of Mo-doped VO_2 nanowire array film by melting-quenching sol-gel method", *The Journal of Physical Chemistry B*, 110(39), 19083-19086, 2006. https://doi.org/10.1021/jp0642701

[90] Ji, C. *et al.* "Al-doped VO_2 films as smart window coatings: Reduced phase transition temperature and improved thermochromic performance", *Solar Energy Materials and Solar Cells*, 176, 174-180, 2018. https://doi.org/10.1016/j.solmat.2017.11.026

[91] Krammer, A. *et al.* "Elevated transition temperature in Ge doped VO_2 thin films", *Journal of Applied Physics*, 122(4), 045304, 2017. https://doi.org/10.1063/1.4995965

[92] Victor, J. L. *et al.* "Doubling of the phase transition temperature of VO_2 by Fe doping", *The Journal of Physical Chemistry Letters*, 12(32), 7792-7796, 2021. https://doi.org/10.1021/acs.jpclett.1c02179

[93] Agrawal, A. K., Das, A., Gupta, N., Kumar, K., and Dhawan, A. "Large-area plasmonic switches based on crystalline au nanoparticles between VO_2 layers for enhanced switching in visible-near-infrared regime", *Advanced Photonics Research*, 3(3), 2100253, 2022. https://doi.org/10.1002/adpr.202100253

[94] Sharma, Y., Tiruveedhula, V. A., Muth, J. F., and Dhawan, A. "VO_2 based waveguide-mode plasmonic nano-gratings for optical switching", *Optics Express*, 23(5), 5822-5849, 2015. https://doi.org/10.1364/OE.23.005822

[95] Kepic, P. *et al.* "Optically tunable Mie resonance VO_2 nanoantennas for metasurfaces in the visible", *ACS Photonics*, 8(4), 1048-1057, 2021. https://doi.org/10.1021/acsphotonics.1c00222

[96] Savaliya, P. B., Thomas, A., Dua, R., and Dhawan, A. "Tunable optical switching in the near-infrared spectral regime by employing plasmonic nanoantennas containing phase change materials", *Optics Express*, 25(20), 23755-23772, 2017. https://doi.org/10.1364/OE.25.023755

[97] Gupta, N., Savaliya, P. B., and Dhawan, A. "Plasmonic nanoantennas on VO_2 films for active switching of near-field intensity and radiation from nanoemitters", *Optics Express*, 28(19), 27476-27494, 2020. https://doi.org/10.1364/OE.391655

[98] Sharma, Y., and Dhawan, A. "Active near-field plasmonic switches based on Sierpiński-fractal nanoantennas on VO_2 films", *Journal of Optics*, 24(6), 065001, 2022. https://doi.org/10.1088/2040-8986/ac6208

[99] Masih, A., and Sharma, Y. "Koch-curve fractal plasmonic nanoantennas on VO_2 for near-field plasmonic switching", *Physica Scripta*, 100(5), 055518, 2025. https://doi.org/10.1088/1402-4896/adc5af

[100] Miller, K. J., Hallman, K. A., Haglund Jr, R. F., and Weiss, S. M. "Silicon waveguide optical switch with embedded phase change material", *Optics Express*, 25(22), 26527-26536, 2017. https://doi.org/10.1364/OE.25.026527

[101] Singh, M., and Datta, A. "Modeling of a vertical hybrid plasmonic switch with VO_2 fin Bragg grating", *IEEE Photonics Technology Letters*, 30(11), 997-1000, 2018. https://doi.org/10.1109/LPT.2018.2826845

[102] Moshfeghifar, S., Abbasian, K., Gilalrlue, M. M., and Jahani, M. A. T. G. "Active tunable plasmonic switch designed by metal-insulator-metal waveguides connected to a nanodisk cavity enabled by a phase-change material ring", *Optical Engineering*, 60(4), 045104, 2021. https://doi.org/10.1117/1.OE.60.4.045104

[103] Singh, M. "Design of hybrid multilayer plasmonic switch-cum-splitter with 90° bends", *Optik*, 178, 902-908, 2019. https://doi.org/10.1016/j.ijleo.2018.10.088

[104] Singh, M. “Modeling of hybrid plasmonic ring resonator based on dielectric filled subwavelength metal grating”, *Plasmonics*, 14, 915-920, 2019. https://doi.org/10.1007/s11468-018-0874-4

[105] Kim, S. *et al.* “Active directional switching of surface plasmon polaritons using a phase transition material”, *Scientific Reports*, 7, 43723, 2017. https://doi.org/10.1038/srep43723

[106] Petronijevic, E. *et al.* “Control of Au nanoantenna emission enhancement of magnetic dipolar emitters by means of VO_2 phase change layers”, *Optics Express*, 27(17), 24260-24273, 2019. https://doi.org/10.1364/OE.27.024260

[107] Sun, M. *et al.* “A photonic switch based on a hybrid combination of metallic nanoholes and phase-change vanadium dioxide”, *Scientific Reports*, 8, 11106, 2018. https://doi.org/10.1038/s41598-018-29476-6

[108] Mandal, P. “Multimetal-VO_2 switchable plasmonic metasurface for high contrast optical switching and control at short wavelength infrared regime”, *Plasmonics*, 18, 2323-2334, 2023. https://doi.org/10.1007/s11468-023-01953-3

[109] Hashemi, M., Gandomi, M., and Ansari, N. “Tuning the functionality of VO_2-based thermal switches with TMDC monolayers and thin layer of gold”, *Optical Materials*, 149, 115107, 2024. https://doi.org/10.1016/j.optmat.2024.115107

[110] Kats, M. A. *et al.* “Thermal tuning of mid-infrared plasmonic antenna arrays using a phase change material”, *Optics Letters*, 38(3), 368-370, 2013. https://doi.org/10.1364/OL.38.000368

[111] Wu, S., Lai, K., and Wang, C. “Passive temperature control based on a phase change metasurface”, *Scientific Reports*, 8, 7684, 2018. https://doi.org/10.1038/s41598-018-26150-9

[112] Wang, Q. *et al.* “Tunable infrared optical switch based on vanadium dioxide”, *Nanomaterials*, 11(11), 2988, 2021. https://doi.org/10.3390/nano11112988

[113] Petronijevic, E. *et al.* “Active infrared tuning of metal-insulator-metal resonances by VO_2 thin film”, *Scientific Reports*, 14, 25324, 2024. https://doi.org/10.1038/s41598-024-75430-0

[114] Li, X. *et al.* “Switchable multifunctional terahertz metasurfaces employing vanadium dioxide”, *Scientific Reports*, 9, 5454, 2019. https://doi.org/10.1038/s41598-019-41915-6

[115] Wang, D., Sun, S., Feng, Z., and Tan, W. “Enabling switchable and multifunctional terahertz metasurfaces with phase-change material”, *Optical Materials Express*, 10(9), 2054-2065, 2020. https://doi.org/10.1364/OME.397173

[116] Ren, Y., Zhou, T., Jiang, C., and Tang, B. “Thermally switching between perfect absorber and asymmetric transmission in vanadium dioxide-assisted metamaterials”, *Optics Express*, 29(5), 7666-7679, 2021. https://doi.org/10.1364/OE.418273

[117] Mandal, P., Mohan, S., Sharma, S., and Goyat, M. S. “Broadband multi-resonant circular dichroism in metal-VO_2 hybrid dagger-like plasmonic structure for switching application”, *Photonics and Nanostructures - Fundamentals and Applications*, 37, 100735, 2019. https://doi.org/10.1016/j.photonics.2019.100735

[118] Jia, Z. *et al.* “Dynamically switching the polarization state of light based on the phase transition of vanadium dioxide”, *Physical Review Applied*, 9(3), 034009, 2018. https://doi.org/10.1103/PhysRevApplied.9.034009

[119] Lv, F. *et al.* “Asymmetric transmission polarization conversion of chiral metamaterials with controllable switches based on VO_2”, *Optical Materials*, 114, 110667, 2021. https://doi.org/10.1016/j.optmat.2020.110667

[120] Zhao, Y. *et al.* “Dual-mode terahertz broadband polarization conversion metasurface with integrated graphene-VO_2”, *Optics Communications*, 510, 127895, 2022. https://doi.org/10.1016/j.optcom.2021.127895

[121] Wu, B. *et al.* "Electric-field-driven phase transition in vanadium dioxide", *Physical Review B*, 84(24), 241410(R), 2011. https://doi.org/10.1103/PhysRevB.84.241410
[122] Qi, J. *et al.* "Independent regulation of electrical properties of VO_2 for low threshold voltage electro-optic switch applications", *Sensors and Actuators A: Physical*, 335, 113394, 2022. https://doi.org/10.1016/j.sna.2022.113394
[123] Xu, Z., Qin, G., Bernussi, A. A., and Fan, Z. "Electrothermally control of dynamic infrared switching of VO_2 thin film on FTO glass", *Journal of Alloys and Compounds*, 858, 157640, 2021. https://doi.org/10.1016/j.jallcom.2020.157640
[124] Chauhan, D., Mola, G. T., and Dwivedi, R. P. "An ultra-compact plasmonic modulator/switch using VO_2 and elasto-optic effect", *Optik*, 201, 163531, 2020. https://doi.org/10.1016/j.ijleo.2019.163531
[125] Chauhan, D. *et al.* "High performance vanadium dioxide based active nano plasmonic filter and switch", *Optik*, 225, 165672, 2021. https://doi.org/10.1016/j.ijleo.2020.165672
[126] Chauhan, D. *et al.* "Theoretical analysis of VO_2 filled double rectangular cavity-based coupled resonators for plasmonic active switch/modulator and band pass filter applications", *Optical Materials*, 125, 112078, 2022. https://doi.org/10.1016/j.optmat.2022.112078
[127] Joushaghani, A. *et al.* "Sub-volt broadband hybrid plasmonic-vanadium dioxide switches", *Applied Physics Letters*, 102(6), 061101, 2013. https://doi.org/10.1063/1.4790834
[128] Kim, J. T. "CMOS-compatible hybrid plasmonic modulator based on vanadium dioxide insulator-metal phase transition", *Optics Letters*, 39(13), 3997-4000, 2014. https://doi.org/10.1364/OL.39.003997
[129] Kruger, B. A., Joushaghani, A., and Poon, J. K. S. "Design of electrically driven hybrid vanadium dioxide (VO_2) plasmonic switches", *Optics Express*, 20(21), 23598-23609, 2012. https://doi.org/10.1364/OE.20.023598
[130] Ooi, K. J. A., Bai, P., Chu, H. S., and Ang, L. K. "Ultracompact vanadium dioxide dual-mode plasmonic waveguide electroabsorption modulator", *Nanophotonics*, 2(1), 13-19, 2013. https://doi.org/10.1515/nanoph-2012-0028
[131] Joushaghani, A. *et al.* "Voltage-controlled switching and thermal effects in VO_2 nano-gap junctions", *Applied Physics Letters*, 104(22), 221904, 2014. https://doi.org/10.1063/1.4881155
[132] Han, C., Parrott, E. P. J., Humbert, G., Crunteanu, A., and MacPherson, E. P. "Broadband modulation of terahertz waves through electrically driven hybrid bowtie antenna-VO_2 devices", *Scientific Reports*, 7, 12725, 2017. https://doi.org/10.1038/s41598-017-13085-w
[133] Becker, M. F., Buckman, A. B., and Walser, R. M. "Femtosecond laser excitation of the semiconductor-metal phase transition in VO_2", *Applied Physics Letters*, 65(12), 1507, 1994. https://doi.org/10.1063/1.112974
[134] Cavalleri, A. *et al.* "Band-selective measurements of electron dynamics in VO_2 using femtosecond near-edge X-ray absorption", *Physical Review Letters*, 95(6), 067405, 2005. https://doi.org/10.1103/PhysRevLett.95.067405
[135] Cavalleri, A., Dekorsy, T., Chong, H. H. W., Kieffer, J. C., and Schoenlein, R. W. "Evidence for a structurally-driven insulator-to-metal transition in VO_2: A view from the ultrafast timescale", *Physical Review B*, 70(16), 161102(R), 2004. https://doi.org/10.1103/PhysRevB.70.161102
[136] Wegkamp, D. *et al.* "Instantaneous band gap collapse in photoexcited monoclinic VO_2 due to photocarrier doping", *Physical Review Letters*, 113(21), 216401, 2014. https://doi.org/10.1103/PhysRevLett.113.216401

[137] Wall, S. *et al.* "Ultrafast changes in lattice symmetry probed by coherent phonons", *Nature Communications*, 3, 721, 2012. https://doi.org/10.1038/ncomms1719
[138] O'Callahan, B. T. *et al.* "Inhomogeneity of the ultrafast insulator-to-metal transition dynamics of VO_2", Nature Communications, 6, 6849, 2015. https://doi.org/10.1038/ncomms7849
[139] Cavalleri, A. *et al.* "Femtosecond structural dynamics in VO_2 during an ultrafast solid-solid phase transition", *Physical Review Letters*, 87(23), 237401, 2001. https://doi.org/10.1103/PhysRevLett.87.237401
[140] Cavalleri, A., Rini, M., and Schoenlein, R. W. "Ultra-broadband femtosecond measurements of the photo-induced phase transition in VO_2: from the mid-IR to the hard X-rays", *Journal of the Physical Society of Japan*, 75(1), 011004, 2006. https://doi.org/10.1143/JPSJ.75.011004
[141] Donges, S. A. *et al.* "Ultrafast nanoimaging of the photoinduced phase transition dynamics in VO_2", *Nano Letters*, 16(5), 3029-3035, 2016. https://doi.org/10.1021/acs.nanolett.5b05313
[142] Kumar, N. *et al.* "Photoinduced surface plasmon switching at VO_2/Au interface", *Optics Express*, 26(11), 13773-13782, 2018. https://doi.org/10.1364/OE.26.013773
[143] Ferrara, D. W., MacQuarrie, E. R., Nag, J., Kaye, A. B., and Haglund Jr, R. F. "Plasmon-enhanced low-intensity laser switching of gold::vanadium dioxide nanocomposites", *Applied Physics Letters*, 98(24), 241112, 2011. https://doi.org/10.1063/1.3593388
[144] Muskens, O. L. *et al.* "Antenna-assisted picosecond control of nanoscale phase transition in vanadium dioxide", *Light: Science & Applications*, 5, e16173, 2016. https://doi.org/10.1038/lsa.2016.173
[145] Bergamini, L. *et al.* "Single-nanoantenna driven nanoscale control of the VO_2 insulator to metal transition", *Nanophotonics*, 10(14), 3745-3758, 2021. https://doi.org/10.1515/nanoph-2021-0250
[146] Hallman, K. A., Miller, K. J., Baydin, A., Weiss, S. M., and Haglund Jr, R. F. "Sub-picosecond all-optical switching in a hybrid VO_2:silicon waveguide at 1550 nm", *Advanced Optical Materials*, 9(4), 2001721, 2021. https://doi.org/10.1002/adom.202001721
[147] Guo, P. *et al.* "Conformal coating of a phase change material on ordered plasmonic nanorod arrays for broadband all-optical switching", *ACS Nano*, 11(1), 693-701, 2016. https://doi.org/10.1021/acsnano.6b07042
[148] Choi, S. B. *et al.* "Nanopattern enabled terahertz all-optical switching on vanadium dioxide thin film", *Applied Physics Letters*, 98(7), 071105, 2011. https://doi.org/10.1063/1.3553504
[149] Cueff, S. *et al.* "VO_2 nanophotonics", *APL Photonics*, 5(11), 110901, 2020. https://doi.org/10.1063/5.0028093
[150] Olivares, I. *et al.* "Optical switching in hybrid VO_2/Si waveguides thermally triggered by lateral microheaters", *Optics Express*, 26(10), 12387-12395, 2018. https://doi.org/10.1364/OE.26.012387
[151] Zhou, Y. *et al.* "Voltage-triggered ultrafast phase transition in vanadium dioxide switches", *IEEE Electron Device Letters*, 34(2), 220-222, 2013. https://doi.org/10.1109/LED.2012.2229457

CHAPTER 3

FINITE DIFFERENCE TIME DOMAIN MODELLING

3.0 Chapter Overview

This chapter presents the fundamental principles and numerical implementation of the Finite Difference Time Domain (FDTD) technique for simulating electromagnetic interactions. It begins with a theoretical introduction to computational electrodynamics, explaining the need for numerical methods like FDTD. The chapter further elaborates on the FDTD solution of the wave equation, the implementation of Yee's algorithm, and the necessary stability conditions for Yee's algorithm. The chapter also introduces preliminary simulation designs of nanostructures using FDTD software tools to validate theoretical models.

3.1 Finite Difference Time Domain (FDTD)

Computational electrodynamics refers to the modelling of complex interactions between electromagnetic fields and matter of arbitrary shape or size using established numerical techniques for the cases where analytical solutions to Maxwell's equations are often unattainable. Among various numerical methods available, such as the Method of Moments [1], Discrete Dipole Approximation [2], and the Fast Multipole Method [3], the Finite Difference Time Domain (FDTD) approach stands out as one of the most efficient and widely used time-domain methods for computational electrodynamic modelling [4-7].

FDTD discretizes the continuous partial differential equations in both space and time domains. Maxwell's equations are approximated using central difference schemes, enabling fast and efficient numerical computation. The method calculates the steady state electric (E) and magnetic (H) fields throughout the simulation domain using a leapfrog time-stepping approach, which is elaborated upon in the subsequent sections.

3.2 FDTD Solution of the Wave Equation

To illustrate the central difference approximation (CDA) concept [4], the one-dimensional scalar wave equation is considered. The wave equation is:

$$\frac{\partial^2 u}{\partial t^2} = c^2 \frac{\partial^2 u}{\partial x^2} \tag{3.1}$$

where, u (x, t) is the wave function dependent on space and time, and 'c' denotes the wave velocity in the medium.

It is well established that if propagating wave solutions of the form

$$u(x,t) = F(x+ct) + G(x-ct) \tag{3.2}$$

are assumed for u (x, t), they satisfy the wave equation.

To obtain a second-order accurate CDA of the wave equation, a Taylor series expansion of u (x, t_n) is performed about the point x_i, considering the spatial points ($x_i + \Delta x$) and ($x_i - \Delta x$) while keeping t_n fixed at a specific observation time. This yields Eq. 3.3 and Eq. 3.4 are obtained:

$$\begin{aligned} u(x_i+\Delta x)|_{t_n} = u|_{xi,\ t_n} + \Delta x.\frac{\partial u}{\partial x}|_{x_i,\ t_n} + \frac{\Delta x^2}{2}\frac{\partial^2 u}{\partial x^2}|_{x_i,\ t_n} \\ + \frac{\Delta x^3}{6}\frac{\partial^3 u}{\partial x^3}|_{x_i,\ t_n} + \frac{\Delta x^4}{24}\frac{\partial^4 u}{\partial x^4}|_{\xi_1,\ t_n} \end{aligned} \tag{3.3}$$

and

$$\begin{aligned} u(x_i-\Delta x)|_{t_n} = u|_{xi,\ t_n} - \Delta x.\frac{\partial u}{\partial x}|_{x_i,\ t_n} + \frac{\Delta x^2}{2}\frac{\partial^2 u}{\partial x^2}|_{x_i,\ t_n} \\ - \frac{\Delta x^3}{6}\frac{\partial^3 u}{\partial x^3}|_{x_i,\ t_n} + \frac{\Delta x^4}{24}\frac{\partial^4 u}{\partial x^4}|_{\xi_2,\ t_n} \end{aligned} \tag{3.4}$$

The last terms in both the Eq. 3.3 and Eq. 3.4 shown above, represent the respective remainder terms over the intervals (x_i, ($x_i + \Delta x$)) and (x_i, ($x_i - \Delta x$)). By adding Eq. 3.3 and Eq. 3.4, Eq. 3.5 is obtained as:

$$\begin{aligned} u(x_i+\Delta x)|_{t_n} + u(x_i-\Delta x)|_{t_n} \\ = 2u|_{xi,\ t_n} + \Delta x^2\frac{\partial^2 u}{\partial x^2}|_{x_i,\ t_n} + \frac{\Delta x^4}{12}\frac{\partial^4 u}{\partial x^4}|_{\xi_3,\ t_n} \end{aligned} \tag{3.5}$$

where, 'ξ_3' denotes a spatial point within the interval (($x_i - \Delta x$), ($x_i + \Delta x$)).

By minor rearrangement, Eq. 3.5 can be expressed in the form of Eq. 3.6:

$$\begin{aligned} \frac{\partial^2 u}{\partial x^2}|_{x_i,\ t_n} = \left[\frac{u(x_i+\Delta x)|_{t_n} + u(x_i-\Delta x)|_{t_n} - 2u|_{xi,\ t_n}}{\Delta x^2}\right] \\ + O[\Delta x^2] \end{aligned} \tag{3.6}$$

By representing the spatial point with the index *i* and the temporal point with the index *n*, Eq. 3.6 can be reformulated as:

$$\frac{\partial^2 u}{\partial x^2}|_{x_i,\ t_n} = \left[\frac{u_{i+1}^n - 2u_i^n + u_{i-1}^n}{\Delta x^2}\right] + O[\Delta x^2] \tag{3.7}$$

The resulting equation (Eq. 3.7) provides a second-order accurate CDA for the second-order spatial partial derivative of u, where 'O' denotes the remainder term. A corresponding expression for the second partial derivative of u with respect to time can be similarly derived, as presented below:

$$\frac{\partial^2 u}{\partial t^2}\Big|_{x_i,\ t_n} = \left[\frac{u_i^{n+1} - 2u_i^n + u_i^{n-1}}{\Delta t^2}\right] + O[\Delta t^2] \tag{3.8}$$

Substituting the above approximations into the wave equation yields the following form of the wave equation:

$$\left[\frac{u_i^{n+1} - 2u_i^n + u_i^{n-1}}{\Delta t^2}\right] + O[\Delta t^2] = c^2\left(\left[\frac{u_{i+1}^n - 2u_i^n + u_{i-1}^n}{\Delta x^2}\right] + O[\Delta x^2]\right) \tag{3.9}$$

Therefore,

$$u_i^{n+1} = (c\Delta t)^2\left[\frac{u_{i+1}^n - 2u_i^n + u_{i-1}^n}{\Delta x^2}\right] + 2u_i^n - u_i^{n-1} + O[\Delta t^2] + O[\Delta x^2] \tag{3.10}$$

The above equation (Eq. 3.10) represents the final solution for the function u (x, t), evaluated in both space and time. As evident from Eq. 3.10, the function on the left-hand side, corresponding to time step (n+1), can be computed using the functions on the right-hand side, which depend on time steps n and (n-1). Once the value at (n+1) is determined, the computation proceeds to the next time step (n+2), and this iterative process allows the solution to be extended to all desired time points. Similarly, values at all spatial locations can also be computed.

The second-order accurate CDA scheme described above yields approximate solutions to the differential form of the wave equation. However, when $c\Delta t/\Delta x$ =1, known as the 'magic time step', is satisfied, the solution becomes exact, as the associated error or remainder terms vanish at this specific time step.

3.3 Yee's Algorithm

Yee proposed an algorithm [8] that serves as the foundation — either in its original or modified form — for solving numerical problems based on Maxwell's equations in all commercially available FDTD solvers. By discretizing both space and time into a grid, he achieved near-accurate solutions to Maxwell's equations through the simultaneous computation of the electric (E) and magnetic (H) fields. This was accomplished using a leapfrog scheme, which will be discussed in detail in this section.

The differential form of Maxwell's equations for a region free of electric and magnetic sources is presented in Eqs. 3.11-3.14:

$$\frac{\partial B}{\partial t} = -\nabla \times E - J_m \tag{3.11}$$

$$\frac{\partial D}{\partial t} = \nabla \times H - J_e \tag{3.12}$$

$$\nabla . D = 0 \tag{3.13}$$

$$\nabla . B = 0 \tag{3.14}$$

where, 'B' denotes the magnetic flux density, 'D' represents the electric flux density, 'E' denotes the electric field, and 'H' denotes the magnetic field. Additionally, 'J_e' denotes the electric conduction current density, while 'J_m' denotes the magnetic conduction current density.

In addition,

$$B = \mu H \tag{3.15}$$

$$D = \varepsilon E \tag{3.16}$$

where 'μ' being the magnetic permeability and 'ε' being the dielectric permittivity are material-specific constants.

Furthermore,

$$J_e = \sigma E \tag{3.17}$$

$$J_m = \rho' H \tag{3.18}$$

where, 'σ' represents the electrical conductivity and 'ρ' denotes the magnetic resistivity.

Based on the above expressions, the following equations are derived:

$$\frac{\partial H}{\partial t} = -\frac{1}{\mu}\nabla \times E - \frac{\rho'}{\mu}H \tag{3.19}$$

$$\frac{\partial E}{\partial t} = \frac{1}{\varepsilon}\nabla \times E - \frac{\sigma}{\varepsilon}H \tag{3.20}$$

These Maxwell's equations can be expressed as a set of coupled scalar equations, as given below:

$$\frac{\partial H_x}{\partial t} = -\frac{1}{\mu}\left(\frac{\partial E_z}{\partial y} - \frac{\partial E_y}{\partial z} - \rho' H_x\right) \tag{3.21}$$

$$\frac{\partial H_y}{\partial t} = -\frac{1}{\mu}\left(\frac{\partial E_x}{\partial z} - \frac{\partial E_z}{\partial x} - \rho' H_y\right) \tag{3.22}$$

$$\frac{\partial H_z}{\partial t} = -\frac{1}{\mu}\left(\frac{\partial E_y}{\partial x} - \frac{\partial E_x}{\partial y} - \rho' H_z\right) \tag{3.23}$$

$$\frac{\partial E_x}{\partial t} = \frac{1}{\varepsilon}\left(\frac{\partial H_z}{\partial y} - \frac{\partial H_y}{\partial z} - \sigma E_x\right) \tag{3.24}$$

$$\frac{\partial E_y}{\partial t} = \frac{1}{\varepsilon}\left(\frac{\partial H_x}{\partial z} - \frac{\partial H_z}{\partial x} - \sigma E_y\right) \tag{3.25}$$

$$\frac{\partial E_z}{\partial t} = \frac{1}{\varepsilon}\left(\frac{\partial H_y}{\partial x} - \frac{\partial H_x}{\partial y} - \sigma E_z\right) \tag{3.26}$$

Yee proposed an algorithm [8] to find solution for the six coupled partial differential equations representing Maxwell's equations. He recommended computing both the electric (E) and magnetic (H) fields simultaneously, rather than solving for either field independently. This approach yields a solution that is closer to the exact one and proves more effective in scenarios involving interactions between coupled electric and magnetic fields. In the three-dimensional implementation of Yee's algorithm, the computational domain is structured such that each E-field vector is surrounded by 4 H-field vectors, and each H-field vector is likewise enclosed by 4 E-field vectors, as illustrated in Fig. 3.1(a). This configuration is analogous to representing the computational domain using continuous contours of Faraday's law and Ampere's law. The dimensions of the unit cell in the three spatial directions are given by Δx, Δy, and Δz.

Additionally, the E and H fields are staggered in time using a leapfrog scheme [4], as depicted in Fig. 3.1(b). At any given time step, the algorithm computes the E-field throughout the entire domain and stores these values in memory. The H-field is then calculated at a slightly later time using the stored E-field values. Once computed, the H-field values are saved, and the E-field at the next time step is evaluated using these updated H-field values, thereby initiating the next iteration. It is important to note that consecutive components of the E-field are spaced by Δx, while adjacent components of E and H are offset by Δx/2.

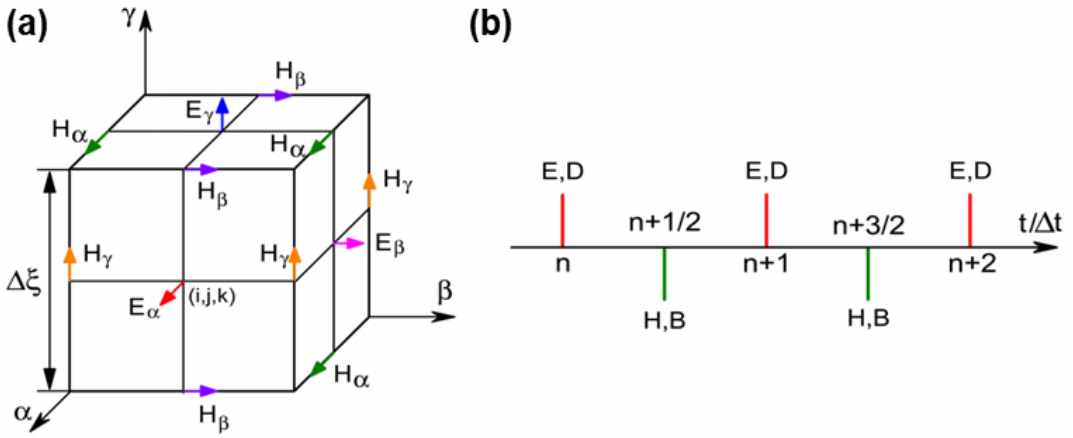

Fig. 3.1 (a) Spatial arrangement of the E and H field components within a standard unit cell of the Yee mesh and **(b)** leapfrog time-stepping scheme used for field calculations [9].

Following this structure, Yee demonstrated that the three-dimensional Maxwell's equations can be solved by approximating the partial derivatives of the E and H fields with respect to both space and time using second-order accurate CDA schemes. These approximations are discussed subsequently.

For Eq. 3.21, the second-order accurate CDA is formulated as follows:

$$\frac{H_x|_{i,j,k}^{n+1/2} - H_x|_{i,j,k}^{n-1/2}}{\Delta t} = \frac{1}{\mu_{i,j,k}}\left[\frac{E_y|_{i,j,k+1/2}^{n} - E_y|_{i,j,k-1/2}^{n}}{\Delta z} - \frac{E_z|_{i,j+\frac{1}{2},k}^{n} - E_z|_{i,j-\frac{1}{2},k}^{n}}{\Delta y} - \rho'_{i,j,k}.H_x|_{i,j,k}^{n}\right] \quad (3.27)$$

This approximation assumes that the spacing between two adjacent E-field components is Δx. Accordingly, the CDA is derived by applying a Taylor series expansion at the points x – Δx/2 and x + Δx/2. A similar approach is employed along the Y and Z directions, as well as in the temporal domain.

In Eq. 3.27, the term H_x on the right-hand side can also be expressed using a semi-implicit approximation, as shown in Eq. 3.28. This implies that the value of H_x can be obtained by averaging its stored value at time step n-1/2 with the computed value at n+1/2.

$$H_x|_{i,j,k}^{n} = \frac{H_x|_{i,j,k}^{n+1/2} + H_x|_{i,j,k}^{n-1/2}}{1/2} \quad (3.28)$$

Consequently, the final form of the equation is obtained as:

$$\frac{H_x|_{i,j,k}^{n+1/2} - H_x|_{i,j,k}^{n-1/2}}{\Delta t} = \frac{1}{\mu_{i,j,k}}\left[\frac{E_y|_{i,j,k+1/2}^{n} - E_y|_{i,j,k-1/2}^{n}}{\Delta z} - \frac{E_z|_{i,j+\frac{1}{2},k}^{n} - E_z|_{i,j-\frac{1}{2},k}^{n}}{\Delta y} - \rho'_{i,j,k}.\frac{H_x|_{i,j,k}^{n+1/2} + H_x|_{i,j,k}^{n-1/2}}{1/2}\right] \quad (3.29)$$

Rearranging the terms to isolate $H_x|_{i,j,k}^{n+1/2}$ yields the following expression:

$$H_x|_{i,j,k}^{n+1/2} = \frac{1-\frac{\rho'_{i,j,k}\Delta t}{2\mu_{i,j,k}}}{1+\frac{\rho'_{i,j,k}\Delta t}{2\mu_{i,j,k}}} H_x|_{i,j,k}^{n-1/2} + \left(\frac{\frac{\Delta t}{\mu_{i,j,k}}}{1+\frac{\rho'_{i,j,k}\Delta t}{2\mu_{i,j,k}}}\right).\left(\frac{E_y|_{i,j,k+1/2}^{n} - E_y|_{i,j,k-1/2}^{n}}{\Delta z} - \frac{E_z|_{i,j+\frac{1}{2},k}^{n} - E_z|_{i,j-\frac{1}{2},k}^{n}}{\Delta y}\right) \quad (3.30)$$

Following a similar approach, the values of all six electromagnetic field components can be determined using Yee's algorithm.

3.4 Stability of the Yee's Algorithm

A fundamental requirement for ensuring the numerical stability of Yee's algorithm is compliance with the Courant stability criterion [4, 5], which states that if the spatial discretization steps along the three directions are Δx, Δy, and Δz, and the temporal step is Δt, then the spatial and temporal grid sizes must satisfy the below condition to maintain the stability of the Yee's algorithm:

$$c\Delta t \leq \frac{1}{\sqrt{\left(\frac{1}{\Delta x^2}+\frac{1}{\Delta y^2}+\frac{1}{\Delta z^2}\right)}} \quad (3.31)$$

In addition to this, the stability of Yee's algorithm is also influenced by other factors, such as boundary conditions, material properties, and the type of meshing used in the simulation [10].

3.5 Preliminary designs of nanostructures using FDTD modelling

A commercial software – Ansys Lumerical FDTD Solver [11] – has been employed for the simulation of all nanophotonic device structures presented in this thesis. As a part of preliminary explorations and to gain proficiency with the FDTD simulation environment, fundamental designs of plasmonic nanostructures, particularly bowtie geometries, were modelled and analyzed. Plasmonic bowties are well-established nanostructures known for their ability to concentrate electromagnetic energy in the nanoscale gap between two triangular metallic arms [12-16]. This intense electric-field confinement arises due to localized surface plasmon resonance (LSPR) [17], making bowties promising candidates for applications in sensing, spectroscopy, and enhanced light-matter interaction. To further explore their tunability, asymmetric bowtie geometries were initially designed and analyzed [18-20].

In the first study, asymmetric plasmonic bowtie nanostructures on silicon dioxide (SiO_2) substrate as shown in Fig. 3.2(a) were designed to study the tunability of the LSPR wavelength over the visible and near infrared wavelength range by manipulating the degree of asymmetry in its geometric parameters. The plasmonic properties of the proposed asymmetric plasmonic bowtie nanostructures are a strong function of its geometric parameters such as the length of the nano-bowtie, the thickness of the nano-bowtie, the flared angle of the nano-bowtie, and the gap between the two triangles of the nano-bowtie (See Fig. 3.2(b, c)), resulting in tunable LSPR characteristics. The plasmonic properties further depend on the material used for the nano-bowtie and the substrate, the angle of incident light, as well as the orientation of the nano-bowtie relative to the incident light.

Expanding upon this, more complex structures — asymmetric plasmonic cross-bowties — were proposed and modelled using FDTD simulations. The proposed asymmetric plasmonic cross-bowties consist of a combination of a gold equilateral triangular bowtie and a gold isosceles triangular bowtie in a crossed manner, deposited on a SiO_2 substrate, as shown in Fig. 3.3(a). FDTD modelling examined the effect of asymmetricity in the flare angle of the crossed bowties, the length of the bowties, and the gap between the vertices of the bowties on the nature of reflectance spectra and electric-field enhancement spectra to exhibit tunable plasmon resonance (See Fig. 3.3(b-d)).

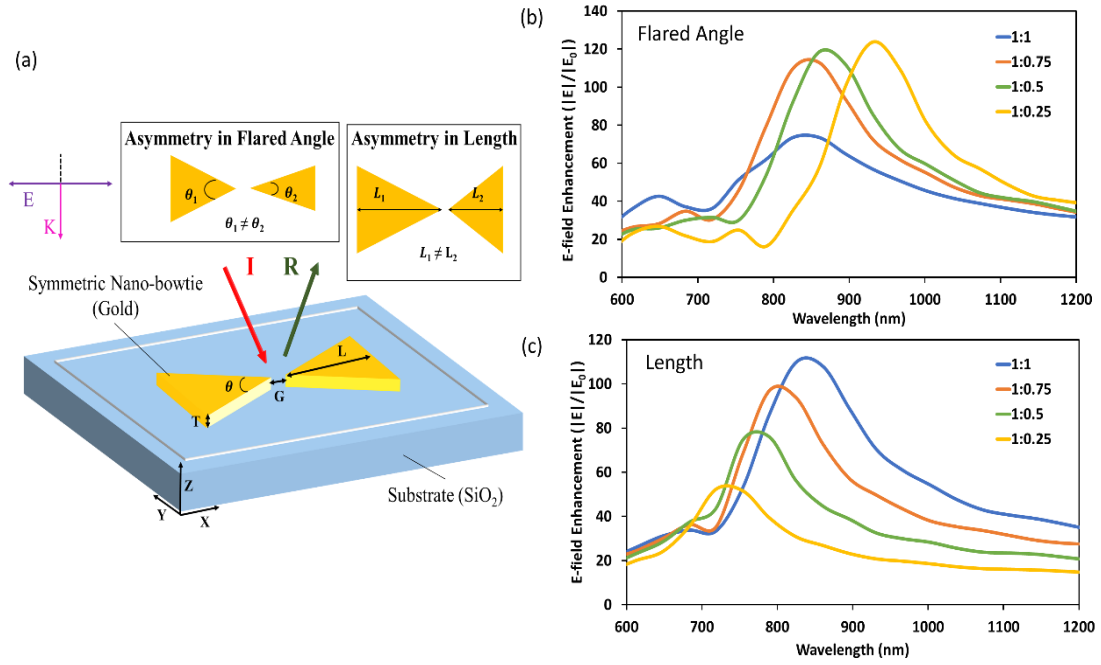

Fig. 3.2 (a) Schematic of asymmetric plasmonic bowtie nanostructure on glass substrate. Effect on the electromagnetic enhancement for asymmetricity with different ratios of **(b)** the flare angle 'θ' and **(c)** the length 'L'.

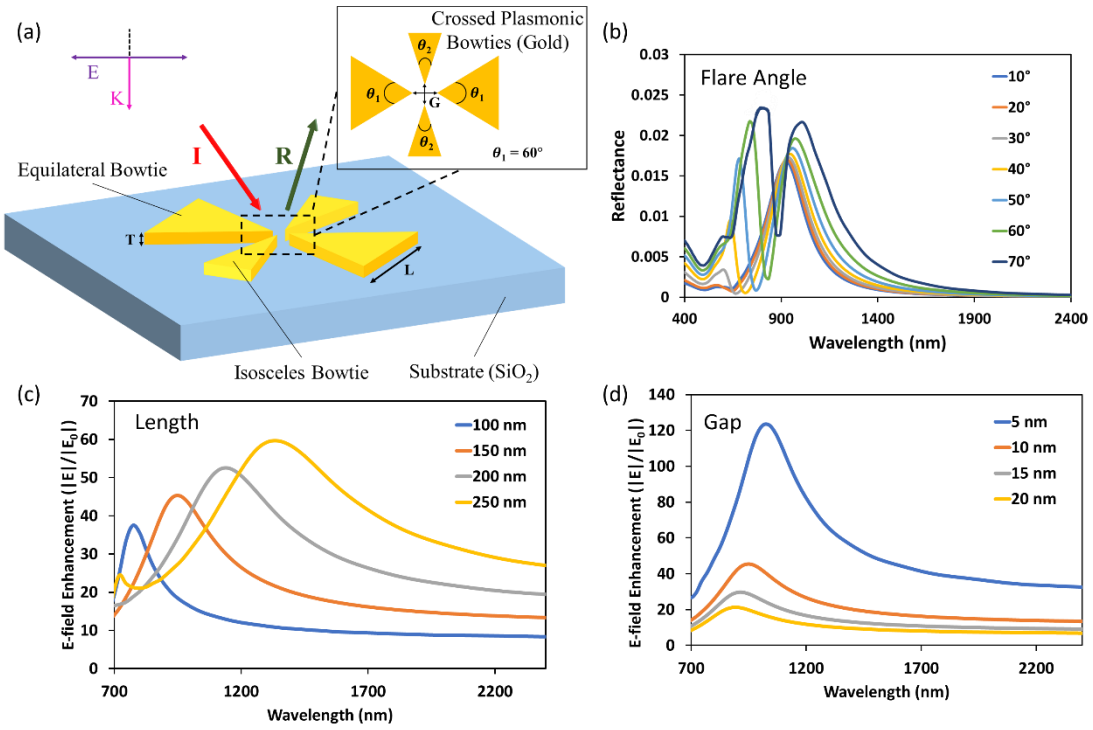

Fig. 3.3 (a) Schematic of the asymmetric plasmonic cross-bowties of gold on silicon dioxide substrate. **(b)** Effect on the reflectance spectra when the flare angle 'θ_2' of the isosceles bowtie of the asymmetric crossed plasmonic bowties is varied. Effect on the electromagnetic enhancement when **(c)** the length '*L*' of the asymmetric crossed plasmonic bowties and **(d)** the gap '*G*' between the asymmetric crossed plasmonic bowties is varied.

Thus, the FDTD modelling confirmed that geometric asymmetry is a powerful tool for tuning plasmonic behavior in nanostructures. These preliminary designs not only provided foundational insights into the impact of structural parameters on plasmonic performance but also established simulation strategies and benchmarking protocols for more complex plasmonic switch structures presented in later chapters of this thesis.

3.6 References

[1] Harrington, R. F. *Field Computation by Moment Methods*. Wiley-IEEE Press, 1993. ISBN: 9780780310148.

[2] Draine, B. T., and Flatau, P. J. "Discrete-dipole approximation for scattering calculations", *Journal of Optical Society of America A*, 11(4), 1491-1499, 1994. https://doi.org/10.1364/JOSAA.11.001491

[3] Engheta, N., Murphy, W. D., Rokhlin, V., and Vassiliou, M. S. "The fast multipole method (FMM) for electromagnetic scattering problems", *IEEE Transactions on Antennas and Propagation,* 40(6), 634-641, 1992. https://doi.org/10.1109/8.144597

[4] Taflove, A., and Hagness, S. C. *Computational electrodynamics: The finite-difference time-domain method*. Artech House, 2005.

[5] Kunz, K. S., and Luebbers, R. J. *The Finite Difference Time Domain Method for Electromagnetics*. CRC Press, 1993. https://doi.org/10.1201/9780203736708

[6] Taflove, A. “Review of the formulation and applications of the finite-difference time-domain method for numerical modeling of electromagnetic wave interactions with arbitrary structures”, *Wave Motion*, 10(6), 547-582, 1988. https://doi.org/10.1016/0165-2125(88)90012-1

[7] Trivedi, R., Sharma, Y., and Dhawan, A. “Plane wave scattering from a plasmonic nanowire-film system with the inclusion of non-local effects”, *Optics Express*, 23(20), 26064-26079, 2015. https://doi.org/10.1364/OE.23.026064

[8] Yee, K. S. “Numerical solution of initial boundary value problems involving Maxwell’s equations in isotropic media”, *IEEE Transactions on Antennas and Propagation*, 14(3), 302-307, 1966. https://doi.org/10.1109/TAP.1966.1138693

[9] Dissanayake, C. M., Premaratne, M., Rukhlenko, I. D., and Agrawal, G. P. “FDTD modeling of anisotropic nonlinear optical phenomena in silicon waveguides”, *Optics Express*, 18(20), 21427-21448, 2010. https://doi.org/10.1364/OE.18.021427

[10] Gedney, S. D. *Introduction to the Finite-Difference Time-Domain (FDTD) Method for Electromagnetics*. Springer Cham, 2011. https://doi.org/10.1007/978-3-031-01712-4

[11] FDTD: 3D Electromagnetic Simulator, Lumerical Inc. [Online]. Available: https://www.ansys.com/en-in/products/optics/fdtd

[12] Butt, M. A., Kazanskiy, N. L., and Khonina, S. N. “Highly sensitive refractive index sensor based on plasmonic bow tie configuration”, *Photonic Sensors*, 10, 223-232, 2020. https://doi.org/10.1007/s13320-020-0588-z

[13] Wang, B., Singh, S. C., Lu, H., and Guo, C. “Design of aluminum bowtie nanoantenna array with geometrical control to tune LSPR from UV to Near-IR for optical sensing”, *Plasmonics*, 15, 609-621, 2020. https://doi.org/10.1007/s11468-019-01071-z

[14] Das, A., Kumar, K., and Dhawan, A. “Periodic arrays of plasmonic crossed-bowtie nanostructures interspaced with plasmonic nanocrosses for highly sensitive LSPR based chemical and biological sensing”, *RSC Advances*, 11(14), 8096-8106, 2021. https://doi.org/10.1039/D0RA09012C

[15] Lin, Y. C., and Lee, P. T. “Efficient optical trapping and detection of nanoparticle via plasmonic bowtie notch”, *IEEE Photonics Journal*, 11(2), 4800610, 2019. https://doi.org/10.1109/JPHOT.2019.2907273

[16] Yao, X. *et al.* “Uniform periodic bowtie SERS substrate with narrow nanogaps obtained by monitored pulsed electrodeposition”, *ACS Applied Materials & Interfaces*, 12(32), 36505-36512, 2020. https://doi.org/10.1021/acsami.0c09357

[17] Chen, C. D., Cheng, S. F., Chau, L. K., and Wang, C. R. S. “Sensing capability of the localized surface plasmon resonance of gold nanorods”, *Biosensors and Bioelectronics*, 22(6), 926-932, 2007. https://doi.org/10.1016/j.bios.2006.03.021

[18] Pena, V. P., Alves, R. A., and Cia, M. N. “From symmetric to asymmetric bowtie nanoantennas: electrostatic conformal mapping perspective”, *Nanophotonics*, 9(5), 1177-1187, 2020. https://doi.org/10.1515/nanoph-2019-0488

[19] Wei, W., Yan, X., Shen, B., and Zhang, X. “Plasmon-induced tansparency in an asymmetric bowtie structure”, *Nanoscale Research Letters*, 14, 246, 2019. https://doi.org/10.1186/s11671-019-3081-0

[20] Yang, Y. L. *et al.* “Steering the optical response with asymmetric bowtie 2-color controllers in the visible and near infrared range”, *Optics Communications*, 284(13), 3474-3478, 2011. https://doi.org/10.1016/j.optcom.2011.03.043

CHAPTER 4

BROADBAND PLASMONIC SWITCHES BASED ON NANODISC-DIMERS WITH PROGRESSIVELY INCREASING DIAMETERS ON A PLASMONIC FILM WITH A VO_2 SPACER

4.0 Chapter Overview

In this chapter, the design and analysis of active broadband plasmonic switches are presented, based on a periodic array of metallic nanodisc-dimers with gradually increasing diameters. These dimers are arranged on a gold-coated silicon dioxide (SiO_2) substrate, with a vanadium dioxide (VO_2) thin film acting as a spacer layer between the nanodiscs and the underlying plasmonic substrate. The periodic arrangement of unit cells comprising plasmonic nanodisc-dimers of varying diameters facilitates the coupling of multiple incident wavelengths into the plasmonic modes of the structure, thereby producing a broadband plasmonic response. The VO_2 spacer layer plays a crucial role in enabling broadband switching by modulating the optical response of the structure. Upon application of external stimuli such as voltage, infrared radiation, or thermal energy, VO_2 undergoes a phase transition from a semiconducting to a metallic state. This transition induces substantial modifications in the material's optical characteristics, leading to corresponding variations in the reflectance spectrum of the nanostructure. As a result, effective switching behavior is achieved across a broad wavelength range encompassing the C, L, and U bands used in optical communication. The proposed design demonstrates a broadband extinction ratio of 5 dB over an operational bandwidth of 650 nm, ranging from 1460 nm to 2110 nm, and an extinction ratio of 4 dB over a 702 nm bandwidth extending from 1432 nm to 2134 nm. Furthermore, the study highlights the inherent trade-off between extinction ratio and bandwidth in the operation of these switches. A comprehensive investigation using Finite Difference Time Domain (FDTD) simulations confirms that the spectral response of these switches can be tailored by adjusting their geometrical parameters, offering the versatility to target different wavelength regions. Owing to these characteristics, the proposed plasmonic switches exhibit strong potential for applications in optical communication systems and as functional elements in integrated plasmonic circuits.

4.1 Motivation

Over the last few decades, there have been numerous efforts to increase the extinction ratio of VO_2 based plasmonic switches [1], however, the operating wavelength range of these switches remains quite narrow. Hence, there are limited reports of broadband plasmonic switching by employing VO_2 as the phase change material [2-7]. Joushanghani *et al.* [2] proposed a hybrid SPP-VO_2 waveguide switch which could provide a maximum extinction ratio of 16.4 dB but the operating wavelength range was only ~100 nm. Mandal *et al.* [3] designed a metal-VO_2 hybrid dagger like geometry to exhibit switching based on circular dichroism where the

broadband operating wavelength was limited to ~200 nm. In addition, Sun *et al.* [4] reported a broadband operating wavelength of ~650 nm for a photonic switch based on the hybrid combination of hexagonal array of aluminium nanoholes and VO_2 with 5 dB as the broadband extinction ratio. Guo *et al.* [5] designed VO_2-coated plasmonic indium tin oxide nanorod arrays for switching in the visible and the infrared region. Hence, for most of the VO_2 based broadband plasmonic switches designed in the literature, the maximum extinction ratio is limited to 5 dB and the operating range of wavelengths over which switching is demonstrated is lower than 500 nm and they do not offer the flexibility of tuning the spectral range of operation. It must be noted that broadband switching, with the flexibility of controlling the operating wavelength range, offers enormous advantage for the design of optical communication networks [8] and optical computing systems [9].

4.2 Introduction

In this chapter, broadband plasmonic switches based on a periodic array of metallic nanodisc-dimers with progressively increasing diameters are proposed. The nanodisc-dimers are placed on a gold coated silicon dioxide (SiO_2) substrate with a vanadium dioxide (VO_2) thin film as a spacer between the discs and the underlying gold-coated substrate (see Fig. 4.1). It is well known that — for a periodic array of circular metallic discs on a substrate, the incident optical radiation is coupled into the plasmonic modes of the nanostructure at specific plasmon resonance wavelengths, thus resulting in narrow and strong dips in the reflection spectrum of the nanostructure [10, 11]. Further, there is a red-shift in the plasmon resonance wavelength due to the retardation of the depolarization field when the diameter of the nanodiscs is increased [12]. It can therefore be inferred that by employing an array of dimers of metallic nanodiscs with progressively increasing diameters as shown in Fig. 4.1, multiple wavelengths can be coupled into the plasmonic modes of the nanostructure such that each nanodisc-dimer with a specific value of diameter results in the coupling of incident radiation into the plasmonic modes of the nanostructure at a specific plasmon resonance wavelength. This coupling of incident radiation to plasmonic modes at multiple wavelengths results in an overall broadband resonance dip in the reflection spectrum of the nanostructure. Therefore, periodic arrays of metallic gold nanodisc-dimers of two, three, four and five sets are employed with progressively increasing diameters – that are capable of exhibiting a broadband plasmonic behavior – in combination with a phase change material, i.e., VO_2 to achieve broadband switching. Finite difference time domain (FDTD) modelling is employed to demonstrate that the operating wavelength range of these switches widens with the inclusion of more sets of nanodisc-dimers of different diameters in a unit cell of the periodic array. It is also demonstrated that with the proper optimization of the values of the diameters of the nanodisc-dimers, which are periodically arranged on the VO_2-coated gold film, these broadband switches can be appropriately designed to span the C, L and U bands of optical communication.

The performance of these switches is measured in terms of extinction ratio (ER) which is the ratio of the reflectance from the switch with VO_2 in its metallic phase and the reflectance from the switch with VO_2 in its semiconducting phase expressed in dB. When a periodic array of five sets of nanodisc-dimers with progressively

increasing diameters is placed on the VO_2-thin film on top of the gold coated SiO_2 substrate, the demonstrates a broadband extinction ratio of 5 dB over an operational bandwidth of 650 nm, covering the wavelength range from 1460 nm to 2110 nm, with a peak extinction ratio exceeding 20 dB. In addition, a trade-off between the extinction ratio and the operating wavelength range of these switches is also shown. It is demonstrated that the proposed switch can even provide an extinction ratio > 8 dB over a broadband operating wavelength range > 530 nm. As VO_2 exhibits an ultrafast switching [13], the proposed switches hold potential for application in high-speed optical communication networks or as switching elements in plasmonic circuits. Moreover, the wavelength range over which switching occurs can be tuned by modifying the diameters of the nanodisc-dimers, thereby enabling their adaptability for operation across different wavelength regimes. Moreover, these switches can be employed with both angled and normally incident light, and specific arrangements such as prism coupling are not needed to couple incident light into plasmonic modes of the metallic nanostructures.

These switches can be fabricated by employing a thin film deposition technique like atomic layer deposition (ALD) [14] or E-beam evaporation [15] to deposit a layer of gold on a SiO_2 substrate. Thereafter, a thin layer of VO_2 can be deposited by using a thin film deposition technique like pulsed laser deposition (PLD) [16]. Subsequently, the gold nanodisc-dimers can be fabricated on top of the VO_2 layer by employing E-beam lithography [17] or helium ion milling [18] to fabricate the proposed switches.

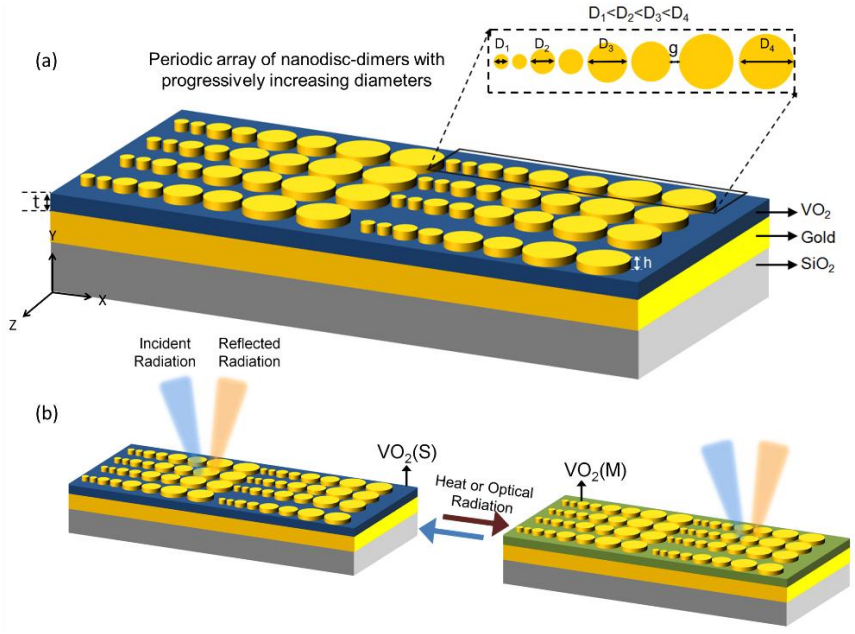

Fig. 4.1 (a) Schematic for the proposed broadband plasmonic switch based on a periodic array of nanodisc-dimers with progressively increasing disc sizes on a plasmonic film with a VO_2 spacer. The diameters of the dimers of nanodiscs are taken such that $D_1 < D_2 < D_3 < D_4$, where D_1, D_2, D_3 and D_4 are the diameters of the first, second, third and fourth set of nanodisc-dimer, respectively. The periodic array of dimers of gold nanodiscs are placed on a gold coated SiO_2 substrate with a thin film of VO_2 as a spacer. **(b)** Schematic showing the switching action of the proposed switch.

4.3 Numerical Methods

A commercial finite difference time domain (FDTD) solver by Lumerical Inc. was used to carry out the 3D FDTD modelling of the proposed switches. A plane wave source with a 1 V/m incident electric field polarized in the X-direction (See Fig. 4.1) was used to illuminate the structure. After careful convergence testing, a uniform mesh size of 1 nm was employed in the X-, Y- and Z-directions of the whole simulation region. The structure was taken to be periodic in the X- and Z-directions, and perfectly matched layer (PML) boundaries were used in the Y-direction. The calculation and subsequent fitting of the dielectric constants for metallic VO_2 and semiconductor VO_2 employed in this work was based on the Lorentz–Drude Model (See Appendix-II, Dielectric Constants of Materials). The diameter of the nanodiscs (D), the thickness of VO_2 layer (t), and the gap between the nanodiscs (g) were varied to analyze the effect of these geometrical parameters on the extinction ratio spectra of the proposed broadband plasmonic switch.

4.4 Results and Discussion

Finite difference time domain (FDTD) modelling is employed to illustrate the broadband switching behavior of the proposed switches based on a periodic array of metallic dimers of nanodiscs with progressively increasing diameters on a gold coated SiO_2 substrate with a VO_2 thin film as a spacer between the discs and the underlying substrate. In this section, the performance of these the switches with two, three, four and five sets of nanodisc-dimers of different diameters periodically arranged on the underlying VO_2 thin film is comprehensively analyzed and compared with an equivalent periodic array of uniform-sized nanodiscs arranged on a VO_2 coated SiO_2 substrate. The height of the nanodisc-dimers is considered to be h, the thickness of VO_2 layer is t, the gap between the nanodiscs is g, and the diameters of the nanodisc-dimers are kept to be variable as shown in Fig. 4.1(a).

To elaborate the utility of the proposed switches for broadband switching, an analysis of the switching behavior of a periodic array of metallic nanodiscs with uniform diameters (UNDs) placed on a VO_2 coated SiO_2 substrate is carried out first. Figs. 4.2(a, b) show the reflectance spectra for such a periodic array of uniform metallic nanodiscs with VO_2 in its semiconductor and metallic state, respectively.

Fig. 4.2(a) shows the reflectance spectra from the periodic array of uniform metallic nanodiscs (UNDs) for different values of diameters placed on a gold coated SiO_2 substrate with the VO_2 spacer in its semiconductor state. It must be noted that for this case of uniform nanodiscs, for each value of the nanodisc diameter, the incident optical radiation is coupled into a plasmonic waveguide mode (M1) around 720 nm and a geometry-dependent plasmonic mode (M2) of the nanostructure at a specific plasmon resonance wavelength resulting in a strong dip in the reflection spectra of the nanostructure. As the underlying layer of VO_2 is switched from its semiconducting state to its metallic state (See Fig. 4.2(b)), the real part of the refractive index of VO_2 decreases leading to a blue shift of the plasmonic dip in the reflectance spectra. Moreover, the dip in the reflectance spectra corresponding to the mode M2 also exhibits a broadening for the case when VO_2 is in its metallic state due to the damping

of the plasmon resonance by the oscillations of mobile electrons in metallic VO_2 [5]. The overall broadening can also be attributed to the overlapping between the plasmonic mode and the plasmonic waveguide mode (at 720 nm). This change in the reflectance spectra as the underlying VO_2 is switched from its semiconducting state to its metallic state, can be utilized for switching.

The switching efficiency of all switches discussed in this chapter is measured in terms of the extinction ratio (ER) which is the ratio of the reflectance from the switch with VO_2 in its metallic phase ($R_M(\lambda)$) and the reflectance from the switch with VO_2 in its semiconducting phase ($R_M(\lambda)$) as shown in Eq. 4.1.

$$ER = 10 * log_{10}\left(\frac{R_M(\lambda)}{R_S(\lambda)}\right) \quad dB \tag{4.1}$$

It can be observed from Figs. 4.2(a, b) that as the diameters of the uniform metallic nanodiscs (UNDs) are varied from 60 nm to 120 nm, the reflectance spectra for the switch for both the semiconducting and metallic states of the underlying VO_2 exhibit a red-shift of the plasmon resonance wavelengths. With VO_2 in its semiconducting state, the switch demonstrates a significant red-shift in the plasmon resonance wavelength from 1320 nm to 2030 nm as the diameter of the nanodiscs is varied from 60 nm to 120 nm. With VO_2 in its metallic state, there is a red-shift in the plasmon resonance wavelength from 880 nm to 990 nm as the diameter of the nanodiscs is varied from 60 nm to 120 nm. This red-shift in the plasmon resonance wavelength is expected due to the retardation of the depolarization field as the diameter of the nanodiscs is increased. As the diameter of the nanodiscs increases, the distance between the charges at the opposite interfaces of the nanodisc increases, thus leading to a lower restoring force causing a red-shift in the plasmon resonance wavelength [12]. Additionally, it must be noted that for both the semiconducting and the metallic state of VO_2, a plasmonic waveguide mode can also be observed around 720 nm, and this dip does not exhibit any red-shift on changing the diameter of the nanodiscs. Fig. 4.2(c) shows the extinction ratio (ER) of the periodic array of uniform metallic nanodiscs (UNDs) for different values of nanodisc diameters. It can be noticed from Fig. 4.2(c) that when the reflectance of the metallic phase is greater than the reflectance of the semiconductor phase (i.e., $R_M(\lambda) > R_S(\lambda)$), the ER is positive. However, when the reflectance of the metallic phase is less than the reflectance of the semiconductor phase (i.e., $R_M(\lambda) < R_S(\lambda)$), the ER becomes negative. It must be noted that although, the switch can be employed for switching in both wavelength regimes, i.e., with positive and negative values of the ER, an extensive analysis and comparison of the switching characteristics of all switches is carried out in the wavelength regime where the ER is positive. It can be seen from Fig. 4.2(c), that, for all values of diameters for the uniform nanodiscs, the operating wavelength range – for the full width at half maxima (FWHM) of the extinction ratio spectrum – remains below 350 nm. It is well known that such narrow bandwidths are not suitable to be employed for applications such as wavelength division multiplexed (WDM) networks [19], free space optical (FSO) networks [20] and passive optical networks (PON) [21], where broadband switching behavior is desirable.

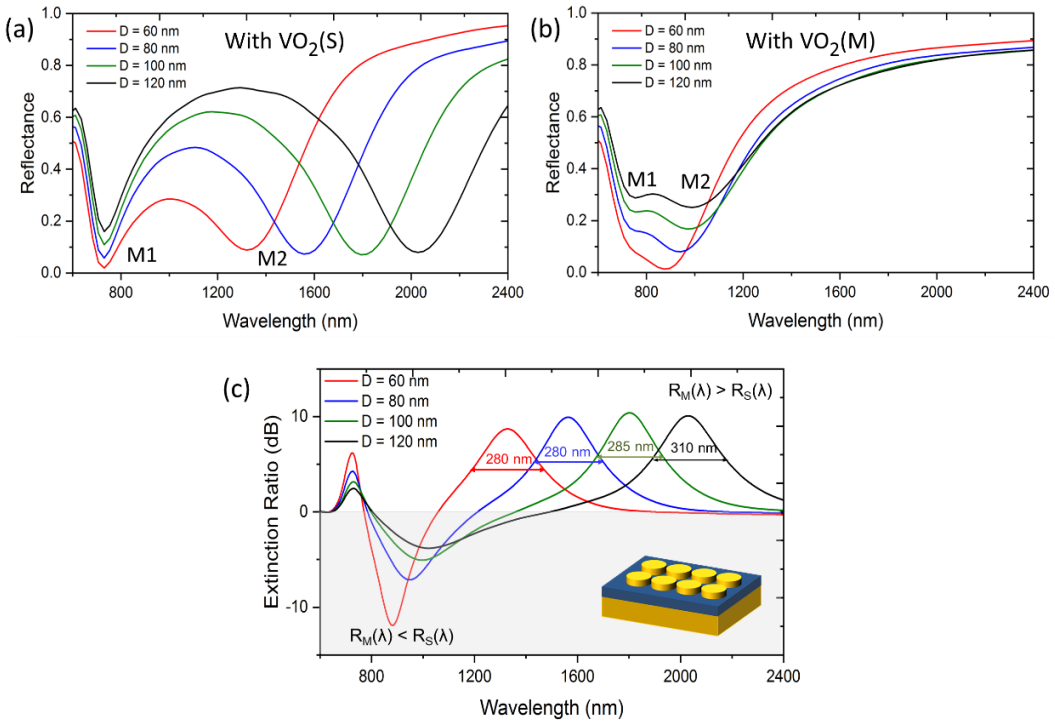

Fig. 4.2 Reflectance spectra of a periodic array of metallic nanodiscs with uniform diameters placed on a gold coated SiO_2 substrate with a thin film of VO_2 as a spacer. The reflectance spectra is shown for the values of the nanodisc diameters varying from 60 nm to 120 nm, when VO_2 is in its **(a)** semiconductor phase and **(b)** metallic phase. **(c)** Extinction ratio (ER) spectra for the periodic array of uniform metallic nanodiscs for different values of diameters placed on a gold coated SiO_2 substrate with a thin film of VO_2 as the spacer. The operating wavelength range at the full width half maximum (FWHM) of the maximum ER is shown for all cases. The VO_2 layer thickness, '*t*', the height of the nanodiscs, '*h*', and the gap between the nanodiscs, '*g*', were taken to be 10 nm, 50 nm, and 5 nm, respectively.

Therefore, for broadband switching, instead of uniform metallic nanodiscs, the analysis is started with a periodic array of two sets of nanodisc-dimers (NDD-D_1-D_2) with progressively increasing diameters D_1 (nm) and D_2 (nm) placed on the VO_2-thin film on top of the gold coated SiO_2 substrate. Each unit cell of this periodic structure comprises of two sets of nanodisc-dimers where the diameters of the first and second set of nanodisc-dimers are 60 nm and 80 nm, respectively, as shown in the inset of Fig. 4.3(a). The proposed switch based on the periodic array formed by these unit cells is called NDD-60-80 in the rest of the chapter for convenience. Fig. 4.3(a) shows the reflectance spectra for this proposed switch with the VO_2 layer in its semiconducting and metallic state. It can be observed from Fig. 4.3(a) that for this case — NDD-60-80 — when the VO_2 layer is in its semiconducting phase, three dips are present in the reflectance spectra at wavelength values of 720 nm (M1), 1250 nm (M2) and 1500 nm (M3). The dips at 1250 nm and 1500 nm are due to the wavelengths in the incident radiation that get coupled into the plasmonic modes arising out of the geometrical resonances of this composite nanostructure, NDD-60-80, with one metallic nanodisc-dimer of a specific diameter corresponding to a one specific plasmon resonance wavelength. In this case, the wavelength of 1250 nm corresponds to the plasmon resonance wavelength of the case when uniform nanodiscs with a

diameter of 60 nm are present alone (See Fig. 4.2(a)). Similarly, the wavelength of 1500 nm can be mapped to the plasmon resonance wavelength of the case when only uniform nanodiscs with a diameter of 80 nm are present alone. The dip in the reflectance spectra at 720 nm occurs due to the coupling of incident radiation into the plasmonic waveguide mode of this composite system [22].

Fig. 4.3(a) also shows the reflectance spectra of the proposed NDD-60-80 switch with VO_2 in its metallic state. On being switched from semiconducting state to its metallic state, the real part of the refractive index of VO_2 decreases leading to a blue shift of the plasmonic dip in the reflectance spectra as shown in Fig. 4.3(a). The dip in the reflectance spectra due to the coupling of light into the plasmonic mode of the nanostructure occurs at 870 nm (M2). Further, the dip in the reflectance spectra due to the coupling of light into the plasmonic waveguide mode of the nanostructure can be seen as a shoulder around ~720 nm (M1).

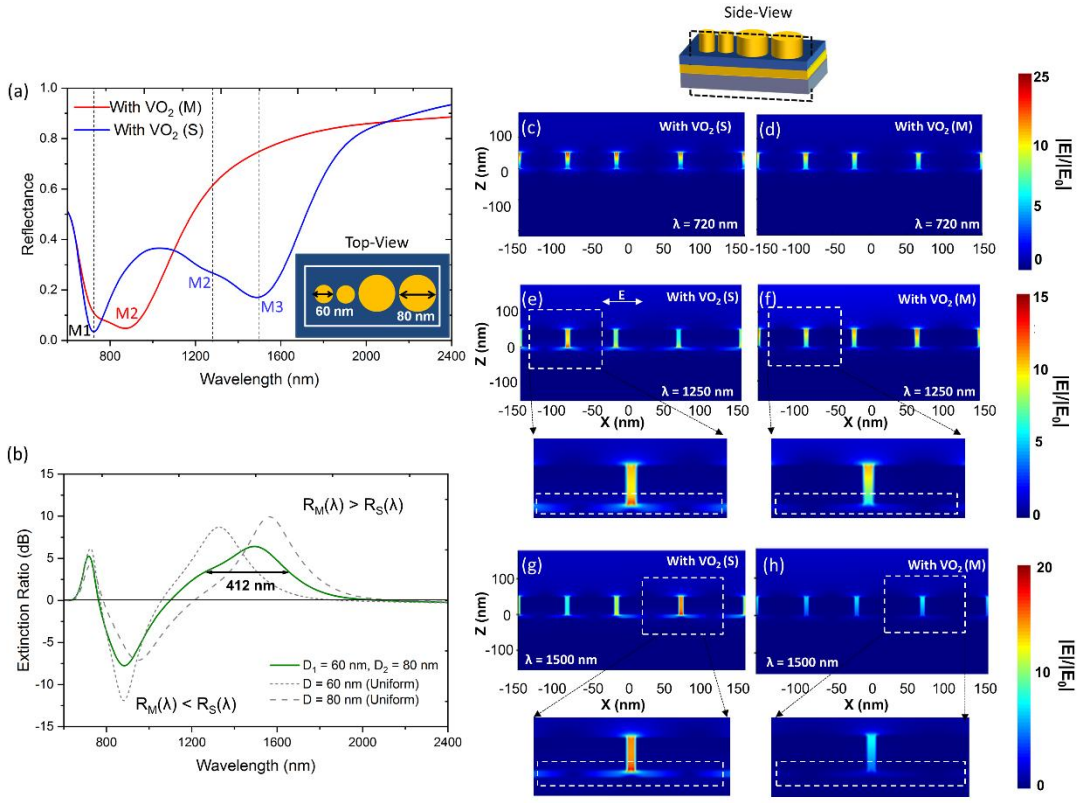

Fig. 4.3 (a) Reflectance spectra of the periodic array of two sets of nanodisc-dimers with the diameters being D_1 (60 nm) and D_2 (80 nm) with VO_2 is in its semiconductor phase and metallic phase. The inset shows one unit cell of the proposed periodic array. **(b)** Extinction ratio (ER) spectra for the proposed switch in comparison to the cases where periodic arrays of uniform nanodiscs with diameters 60 nm and 80 nm are present. E-field profile for the proposed switch at a wavelength of 720 nm with VO_2 in its **(c)** semiconductor phase, and **(d)** metallic phase. E-field profile for the proposed switch at a wavelength of 1250 nm with VO_2 in its **(e)** semiconductor phase, and **(f)** metallic phase. E-field profile for the proposed switch at a wavelength of 1500 nm with VO_2 in its **(g)** semiconductor phase, and **(h)** metallic phase. The thickness of VO_2, '*t*', the height of the nanodiscs, '*h*', and the gap between the nanodiscs, '*g*', were taken to be 10 nm, 50 nm, and 5 nm, respectively.

Fig. 4.3(b) shows the extinction ratio (ER) spectrum for the switch based on the periodic array of two sets of nanodisc-dimers (NDD-60-80) on the VO_2 coated plasmonic substrate. Further, for comparison, the figure also shows the ER spectra for the periodic array of uniform nanodiscs with disc diameters of 60 nm and 80 nm alone (discussed earlier in Fig. 4.2) on the VO_2 coated metallic substrate. It can be observed that the ER spectrum of the NDD-60-80 switch has peaks at the wavelengths of maximum ER for the switches with uniform nanodiscs of diameters 60 nm and 80 nm respectively, thus exhibiting an overall broadband behavior of the ER spectrum. It can be seen from Fig. 4.3(b) that the proposed switch with two sets of nanodisc-dimers is capable of providing a broadband ER of 3.2 dB over an operating wavelength range of 412 nm spanning from 1250 nm to 1662 nm. This is significantly higher than the operating wavelength range of 280 nm which was achieved using periodic arrays of uniform nanodiscs of 60 nm or 80 nm alone. Moreover, the operating wavelengths for the proposed switch span the C, L, and U bands of optical communication and thus, it can be employed at any wavelength of choice over these bands.

Figs. 4.3(c–h) show the electric-field enhancement profiles for the proposed switch with periodic arrays of two sets of nanodisc-dimers, with the semiconducting and metallic states of VO_2 at wavelengths of 720 nm, 1250 nm and 1500 nm. These wavelengths correspond to the dips in the reflectance spectra of the proposed switch with VO_2 in its semiconducting state. The E-field profile at 720 nm for the proposed switch with VO_2 in its semiconducting and metallic state is shown in Fig. 4.3(c, d). It can clearly be seen that at 720 nm, the field is confined equally in all the gaps between the adjacent nanodiscs as the plasmonic waveguide mode between adjacent nanodiscs depends only on the gap between the nanodiscs (i.e., the width of the insulator region of the resultant metal–insulator–metal waveguide). As the inter-nanodisc gap is uniformly 5 nm between all nanodiscs, the field is equally confined in all waveguides formed between adjacent nanodiscs, and is not dependent on the geometry of the nanodiscs. The electric-field profile of the composite structure in Fig. 4.3(e) (with VO_2 in the semiconducting state) shows that, at a wavelength of 1250 nm (M2), the incident energy is localized in the gap between the two nanodiscs with a diameter of 60 nm. It must be noted that the wavelength of 1250 nm corresponds to the plasmon resonance wavelength for the case when an array of uniform nanodiscs of diameter 60 nm were present alone on the VO_2-coated plasmonic substrate. For the case when VO_2 is in its metallic state (see Fig. 4.3(f)), the composite structure shows minimum localization of energy in the nanostructure at 1250 nm due to less plasmonic coupling of the incident radiation as compared to the semiconductor state. Additionally, the enlarged view of the E-field distribution at the boundary between VO_2 and the underlying gold substrate in Fig. 4.3(e, f) shows that while the field is present at the boundary between VO_2 and the underlying gold substrate when VO_2 is in its semiconducting state, the field vanishes as VO_2 transitions to its metallic phase. Further, at the resonance wavelength of the second plasmonic mode, i.e., at 1500 nm, the E-field profile of the composite structure in Fig. 4.3(g) (with VO_2 in the semiconducting state) shows the electromagnetic energy being localized between the nanodiscs with a diameter of 80 nm. As discussed earlier, Fig. 4.2(a) showed that a wavelength of 1500 nm is also the plasmon resonance wavelength for the case when an array of uniform nanodiscs of diameter 80 nm were present alone on the VO_2-coated

plasmonic substrate. Fig. 4.3(h) shows that with VO_2 in its metallic state, only a minimal amount of incident radiation is coupled into the plasmonic modes of the switch – and hence incident radiation is mostly reflected from the nanostructure. Thus, it can be inferred that this composite periodic structure with two sets of nanodisc dimers (NDD-60-80) exhibits the combined plasmonic behavior of two structures — a periodic array of uniform nanodiscs of diameter 60 nm, and another periodic array of uniform nanodiscs of diameter 80 nm on the VO_2-coated plasmonic substrate.

In coupled plasmonic systems like the periodic array of nanodisc-dimers on the VO_2 coated plasmonic substrate proposed in this chapter, the plasmon hybridization may lead to the emergence of bright and dark modes as a result of the in-phase and out-of-phase coupling of the dipole moments of the nanodiscs, respectively. However, in this work, only bright modes with a strong dipolar nature are present for both cases, i.e., when the proposed switch has VO_2 in its semiconductor and metallic state.

Bright modes are modes with a strong dipolar character due to which they couple efficiently to the far field and thus decay radiatively. On the contrary, dark modes exhibit a weak dipole moment and thus their radiative decay channel is suppressed [23-27]. Hence, the dark modes with vanishing dipole moments are capable of storing electromagnetic energy more efficiently than bright modes and thus, lead to a narrower spectral line width as compared to bright modes. However, it must be noted that the dark plasmon modes, in general, cannot be excited directly with linearly polarized light. These have to be excited by employing sophisticated excitation schemes such as excitation by employing focused electron beams, or by employing spatially inhomogeneous fields, evanescent excitation, non-normal incidence, spatial phase shaping, etc. [23, 24]. In this work, any such scheme has not been employed, and as expected, all modes excited in the nanostructure are bright modes. Further it can be seen in Fig. 4.4(a) that the spectral line width of any of the modes excited for cases when VO_2 is in its semiconductor or metallic state is not narrow, thus strengthening the argument that these modes are bright modes.

To validate the existence of these bright modes, additional simulations have been carried out to obtain the charge density profiles for the case when a periodic array of two sets of nanodisc-dimers with the diameters being D_1 (60 nm) and D_2 (80 nm) are present on the VO_2-coated plasmonic substrate. These simulations are carried out for both cases, i.e., for the switch with VO_2 is in its semiconductor phase and metallic phase. Figs. 4.4(b-d) show the charge density profiles at the plasmon resonance wavelengths for Mode 1 (M1 at 720 nm), Mode 2 (M2 at 1250 nm) and Mode 3 (M3 at 1500 nm) for the case when VO_2 is present in its semiconducting state. It can be clearly seen that the dipoles are strongly aligned with each other and hence these modes are bright modes. Figs. 4.4(e, f) show the charge density profiles at the plasmon resonance wavelengths for Mode 1 (M1 at 720 nm) and Mode 2 (M2 at 870 nm) for the case when VO_2 is present in its metallic state. For this case, the charge density profiles show a strong dipolar characteristic where the net dipole moment is not zero, hence, these modes are also bright modes. Therefore, for the proposed switch, with both VO_2 (S) and VO_2 (M) — when illuminated with linearly polarized light — there is no existence of dark modes.

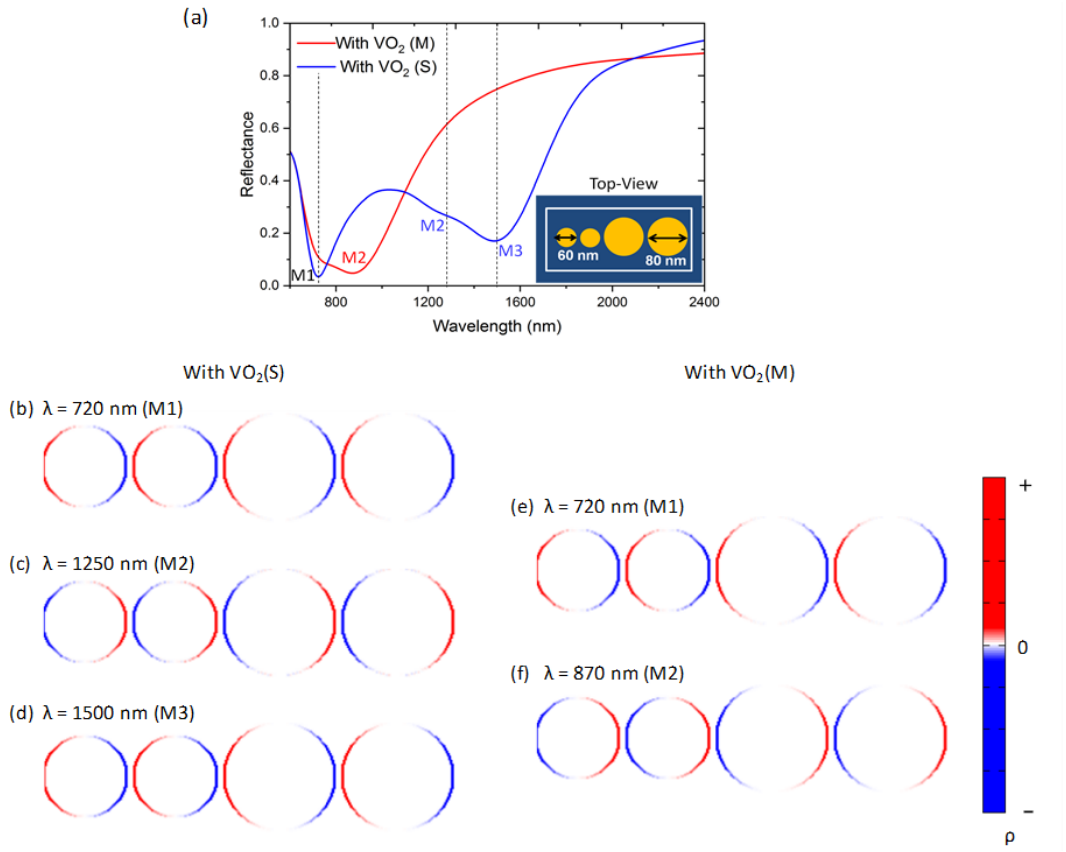

Fig. 4.4 (a) Reflectance spectra of the periodic array of two sets of nanodisc-dimers with the diameters being D_1 (60 nm) and D_2 (80 nm) with VO_2 is in its semiconductor phase and metallic phase. Charge density profiles for the proposed switch with VO_2 in its semiconductor phase at **(b)** λ = 720 nm **(c)** λ = 1250 nm and **(d)** λ = 1500 nm. Charge density profiles for the proposed switch with VO_2 in its metallic phase at **(e)** λ = 720 nm and **(f)** λ = 870 nm. The thickness of VO_2, '*t*', the height of the nanodiscs, '*h*', and the gap between the nanodiscs, '*g*', were taken to be 10 nm, 50 nm, and 5 nm, respectively.

In order to increase the operating wavelength range of the proposed switches, a periodic array of three sets of nanodisc-dimers (NDD-60-80-100) with progressively increasing diameters (D_1 being 60 nm, D_2 being 80 nm and D_3 being 100 nm) placed on the VO_2-thin film on top of the gold coated SiO_2 substrate is analyzed in Fig. 4.5. It can be observed from the reflectance spectra shown in Fig. 4.5(a) that for this case with three sets of nanodisc-dimers, when the VO_2 layer is in its semiconducting phase, four dips are present in the reflectance spectra at wavelength values of 720 nm (M1), 1250 nm (M2), 1500 nm (M3) and 1750 nm (M4), where the dip at 720 nm corresponds to the coupling of incident radiation into a plasmonic waveguide mode of the nanostructure. The plasmonic dips at 1250 nm, 1500 nm and 1750 nm closely correspond to the plasmon resonance dips of periodic arrays of uniform nanodiscs (UNDs) with diameters 60 nm, 80 nm, and 100 nm on the VO_2-coated plasmonic substrate, respectively. It can be observed from the extinction ratio (ER) spectra shown in Fig. 4.5(b) that the proposed switch with three sets of nanodisc-dimers has peaks at three wavelengths, each corresponding to one of the peaks of the ER spectra for the three cases when uniform nanodiscs with diameter 60 nm, 80 nm

and 100 nm are present on the VO_2-coated substrate (See Fig. 4.2). The overall ER of the NDD-60-80-100 switch shows a broadband behavior and is capable of providing a broadband ER of 2.3 dB over an operating wavelength range of 604 nm spanning from 1304 nm to 1908 nm. This is significantly higher than the operating wavelength range of 285 nm which could be achieved using periodic arrays of uniform nanodiscs of 60 nm, 80 nm, or 100 nm alone.

Figs. 4.5(c–j) show the electric-field enhancement profiles for the proposed switch with periodic arrays of three sets of nanodisc-dimers, with the semiconducting and metallic states of VO_2 at wavelengths of 720 nm, 1250 nm, 1500 nm and 1750 nm. The E-field profiles corresponding to the plasmonic waveguide mode at the wavelength of 720 nm for the cases when VO_2 is present in its semiconductor and metallic state are shown in Figs. 4.5(c, d). It can be observed from Figs. 4.5(e, g, i) that with VO_2 in the semiconducting state, the incident energy is localized in the gap between the two nanodiscs with a diameter of 60 nm, 80 nm, and 100 nm at a wavelength of 1250 nm, 1500 nm, and 1750 nm, respectively. It must be noted that the wavelengths of 1250 nm, 1500 nm, and 1750 nm correspond to the plasmon resonance wavelengths for the cases when an array of uniform nanodiscs of diameter 60 nm, 80 nm and 100 nm, respectively, were present alone on the VO_2-coated plasmonic substrate. Further, for the case when VO_2 is in its metallic state, Figs. 4.5(f, h, j) show minimum localization of energy in the nanostructure at wavelengths of 1250 nm, 1500 nm, and 1750 nm, respectively due to less plasmonic coupling of the incident radiation as compared to the semiconductor state. Thus, it can be inferred that this composite periodic structure with three sets of nanodisc-dimers (NDD-60-80-100) exhibits the combined plasmonic behavior of three structures — a periodic array of uniform nanodiscs of diameter 60 nm, periodic array of uniform nanodiscs of diameter 80 nm and another periodic array of uniform nanodiscs of diameter 100 nm on the VO_2-coated plasmonic substrate.

Fig. 4.6 shows the reflectance spectra and the ER spectra for a periodic array of a set of four nanodisc-dimers (NDD-60-80-100-120) on a VO_2-coated substrate such that the values of the diameters for the sets of nanodisc-dimers are 60 nm, 80 nm, 100 nm, and 120 nm, respectively (See schematic in Fig. 4.6(a)). Figs. 4.6(b, c) show the effect of varying the thickness of VO_2 layer on the reflectance spectra when VO_2 is in its semiconducting and metallic state, respectively. It can be noticed from Fig. 4.6(b) that for the case when VO_2 is in its semiconductor state and when the thickness of the VO_2 layer is less than 25 nm, there is a blue-shift in the dips of the reflectance spectra when the VO_2 thickness is increased from 10 nm to 20 nm. This is due to the coupling of the incident radiation into the plasmonic waveguide mode in the VO_2 spacer layer (between the gold nanodiscs and the underlying gold film) for sub-20 nm values of spacer thickness. Thus, the plasmon resonance wavelength blue-shifts with increasing VO_2 spacer thickness as expected [28]. However, as the thickness of VO_2 layer is further increased, this plasmonic waveguide mode becomes weak and the plasmonic characteristics of the nanostructure can be attributed to the geometrical resonance arising out of the nanodiscs on the VO_2-coated plasmonic film. When the thickness of VO_2 layer is increased beyond 20 nm, the plasmonic dips of the nanostructure exhibit a red-shift with increasing thickness. This

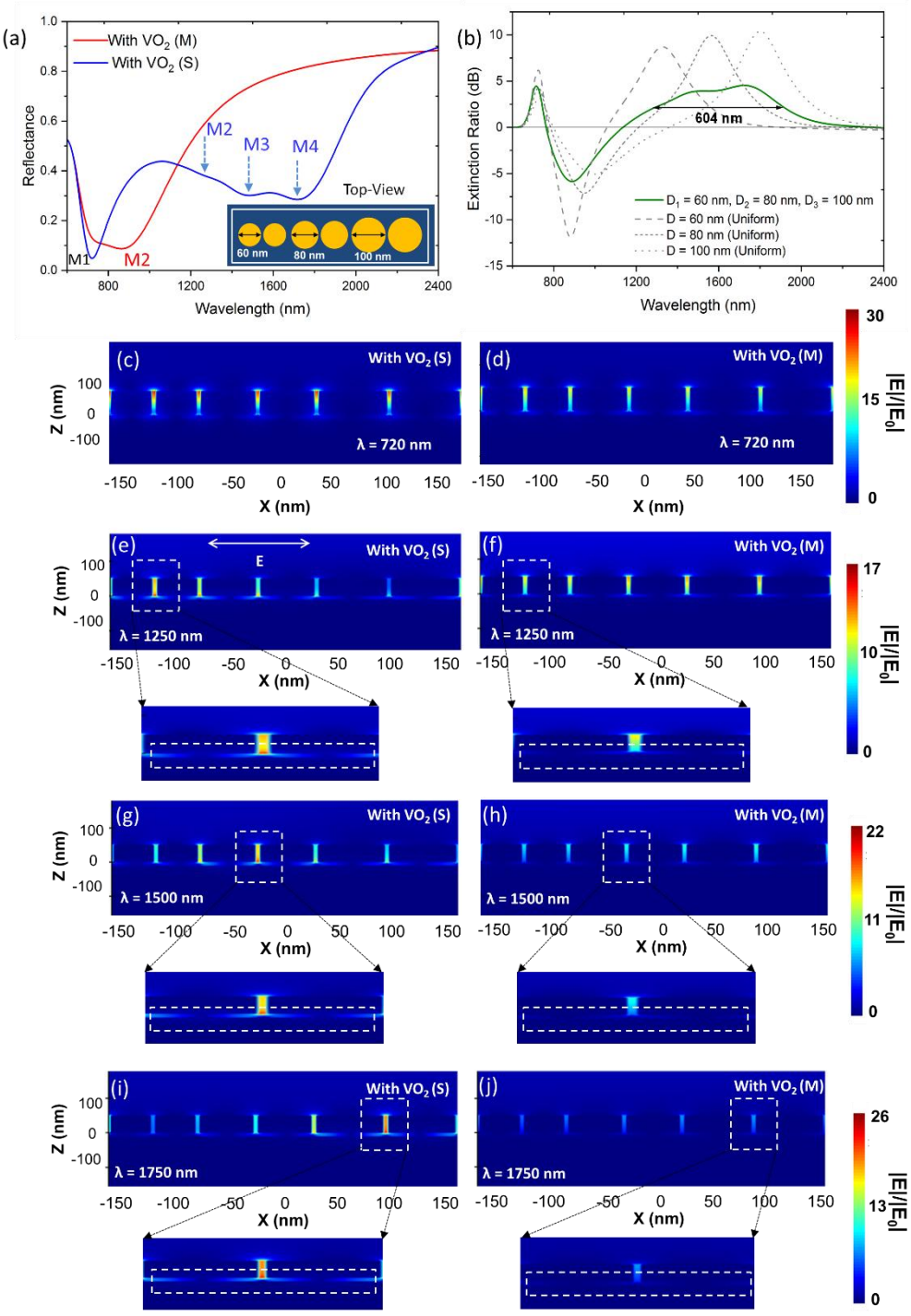

Fig. 4.5 (a) Reflectance spectra for the periodic array of three sets of nanodisc-dimers with the diameters being D_1 (60 nm), D_2 (80 nm) and D_3 (100 nm) when VO_2 is present in its semiconductor phase and metallic phase. The inset shows one unit cell of the proposed periodic array. **(b)** ER spectra for the proposed switch in comparison to the cases when periodic arrays of uniform nanodiscs with diameters 60 nm, 80 nm, and 100 nm are present. E-field profile for the proposed switch at a wavelength of **(c, d)** 720 nm, **(e, f)** 1250 nm, **(g, h)** 1500 nm, and **(i, j)** 1750 nm with VO_2 in its semiconductor phase and metallic phase, respectively. The thickness of VO_2, '*t*', the height of the nanodiscs, '*h*', and the gap between the nanodiscs, '*g*', were taken to be 10 nm, 50 nm, and 5 nm, respectively.

can be understood by applying the effective medium theory for the underlying substrate, i.e., VO_2 (S) on top of gold, whose effective permittivity is expected to increase with an increase in the thickness of VO_2 layer (See Appendix-II, Dielectric Constants of Materials). This leads to a red-shift in the plasmon resonance wavelength with an increase in the thickness of VO_2 layer. For the case when VO_2 is in its metallic state, the reflectance spectra as a function of the thickness of the VO_2 layer are shown in Fig. 4.6(c). It can be observed that as the thickness of the VO_2 layer is increased, there is a red-shift in the plasmon resonance wavelength. This can also be understood by applying effective medium theory to the underlying substrate, i.e., VO_2 (M) on top of gold. It is known that for values of wavelength below 1130 nm, the permittivity of VO_2 (M) is positive. This results in an increase in the permittivity of the effective substrate as the thickness of VO_2 layer is increased, thus leading to a red-shift in the plasmon resonance wavelength. The electric-field enhancement profiles for the proposed switch with periodic arrays of four sets of nanodisc-dimers (NDD-60-80-100-120) on 10 nm thick VO_2 layer, with the semiconducting and metallic states of VO_2 at wavelengths of 1250 nm, 1500 nm, 1750 nm, and 2050 nm (corresponding to the dips in the reflectance spectra of the proposed switch with VO_2 in its semiconducting state) are shown in Fig. 4.7.

Figs. 4.6(d–i) show the effect of varying the VO_2 thickness from 10 nm to 80 nm on the extinction ratio spectra for a periodic array of four sets of nanodisc-dimers on a VO_2-coated substrate. The operating wavelength range for the switch is shown at the full width at half maxima (FWHM) of the ER for each value of thickness (shown in red color). The range of operating wavelengths over which switching can be done is also shown with the values of the ER being 3 dB (blue), 4 dB (green) and 5 dB (orange) for comparison with other configurations of the switch and switches proposed in the past. The maximum ER, the operating wavelength range at the FWHM of the ER, and the operating wavelength ranges for the extinction ratio of 3 dB, 4 dB and 5 dB are tabulated in Table 4.1. The table shows that the values of ER — and the range of wavelengths over which the switch can be efficiently employed — can be optimized by varying the thickness of VO_2 layer. These switches can be employed to obtain a maximum ER of 25 dB for a 50 nm thick layer of VO_2. Table 4.1 shows that an operating wavelength range of ~730 nm with an ER of 3 dB and an operating wavelength range of ~640 nm with an ER of 4 dB can be achieved by employing an 80 nm thick layer of VO_2. Further, an operating wavelength range of ~574 nm can be achieved with an ER of 5 dB by employing a 50 nm thick VO_2 layer under the periodic array of four sets of nanodisc-dimers (NDD-60-80-100-120). It can be seen from Table 4.1 that the proposed switch with four sets of nanodisc-dimers can be employed for broadband switching in the C, L and U bands of optical communication.

It should also be noted that, in this work, periodic arrays of nanodisc-dimers with different diameters were chosen over arrays of single nanodiscs of variable diameters as their ER spectra exhibited a wider operating wavelength range, making them more suitable for broadband switching. The ER spectra for arrays of single nanodiscs and nanodisc-dimers of varying diameters are shown for comparison in Fig. 4.8.

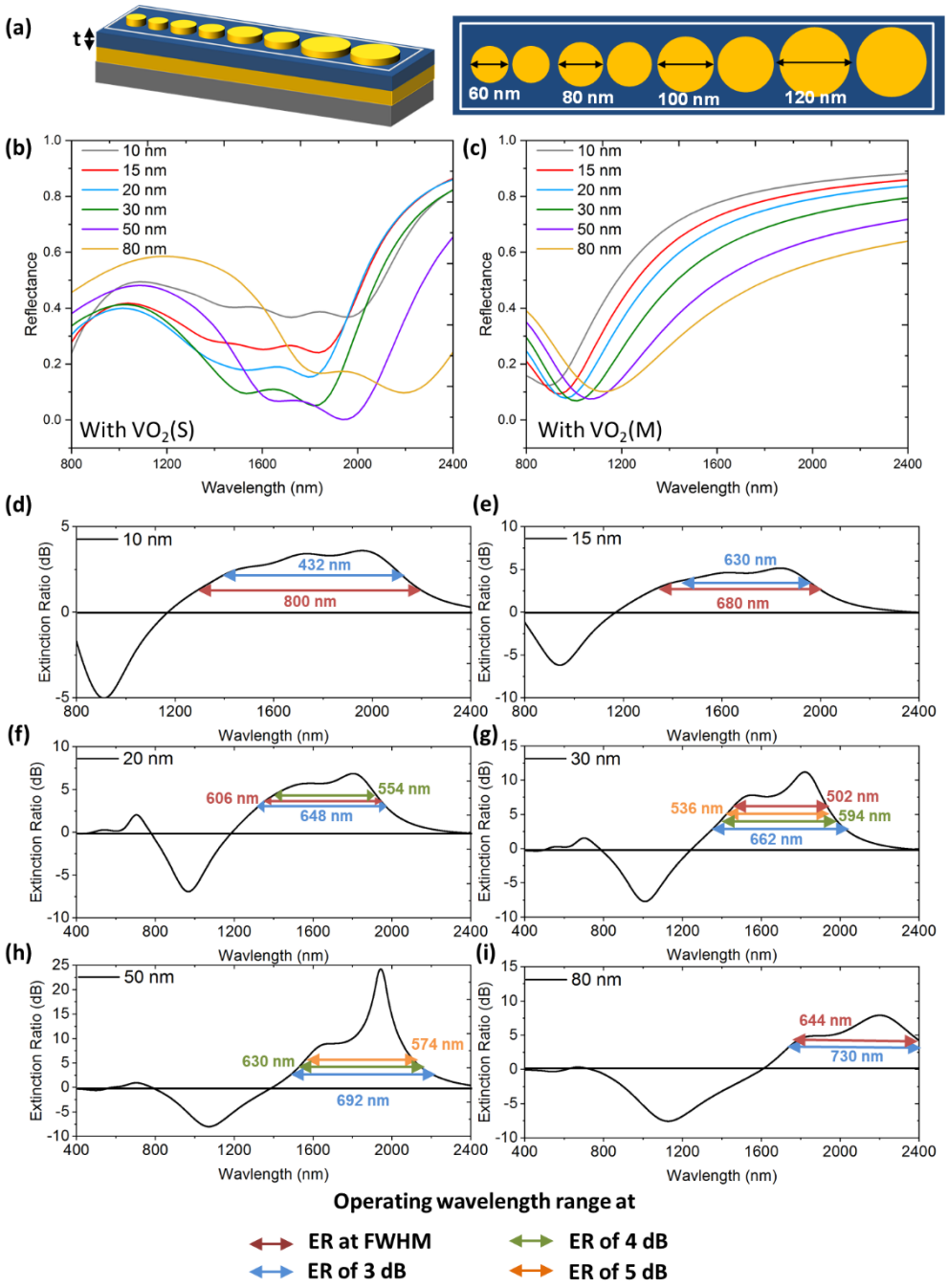

Fig. 4.6 (a) Schematic showing the periodic array of four sets of nanodisc-dimers on a VO_2 coated plasmonic film with the diameters of the nanodisc-dimers being D_1 (60 nm), D_2 (80 nm), D_3 (100 nm) and D_4 (120 nm). Reflectance spectra of the periodic array of four sets of nanodisc-dimers showing the effect of increasing the thickness of VO_2, '*t*', from 10 nm to 80 nm when VO_2 is in its **(b)** semiconductor phase and **(c)** metallic phase. Extinction ratio (ER) spectra showing the operating wavelength range for an ER of 3 dB, 4 dB, 5 dB and for the FWHM of the maximum ER when the thickness of VO_2, '*t*', is **(d)** 10 nm **(e)** 15 nm **(f)** 20 nm **(g)** 30 nm **(h)** 50 nm and **(i)** 80 nm. The height of the nanodiscs, '*h*', and the gap between the nanodiscs, '*g*', were kept constant at 50 nm, and 5 nm, respectively, for all the above cases.

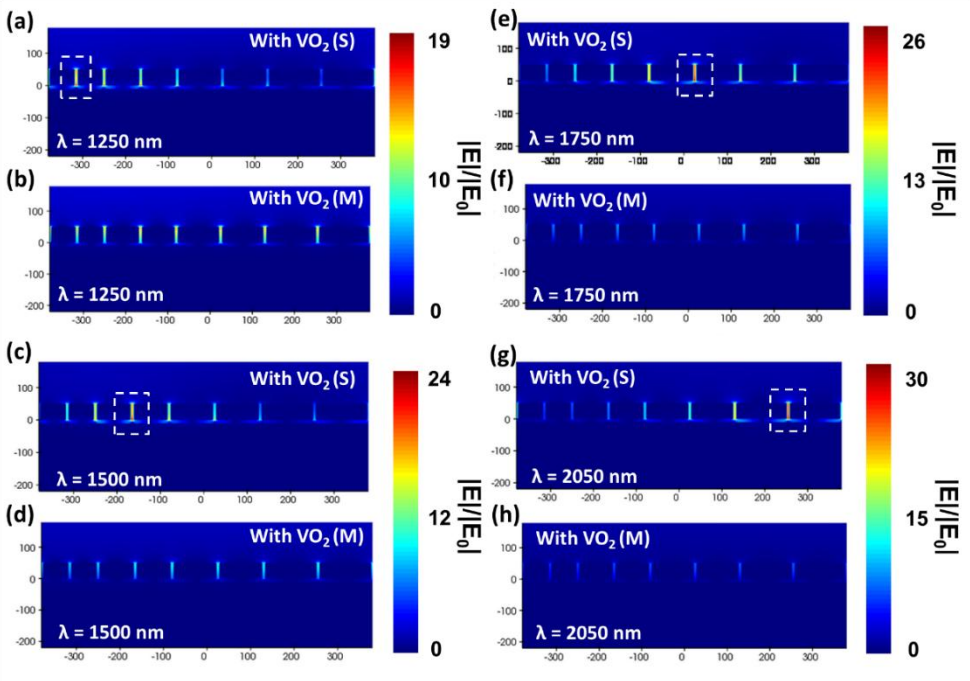

Fig. 4.7 E-field profile for the side view of the periodic array of a set of four nanodisc-dimers at a wavelength of **(a, b)** 1250 nm, **(c, d)** 1500 nm, **(e, f)** 1750 nm, and **(g, h)** 2050 nm with VO_2 in its semiconductor phase and metallic phase, respectively. The diameters of the set of four nanodisc-dimers are taken as D_1 (60 nm), D_2 (80 nm), D_3 (100 nm) and D_4 (120 nm), respectively. The thickness of VO_2, '*t*', the height of the nanodiscs, '*h*', and the gap between the nanodiscs, '*g*', were kept constant at 10 nm, 50 nm, and 5 nm, respectively.

Table 4.1 Operating wavelength range and the extinction ratio for a periodic array of four sets of nanodisc-dimers with progressively increasing diameters (NDD-60-80-100-120) on a gold coated SiO_2 substrate with a VO_2 spacer when the thickness of the VO_2 spacer is varied from 10 nm to 80 nm

Thickness of VO_2 Layer	**10 nm**	**15 nm**	**20 nm**	**30 nm**	**50 nm**	**80 nm**
Maximum ER	3.6 dB	5.2 dB	6.9 dB	11.3 dB	25 dB	7.94 dB
FWHM	800 nm (1350-2150 nm)	680 nm (1320-2000 nm)	606 nm (1345-1951 nm)	502 nm (1442-1944 nm)	-	644 nm (1768-2412 nm)
Operating wavelength range at **ER = 3 dB**	432 nm (1622-2054 nm)	630 nm (1350-1980 nm)	648 nm (1320-1968 nm)	662 nm (1356-2018 nm)	692 nm (1498-2190 nm)	730 nm (1730-2460 nm)
Operating wavelength range at **ER =4 dB**	-	442 nm (1490-1932 nm)	554 nm (1376-1930 nm)	594 nm (1390-1984 nm)	630 nm (1522-2152 nm)	640 nm (1770-2410 nm)
Operating wavelength range at **ER = 5 dB**	-	-	448 nm (1450-1898 nm)	536 nm (1422-1958 nm)	574 nm (1546-2120 nm)	404 nm (1960-2364 nm)

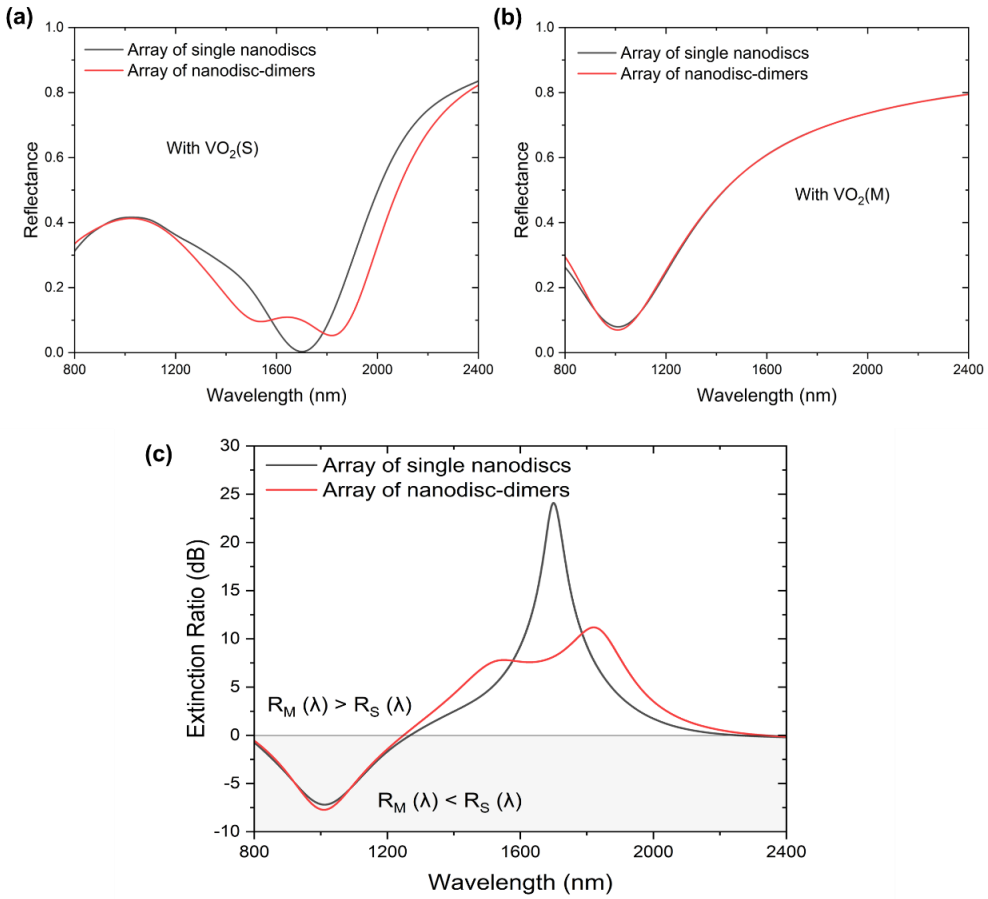

Fig. 4.8 Reflectance spectra of a periodic array of a set of four metallic nanodiscs with the diameters being D_1 (60 nm), D_2 (80 nm), D_3 (100 nm) and D_4 (120 nm) for the cases when an array of single nanodiscs with variable diameters and an array of nanodisc-dimers with variable diameters are considered with VO_2 in its **(a)** semiconductor phase, and **(b)** metallic phase. **(c)** ER spectra for the two cases showing the broadband behavior for the case when a periodic array of nanodisc-dimers is employed. The thickness of VO_2, the gap between the nanodiscs, and the height of the nanodiscs were taken as 30 nm, 5 nm, and 50 nm, respectively.

Further, a detailed analysis for the effect of reduction of diameters of the nanodisc-dimers on the reflectance spectra and the extinction ratio spectra is carried out next in two sub-sections. First, the effect of reducing the diameters of the nanodiscs on the reflectance spectra and the extinction ratio is analyzed when a periodic array of four sets of nanodisc-dimers on a VO_2-coated plasmonic film is employed. Figs. 4.9(a, b) show the reflectance spectra of the proposed switch when VO_2 is present in its semiconductor and metallic state, respectively. In both the cases, it can be seen that as the diameters of the nanodiscs are reduced from the larger diameter set (D_1 = 60 nm, D_2 = 80 nm, D_3 = 100 nm and D_4 = 120 nm) to the smaller diameter set (D_1 = 20 nm, D_2 = 40 nm, D_3 = 60 nm and D_4 = 80 nm) the plasmonic dips in the reflectance spectra exhibit a blue-shift. Fig. 4.9(c) shows the effect of reduction of diameters on the extinction ratio spectra for the proposed switch. It can be seen that the operating wavelength range can be blue-shifted by employing smaller values of nanodisc diameters.

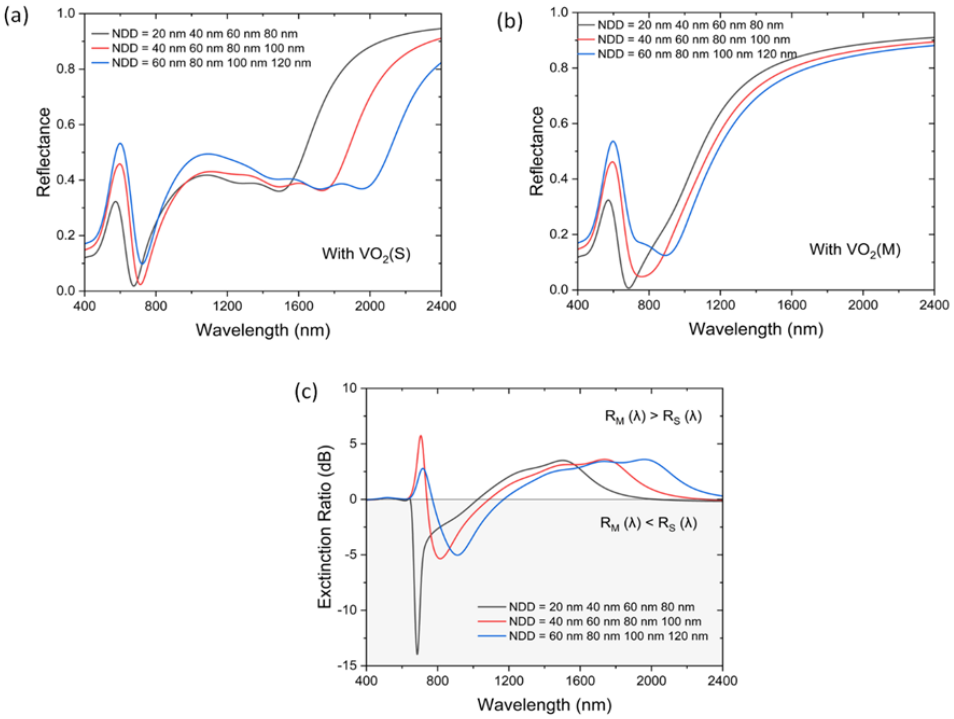

Fig. 4.9 Reflectance spectra for the periodic array of four sets of nanodisc-dimers on a VO_2-coated plasmonic film with different diameters when VO_2 is in its **(a)** semiconductor phase, and **(b)** metallic phase. **(c)** The extinction ratio spectra for the periodic array of four sets of nanodisc-dimers on a VO_2-coated plasmonic film with different diameters of the nanodiscs. The thickness of VO_2, '*t*', the height of the nanodiscs, '*h*', and the gap between the nanodiscs, '*g*', were kept constant at 10 nm, 50 nm and 5 nm, respectively.

Secondly, the effect of reducing the number of sets of nanodisc-dimers in a unit cell of the periodic array on the reflectance spectra and the extinction ratio spectrum is analyzed. It can be seen from Fig. 4.10(a) that as the number of sets of nanodisc dimers with progressively increasing disc sizes is decreased from five sets to two sets — for the case when VO_2 is present in the semiconducting phase — the plasmonic dip corresponding to Mode 2 in the reflectance spectra becomes narrower and deeper, and exhibits a blue-shift as the diameters of the nanodisc-dimers are reduced. A similar effect can be seen in Fig. 4.10(b) for the case when VO_2 is present in the metallic phase. Fig. 4.10(c) shows the extinction ratio spectra for the cases when different number of sets of nanodisc-dimers are employed. It can be seen from Fig. 4.10(c) that there is a trade-off between the highest extinction ratio and the operating wavelength range over which broadband switching is obtained. As the number of sets of nanodisc-dimers is reduced, the highest ER achievable using the proposed switch increases but the operating wavelength range considerably reduces. It can be seen from Fig. 4.10(c) that the operating wavelength range (at the FWHM of the highest ER) reduces from 1002 nm to 412 nm as the number of sets of nanodisc-dimers are decreased from five to two.

Fig. 4.11(a) shows the schematic for another configuration of the proposed switch where a periodic array of five sets of nanodisc-dimers (NDD-40-60-80-100-120) are placed on VO_2-coated substrate to allow additional wavelengths to be coupled

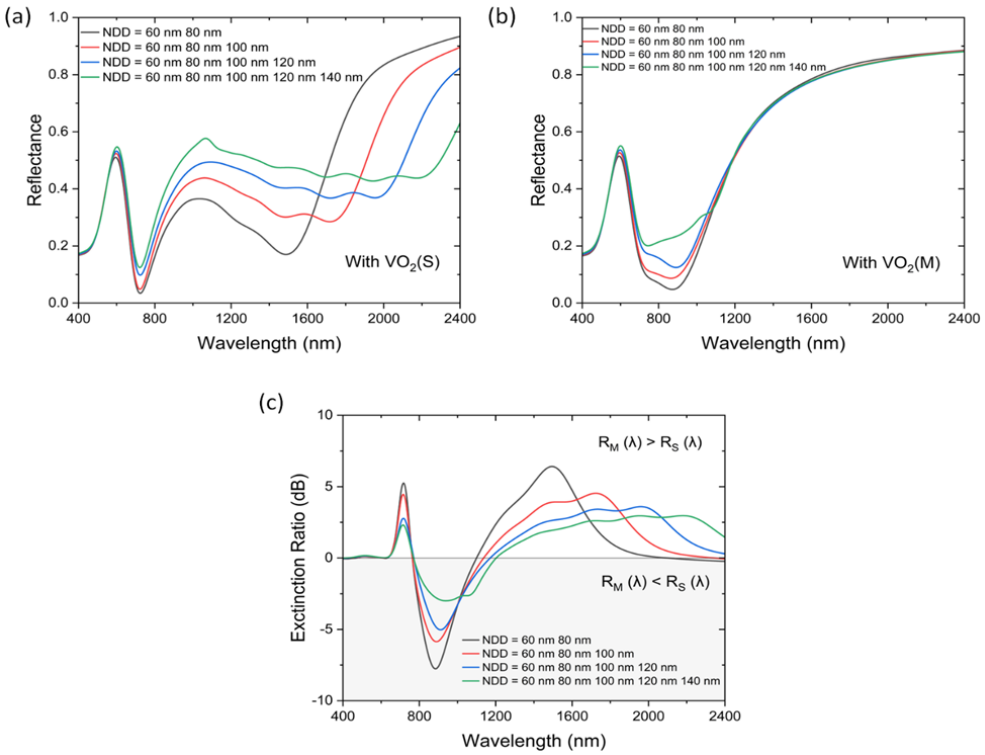

Fig. 4.10 Reflectance spectra for the periodic array of two, three, four and five sets of nanodisc-dimers on a VO_2-coated plasmonic film with VO_2 in its **(a)** semiconductor phase, and **(b)** metallic phase. **(c)** The extinction ratio spectra for the periodic array of two, three, four and five sets of nanodisc-dimers on a VO_2-coated plasmonic film. The thickness of VO_2, '*t*', the height of the nanodiscs, '*h*', and the gap between the nanodiscs, '*g*', were kept constant at 10 nm, 50 nm and 5 nm, respectively.

into the plasmonic modes of the structure, thereby allowing the operating wavelength range to increase further. The effect of varying the thickness of VO_2 layer on the reflectance spectra of the NDD-40-60-80-100-120 switch is shown in Fig. 4.11(b, c) for the semiconducting and metallic state of VO_2, respectively. Figs. 4.11(d-i) show the effect of varying the thickness of the underlying VO_2 layer on the ER spectra for this configuration of the switch. The maximum ER, the operating wavelength range for the FWHM of the ER, and the operating wavelength range at the extinction ratio of 3 dB, 4 dB and 5 dB for this case are tabulated in Table 4.2. When a 50 nm thick VO_2 layer is employed, the proposed configuration of the switch is capable of offering an extinction ratio of 5 dB with a broadband operating wavelength range of ~650 nm over a wavelength range of 1460 nm to 2110 nm spanning the C, L and U bands of optical communication.

As discussed earlier, the proposed switches can be fabricated with the state-of-the-art fabrication processes like E-beam lithography or Focused Ion beam milling. However, the fabrication of sub−10 nm gaps between the gold nanodisc-dimers can be challenging even by using these sophisticated fabrication methodologies. Therefore, an analysis of the effect of the inter-nanodisc gap on the extinction ratio spectra is also carried out (See schematic in Fig. 4.12(a)). Figs. 4.12(b, c) show the effect of varying the gap between the nanodiscs (g) for a periodic array of

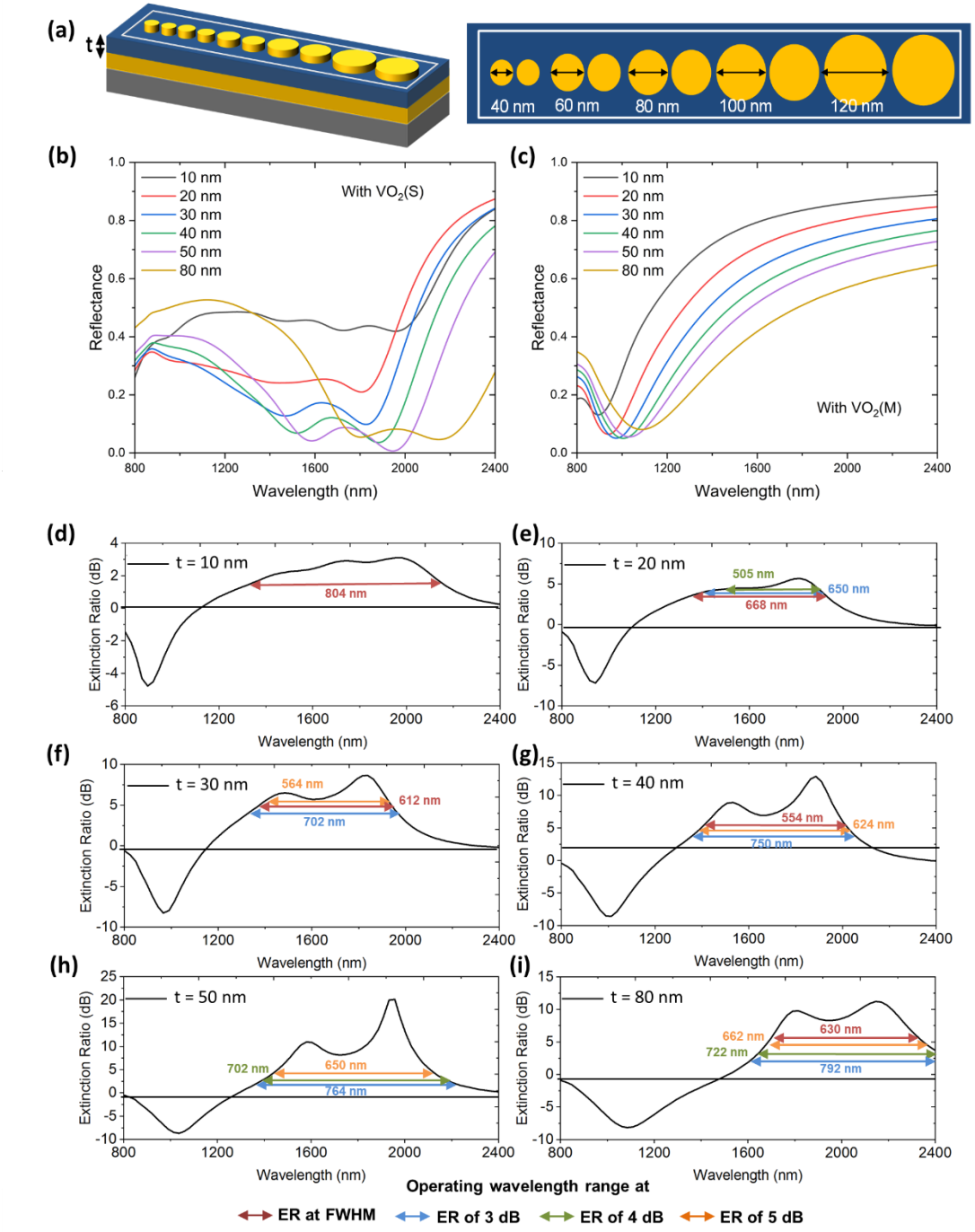

Fig. 4.11 (a) Schematic showing the periodic array of five sets of nanodisc-dimers on a VO_2-coated plasmonic film with the diameters of the nanodisc-dimers being D_1 (40 nm), D_2 (60 nm), D_3 (80 nm), D_4 (100 nm) and D_5 (120 nm). Reflectance spectra of NDD-40-60-80-100-120 showing the effect of increasing the thickness of VO_2, '*t*', from 10 nm to 80 nm when VO_2 is in its **(b)** semiconductor phase, and **(c)** metallic phase. Extinction ratio (ER) spectra showing the operating wavelength ranges for an ER of 3 dB, 4 dB, 5 dB and at the FWHM of the ER when the thickness of VO_2, '*t*', is **(d)** 10 nm **(e)** 20 nm **(f)** 30 nm **(g)** 40 nm **(h)** 50 nm, and **(i)** 80 nm. The height of the nanodiscs, '*h*', and the gap between the nanodiscs, '*g*', were kept constant at 50 nm, and 5 nm, respectively, for all the above cases.

Table 4.2 Operating wavelength range and the extinction ratio for a periodic array of five sets of nanodisc-dimers with progressively increasing diameters (NDD-40-60-80-100-120) on a gold coated SiO_2 substrate with a VO_2 spacer when the thickness of the VO_2 spacer is varied from 10 nm to 80 nm

Thickness of VO_2 Layer	**10 nm**	**20 nm**	**30 nm**	**40 nm**	**50 nm**	**80 nm**
Maximum ER	3.15 dB	5.68 dB	8.66 dB	12.92 dB	20.2 dB	11.2 dB
FWHM	804 nm (1346-2150 nm)	668 nm (1288-1956 nm)	612 nm (1344-1956 nm)	554 nm (1438-1992 nm)	-	630 nm (1700-2330 nm)
Operating wavelength range at **ER = 3 dB**	-	650 nm (1300-1950 nm)	720 nm (1280-2000 nm)	750 nm (1330-2080 nm)	764 nm (1402-2166 nm)	792 nm (1638-2430 nm)
Operating wavelength range at **ER = 4 dB**	-	505 nm (1404-1909 nm)	638 nm (1328-1966 nm)	680 nm (1366-2046 nm)	702 nm (1432-2134 nm)	722 nm (1664-2386 nm)
Operating wavelength range at **ER = 5 dB**	-	-	564 nm (1374-1938 nm)	624 nm (1397-2021 nm)	650 nm (1460-2110 nm)	662 nm (1686-2348 nm)

a set of four nanodisc-dimers (NDD-60-80-100-120) with 10 nm and 50 nm thick layers of VO_2, respectively. It can be observed from Fig. 4.12(b) that for a gap of 5 nm between the nanodiscs, and the operating wavelength range at the FWHM of the ER is ~800 nm over a wavelength span of 1350 nm to 2150 nm. As the gap between the nanodiscs is increased from 5 nm to 20 nm, a slight drop in the extinction ratio can be observed from Fig. 4.12(b) along with a blue-shift in the plasmon resonance wavelengths as expected [28]. However, the operating wavelength range remains sufficiently broad band (~828 nm) even for higher inter-nanodisc gaps such as 20 nm which can be easily fabricated with the state-of-the-art fabrication processes.

Fig. 4.12(c) shows the extinction ratio (ER) spectra for the case when a periodic array of a set of four nanodisc-dimers (NDD-60-80-100-120) are placed on a 50 nm thick VO_2 layer on top of a SiO_2 substrate. It can be seen from Fig. 4.12(c) that an extinction ratio of 4 dB can be achieved over an operating wavelength range of ~630 nm for the gap being 5 nm. As the gap is increased to 10 nm, 15 nm and 20 nm, the operating wavelength ranges for an extinction ratio of 4 dB become ~680 nm, ~684 nm and ~620 nm, respectively. This shows that the proposed switch can be employed even when the inter-nanodisc gaps are higher, which makes these switches more amenable to fabrication. Moreover, the wavelength range over which the switching can be obtained exhibits a blue-shift as the gap between the nanodiscs is increased [28]. Hence, the gap between the nanodiscs can also be employed to tune the broad switching band over the wavelength of choice. Moreover, the geometrical parameters of these switches can be further optimized to enable the usage of these switches for the visible range of the spectrum.

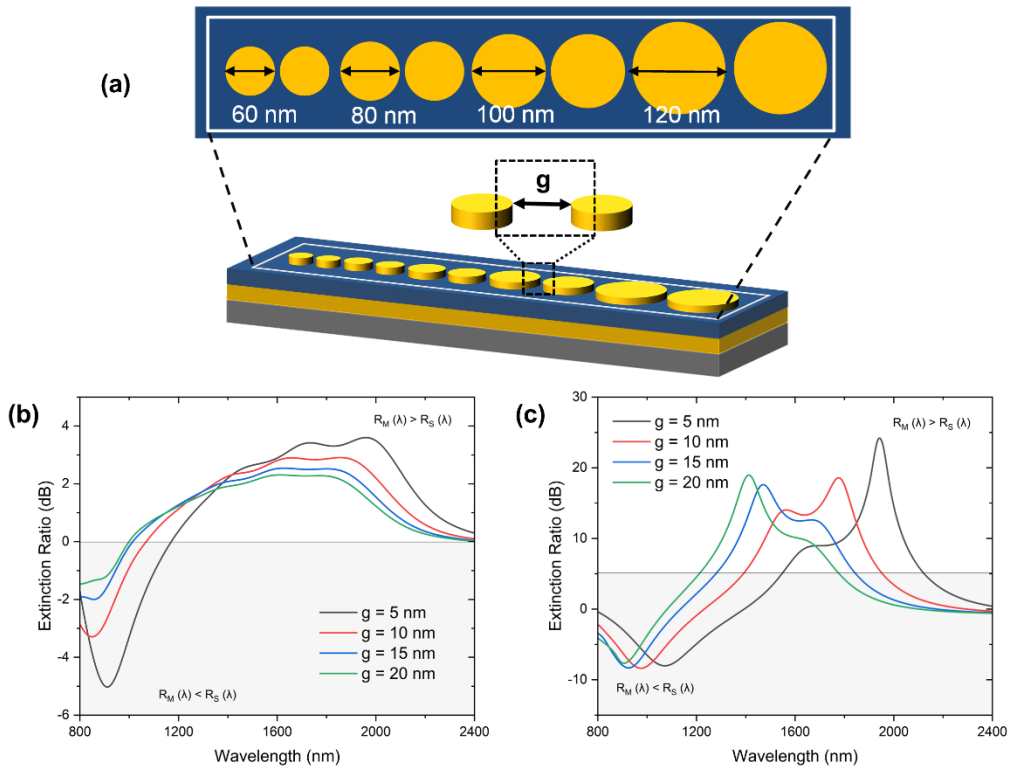

Fig. 4.12 (a) Schematic showing the periodic array of four sets of nanodisc-dimers on a VO_2-coated plasmonic film with the diameters of the nanodisc-dimers being D_1 (60 nm), D_2 (80 nm), D_3 (100 nm) and D_4 (120 nm). Extinction ratio (ER) spectra for the proposed switch showing the effect of varying the gap, '*g*', between the nanodiscs from 5 nm to 20 nm, when the thickness of VO_2, '*t*', is **(b)** 10 nm, and **(c)** 50 nm. The height of the nanodiscs, '*h*', is kept constant at 50 nm for both the cases.

4.5 Chapter Summary

This chapter proposed active broadband plasmonic switches consisting of a periodic array of metallic nanodisc-dimers with gradually increasing diameters, fabricated on a gold-coated SiO_2 substrate. A VO_2 thin film was employed as a spacer layer between the nanodiscs and the underlying plasmonic substrate. Broadband switching was demonstrated over the C, L, and U bands of optical communication with an operating wavelength range of ~650 nm for an extinction ratio of 5 dB, and an operating wavelength range of ~700 nm for an extinction ratio of 4 dB. These switches exhibited a trade-off between the extinction ratio and the operating wavelength range making them amenable to be used as narrowband switches with high extinction ratio or broadband switches with a moderate extinction ratio. Moreover, optimization of the geometrical parameters of these switches could lead to tunability of the spectral range over which broadband operation could be obtained. As these switches were based on VO_2, which can potentially exhibit ultra-fast switching, these switches are capable of being employed for high-speed optical communication networks or as switching components in plasmonic circuits.

4.6 References

[1] Sharma, Y., Tiruveedhula, V. A., Muth, J. F., and Dhawan, A. "VO_2 based waveguide-mode plasmonic nano-gratings for optical switching", *Optics Express*, 23(5), 5822-5849, 2015. https://doi.org/10.1364/OE.23.005822

[2] Joushaghani, A. *et al.* "Sub-volt broadband hybrid plasmonic-vanadium dioxide switches", *Applied Physics Letters*, 102, 061101, 2013. https://doi.org/10.1063/1.4790834

[3] Mandal, P., Mohan, S., Sharma, S., and Goyat, M. S. "Broadband multi-resonant circular dichroism in metal-VO_2 hybrid dagger-like plasmonic structure for switching application", *Photonics and Nanostructures - Fundamentals and Applications*, 37, 100735, 2019. https://doi.org/10.1016/j.photonics.2019.100735

[4] Sun, M. *et al.* "A photonic switch based on a hybrid combination of metallic nanoholes and phase-change vanadium dioxide", *Scientific Reports*, 8, 11106, 2018. https://doi.org/10.1038/s41598-018-29476-6

[5] Guo, P. *et al.* "Conformal coating of a phase change material on ordered plasmonic nanorod arrays for broadband all-optical switching", *ACS Nano*, 11(1), 693-701, 2016. https://doi.org/10.1021/acsnano.6b07042

[6] Schalch, J. S. *et al.* "Broadband electrically tunable VO_2-metamaterial terahertz switch with suppressed reflection", *Microwave and Optical Technology Letters*, 62, 2782-2790, 2020. https://doi.org/10.1002/mop.32354

[7] Han, C., Parrott, E. P. J., Humbert, G., Crunteanu, A., and MacPherson, E. P. "Broadband modulation of terahertz waves through electrically driven hybrid bowtie antenna-VO_2 devices", *Scientific Reports*, 7, 12725, 2017. https://doi.org/10.1038/s41598-017-13085-w

[8] Chai, Z. *et al.* "Ultrafast all-optical switching", *Advanced Optical Materials*, 5, 1600665, 2017. https://doi.org/10.1002/adom.201600665

[9] Davis, T. J., Gomez, D. E., and Roberts, A. "Plasmonic circuits for manipulating optical information", *Nanophotonics*, 6(3), 543-559, 2016. https://doi.org/10.1515/nanoph-2016-0131

[10] Imura, K. *et al.* "Plasmon modes in single gold nanodiscs", *Optics Express*, 22(10), 12189-12199, 2014. https://doi.org/10.1364/OE.22.012189

[11] Hassan, N. A., and Hashim, A. M. "The effect of size of Au nanodisc on the localized surface plasmon resonance simulated using finite-difference time-domain (FDTD) method", *Materials Today: Proceedings*, 7(2), 607-611, 2019. https://doi.org/10.1016/j.matpr.2018.12.014

[12] Maier, S. A. *Plasmonics: Fundamentals and applications*. Springer, 2007. ISBN: 9780387331508. https://doi.org/10.1007/0-387-37825-1

[13] Cueff, S. *et al.* "VO_2 nanophotonics", *APL Photonics*, 5(11), 110901, 2020. https://doi.org/10.1063/5.0028093

[14] Liu, M., Li, X., Karuturi, S. K., Tok, A. I. Y., and Fan, H. J. *et al.* "Atomic layer deposition for nanofabrication and interface engineering", *Nanoscale*, 4, 1522-1528, 2012. https://doi.org/10.1039/C2NR11875K

[15] Kasani, S., Zheng, P., Bright, J., and Wu, N. "Tunable visible-light surface plasmon resonance of molybdenum oxide thin films fabricated by E-beam evaporation", *ACS Applied Electronic Materials*, 1(11), 2389-2395, 2019. https://doi.org/10.1021/acsaelm.9b00555

[16] Kim, D. H., and Kwok, H. S. "Pulsed laser deposition of VO_2 thin film", *Applied Physics Letters*, 65(25), 3188, 1994. https://doi.org/10.1063/1.112476

[17] Petti, L. *et al.* "A plasmonic nanostructure fabricated by electron beam lithography as a sensitive and highly homogeneous SERS substrate for bio-sensing applications",

Vibrational Spectroscopy, 82, 22-30, 2016. https://doi.org/10.1016/j.vibspec.2015.11.007

[18] He, S., Tian, R., Wu, W., Li, W. D., and Wang, D. "Helium-ion-beam nanofabrication: extreme processes and applications", *International Journal of Extreme Manufacturing*, 3(1), 012001, 2020. https://doi.org/10.1088/2631-7990/abc673

[19] Papaioannou, S. *et al.* "Active plasmonics in WDM traffic switching applications", *Scientific Reports*, 2, 652, 2012. https://doi.org/10.1038/srep00652

[20] Kartalopoulos, S. V. *Free space optical networks for ultra-broad band services*. Wiley-IEEE Press, 2011. ISBN: 978-0-470-64775-2

[21] Lu, Y. *et al.* "Triple functional shared channel in WDM PON by orthogonal modulation and network coding", *Optics Communications*, 336, 103-105, 2015. https://doi.org/10.1016/j.optcom.2014.09.070

[22] Lassiter, J. B. "Plasmonic waveguide modes of film-coupled metallic nanocubes", *Nano Letters*, 13(12), 5866-5872, 2013. https://doi.org/10.1021/nl402660s

[23] Gomez, D. E. *et al.* "The dark side of plasmonics", *Nano Letters*, 13(8), 3722-3728, 2013. https://doi.org/10.1021/nl401656e

[24] Parramon, J. S., and Bosch, S. "Dark modes and Fano resonances in plasmonic clusters excited by cylindrical vector beams", *ACS Nano*, 6(9), 8415-8423, 2012. https://doi.org/10.1021/nn303243p

[25] Schmidt, F. P. *et al.* "Dark plasmonic breathing modes in silver nanodiscs", *Nano Letters*, 12(11), 5780-5783, 2012. https://doi.org/10.1021/nl3030938

[26] Schertz, F. *et al.* "Near field of strongly coupled plasmons: Uncovering dark modes", *Nano Letters*, 12(4), 1885-1890, 2012. https://doi.org/10.1021/nl204277y

[27] Downing, C. A., and Weick, G. "Plasmonic modes in cylindrical nanoparticles and dimers", *Proceedings of the Royal Society A*, 476(2244), 20200530, 2020. https://doi.org/10.1098/rspa.2020.0530

[28] Huang, Y. "Hybridized plasmon modes and near-field enhancement of metallic nanoparticle-dimer on a mirror", *Scientific Reports*, 6, 30011, 2016. https://doi.org/10.1038/srep30011

CHAPTER 5

VO_2 BASED POLARIZATION-INDEPENDENT DUAL-WAVELENGTH PLASMONIC SWITCHES USING U AND C SHAPED NANOSTRUCTURES

5.0 Chapter Overview

Vanadium dioxide (VO_2) based polarization-independent dual-wavelength plasmonic switches using a periodic combination of U and C shaped gold nanostructures on a gold coated silicon dioxide (SiO_2) substrate with a thin VO_2 film as spacer between the nanostructures and the underlying substrate are proposed in this chapter. A spatial offset between the two nanostructures is taken such that high switching efficiency is obtained simultaneously at two wavelengths for all polarization angles of incident light. The switching mechanism is based on the transformation of the phase change material, VO_2, from its monoclinic semiconductor state to its tetragonal metal state when exposed to an external stimulus. This transformation leads to a significant change in the optical behavior of the proposed switch, leading to an effective transition from ON to OFF state. Finite difference time domain (FDTD) modelling shows that the proposed switches are capable of achieving a high extinction ratio of ~ 20 dB at two wavelengths — 1560 nm and 2130 nm — for incident light with any polarization angle. To demonstrate the spectral tunability of switching wavelengths, the optimization of the geometrical parameters is also carried out. These switches can be employed in telecommunication networks, optical communications, and integrated photonic circuits.

5.1 Motivation

Many VO_2 based plasmonic switches have been developed in the past, however, there have been limited reports of plasmonic switches showing multi-wavelength switching operation (i.e., simultaneous switching operation at more than one wavelength) as well as polarization-independent switching (i.e., same switching efficiency at any polarization angle of incident light). Multi-wavelength switching is important as a single switch can operate at multiple wavelengths with almost the same switching efficiency, thus, eliminating the need of different switches for different operational wavelengths. In addition, polarization independence allows the switch to be used with un-polarized light, thus alleviating the need to employ a polarizer. Among the few reports of multi-wavelength switching in the past, Rashidi *et al.* [1] proposed switchable VO_2 embedded photonic crystals that displayed six resonant peaks with absorption ~ 0.6 in the near-infrared regime. Sharma *et al.* [2] proposed gold nano-gratings coated with VO_2 that exhibited a maximum differential reflectance of ~ 41%. In addition, single wavelength polarization independence has been proposed by Long *et al.* [3] using a VO_2 metasurface that exhibited a high emittance of ~ 0.95 at 5 μm for multiple polarization angles from 0° to 180°. However, it must be noted that in all these previous reports, both polarization-independent and multi-wavelength switching

has not been reported simultaneously. In addition, for the few reports on multi-wavelength switching, the extinction ratios for the switches have remained well below 15 dB.

5.2 Introduction

In this chapter, VO_2 based polarization-independent and dual-wavelength plasmonic switches using a periodic combination of U and C shaped gold nanostructures on a gold coated SiO_2 substrate with a thin VO_2 film spacer between the nanostructures and the underlying plasmonic substrate are proposed (See Fig. 5.1(a)). The U and C shaped nanopillars are placed on the underlying substrate such that there is a spatial offset between them (See Fig. 5.1(a)). The spatial offset is defined as the distance between the axis passing through the center of U shaped nanostructure (a_u) and the axis passing through the center of C shaped nanostructure (a_c). It is well known that when three nanopillars are arranged in a U shaped nanostructure, two plasmonic modes — a short wavelength mode and a long wavelength mode — are generated when the incident light is X-polarized (i.e., polarization angle 'ϕ' = 0°), whereas a single plasmonic mode is generated when the incident light is Y-polarized (i.e., polarization angle 'ϕ' = 90°) [4].

For the C shaped nanostructure, this situation becomes inverted, with two plasmonic modes being excited for Y-polarized light and one plasmonic mode being excited for X-polarized light. However, when both U and C shaped nanostructures are placed together to form a U-C type plasmonic switch, two plasmonic modes — a short wavelength mode and a long wavelength mode — are generated for both X- and Y-polarized incident light. Due to the excitation of two plasmonic modes at both polarization angles of incident light, these U-C type plasmonic nanostructures are employed in this chapter to realize an efficient polarization-independent multi-wavelength switch by placing them on a VO_2 coated plasmonic substrate as shown in Fig. 5.1. As VO_2 changes from its monoclinic semiconductor state to tetragonal metal state while exposed to an external stimulus (See Fig. 5.1(a)), it undergoes a change in its refractive index, leading to a significant change in the overall plasmonic response of the switch. The transformation of VO_2 leads to a change in the plasmon resonance wavelengths of both the plasmonic modes, thus leading to efficient simultaneous switching at two wavelengths. The switching ability of the proposed plasmonic switches is analyzed in terms of extinction ratio (ER) — which is the ratio of the reflectance from the switch when VO_2 is in its metal state (i.e., OFF state) to the reflectance from the switch when VO_2 is in its semiconductor state (i.e., ON state). The proposed U-C type plasmonic switches exhibit an ER of ~ 20 dB simultaneously at two wavelengths — at ~ 1560 nm and at ~ 2130 nm — for a linearly polarized incident light with any polarization angle from 0° to 90° as shown in Fig. 5.1(b). The tunability of the wavelengths of maximum ER is also demonstrated in this chapter by optimizing the various geometric parameters of the proposed switches such as the gap 'G' between the adjacent U and C shaped nanostructures, the thickness of VO_2 film 't', and the aspect ratio 'AR' — which is the ratio of the length 'L' of the nanopillars to the width 'W' of the nanopillars (See Fig. 5.1(a)).

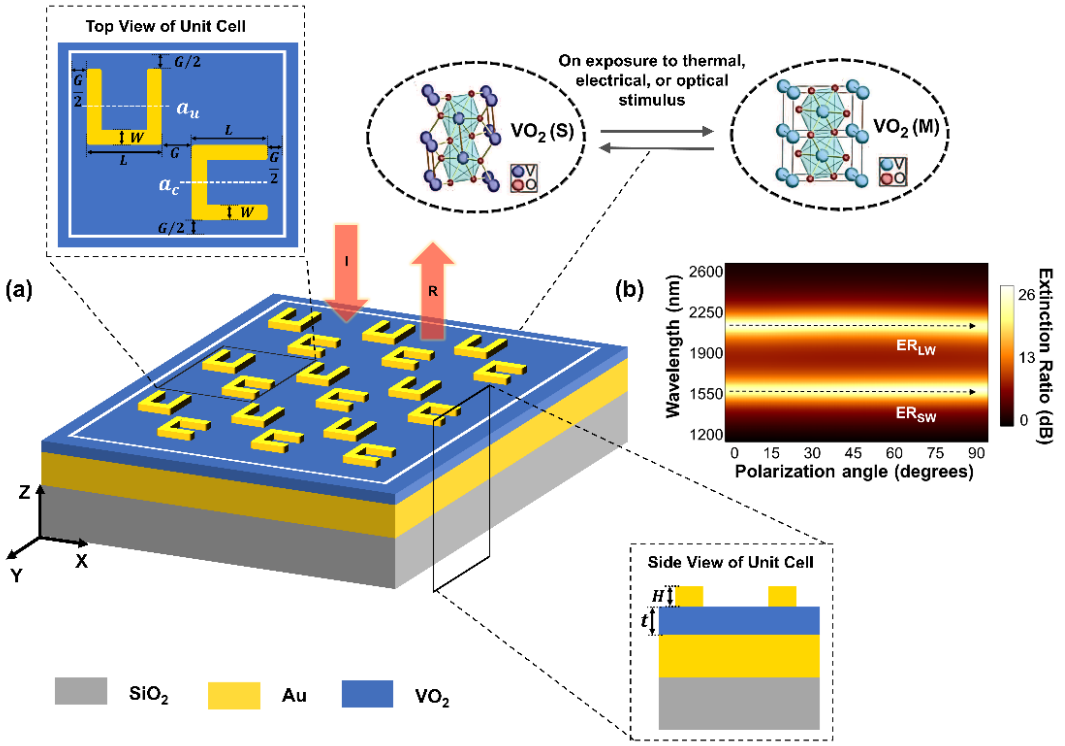

Fig. 5.1 Schematic and working principle of the proposed U-C type switch. **(a)** Schematic of the VO_2 based polarization-independent and dual-wavelength U-C type plasmonic switch using a periodic combination of U and C shaped gold nanopillars on a gold coated SiO_2 substrate with a thin VO_2 film spaced between the nanostructures and the underneath plasmonic substrate. The geometrical parameters such as length '*L*', width '*W*', height '*H*', spatial offset '$|a_u - a_c|$', gap '*G*', and thickness of VO_2 film '*t*' are denoted in the top and side views of the unit cell. The phase transition mechanism of VO_2 is also depicted. **(b)** Colormap showing the effect of varying the polarization angle of the incident light on the extinction ratio spectra of the proposed plasmonic switch.

5.3 Numerical Methods

The 3D electromagnetic modelling of the proposed plasmonic switches has been carried out by using a commercial software – Ansys Lumerical Finite Difference Time Domain (FDTD) Solver – to illustrate the polarization-independent and dual-wavelength behavior of the proposed plasmonic switches. To illuminate the proposed plasmonic switches, a linearly polarized plane wave source with incident electric field (E_0) of 1 Vm^{-1} has been used. The electric field enhancement at a point is calculated as the ratio of electric field at the point (E) and the incident electric field (E_0). The simulation boundary conditions have been chosen such that the U and C shaped nanostructures are periodic in the X and Y directions, whereas perfectly matched layers (PML) have been employed in the Z direction. Further, a uniform mesh size of 1 nm has been applied on the entire simulation region in all the X, Y, and Z directions. The edges of the nanostructures are designed with a rounding radius of 4 nm to accommodate the practical fabrication anomalies [5]. The material constants of gold, semiconductor VO_2, and metal VO_2 have been taken according to the Lorentz-Drude model (See Appendix-II, Dielectric Constants of Materials).

5.4 Results and Discussion

FDTD modelling is employed to illustrate the polarization-independent and dual-wavelength behavior of the proposed U-C type plasmonic switches. The proposed switches can simultaneously operate at two different wavelengths — short wavelength and long wavelength — with any polarization angle of incident light. The comprehensive performance analysis of the proposed switches is computed in terms of extinction ratio (ER) as calculated from Eq. 5.1 given below:

$$ER = 10 * log_{10}\left(\frac{R_M(\lambda)}{R_S(\lambda)}\right) \quad dB \tag{5.1}$$

where, $R_M(\lambda)$ is the reflectance from the switch when VO_2 is in its metal state (i.e., OFF state) and $R_S(\lambda)$ is the reflectance from the switch when VO_2 is in its semiconductor state (i.e., ON state).

In order to understand the working principles of the U-C type plasmonic switch proposed in this chapter, a preliminary discussion of the building units of the proposed switch, i.e., the polarization dependent U shaped and C shaped plasmonic switches is necessary. The U shaped or the C shaped nanostructures can be viewed as two parallel nanopillars connected through a bottom bridging nanopillar. Fig. 5.2(a) shows a schematic of the VO_2 based periodic U shaped plasmonic switch, where the length of U shaped nanopillars '*L*', the width of U shaped nanopillars '*W*', the height of U shaped nanopillars '*H*', the gap '*G*' between adjacent U shaped nanostructures, and the thickness of VO_2 film '*t*' is taken to be 100 nm, 20 nm, 50 nm, 30 nm, and 100 nm, respectively. Fig. 5.2(b) shows the reflectance spectra of U shaped plasmonic switch with VO_2 in its semiconductor and metal states for X-polarized ('ϕ' = 0°) and Y-polarized ('ϕ' = 90°) incident light. It can be observed from Fig. 5.2(b) that when X-polarized light is incident on the U-shaped nanostructures with VO_2 in its semiconductor state (i.e., VO_2 (S)), two longitudinal modes are primarily excited at wavelengths of 1320 nm and 2630 nm, respectively. These two modes can be well explained by the plasmon hybridization theory [6]. With smaller values of gap between the adjacent U-shaped nanopillars, the hybridization of the elementary plasmons of the U shaped nanopillars results in the splitting of the dipolar mode into a bonding mode (longer wavelength mode), and an antibonding mode (shorter wavelength mode). Further, as the VO_2 film is switched from its semiconductor state to its metal state, a blue-shift in the plasmon resonance wavelength is observed such that the plasmonic modes shift to 790 nm and 1290 nm, respectively. This shift in the plasmonic modes supported by the U-shaped nanostructures upon phase transformation of the underlying VO_2 layer can be understood by effectively modelling the proposed switch as a U shaped nanopillar array placed on top of a substrate with an effective dielectric permittivity, ε_{eff}. As a thick gold layer is present on top of the SiO_2 layer, the substrate can be treated equivalent to a layer of VO_2 on top of a gold substrate. The effective medium constants can then be modelled using the well-known Bruggeman's effective medium approximation [7]. The calculation of the effective permittivity of the substrate is shown in Appendix-II (See Appendix-II, Dielectric Constants of Materials). It can be observed from the effective dielectric constants shown in Fig.

II.1(d) (See Appendix-II, Dielectric Constants of Materials) that as the VO_2 layer transforms from its semiconductor state to its metal state, there is a decrease in the real part of the dielectric permittivity of the effective substrate under the U shaped nanopillars, thus leading to a blue-shift of the plasmon resonance wavelengths [8]. Further, it should be noted that the imaginary part of the effective dielectric permittivity for the VO_2-Au substrate increases as VO_2 transforms from a semiconductor state to its metal state, thus leading to a higher loss which can be seen as the reduction in the magnitude of plasmon coupling leading to a smaller dip in the reflectance spectra of the switch with VO_2 (M). This case, with VO_2 (M) can also be explained by a parallel theory based on plasmon hybridization and charge transfer [9]. In such cases where metal nanostructures capable of plasmon hybridization are present on a metallic substrate (VO_2 (M) – Au substrate), the incident light induces a strong coupling between the U and C nanopillars giving rise to a screened bonding dimer (SBD) plasmon resonance at 790 nm with a strong dipolar character. In addition, for such metal nanostructure on metal systems, the presence of the conductive surface (VO_2 (M) on Au) underneath the U shaped nanopillars, induces a net charge transfer between the nanopillars often leading to a charge transfer mode (CTP) at a higher wavelength. However, due to substrate screening, electric dipole moment of the CTP mode (~ 1290 nm) is often screened, making it sub-radiant and hidden within the spectra. On the other hand, it can also be observed from Fig. 5.2(b) that when the incident light is polarized in the Y direction, only one longitudinal mode is excited at wavelength of 2100 nm with VO_2 (S). Similar to the X-polarized case, when the VO_2 film is switched from its semiconductor state to its metal state, this plasmonic mode is blue-shifted to 1040 nm. It must be noted that the dips corresponding to the longitudinal modes in the reflectance spectra of the U shaped plasmonic switch with VO_2 (S) appear as peaks in the ER spectra of the switch (See Fig. 5.2(c)). It must also be noted that the plasmonic switch can operate in both the ER regimes, i.e., the positive ER regime where $R_M(\lambda) > R_S(\lambda)$ and the negative ER regime where $R_M(\lambda) < R_S(\lambda)$. However, only the positive ER regime is chosen to carry out the comprehensive analysis of the switching performance of all the proposed plasmonic switches in this chapter as this regime overlaps with the conventionally employed and futuristic communication bands.

Fig. 5.2(c) shows that for an X-polarized light, maximum ER is achieved at two distinct wavelengths – an ER of ~ 8 dB at a short wavelength ($ER_{X\text{-}SW}$) of 1320 nm and an ER of ~ 21 dB at a long wavelength ($ER_{X\text{-}LW}$) of 2630 nm. In contrast, for a Y-polarized light, maximum ER of ~ 6 dB is observed at a single wavelength (ER_Y) of 2100 nm. It must be noted that although switching is obtained at two different wavelengths for X-polarized light, this switch cannot truly be called a dual-wavelength switch because the magnitude of ER at both the wavelengths (i.e., ~ 8 dB at 1320 nm and ~ 21 dB at 2630 nm) is not equal. The charge density profiles for the U shaped plasmonic switch, with both X- and Y-polarized light, are shown in Fig. 5.2(d) at the resonance wavelengths of the reflectance spectra of the switch with VO_2 (S) and VO_2 (M). Further, to show the ON and OFF states of the switch, the electric field profiles of the U shaped plasmonic switch with VO_2 (S) and VO_2 (M) are shown in Fig. 5.2(e) at wavelengths corresponding to the peaks of the ER spectra. With VO_2 (S), the field profile at 1320 nm shows the excitation of a longitudinal plasmon mode with a pin like

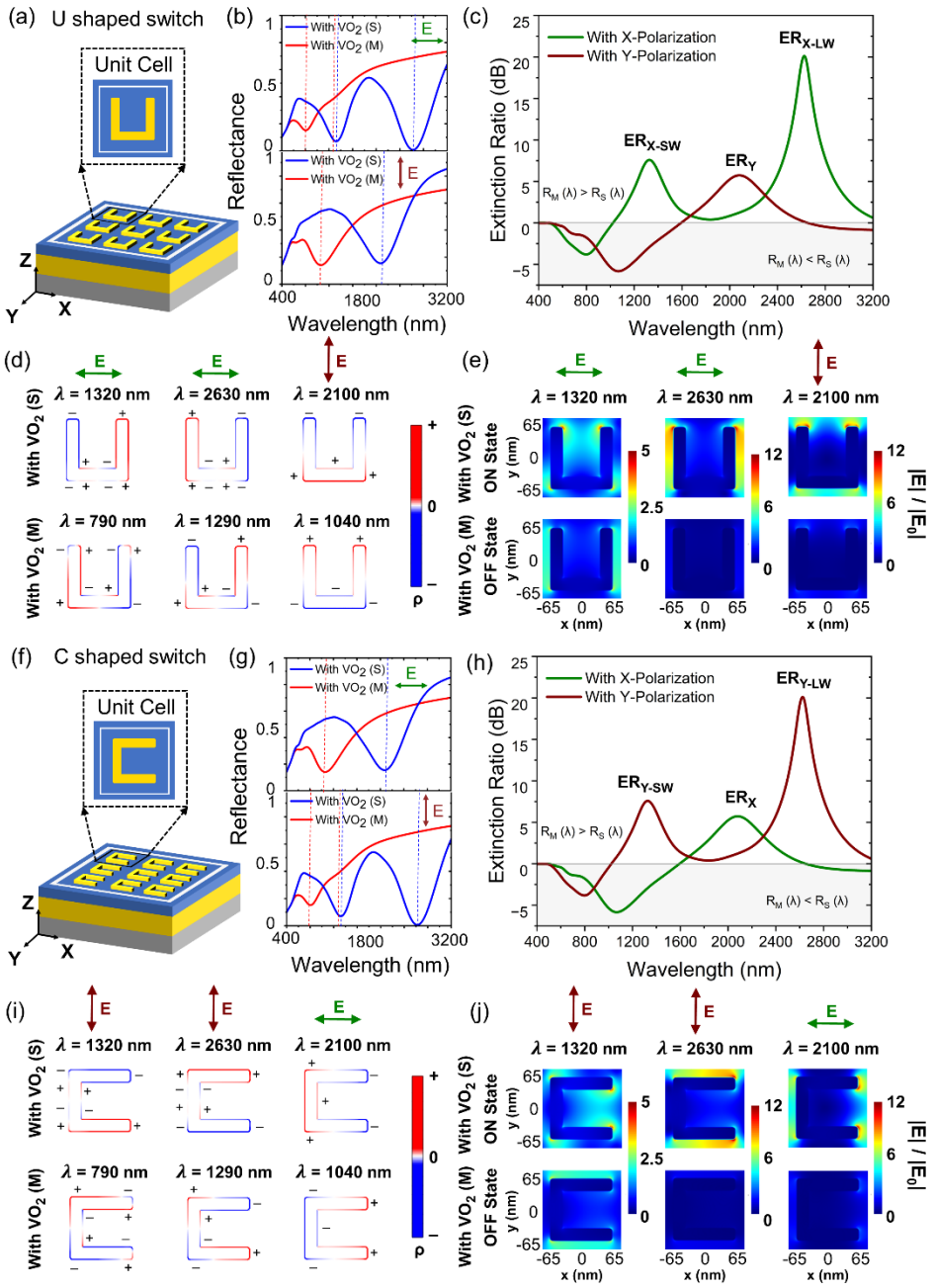

Fig. 5.2 U and C shaped nanopillar based switches. **(a)** Schematic of VO_2 based U shaped plasmonic switch consisting of periodic U shaped gold nanopillars on gold coated SiO_2 substrate. **(b)** Reflectance spectra, **(c)** extinction ratio spectra, **(d)** charge density profiles, and **(e)** electric field profiles of U shaped plasmonic switch with VO_2 in its semiconductor and metal states for X- and Y-polarized incident light. **(f)** Schematic of VO_2 based C shaped plasmonic switch consisting of periodic C shaped gold nanopillars on gold coated SiO_2 substrate. **(g)** Reflectance spectra, **(h)** extinction ratio spectra, **(i)** charge density profiles, and **(j)** electric field profiles of C shaped plasmonic switch with VO_2 in its semiconductor and metal states for X- and Y-polarized incident light. The length '*L*', width '*W*', and height '*H*' of the U and C shaped nanopillars is taken to be 100 nm, 20 nm, and 50 nm, respectively. The gap '*G*' between adjacent nanostructures and the thickness of VO_2 film '*t*' is taken as 30 nm and 100 nm, respectively.

E-field distribution in the vertical nanopillars of the U shaped nanostructures such that there is a significant E-field coupling between the two vertical nanopillars. On the contrary, the field profile of the U shaped switch with VO_2 (M) at the 1320 nm wavelength shows an OFF state as almost negligible field enhancement is observed. In addition, the field profile at 2630 nm, with VO_2 (S), shows another longitudinal plasmon mode such that strong E-field coupling occurs between the two vertical nanopillars of adjacent U shaped nanostructures instead of the coupling between the nanopillars of the same U shaped nanostructure. The field profile of the U shaped switch, with VO_2 (M), at 2630 nm shows an OFF state. When the incident light is polarized in the Y direction, a longitudinal plasmon mode at ER_Y (i.e., at 2100 nm) is excited in the vertical nanopillars such that strong field coupling occurs along the Y direction between the adjacent U shaped nanostructures placed vertically as an array. There is no coupling between the U shaped nanostructures along the X direction for this mode. The E-field profile with VO_2 (M) at 2100 nm shows an OFF state of the switch.

Additionally, as expected, it can be observed from Figs. 5.2(f-j) that as the orientation of the U shaped plasmonic switch is changed to a C shaped plasmonic switch, the reflectance spectra as well as the ER spectra get reversed for the X-polarized light and Y-polarized light as compared to that of the U shaped plasmonic switch. Thus, two plasmonic modes are excited at $ER_{Y\text{-}SW}$ (i.e., at 1320 nm) and $ER_{Y\text{-}LW}$ (i.e., at 2630 nm) for Y-polarized light and one plasmonic mode is excited at ER_X (i.e., 2100 nm) for X-polarized light, when VO_2 is in its semiconductor state. Hence, neither the U shaped nor the C shaped plasmonic switches alone are truly dual-wavelength due to significantly different ERs being obtained at different wavelengths. Moreover, both these switches are heavily polarization dependent with a very different switching behavior for X- and Y-polarization.

Therefore, to realize a polarization-independent plasmonic switch, a hybrid combination of U shaped nanopillars and C shaped nanopillars to form a U-C type plasmonic switch is used (See Fig. 5.3). In addition, to make these switches truly dual-wavelength, i.e., to obtain similar ER at both wavelengths of switching (ER at short wavelength (ER_{SW}) and ER at long wavelength (ER_{LW})), an extensive analysis of the spatial offset between the U and C shaped nanostructures is also carried out. The spatial offset is taken as the distance between the axis passing through the center of U shaped nanostructure (a_u) and the axis passing through the center of C shaped nanostructure (a_c). A comprehensive analysis of the ER spectra of the proposed U-C type plasmonic switches with varying spatial offsets is shown in Fig. 5.3. The length of nanopillars of U and C shaped nanostructures '*L*', the width of nanopillars '*W*', the height of nanopillars '*H*', the gap '*G*' between adjacent U and C shaped nanostructures, and the thickness of VO_2 film '*t*' is taken to be 100 nm, 20 nm, 50 nm, 30 nm, and 100 nm, respectively. Fig. 5.3(a) shows the schematic of a unit cell of VO_2 based U-C type plasmonic switch consisting of periodic U and C shaped gold nanostructures with zero spatial offset, i.e., no offset between a_u and a_c. It can be observed from Fig. 5.3(b) that there are two dips in the reflectance spectra of the U-C (Offset = 0) type plasmonic switch with VO_2 (S) for both X- and Y-polarized light, which are expressed as the peaks in ER spectra. However, it can be noted from the ER spectra shown in Fig. 5.3(c)

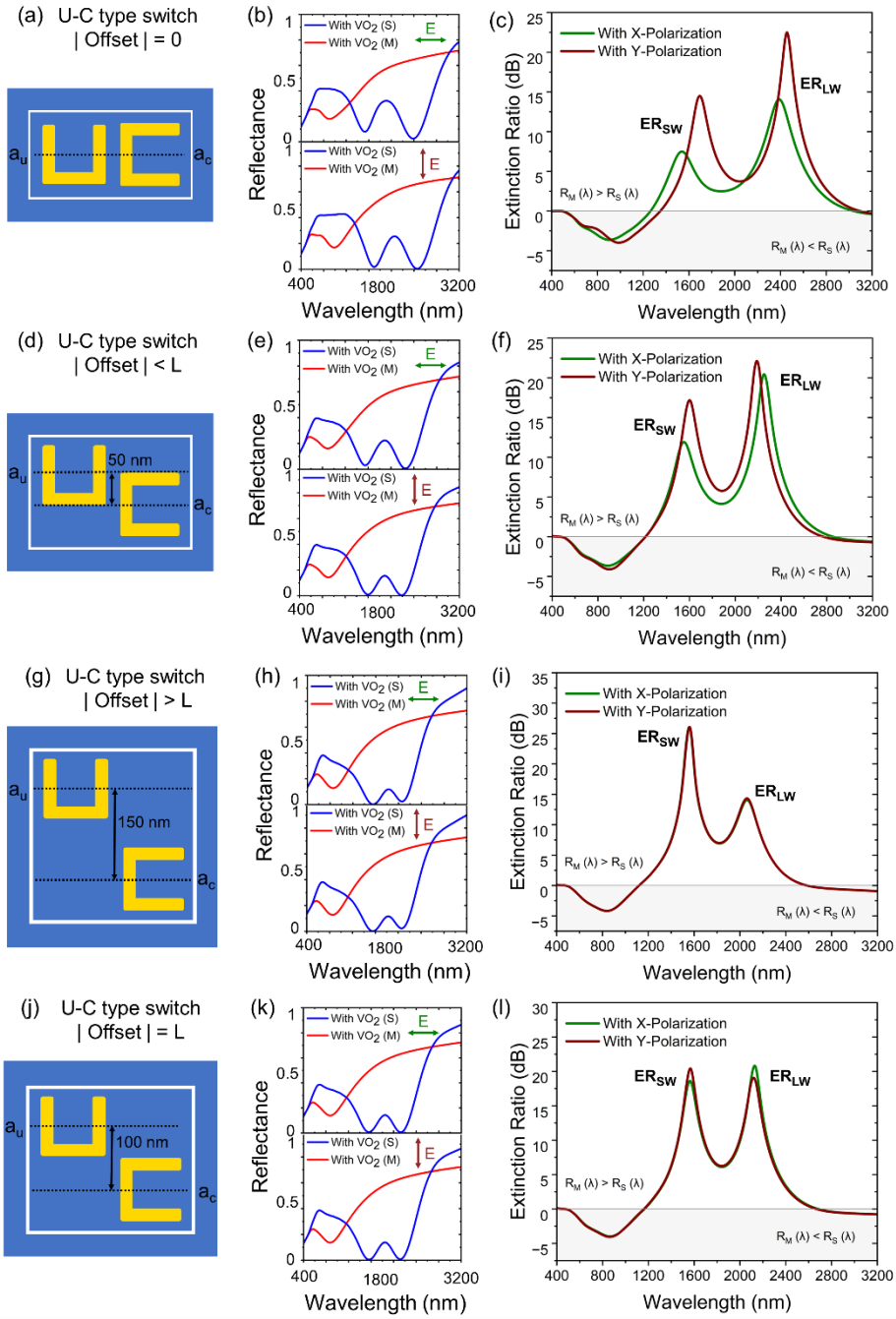

Fig. 5.3 U-C shaped nanopillar based switches with different offsets. **(a)** Schematic, **(b)** reflectance spectra, and **(c)** extinction ratio spectra of U-C (Offset = 0) type plasmonic switch for X- and Y-polarized incident light. **(d)** Schematic, **(e)** reflectance spectra, and **(f)** extinction ratio spectra of U-C (Offset = 50) type plasmonic switch for X- and Y-polarized incident light. **(g)** Schematic, **(h)** reflectance spectra, and **(i)** extinction ratio spectra of U-C (Offset = 150) type plasmonic switch for X- and Y-polarized incident light. **(j)** Schematic, **(k)** reflectance spectra, and **(l)** extinction ratio spectra of U-C (Offset = 100) type plasmonic switch for X- and Y-polarized incident light. The length '*L*', width '*W*', and height '*H*' of the U and C shaped nanopillars is taken to be 100 nm, 20 nm, and 50 nm, respectively. The gap '*G*' between adjacent nanostructures and the thickness of VO_2 film '*t*' is taken as 30 nm and 100 nm, respectively.

that the ER is different at the short wavelength (ER_{SW}) and long wavelength (ER_{LW}) for X-polarized (ER of ~ 7.5 dB at 1535 nm and ER of ~ 14.5 dB at 2385 nm) and Y-polarized (ER of ~ 15 dB at 1700 nm and ER of ~ 24 dB at 2455 nm) light.

As shown in Figs. 5.3(d-f), on introducing a spatial offset which is less than the length of the nanopillars '*L*' (i.e., 50 nm offset between a_u and a_c), it can be observed from the ER spectra that an ER of ~ 12 dB at 1550 nm and an ER of ~ 21.5 dB at 2250 nm is obtained with X-polarized light and an ER of ~ 18 dB at 1600 nm and an ER of ~ 23 dB at 2190 nm is obtained with a Y-polarized light. It must be noted that although the switching performance is significantly better in this case, it is still neither truly polarization-independent nor truly dual-wavelength switchable. When the spatial offset is increased beyond the length of the nanopillars '*L*' (i.e., 150 nm offset between a_u and a_c) as shown in Figs. 5.3(g-i), the switch becomes polarization-independent. For both X- and Y-polarized light, an ER of ~ 28 dB at 1565 nm and an ER of ~ 14.5 dB at 2065 nm is obtained. Although this spatial offset results in polarization-independence, this switch is not truly dual-wavelength due to the different ERs at the two wavelengths of switching. Hence, to make the U-C type plasmonic switch polarization-independent as well as dual-wavelength, the spatial offset between the U and C shaped nanostructures is set equal to the length of the nanopillars '*L*' (i.e., 100 nm offset between a_u and a_c) as shown in Figs. 5.3(j-l). It can be observed from the ER spectra of the plasmonic switch with a spatial offset equal to length '*L*' (See Fig. 5.3(l)) that that the switching performance is almost equal at both the wavelengths — i.e., an ER of ~ 20 dB at 1560 nm and 2130 nm — for both X- and Y- polarized light. Hence, U-C type plasmonic switches with the spatial offset equal to length '*L*' have been proposed to realize truly dual-wavelength polarization-independent active switching. In addition, it must be noted that plasmonic switches capable of achieving polarization independence with a high ER of ~ 20 dB at two different telecommunication wavelengths of 1560 nm and 2130 nm have not been reported so far. Further, it should be noted that 1560 nm lies in the low loss C-band which is most widely used in optical communication networks such as free space optics (FSO) and dense wavelength division multiplexing (DWDM). Moreover, with the advent of the 2000 nm waveband technologies such as — edge-couple photodetectors based on InGaAs, thulium-doped fiber amplifiers (TDFA) and laser injection locking, the 2000 nm waveband has recently been suggested for futuristic optical communications [10]. Hence, the switches proposed in this chapter could potentially be utilized for both the conventional C-band (1530-1565 nm) and for the futuristic 2000 nm band as they offer simultaneous high ER at 1560 nm and at 2130 nm, with a polarization-independent operation. The switching performance of the proposed U-C type plasmonic switches with variable spatial offsets is also tabulated in Table 5.1. The switching behavior of another polarization-independent design based on four symmetrically rotated U shaped nanopillars [11] is also shown in Fig. 5.4 to highlight the advantage of introducing spatial offset in designing truly dual-wavelength plasmonic switches proposed in this chapter. In addition, a comparison of our work with dual-wavelength or polarization-independent VO_2 based plasmonic switches is given in Table 5.2.

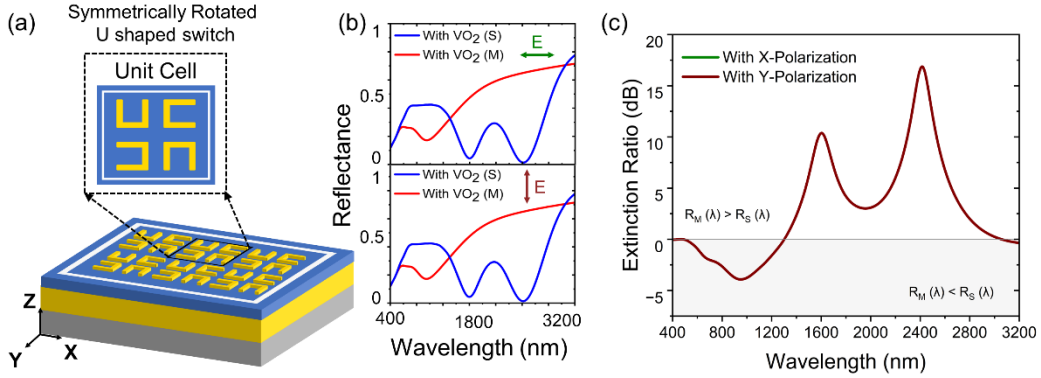

Fig. 5.4 Symmetrically rotated U shaped plasmonic switch. **(a)** Schematic of VO_2 based plasmonic switch using a periodic combination of symmetrically rotated U shaped gold nanopillars on a gold coated SiO_2 substrate with a thin film of VO_2 as a spacer between the nanostructures and the underlying plasmonic substrate [11]. **(b)** Reflectance spectra and **(c)** extinction ratio spectra of symmetrically rotated U shaped plasmonic switch with X- and Y-polarized incident light. The length '*L*', width '*W*', and height '*H*' of the U shaped nanopillars is taken to be 100 nm, 20 nm, and 50 nm, respectively. The gap '*G*' between adjacent nanostructures and the thickness of VO_2 film '*t*' is taken as 30 nm and 100 nm, respectively.

Table 5.1 Switching performance of the proposed U-C type plasmonic switches with variable spatial offsets

Offset	**ER_{SW}**		**ER_{LW}**		**Polarization-independent**	**Dual-wavelength**
	$\phi = 0°$	**$\phi = 90°$**	**$\phi = 0°$**	**$\phi = 90°$**		
| Offset | = 0	7.5 dB at 1535 nm	15 dB at 1700 nm	14.5 dB at 2385 nm	24 dB at 2455 nm	–	–
| Offset | < *L*	12 dB at 1550 nm	18 dB at 1600 nm	21.5 dB at 2250 nm	23 dB at 2190 nm	–	–
| Offset | > *L*	28 dB at 1565 nm	28 dB at 1565 nm	14.5 dB at 2065 nm	14.5 dB at 2065 nm	Yes	–
| Offset | = *L*	19.5 dB at 1560 nm	21.5 dB at 1565 nm	22 dB at 2130 nm	19.5 dB at 2125 nm	Yes	Yes

A detailed analysis of the effect of polarization angle 'ϕ' on the U-C (Offset = *L*) type plasmonic switches is shown in Fig. 5.5. Fig. 5.5(a) shows the ER spectra for the proposed switch as the polarization angle of incident light 'ϕ' is varied from 0° to 90°. It can be observed from Fig. 5.5(a) that the ER spectra are almost the same at both the short wavelength mode (ER_{SW}) and the long wavelength mode (ER_{LW}) for all the polarization angles, with the maximum ER of ~ 20 dB simultaneously at two wavelengths — 1560 nm and 2130 nm. Fig. 5.5(b) shows the polar plot for ER of U-C (Offset = *L*) type plasmonic switches at short wavelength mode (1560 nm) and long wavelength mode (2130 nm) with polarization angles of incident light 'ϕ' being varied from 0° to 360°. It can be observed from Fig. 5.5(b) that the proposed switch gives almost the same switching performance for all the polarization angles, thus illustrating that the proposed switch is a polarization-independent as well as dual-wavelength plasmonic switch. Figs. 5.5(c-f) show the electric field enhancement profiles and the charge density profiles for the proposed U-C (Offset = *L*) type plasmonic switches with VO_2 in its semiconductor and metal states at the wavelengths of the highest ER, i.e.,

Table 5.2 Comparison of the proposed U-C type plasmonic switches with previous work in dual-wavelength or polarization-independent VO_2-based plasmonic switches

Ref.	Description of plasmonic switch	Figure of merit	Polarization-independent	Dual-wavelength
Rashidi *et al.* [1]	VO_2 embedded photonic crystals	Maximum Reconfigurable Absorption (Δ Absorption) ~ 0.6	No	Yes
Long *et al.* [3]	VO_2 metasurface based switch	Emittance of ~ 0.95	Yes	No
Pradhan *et al.* [12]	Gold micro-disks on VO_2 coated ITO substrate	Reflectivity change(ΔR): 13% to 89% at 6 μm, and 15% to 93% at 9.2 μm (Mid infrared)	No	Yes
Guo *et al.* [13]	2D periodic triple-layer Ag–VO_2–Ag cube array	Transmittance difference of more than one order of magnitude	No	Yes
Sharma *et al.* [2]	Gold nano-gratings coated with VO_2	Differential Reflectance ~ 41%	No	Yes
Our work	U-C type plasmonic switch	ER ~ 20 dB	Yes	Yes

at 1560 nm and 2130 nm, for X- and Y-polarized incident light. At a polarization angle of 0° for the incident light, Fig. 5.5(c) shows that, at a wavelength of 1560 nm, with VO_2 in its semiconductor state (ON state of the switch), $Mode_{SW}$ is excited in the U-C type plasmonic switch which consists of two modes excited in the U and C shaped nanostructures, respectively, with a weak coupling between them. The U shaped nanostructure exhibits a longitudinal mode LM I such that the E-field is localized between the two vertical arms of the U shaped nanostructure while the C shaped nanostructure supports a longitudinal mode LM II with a pin-like distribution of the field on the parallel arms of the C shaped nanostructure. With VO_2 in its metal state, however, the field enhancement is negligible at this wavelength, and hence the switch is in its OFF state. At a wavelength of 2130 nm, with VO_2 (S), $Mode_{LW}$ is excited in the U-C type plasmonic switch which is made up of two longitudinal modes — LM III and LM II (See Fig. 5.5(c)) — being excited in the U and C shaped nanostructure, respectively, with weak coupling between the two modes. With VO_2 (M), the switch exhibits negligible field enhancement at 2130 nm, hence signifying the OFF state of the switch. The charge density profiles for the U-C (Offset = L) type plasmonic switches are shown in Fig. 5.5(d) at wavelengths of 1560 nm and 2130 nm with the VO_2 in its semiconductor and metal states, respectively. These charge density profiles clearly show the excitation of mode $Mode_{SW}$ (consisting of mode LM I and mode LM II) at a wavelength of 1560 nm, and the excitation of mode $Mode_{LW}$ (consisting of mode LM III and mode LM II) at a wavelength of 2130 nm in these nanostructures, when VO_2 is in its semiconductor state. It may be noted that the charge density profiles at the wavelengths of maximum ER, i.e., 1560 nm and 2130 nm, for the switch when VO_2 is in its metal state do not correspond to the same modes with VO_2 (S) because

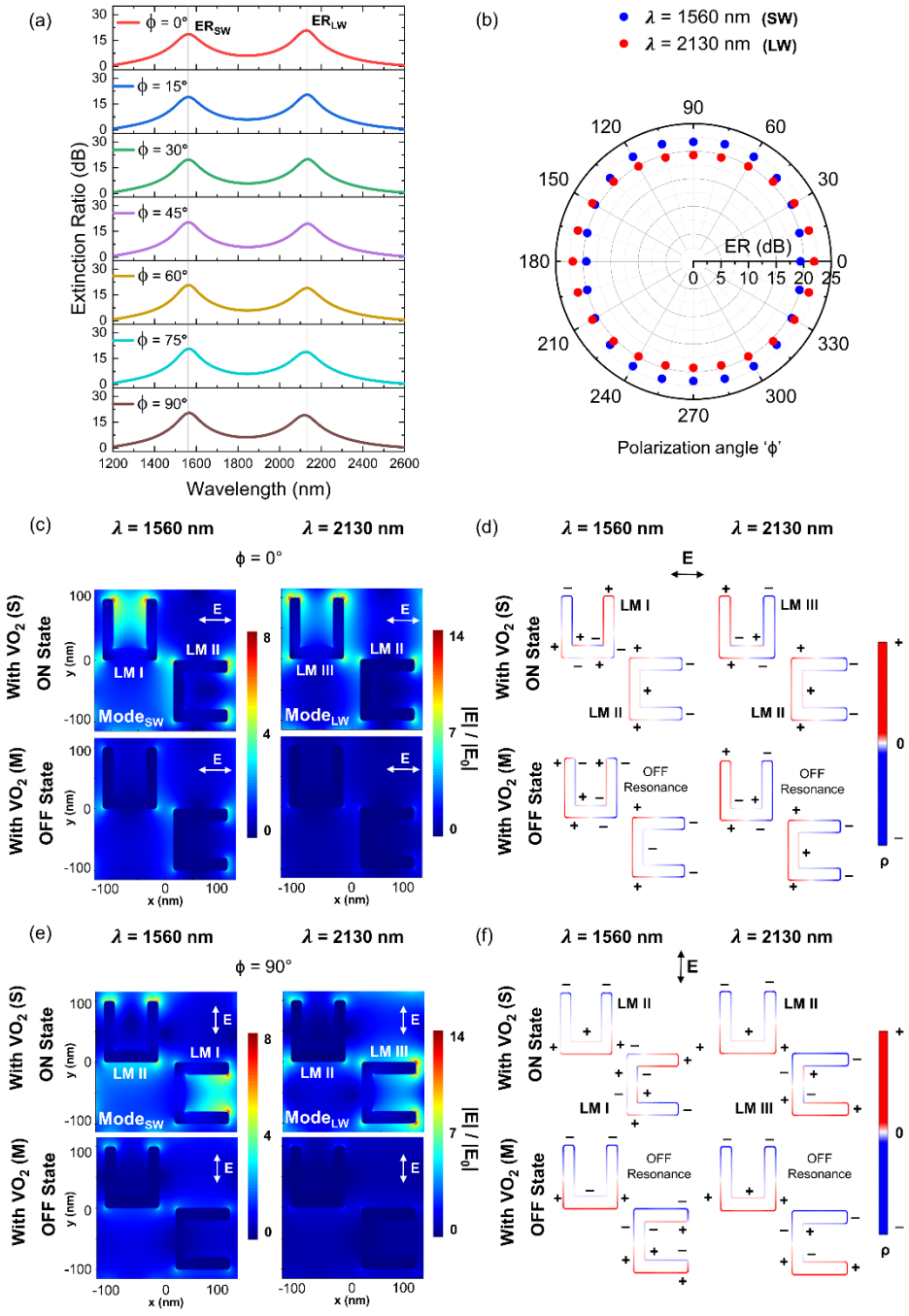

Fig. 5.5 Polarization independence in U-C (Offset = *L*) type plasmonic switches. **(a)** Extinction ratio spectra and **(b)** polar plot for U-C (Offset = *L*) type plasmonic switch with various polarization angles 'ϕ' of incident light at short wavelength mode (1560 nm) and long wavelength mode (2130 nm). Electric field profiles and charge density profiles of U-C (Offset = *L*) type plasmonic switch at short wavelength mode (1560 nm) and long wavelength mode (2130 nm) when VO_2 is in its semiconductor and metal states with polarization angle 'ϕ' being **(c, d)** 0° and **(e, f)** 90°, respectively. The length '*L*', width '*W*', and height '*H*' of the U and C shaped nanopillars is taken to be 100 nm, 20 nm, and 50 nm, respectively. The gap '*G*' between adjacent nanostructures and the thickness of VO_2 film '*t*' is taken as 30 nm and 100 nm, respectively.

the modes for the switch undergo a significant blue-shift (See Fig. 5.3(k)) when VO_2 transforms from semiconductor to a metal. The field enhancement profiles and the charge density profiles for the case when the polarization angle of the incident light is 90° are shown in Fig. 5.5(e) and Fig. 5.5(f), respectively. As expected, the modes excited in the U and C shaped nanostructures are reversed as compared to the case when the polarization angle of the incident light is 0°.

The switching performance of the proposed U-C (Offset = L) type plasmonic switch can be optimized by choosing the right value for the design parameters such as the gap 'G' between the U and C shaped nanostructures and the thickness of VO_2 film 't'. Further, the wavelengths of maximum ER can also be spectrally tuned by tweaking these geometrical parameters. Fig. 5.6(b) shows the effect of varying the thickness of VO_2 film on the reflectance spectra of the proposed switches with X-polarized light, for the case when VO_2 is in its semiconductor state. It can be seen from the inset of Fig. 5.6(b) that as the thickness of the underlying VO_2 film 't' is increased from 80 nm to 120 nm, there is a significant red-shift in the plasmon resonance wavelength for the $Mode_{SW}$ from 1425 nm to 1680 nm and for $Mode_{LW}$ from 2070 nm to 2230 nm. A similar red-shifting of the plasmon resonance wavelength is observed for the case when VO_2 is in its metal state, as shown in Fig. 5.6(c). It is well known that the plasmon resonance wavelength of a plasmonic nanostructure is strongly dependent on the substrate on which the nanostructure is present [14]. Thus, the effect of thickness of the VO_2 layer on the plasmonic modes of the U-C shaped nanopillars can be understood by effectively modelling the proposed switch as a U-C shaped nanopillar array placed on top of a substrate with an effective dielectric permittivity 'ε_{eff}'. As a thick gold layer is present on top of the SiO_2 layer, the substrate can be treated equivalent to a layer of VO_2 on top of a gold substrate. The effective medium constants can then be modelled using an effective medium approximation. For this analysis, the well-known Bruggeman's effective medium approximation [7] has been used to model the effective dielectric permittivity of the resulting substrate using the following equations:

$$f_{VO_2(S)}\left(\frac{\varepsilon_{VO_2(S)} - \varepsilon_{eff}}{\varepsilon_{VO_2(S)} + 2\varepsilon_{eff}}\right) + \left(1 - f_{VO_2(S)}\right)\left(\frac{\varepsilon_{Au} - \varepsilon_{eff}}{\varepsilon_{Au} + \varepsilon_{eff}}\right) = 0 \;\; ; \quad with\, VO_2\,(S) \tag{5.2}$$

$$f_{VO_2(M)}\left(\frac{\varepsilon_{VO_2(M)} - \varepsilon_{eff}}{\varepsilon_{VO_2(M)} + 2\varepsilon_{eff}}\right) + \left(1 - f_{VO_2(M)}\right)\left(\frac{\varepsilon_{Au} - \varepsilon_{eff}}{\varepsilon_{Au} + \varepsilon_{eff}}\right) = 0 \;\; ; \quad with\, VO_2\,(M) \tag{5.3}$$

where $\varepsilon_{VO_2(S)}$, $\varepsilon_{VO_2(M)}$, ε_{Au} and ε_{eff} are the wavelength dependent dielectric constants of VO_2 (S), VO_2 (M), gold and the modelled effective medium, respectively. The filling factor ($f_{VO_2(M)}$ or $f_{VO_2(S)}$), corresponds to the volume fraction of the VO_2 film. The real and imaginary parts of the modelled effective media have been calculated using the above equation using a mathematical solver for different thicknesses of the VO_2 layer, for the case when VO_2 is present in its semiconductor and metallic states, respectively, and are shown in Fig. 5.7.

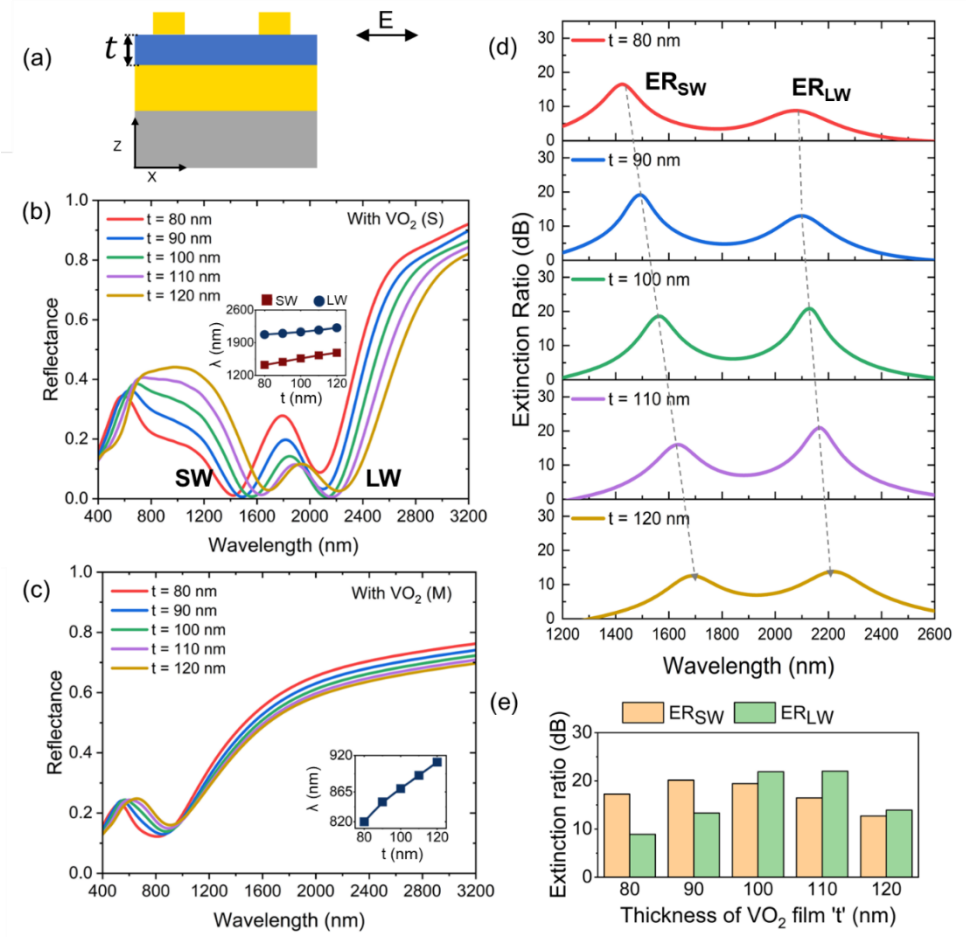

Fig. 5.6 Effect of the thickness of VO_2 film on the performance of U-C (Offset = *L*) type plasmonic switches. **(a)** Schematic of a unit cell of U-C (Offset = *L*) type plasmonic switch showing the thickness of VO_2 film '*t*'. **(b)** Reflectance spectra of U-C (Offset = *L*) type plasmonic switch with VO_2 (S) and **(c)** VO_2 (M) for various values of the thickness of VO_2 film '*t*'. **(d)** Extinction ratio spectra of U-C (Offset = *L*) type plasmonic switch for various values of the thickness of VO_2 film '*t*'. **(e)** Bar graph of U-C (Offset = *L*) type plasmonic switch showing the extinction ratio at short wavelength mode and long wavelength mode for various values of the thickness of VO_2 film '*t*'. The length '*L*', width '*W*', and height '*H*' of the U and C shaped nanopillars is taken to be 100 nm, 20 nm, and 50 nm, respectively. The gap '*G*' between adjacent nanostructures is kept as 30 nm.

It can be clearly seen from Fig. 5.7 that as the thickness of the VO_2 layer increases, the real part of the effective dielectric permittivity (See Figs. 5.7(a, c)) for the underlying substrate increases, for both VO_2 (M) and VO_2 (S). It has previously been well demonstrated by Perera *et al.* [15], Xu *et al.* [16], and Malinsky *et al.* [14] that an increase in the real part of the dielectric permittivity of the substrate leads to the plasmon resonance condition being met at a higher wavelength of incident light, thus leading to a red-shift of the plasmon resonance wavelength. Hence, an increase in the thickness of the VO_2 layer leads to red-shifting of the plasmonic $Mode_{SW}$ and $Mode_{LW}$, for cases when VO_2 is in its semiconductor or metal state, as shown in Figs. 5.6(b, c). The ER spectra as a function of thickness are shown in Fig. 5.6(d) with X-polarized incident light (See Fig. 5.11(a) for Y-polarized light). It can be observed from

Fig. 5.6(d) that as the thickness of VO_2 film is increased from 80 nm to 120 nm, the short wavelength mode (ER_{SW}) shows a red-shift from 1425 nm to 1680 nm and the long wavelength mode (ER_{LW}) shows a red-shift from 2070 nm to 2230 nm as the thickness of VO_2 film '*t*' is increased from 80 nm to 120 nm. Further, it can be observed from the bar graph for the magnitude of ER shown in Fig. 5.6(e) that t = 100 nm is the most optimized thickness of VO_2 film where almost equal switching performance of ~ 20 dB can simultaneously be achieved at both the wavelengths.

The switching performance of the proposed U-C (Offset = *L*) type plasmonic switch can be optimized by choosing the right value for the design parameters such as the gap '*G*' between the U and C shaped nanostructures. In order to understand the trends observed on varying the values of the thickness of the VO_2 layer, the effect of gap on the switching performance of the proposed switches for varying values of thickness of the VO_2 layer has been analyzed. For the proposed switch with VO_2 (S), Fig. 5.8 shows the effect of gap '*G*' with X-polarized light on the two modes in the short and long wavelength regime, for different values of thickness of the VO_2 layer. Fig. 5.8(b) shows the effect of gap '*G*' on the reflectance spectra of the proposed switch with the thickness of the VO_2 layer being 120 nm, and for the case when VO_2 is in its semiconductor state. It can clearly be seen that the behavior of the two modes

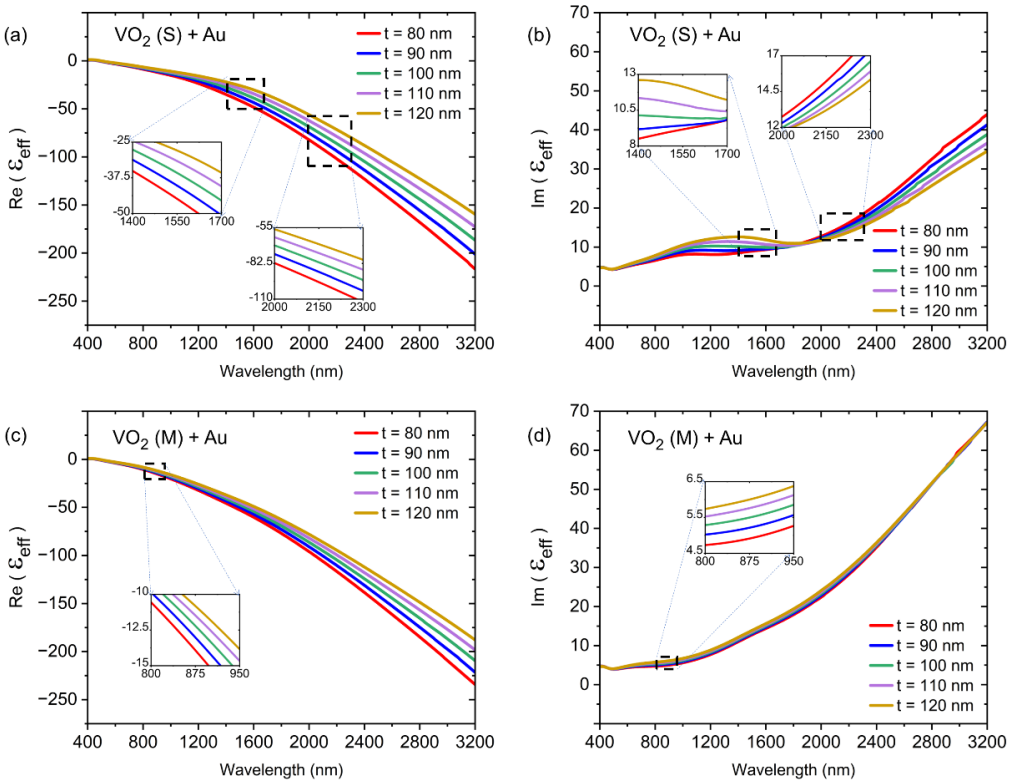

Fig. 5.7 Wavelength dependence of **(a)** real and **(b)** imaginary parts of the effective permittivity (ε_{eff}) for VO_2 (S) and Au. Wavelength dependence of **(c)** real and **(d)** imaginary parts of the effective permittivity (ε_{eff}) for VO_2 (M) and Au. The thickness of the gold layer is taken to be 200 nm as employed in the simulation. The thickness of the VO_2 layer '*t*' is varied from 80 nm to 120 nm.

in Fig. 5.8(b) can be well explained by the plasmon hybridization theory [6, 17]. It must be noted that for this value of thickness, the gold mirror beneath the VO_2 (S) spacer has minimal effect on the hybridization of the plasmonic modes. Thus, with smaller values of gap '*G*', the hybridization of the elementary plasmons of the U and C shaped nanopillars results in the splitting of the dipolar mode into a bonding mode (longer wavelength mode), and an antibonding mode (shorter wavelength mode). As the value of gap between the nanopillars is increased from 10 nm to 120 nm, the bonding mode continues to blue-shift, while the antibonding mode continues to red-shift, as expected [6, 17], till the splitting between the modes almost disappears at a gap of ~ 120 nm. The plasmon shift ($\Delta\lambda$) versus the gap '*G*' for both the short and the long wavelength mode for $t \sim 120$ nm is also shown in the inset for Fig. 5.8(b). For the same thickness, as the phase of the VO_2 layer changes to a metal, the effective system changes to an array of U-C nanopillars on a metallic substrate with an effective dielectric permittivity calculated as shown in Eq. 5.3. For this system, the incident light induces a strong coupling between the U and C nanopillars giving rise to a screened bonding dimer (SBD) plasmon resonance in the wavelength range ~ 800 nm to 1000 nm (See Fig. 5.8(c)) with a strong dipolar character. In addition, for such metal nanostructure on metal systems [9], the presence of the conductive surface (VO_2 (M) on Au) underneath the UC nanopillars, induces a net charge transfer between the nanopillars often leading to a charge transfer plasmon mode (CTP) at a higher wavelength. However, due to substrate screening, electric dipole moment of the CTP mode is often screened, making it sub-radiant and hidden within the spectra. For the SBD mode, as expected, an increase in the gap '*G*' leads to reduction in the dipolar interaction, and hence a blue shift as shown in Fig. 5.8(c). The resultant ER bar graphs at the two switching wavelengths for the various gaps for t being 120 nm are shown in Fig. 5.8(d).

Interestingly, as the value of the thickness of VO_2 layer is reduced to 100 nm, the effects of the underlying gold film beneath the VO_2 layer begin to disrupt the plasmon hybridization between the nanopillars, for the case when VO_2 is in its semiconductor state. This has also been discussed previously by Nordlander *et. al.* [18] in complex systems where nanostructures are placed over a dielectric-spacer-separated metallic films. Fig. 5.8(e) shows that as the gap is increased, the longer wavelength mode blue-shifts as expected. The plasmon shift ($\Delta\lambda$) versus the gap '*G*' is shown in the inset of Fig. 5.8(e). However, the short wavelength mode displays an interesting behavior. As the gap is increased from 10 nm to 40 nm, the plasmon resonance wavelength red-shifts, after which it blue-shifts as the gap is increased to 120 nm. This is most likely due to the interplay of the plasmon hybridization and the interaction of the nanopillar plasmons with their images in the gold layer. For the case when VO_2 transforms to its metal state, the increase in the gap '*G*' leads to an expected blue-shift as shown in Fig. 5.8(f) due to the SBD mode as discussed earlier. The resultant ER bar graphs for the various gaps for t being 100 nm are shown in Fig. 5.8(g). It can be observed from the bar graph shown in Fig. 5.8(g) that $G = 30$ nm is the most optimized gap for the proposed switch as almost equal ER of ~ 20 dB can be achieved at both the switching wavelengths. However, if desired, an appropriate gap can be chosen to tune the operating wavelength at which high ER is needed.

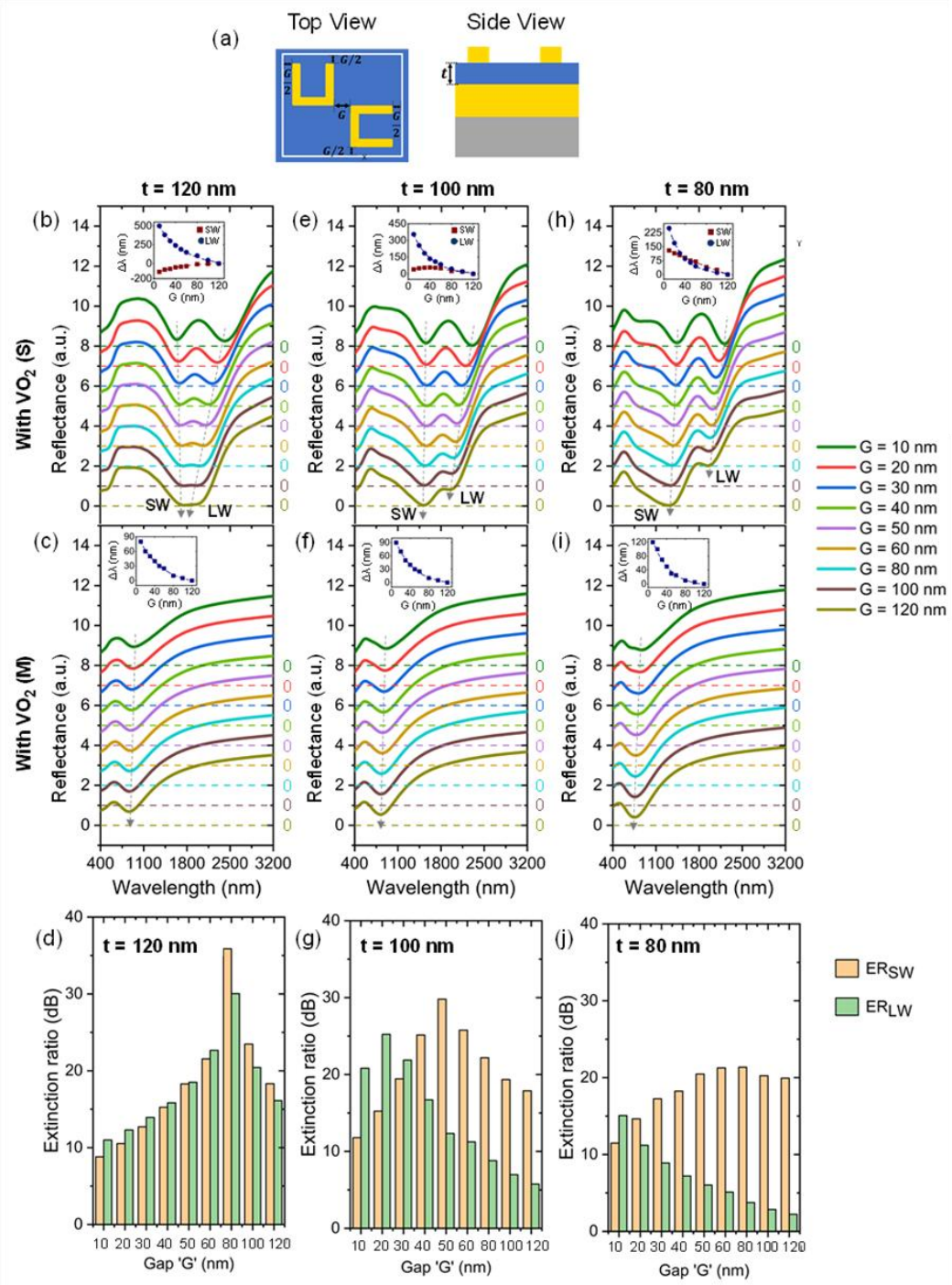

Fig. 5.8 Effect of the gap '*G*' on the performance of U-C (Offset = *L*) type plasmonic switches. **(a)** Schematic showing the gap '*G*' and thickness '*t*' of the proposed switches from the top view and the side view of the switch. Effect of the gap '*G*' between the U and C shaped nanostructures on the reflectance spectra of the U-C (Offset = *L*) type plasmonic switch with **(b)** VO_2 (S) with t = 120 nm, **(c)** VO_2 (M) with t = 120 nm, **(e)** VO_2 (S) with t = 100 nm, **(f)** VO_2 (M) with t = 100 nm, **(h)** VO_2 (S) with t = 80 nm, and **(i)** VO_2 (M) with t = 80 nm. Extinction ratio bar graph showing magnitude of ER at the long wavelength and the short wavelength for **(d)** t = 120 nm, **(e)** t = 100 nm and **(f)** t = 80 nm. The length '*L*', width '*W*', and height '*H*' of the U and C shaped nanopillars is taken to be 100 nm, 20 nm, and 50 nm, respectively.

The role of the underlying gold mirror in perturbing the plasmon hybridization is confirmed through the reflectance spectra plotted in Fig. 5.8(h) for various values of gaps when the thickness of the VO_2 (S) layer is further reduced to 80 nm. For VO_2 (S), this reduced thickness implies an increased interaction of the nanopillar plasmons with their images in the underlying gold layer [18]. Thus, both modes at the short and long wavelength, display dipolar behavior and exhibit a blue-shift in the plasmon resonance wavelength as the gap '*G*' increases from 10 nm to 120 nm as shown in Fig. 5.8(h). Further, it can be observed from the insets of Fig. 5.8(e) and Fig. 5.8(h) that as the thickness of the VO_2 layer is decreased from 100 nm to 80 nm, the rate at which the longer wavelength mode blue-shifts with a variation in gap, also reduces. For the case when VO_2 transforms to its metal state, the increase in the gap '*G*' leads to an expected blue shift as shown in Fig. 5.8(i). The resultant ER bar graphs for the various gaps for *t* being 80 nm are shown in Fig. 5.8(j).

The switching performance of the proposed U-C type plasmonic switch also depends upon the geometrical parameters of the U and C shaped nanopillars such as the length of the nanopillars '*L*', the width of the nanopillars '*W*', and the height of the nanopillars '*H*'. This geometrical dependence of the proposed switch with X-polarized light (See Fig. 5.11(c) for Y-polarized light) is analyzed in terms of an aspect ratio 'AR' – which is the ratio of the length '*L*' of the nanopillars to the width '*W*' of the nanopillars (See Fig. 5.9). The reflectance spectra of the proposed U-C type plasmonic switch with VO_2 (S) and VO_2 (M) for various aspect ratios are shown in Fig. 5.9(a, b). Fig. 5.9(a) shows that with a lower aspect ratio 'AR' of 3 (i.e., L = 60 nm and W = 20 nm), only one lower order plasmonic mode at a wavelength of 1640 nm is supported by the switch with VO_2 (S). However, as the value of 'L' is increased, Fig. 5.9(a) shows the emergence of another peak at a short wavelength (SW) in the reflectance spectra for the switch. This additional peak at a lower wavelength can be attributed to the excitation of additional higher order plasmonic modes in the plasmonic switch with VO_2 (S) due to an increased length of the nanopillars It should also be noted that both short and the long wavelength mode exhibit a significant red-shift on increasing the aspect ratio. The red-shift of the plasmon resonance wavelength can be explained by approximating the interaction between the U and C shaped nanopillars to be equivalent to the one between interacting nanorods. According to Ganz theory, higher aspect ratios of interacting nanorods imply the resonance condition getting satisfied at higher values of λ. Further, this model leads to a linear dependence of the plasmon resonance wavelength on the aspect ratio [19, 20]. As can be seen in Fig. 5.9(a), the red-shifts observed for both the short and long wavelength mode are found to be linear. Fig. 5.9(b) shows the effect of the aspect ratio on the reflectance spectra of the switch with VO_2 (M). It is found that the plasmon resonance wavelength corresponding to the SBD mode [20] remains almost the same as the AR is changed. It can be observed from the ER spectra shown in Fig. 5.9(c) that as the aspect ratio 'AR' is increased from 4 (i.e., L = 80 nm and W = 20 nm) to 7 (i.e., L = 140 nm and W = 20 nm), the ER at the short wavelength mode (ER_{SW}) increases linearly from ~ 9 dB to ~ 29 dB with a red-shift in the plasmon resonance wavelength from 1460 nm to 1790 nm. In addition, the long wavelength mode (ER_{LW}) also shows a red-shift from 1830 nm to 2810 nm as the aspect ratio 'AR' is increased from 4 to 7. Further, it can be noted that an aspect ratio of 5 (i.e., L = 100 nm and W = 20 nm) is

the most optimized aspect ratio where almost equal switching performance can simultaneously be achieved at both the wavelengths. The results for the effect of aspect ratio on the performance of the switch for the width '*W*' being 25 nm are also shown in Fig. 5.10.

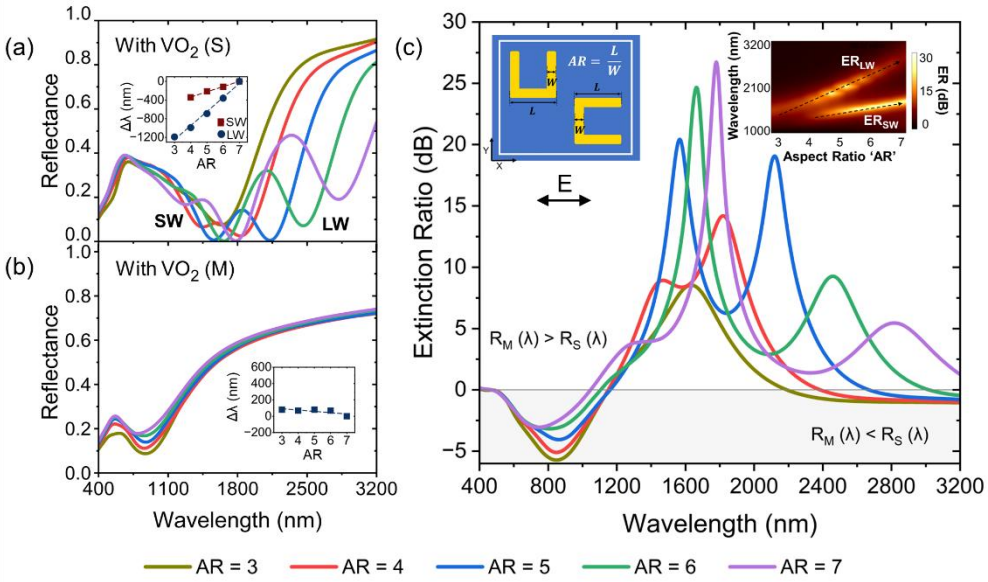

Fig. 5.9 Effect of the aspect ratio on the performance of U-C type plasmonic switches. Effect of AR of the UC shaped nanopillars on the **(a)** Reflectance spectra of the switch with VO_2 (S), and **(b)** with VO_2 (M). **(c)** Extinction ratio spectra of the plasmonic switch. Colormap of U-C type plasmonic switch showing the extinction ratio at short wavelength mode and long wavelength mode for various aspect ratios is shown as an inset. The width '*W*' and height '*H*' of nanopillars, gap '*G*' between adjacent nanostructures, and the thickness of VO_2 film '*t*' is taken as 20 nm, 50 nm, 30 nm and 100 nm, respectively.

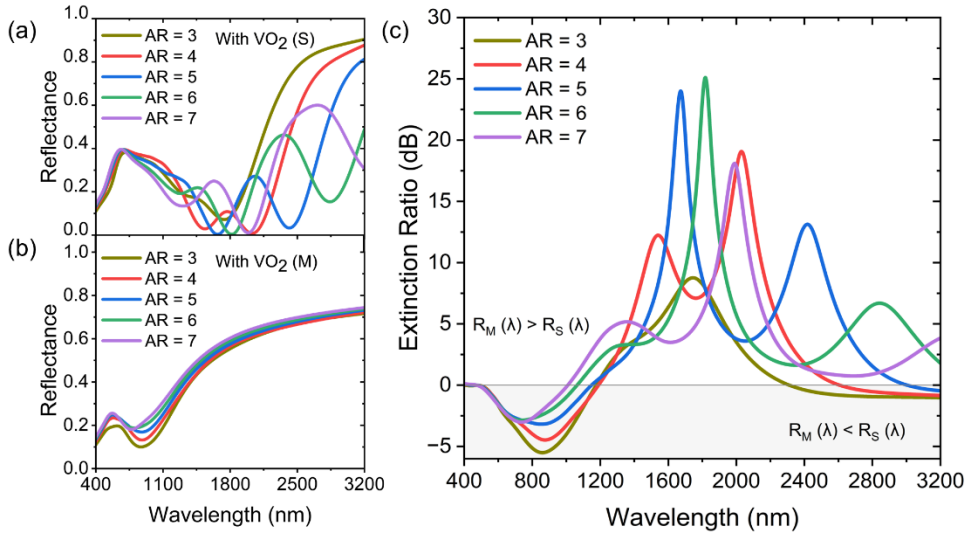

Fig. 5.10 Effect of AR of the U-C shaped nanopillars on the **(a)** Reflectance spectra of the switch with VO_2 (S), and **(b)** with VO_2 (M). **(c)** Extinction ratio spectra of the plasmonic switch. The width '*W*' and height '*H*' of nanopillars, gap '*G*' between adjacent nanostructures, and the thickness of VO_2 film '*t*' is taken as 25 nm, 50 nm, 30 nm and 100 nm, respectively.

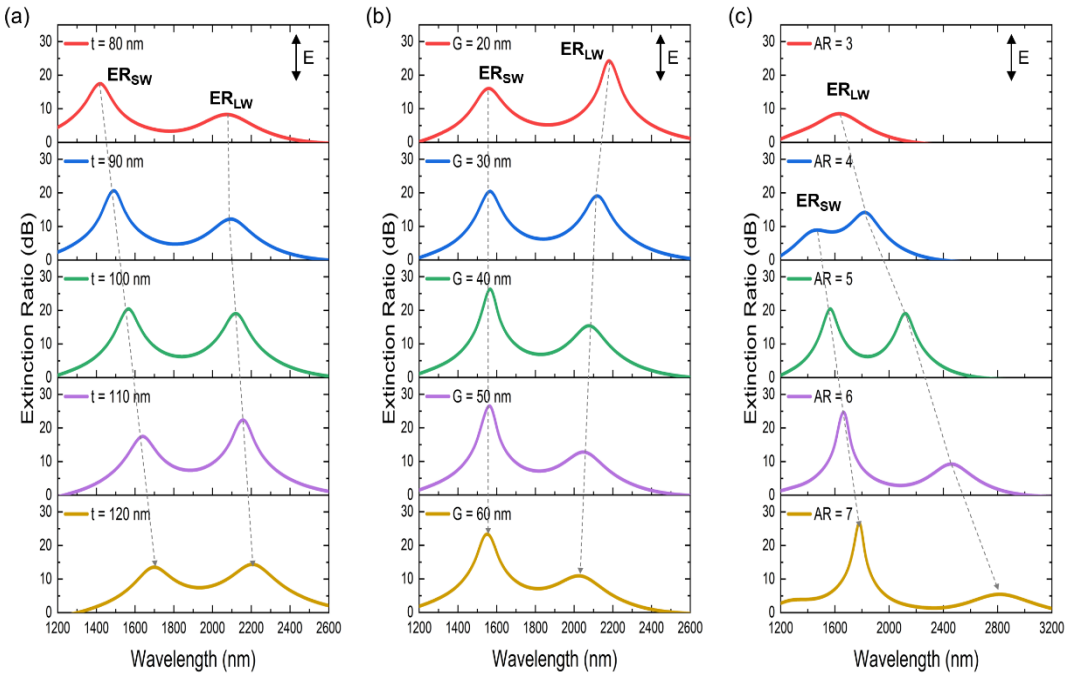

Fig. 5.11 Effect of **(a)** thickness of VO_2 film '*t*', **(b)** gap '*G*', and **(c)** aspect ratio 'AR' on the extinction ratio spectra for U-C (Offset = *L*) type plasmonic switch with Y-polarized incident light ($\phi = 90°$). The length '*L*', width '*W*', and height '*H*' of the U and C shaped nanopillars is taken to be 100 nm, 20 nm, and 50 nm, respectively. The gap '*G*' between adjacent nanostructures and the thickness of VO_2 film '*t*' is taken as 30 nm and 100 nm, respectively.

Further, the proposed U-C type plasmonic switches can be fabricated with the help of the existing state-of-the-art fabrication techniques as shown in Fig. 5.12. E-beam evaporation [21-24] can be used to coat the SiO_2 substrate with gold. Thereafter, pulsed laser deposition (PLD) [25, 26] or atomic layer deposition (ALD) [27] can be used to deposit the thin film of VO_2. Subsequently, a PDMS stamp in conjunction with E-beam lithography (EBL) on silicon can be used to transfer the U and C shaped gold nanostructures on top of the VO_2 thin film [28].

Therefore, the proposed VO_2 based plasmonic switches using U and C shaped nanostructures with spatial offset are capable of exhibiting polarization-independent as well as dual-wavelength operations with high extinction ratio of ~ 20 dB in the conventional C-band and the futuristic 2000 nm communication band.

5.5 Chapter Summary

VO_2 based polarization-independent and dual-wavelength U-C type plasmonic switches using arrays of U and C shaped gold nanostructures with a spatial offset were proposed in this chapter. Finite difference time domain (FDTD) modelling showed that the proposed plasmonic switches exhibited a polarization-independent operation and offered a high extinction ratio of ~ 20 dB simultaneously at two wavelengths — in the conventional C-band and the futuristic 2000 nm communication band. It was also demonstrated that the geometrical parameters of the proposed plasmonic switches could be varied to maximize the switching efficiency and to fine

tune the wavelength of operation of these switches. The switches proposed in this chapter could be potentially employed in the conventional and the future communication networks, along with their application in integrated photonic circuits.

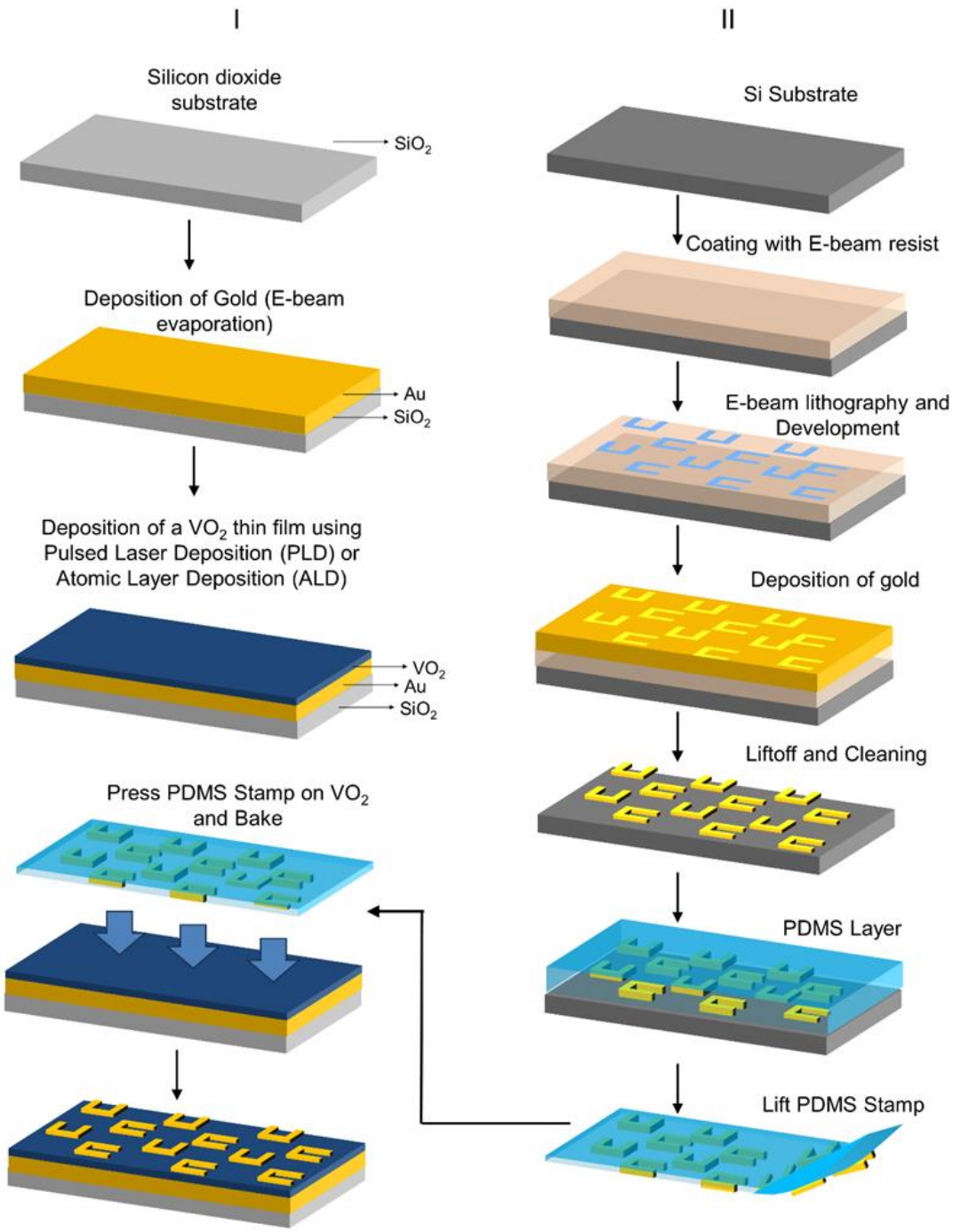

Fig. 5.12 Fabrication methodology to fabricate the proposed VO_2 based polarization-independent dual-wavelength U-C type plasmonic switch using a periodic combination of U and C shaped gold nanopillars on a gold coated SiO_2 substrate with a thin film of VO_2 as a spacer between the nanostructures and the underlying plasmonic substrate.

5.6 References

[1] Rashidi, A., Entezar, S. R., and Hatef, A. "Tunable multispectral near-infrared absorption with a phase transition of VO_2 nanoparticles hybridized with 1D photonic crystals", *Nanotechnology*, 31(33), 335701, 2020. https://doi.org/10.1088/1361-6528/ab8e76

[2] Sharma, Y. *et al.* "Plasmonic switches based on arrays of plasmonic nanostructures surrounded by VO_2 thin films", *Quantum Sensing and Nano Electronics and Photonics XVI*, 109262S, 2019. https://doi.org/10.1117/12.2511206

[3] Long, L., Taylor, S., and Wang, L. "Enhanced infrared emission by thermally switching the excitation of magnetic polariton with scalable microstructured VO_2 metasurfaces", *ACS Photonics*, 7(8), 2219-2227, 2020. https://doi.org/10.1021/acsphotonics.0c00760

[4] Zhang, Z., and Zhao, Y. "Optical properties of U-shaped Ag nanostructures", *Journal of Physics: Condensed Matter*, 20(34), 345223, 2008. https://doi.org/10.1088/0953-8984/20/34/345223

[5] Chen, Y. *et al.* "Sub-10 nm fabrication: methods and applications", *International Journal of Extreme Manufacturing*, 3(3), 032002, 2021. https://doi.org/10.1088/2631-7990/ac087c

[6] Nordlander, P., Oubre, C., Prodan, E., Li, K., and Stockman, M. I. "Plasmon hybridization in nanoparticle dimers", *Nano letters*, 4(5), 899-903, 2004. https://doi.org/10.1021/nl049681c

[7] Niklasson, G. A., Granqvist, C. G., and Hunderi O. "Effective medium models for the optical properties of inhomogeneous materials", *Applied Optics*, 20(1), 26-30, 1981. https://doi.org/10.1364/AO.20.000026

[8] Maier, S. A. *Plasmonics: Fundamentals and applications*. Springer, 2007. https://doi.org/10.1007/0-387-37825-1

[9] Gerislioglu, B. *et al.* "Monolithic metal dimer-on-film structure: New plasmonic properties introduced by the underlying metal", *Nano Letters*, 20(3), 2087-2093, 2020. https://doi.org/10.1021/acs.nanolett.0c00075

[10] Gunning, F. C. G. *et al.* "Key enabling technologies for optical communications at 2000 nm", *Applied Optics*, 57(22), E64-E70, 2018. https://doi.org/10.1364/AO.57.000E64

[11] Tobing, L. Y. M. *et al.* "Polarization invariant plasmonic nanostructures for sensing applications", *Scientific Reports*, 7, 7539, 2017. https://doi.org/10.1038/s41598-017-08020-y

[12] Pradhan, J. K. *et al.* "High contrast switchability of VO_2 based metamaterial absorbers with ITO ground plane", *Optics Express*, 25(8), 9116-9121, 2017. https://doi.org/10.1364/OE.25.009116

[13] Guo, Y. *et al.* "Dual-band polarized optical switch with opposite thermochromic properties to vanadium dioxide", *Applied Physics Letters*, 121, 2022. https://doi.org/10.1063/5.0123589

[14] Malinsky, M. D., Kelly, K. L., Schatz, G. C., and Duyne, R. P. V. "Nanosphere lithography: Effect of substrate on the localized surface plasmon resonance spectrum of silver nanoparticles", *The Journal of Physical Chemistry B*, 105(12), 2343-2350, 2001. https://doi.org/10.1021/jp002906x

[15] Perera, M. N. M. N., Schmidt, D., Gibbs, W. E. K., Juodkazis, S., and Stoddart, P. R. "Influence of the dielectric substrate on the effective optical constants of silver plasmonic films", *Applied Optics*, 58(22), 6038-6044, 2019. https://doi.org/10.1364/AO.58.006038

[16] Xu, G., Chen, Y., Tazawa, M., and Jin P. "Influence of dielectric properties of a substrate upon plasmon resonance spectrum of supported Ag nanoparticles", *Applied Physics Letters*, 88, 043114, 2006. https://doi.org/10.1063/1.2167827

[17] Prodan, E., Radloff, C., Halas, N. J., and Nordlander, P. “A hybridization model for the plasmon response of complex nanostructures”, *Science*, 302(5644), 419-422, 2003. https://doi.org/10.1126/science.1089171

[18] Nordlander, P., and Prodan, E. “Plasmon hybridization in nanoparticles near metallic surfaces”, *Nano Letters*, 4(11), 2209-2213, 2004. https://doi.org/10.1021/nl0486160

[19] Link, S., and El-Sayed, M. A. “Simulation of the optical absorption spectra of gold nanorods as a function of their aspect ratio and the effect of the medium dielectric constant”, *The Journal of Physical Chemistry B*, 109(20), 10531-10532, 2005. https://doi.org/10.1021/jp058091f

[20] Lu, H. *et al.* “The generalized analytical expression for the resonance frequencies of plasmonic nanoresonators composed of folded rectangular geometries”, *Scientific Reports*, 9, 52, 2019. https://doi.org/10.1038/s41598-018-37275-2

[21] Chen, G., and Hui, P. “Thermal conductivities of evaporated gold films on silicon and glass”, *Applied Physics Letters*, 74, 2942-2944, 1999. https://doi.org/10.1063/1.123973

[22] Netterfield, R. P., and Martin, P. J. “Nucleation and growth studies of gold films prepared by evaporation and ion-assisted deposition”, *Applied Surface Science*, 25(3), 265-278, 1986. https://doi.org/10.1016/0169-4332(86)90059-0

[23] Malabi, R. *et al.* “Growth and characterisation of gold thin film layer using an ebeam evaporation system for surface plasmon resonance applications”, *Plasmonics in Biology and Medicine XVI*, 108941E, 2019. https://doi.org/10.1117/12.2509972

[24] Zheng, M. *et al.* “Fabrication of gold nanostructures using wet lift-off without adhesion promotion”, *Microelectronic Engineering*, 233, 111420, 2020. https://doi.org/10.1016/j.mee.2020.111420

[25] Marvel, R. E., Harl, R. R., Craciun, V., Rogers, B. R., and Haglund Jr, R. F. “Influence of deposition process and substrate on the phase transition of vanadium dioxide thin films”, *Acta Materialia*, 91, 217-226, 2015. https://doi.org/10.1016/j.actamat.2015.03.009

[26] McGee, R. *et al.* “Sharpness and intensity modulation of the metal-insulator transition in ultrathin films by interfacial structure manipulation”, *Physical Review Materials*, 2, 034605, 2018. https://doi.org/10.1103/PhysRevMaterials.2.034605

[27] Kozen, A. C. *et al.* “Structural characterization of atomic layer deposited vanadium dioxide”, *The Journal of Physical Chemistry C*, 121(35), 19341-19347, 2017. https://doi.org/10.1021/acs.jpcc.7b04682

[28] Boyce, A. M. *et al.* “Actively tunable metasurfaces via plasmonic nanogap cavities with sub-10-nm VO_2 films”, *Nano Letters*, 22(9), 3525-3531, 2022. https://doi.org/10.1021/acs.nanolett.1c04175

CHAPTER 6

MULTI-WAVELENGTH AND BROADBAND PLASMONIC SWITCHING WITH V-SHAPED PLASMONIC NANOSTRUCTURES ON A VO_2 COATED PLASMONIC SUBSTRATE

6.0 Chapter Overview

In this chapter, periodic arrays of identical V-shaped gold nanostructures and variable V-shaped gold nanostructures are designed on top of a gold-coated silicon dioxide (SiO_2) substrate with a thin spacer layer of vanadium dioxide (VO_2) to realize multi-wavelength and broadband plasmonic switches, respectively. The periodic array of identical V-shaped nanostructures (IVNSs) with small inter-particle separation leads to coupled interactions of the elementary plasmons of a V-shaped nanostructure (VNS), resulting in a hybridized plasmon response with two longitudinal plasmonic modes in the reflectance spectra of the proposed switches when the incident light is polarized in the x-direction. The x-direction is oriented along the axis that joins the V-junctions of all VNSs in one unit cell of the periodic array. On exposure to temperature, electric field, or optical stimulus, the VO_2 layer transforms from its monoclinic semiconducting state to its rutile metallic state, leading to an overall change in the reflectance spectra obtained from the proposed nanostructures and resulting in an efficient multi-wavelength switching action. Finite difference time domain (FDTD) modelling is employed to demonstrate that an extinction ratio > 12 dB at two wavelengths can be achieved by employing the proposed switches based on periodic arrays of IVNSs. Further, plasmonic switches based on variable V-shaped nanostructures (VVNSs) — i.e., multiple VNSs with variable arm lengths in one unit cell of a periodic array — are proposed for broadband switching. In the broadband operation mode, an extinction ratio > 5 dB over an operational wavelength range > 1400 nm in the near-IR spectral range spanning over all optical communication bands, i.e., the O, E, S, C, L and U bands, is reported. Further, it is also demonstrated that the wavelength of operation for these switches can be tuned by varying the geometrical parameters of the proposed switches. These switches have the potential to be employed in communication networks where ultrasmall and ultrafast switches with multi-wavelength operation or switching over a wide operational bandwidth are inevitably required.

6.1 Motivation

Numerous plasmonic switches based on phase change materials have been proposed previously [1-3], however, there have been limited reports of plasmonic switches offering multi-wavelength switching (i.e., simultaneous switching at multiple wavelengths) and broadband operation (i.e., switching over a wide range of wavelengths) with VO_2 as the phase change material. Multi-wavelength and

broadband switching are particularly important in designing optical communication networks [4] and optical computing systems [5], where the switching is desired to be flexible and independent of the wavelength of operation. For multi-wavelength plasmonic switching, Rashidi *et al.* [6] have previously proposed switchable VO_2 embedded photonic crystals with six resonant peaks in the near-infrared regime at absorption ~ 0.6 and Sharma *et al.* [7] have proposed VO_2 coated gold nano-gratings with a maximum differential reflectance of ~ 41%. For broadband plasmonic switching, Joushaghani *et al.* [8] proposed hybrid SPP-VO_2 geometry with bandwidth of ~ 100 nm at 20 dB extinction ratio, Sun *et al.* [9] proposed hybrid combination of aluminium nanohole arrays and VO_2 with bandwidth of ~ 650 nm at 5 dB extinction ratio, Mandal *et al.* [10] proposed metal-VO_2 hybrid dagger like plasmonic nanostructure with operational bandwidth of ~ 200 nm, and Guo *et al.* [11] proposed VO_2 coated plasmonic indium tin oxide nanorod arrays with bandwidth of ~ 250 nm. However, it must be noted that in all these previously proposed switches, the operational wavelength range over which the switching could be achieved remained well below 700 nm.

6.2 Introduction

In this chapter, V-shaped plasmonic nanostructures on VO_2 coated plasmonic substrates are employed to realize multi-wavelength and broadband plasmonic switching. Two kinds of plasmonic nanostructures – a periodic array of identical V-shaped nanostructures (IVNSs) and a periodic array of variable V-shaped nanostructures (VVNSs) – placed on a thin film of VO_2 on a gold coated SiO_2 substrate are proposed that are capable of offering multi-wavelength and broadband plasmonic switching, respectively, in the near infrared regime (see Fig. 6.1). The periodic array of IVNSs is designed with V-shaped nanostructures (VNSs) of gold with all VNSs having identical arm lengths, whereas the periodic array of VVNSs is designed with periodic unit cells such that each unit cell consists of gold VNSs of variable (i.e., sequentially decreasing) arm lengths. Plasmonic switches based on periodic arrays of IVNSs are employed for multi-wavelength switching due their capability to support two longitudinal plasmonic modes when x-polarized light is vertically incident on them (See Fig. 6.1). This is expected as the interaction of the VNSs with small inter-particle separation in an array, results in the coupled interactions of their elementary plasmons, thus generating hybridized plasmon response with two longitudinal plasmonic modes [12, 13]. When the underlying VO_2 layer is switched from its semiconducting state to its metallic state on exposure to a thermal, electrical, or optical stimulus, there is a change in the optical behavior of the proposed switches, which can be numerically measured in terms of the extinction ratio. The extinction ratio (ER) is calculated from the ratio of the reflectance from the plasmonic switch when VO_2 is in its metallic state (R_M) and the reflectance from the plasmonic switch when VO_2 is in its semiconducting state (R_S). Finite difference time domain (FDTD) modelling is employed to demonstrate that the multi-wavelength plasmonic switches proposed in this chapter are capable of achieving an extinction ratio > 12 dB at two wavelengths in the optical communication window, and these two wavelengths can be controlled by varying the geometrical parameters of the proposed switches as discussed in the later sections. Moreover, according to the previous studies on the plasmonic properties

of V-shaped plasmonic nanostructures [14-17], it is well known that there is a linear relationship between the plasmon resonance wavelength and the arm length of the VNS. In this chapter, this linear dependence is exploited by proposing periodic arrays of unit cells of VNSs such that each unit cell has VNSs of variable arm lengths – with VNS of each specific arm length leading to its own specific plasmon resonance wavelength. When multiple VNSs with variable arm lengths are present in one unit cell, there is an overlap of these individual plasmon resonances in the reflectance spectra, thus leading to an overall broadband plasmon response from the periodic arrays of VVNSs. In the broadband operation mode, an extinction ratio > 5 dB over an ultra-wide operational wavelength range > 1400 nm is reported in the near-IR spectral range, which has not been previously reported. This is the first report of a plasmonic switch which offers broadband operation spanning over a wide spectral range of 1400 nm covering all optical communication bands, i.e., the O, E, S, C, L and U bands. Moreover, the switches proposed in this chapter are capable of demonstrating an ultrafast phase transition at picosecond to femtosecond timescales when triggered optically [18, 19] and at microsecond to nanosecond timescales when triggered thermally or with an electric field [20, 21]. Thus, the proposed switches have the potential to be employed in communication networks where ultrasmall and ultrafast switches with wide operational bandwidth is a necessary requirement so that the switches are suitable for operation at all wavelengths of interest.

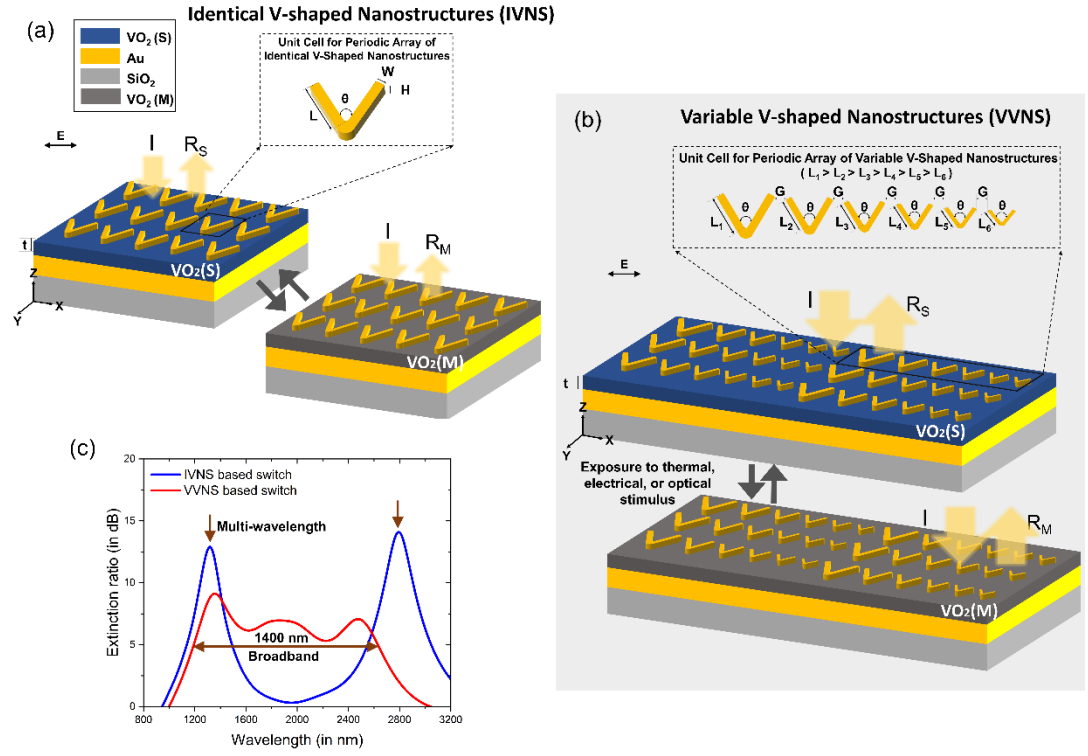

Fig. 6.1 (a) Schematic showing a multi-wavelength plasmonic switch based on identical V-shaped nanostructures (IVNS) on VO_2 coated plasmonic substrates. **(b)** Schematic showing a broadband plasmonic switch based on variable V-shaped nanostructures (VVNS) on VO_2 coated plasmonic substrates. **(c)** Extinction ratio spectra obtained from a multi-wavelength IVNS based plasmonic switch and a broadband VVNS based plasmonic switch.

The plasmonic switches proposed in this chapter can be fabricated with state-of-the-art fabrication methodologies. The metallic film of gold can be deposited on the SiO_2 substrate with the help of thin film deposition techniques such as E-beam evaporation [22] and atomic layer deposition (ALD) [23]. The VO_2 spacer layer can be deposited on top of the gold coated SiO_2 substrate by employing the pulsed laser deposition (PLD) technique [24]. Subsequently, the V-shaped nanostructures of gold can be fabricated on the VO_2 layer by using E-beam lithography only [25] or a combination of E-beam lithography and helium ion beam milling [26]. For large-scale production, a variant of E-Beam Lithography — Massively Parallel E-beam Lithography (MPEBL) — can be employed to fabricate the proposed switches on a large area [27-29]. In this system, a large number of parallel electron beams are generated through a 2-dimensional array of apertures, such that each beam writes a part of the overall pattern. This leads to a significant increase in the writing speed, and thus, this process can be used for large area fabrication. It must, however, be noted that MPEBL requires an optimization of the exposure variation, dose, line edge roughness, dose latitude, aperture size, the position error of the beam and other lithographic parameters to ensure a good writing quality.

The proposed plasmonic switches can be integrated with photonic circuits by fabricating input and output waveguides having polished facets to carry light to the chip containing the plasmonic switch and to collect light reflected from the chip. The plasmonic chip can be placed at an angle inside a size-appropriate groove such that the light is incident from the input waveguide on the planar surface of the chip. The groove for the placement of the plasmonic switch chip can be made with either by employing photolithography, maskless lithography, or focused ion-beam milling. The primary challenges that need to be addressed for such integration will involve precise alignment, bonding, minimization of the insertion loss, and mode matching.

It must be noted that thermal management strategies may be required when these switches are integrated with other devices to avoid adverse effects on surrounding components. This can be done by isolating the switch from the other components by employing materials with low thermal conductivity [30], employing heat sinks and Peltier coolers, and by introducing heat dissipation layers in the design to ensure that VO_2 based regions are well separated from any temperature-sensitive components.

6.3 Numerical Methods

Ansys Lumerical FDTD Solver software [31] was used to carry out the 3D electromagnetic simulations for the VNSs based plasmonic switches designed in this chapter. A linearly polarized plane wave source of 1 V/m incident electric field has been used to illuminate the plasmonic switches. Perfectly matched layer (PML) boundary conditions have been employed in the z direction. Periodic boundary conditions have been employed in the x and y directions to generate a periodic array of VNSs. After carefully testing the convergence in the proposed plasmonic switches, a 1 nm uniform mesh size has been employed in all the directions – x, y, and z – of the entire simulation region. Figs. 6.1(a, b) show the schematics for the plasmonic switches based on a periodic array of IVNSs and a periodic array of VVNSs. A VO_2

film of thickness 't' nm has been placed between the VNSs and the gold coated SiO_2 substrate. The dielectric constants of the semiconductor VO_2 and the metallic VO_2 have been taken in accordance with the Lorentz-Drude model [32] (See Appendix-II, Dielectric Constants of Materials). The periodic array of IVNSs consists of VNSs with similar arm lengths, 'L' nm, width 'W' nm, height 'H' nm, angle 'θ' degrees between two arms of a VNS, and gap 'G' nm between the adjacent VNSs. On the other hand, the periodic array of VVNSs is made with a unit cell consisting of VNSs with sequentially decreasing lengths such that $L_1 > L_2 > L_3 > L_4 > L_5 > L_6$, where L_x denotes the length of x^{th} VNS. Further, the edges of the VNSs are designed with a rounding radius of 2 nm, as features with sharp corners cannot be fabricated by employing state-of-the-art lithography techniques. The geometrical parameters such as – the arm length of the VNS (L), the thickness of VO_2 layer (t), the gap between the adjacent VNSs (G), and the angle between the two arms of the VNS (θ) – are varied from – 40 nm to 140 nm, 60 nm to 160 nm, 10 nm to 40 nm, and 30° to 75°, respectively – to analyse their effect on the extinction ratio spectra of the proposed multi-wavelength and broadband plasmonic switches.

6.4 Results and Discussion

Finite Difference Time Domain (FDTD) modelling is employed to design and numerically analyze the proposed plasmonic switches based on periodic arrays of V-shaped nanostructures (VNSs) on a VO_2 coated plasmonic substrate. The proposed plasmonic switches can be used in two operational modes – multi-wavelength operation mode and broadband operation mode – by employing a periodic array of identical V-shaped nanostructures (IVNSs) and a periodic array of variable V-shaped nanostructures (VVNSs), respectively. In this section, the switching efficiency of these proposed switches is comprehensively analyzed for both the operational modes in terms of extinction ratio (ER) as calculated by Eq. 6.1 given below:

$$ER = 10 * log_{10}\left(\frac{R_M(\lambda)}{R_S(\lambda)}\right) \quad dB \tag{6.1}$$

Here, $R_M(\lambda)$ represents the reflectance from the plasmonic switch when VO_2 is in its metallic state (i.e., ON state) and $R_S(\lambda)$ represents the reflectance from the plasmonic switch when VO_2 is in its semiconducting state (i.e., OFF state).

The multi-wavelength mode of operation can be realized by using a periodic array of IVNSs on top of a VO_2 coated plasmonic substrate as shown in Fig. 6.1(a). Figs. 6.2(a, b) show the reflectance spectra for the proposed multi-wavelength IVNSs based switch with VO_2 in its semiconducting state and metallic state, respectively. For this analysis, the thickness of the VO_2 film (t), width of VNS (W), height of VNS (H), angle between two arms of VNS (θ), and gap (G) between adjacent VNSs is taken to be 100 nm, 20 nm, 50 nm, 60°, and 30 nm, respectively. Fig. 6.2(a) shows the reflectance spectra for the IVNS based switch for different values of arm lengths of the V-shaped nanostructure (VNS) with VO_2 in its semiconducting state. As it is well known, for a VNS, there is a possibility of exciting longitudinal and transverse modes depending on the orientation of the incident electric field [14]. However, in this chapter, the incident E-field along the x-direction has been chosen (See Fig. 6.1) such

that longitudinal localized surface plasmon modes (LSPs) are predominantly excited. In accordance with the previously proposed plasmon hybridization model [33], as the individual VNSs are placed in a periodic array with close interparticle distances, there is splitting of the longitudinal LSP mode of a single VNS, and hence, two plasmonic modes — M1 and M2 — are observed in the reflectance spectra of these proposed switches. When compared to the modes of the individual VNS, mode M1 is red-shifted to higher wavelengths, and mode M2 is blue-shifted to lower wavelengths. Thus, with VO_2 in the semiconducting state, the reflectance spectra from the switch shows two dips for all values of arm lengths (See Fig. 6.2(a)), which correspond to the plasmonic longitudinal modes that are excited in the periodic array of the IVNSs. Further, as discussed in later sections, it must be noted that incident light coupled into the plasmonic mode M2 primarily leads to the localization of energy between the two arms of an individual VNS, whereas light coupled into mode M1 leads to the localization of energy between the arm tips of adjacent VNSs. It can be observed from Fig. 6.2(a) that for VNSs with lower arm lengths, i.e., for arm lengths being 40 nm and 60 nm, the strength of coupling of incident light into mode M2 is not significant, and the incident light is predominantly coupled to mode M1. However, at higher values of arm lengths, a significant amount of incident light gets coupled into mode M2. This is expected as the amount of light coupled into the plasmonic mode M2 depends on the oscillator strength between the two arms of the VNS and is expected to increase with the arm length of the VNSs [34]. Moreover, it can be observed from Fig. 6.2(a) that both modes M1 and M2 exhibit a red-shift of their respective plasmon resonance wavelengths as the arm length of the VNSs is increased. As the arm length is varied from 80 nm to 140 nm, the plasmon resonance wavelength for mode M1 red-shifts from 2065 nm to 2800 nm, and the plasmon resonance wavelength for mode M2 red-shifts from 1200 nm to 1320 nm. It must be noted that the rate of red-shifting for the plasmon resonance wavelength corresponding to the higher energy mode, M2, is lesser than that of the lower energy mode, M1, due to the larger radiative damping of mode M1 [33].

Fig. 6.2(b) shows the reflectance spectra for the IVNS based plasmonic switches for different values of arm lengths of VNSs with VO_2 in its metallic state. As shown in Fig. 6.2(b), as the thin film of VO_2 is switched from its semiconducting state to its metallic state, the real part of the refractive index of VO_2 decreases, leading to a blue-shift in the plasmon resonance wavelength of modes M1 and M2 as compared to the case when VO_2 is in its semiconducting state. However, both modes, M1 and M2, exhibit a red-shift in the plasmon resonance wavelength as the arm length of the VNSs is increased. As compared to the case when VO_2 is in its semiconducting state, the decrease in the strength of the plasmonic modes is expected as the plasmon resonance is significantly damped by the oscillations of mobile electrons in metallic VO_2 [11]. It must be noted that the contribution to the reflectance comes equally from the geometrical parameters of the V-shaped nanostructures and the material constants of the metallic nanostructures, the VO_2 layer, and the underlying substrate for the VNS based switch.

Fig. 6.2(c) shows the extinction ratio spectra, calculated in accordance with Eq. 6.1, for the IVNS based plasmonic switch for different values of arm length of the VNSs. It must be noted that although the plasmonic switch can be operated in

both the positive ER regime (i.e., when $R_M\ (\lambda) > R_S\ (\lambda)$) as well as the negative ER regime (i.e., when $R_M\ (\lambda) < R_S\ (\lambda)$), it has been chosen to carry out the extensive analysis of the switching efficiency of the proposed plasmonic switches only in the positive regime of the extinction ratio spectra, which overlaps with the NIR region of the spectrum. It can be observed from Fig. 6.2(c) that as the arm length of VNSs is varied from 40 nm to 120 nm, the highest achievable extinction ratio (extinction ratio at the higher wavelength, ER_{HW}) increases from ~ 8 dB at a wavelength of 1710 nm to 24 dB at a wavelength of 2520 nm, along with a significant red-shift in the wavelength at which the maximum ER is obtained. Moreover, as the length is increased above 80 nm, there is an emergence of a second lower wavelength ~ 1280 nm at which significant ER can be achieved, and is shown as ER_{LW} in Fig. 6.2(c). In addition, as the arm length is increased further, this additional ER_{LW} peak exhibits a steady increase in its magnitude. It can be observed from Fig. 6.2(c) that for VNSs with an arm length of 140 nm, a high extinction ratio of ~ 14 dB can be obtained at two wavelengths (i.e., 1320 nm and 2800 nm), thus exhibiting the potential of these switches to be employed for multi-wavelength plasmonic switching.

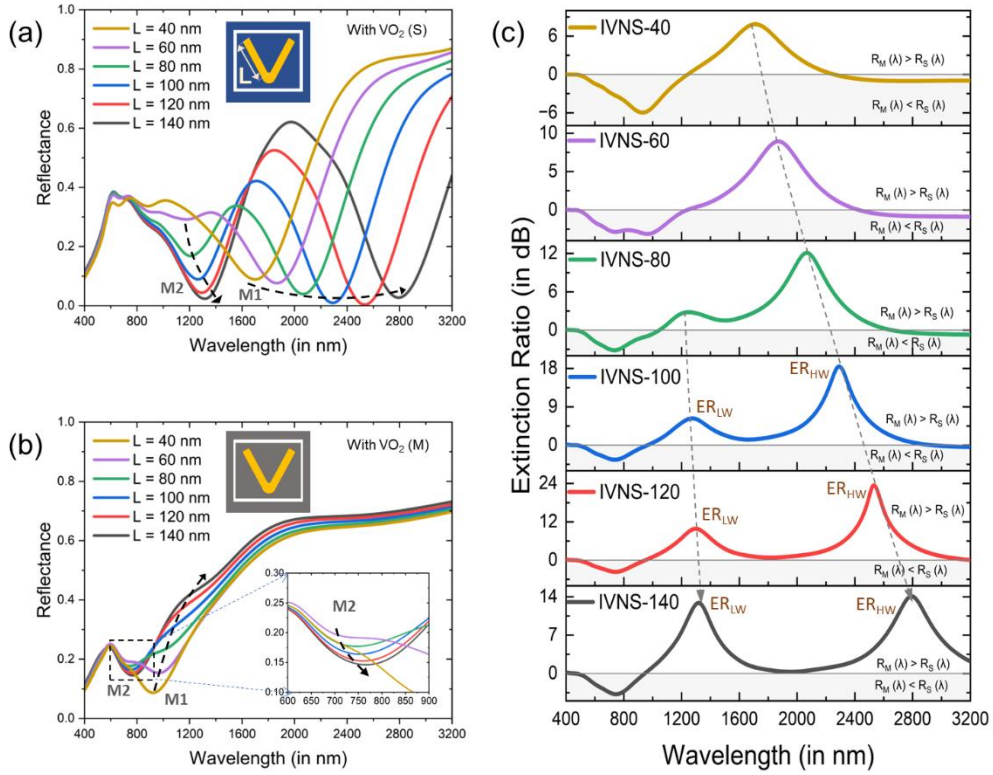

Fig. 6.2 Reflectance spectra obtained from an IVNS based plasmonic switch for different values of arm lengths of the VNSs placed on a gold coated SiO_2 substrate with VO_2 in its **(a)** semiconducting state and **(b)** metallic state. **(c)** Extinction ratio spectra for the IVNS based plasmonic switch for different values of arm lengths of the VNSs placed on a VO_2 coated gold SiO_2 substrate. The thickness of the VO_2 film (t), width of VNS (W), height of VNS (H), angle between two arms of VNS (θ), and gap (G) between adjacent VNSs is taken to be 100 nm, 20 nm, 50 nm, 60°, and 30 nm, respectively. The arm length of VNS (L) is varied from 40 nm to 140 nm.

In the case of the IVNS based switches proposed above, it could be clearly seen that the relationship between the wavelength of maximum extinction ratio (ER_{HW}) and the arm length of the VNSs is nearly linear. Hence, an additional design of the proposed switches is also proposed — with IVNSs replaced by V-shaped nanostructures with variable arm lengths (VVNSs) — for broadband operation. In these VVNS based switches, the unit cell of the periodic array forming the nanostructures, is designed with multiple VNSs, each with a different arm length. As each VNS with a different value of arm length contributes to its own specific wavelength of maximum ER, an overall broadband response for the ER is obtained from the VVNS based switches. Fig. 6.3 shows the behavior of the proposed switches as they progressively shift from exhibiting a multi-wavelength to a broadband operation by increasing the variability in the arm lengths of the subsequent VNSs in the unit cell. Figs. 6.3(a-j) show the reflectance spectra (with VO_2(S) and VO_2(M)) and the extinction ratio spectra of plasmonic switches based on a periodic array of variable V-shaped nanostructures (VVNSs) as the number of VNSs with different arm lengths in a periodic unit cell is varied from two to six. The schematic unit cells for the various VVNS based switches are shown as insets in the figures.

Fig. 6.3(a) shows the reflectance spectra of the switch with VO_2 in its semiconducting state and metallic state when a periodic array of VVNSs is employed such that one-unit cell of the periodic array consists of two VNSs — with the length of first VNS (L_1) being 140 nm and the length of second VNS (L_2) being 120 nm. It can be seen that there is one dip in the reflectance spectra at 790 nm when VO_2 is in its metallic state and two dips in the reflectance spectra at 1320 nm and 2670 nm when VO_2 is in its semiconducting state. These dips in the reflectance spectra emerge out as peaks of the extinction ratio spectra as shown in Fig. 6.3(b). Hence, multi-wavelength switching can be achieved at two wavelengths — at 1320 nm with an extinction ratio ~ 12 dB and at 2670 nm with an extinction ratio ~ 15 dB. The extinction ratio spectra for plasmonic switches based on IVNS-120 and IVNS-140 are also shown in grey for comparison. For further discussion, a generalized VVNS based switch is designated as VVNS-X-Y-Z indicating a switch based on a periodic array of VNSs where one unit cell of the array consists of varying arm lengths of VNSs with the lengths being X, Y and Z nm. Figs. 6.3(c, d) show the reflectance spectra and the extinction ratio for VVNS-140-120-100. With this configuration, multi-wavelength switching can be achieved at wavelengths of 1320 nm with an ER ~ 11 dB and at 2570 nm with an ER ~ 14 dB. With four different VNSs, the VVNS-140-120-100-80 based switch exhibits multi-wavelength switching at two wavelengths — an ER ~ 9.5 dB at a wavelength of 1320 nm and an ER ~ 11 dB at a wavelength of 2500 nm (See Figs. 6.3(e, f)). For this case, there is an emergence of a third peak at a wavelength of ~ 2065 nm with a very low ER. However, as the degree of anisotropy in arm lengths is increased further, i.e., in VVNS-140-120-100-80-60 with 5 different VNSs in one unit cell, it can be seen from Figs. 6.3(g, h), that there is a progressive change in the operation mode of the switch from being multi-wavelength to a broadband switch. With VVNS-140-120-100-80-60, the reflectance spectra for the switch with VO_2 in its semiconducting and metallic state is shown in Fig. 6.3(g). By employing this switch, an ER ~ 4 dB can be achieved over a broad operating wavelength range from 1150 nm to 2720 nm as shown in Fig. 6.3(h). The magnitude of broadband ER can be increased further by increasing

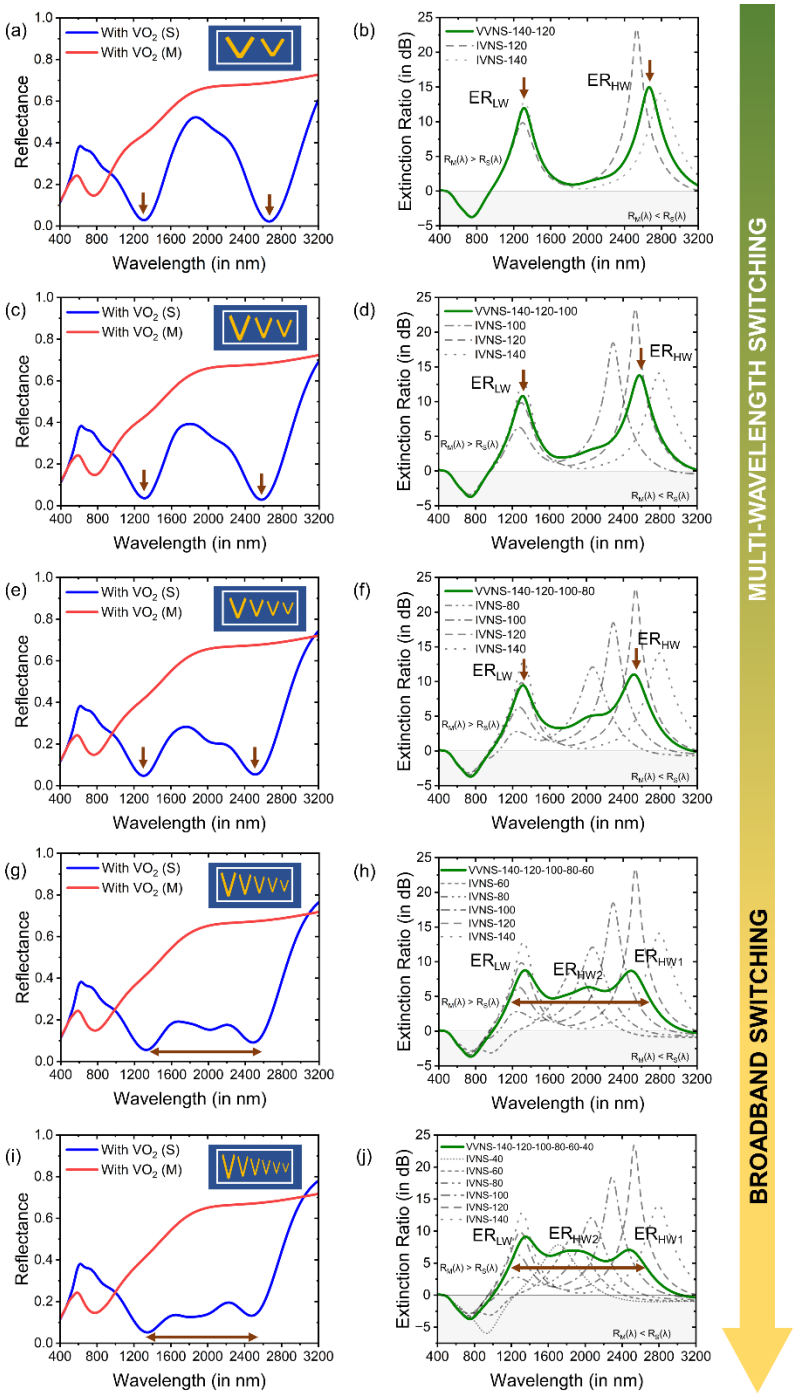

Fig. 6.3 (a) Reflection spectra with VO_2(M) and VO_2(S), and **(b)** Extinction ratio spectra for a VVNS-140-120 based plasmonic switch. **(c)** Reflection spectra with VO_2(M) and VO_2(S), and **(d)** Extinction ratio spectra for a VVNS-140-120-100 based plasmonic switch. **(e)** Reflection spectra with VO_2(M) and VO_2(S), and **(f)** Extinction ratio spectra for a VVNS-140-120-100-80 based plasmonic switch. **(g)** Reflection spectra with VO_2(M) and VO_2(S), and **(h)** Extinction ratio spectra for a VVNS-140-120-100-80-60 based plasmonic switch. **(i)** Reflection spectra with VO_2(M) and VO_2(S), and **(j)** Extinction ratio spectra for a VVNS-140-120-100-80-60-40 based plasmonic switch. The thickness of the VO_2 film (t), width of VNSs (W), height of VNSs (H), angle between two arms of VNSs (θ), and gap (G) between adjacent VNSs is taken to be 100 nm, 20 nm, 50 nm, 60°, and 30 nm, respectively.

the anisotropy in the VNSs in one unit cell of the periodic array of nanostructures on the VO_2 coated plasmonic substrate. With 6 different arm lengths, the VVNS-140-120-100-80-60-40 based switch offers a broadband operating range of 1430 nm with an ER ~ 5 dB as shown in Fig. 6.3(j), spanning over 1200 nm to 2630 nm and covering all optical communication bands, i.e., the O, E, S, C, L and U bands. These observations are also tabulated in Table 6.1 for further clarity. Fig 6.3, thus, shows that as the operational mode of the switch progresses from being multi-wavelength to broadband on increasing the anisotropy of the VNSs in a unit cell of the periodic array of nanostructures placed on a VO_2 coated plasmonic substrate, there is a trade-off between the highest achievable ER and the operational wavelength range of the switch. With lower anisotropy in the arm lengths of VNSs, high ER can be achieved at a limited number of wavelengths. However, as the anisotropy in the arm lengths is increased, although the ER decreases as compared to multi-wavelength switching, a large operational bandwidth > 1400 nm can be achieved. It must be noted that the operational bandwidth starts to saturate with six variable arm lengths for a VVNS based plasmonic switch; and hence, operational bandwidth cannot be increased further without compromising on the extinction ratio.

Fig. 6.4 shows the charge density profiles and the electric field profiles for the multi-wavelength plasmonic switch based on a periodic array of identical V-shaped nanostructures with length of VNSs as 140 nm (i.e., IVNS-140). When x-polarized light is incident on the switch with VO_2 in its semiconducting state, two longitudinal hybrid plasmonic modes M1 — at a higher wavelength — and M2 — at a lower wavelength — are observed in the reflectance spectrum of these switches as shown in Fig. 6.4(a). The charge density profiles of these hybrid modes are shown at their respective plasmon resonance wavelengths in Figs. 6.4(b, c). Figs. 6.4(f, g) show the E-field profiles for modes M1 and M2 of the IVNS based switches with VO_2 in its semiconducting state. It can be observed from Fig. 6.4(f) that light coupled into the plasmonic mode M1 primarily leads to the E-field being localized in the gaps between the tips of the adjacent V-shaped nanostructures. Fig. 6.4(g) shows that light coupled into plasmonic mode M2 leads to the localization of E-field between the two arms of the individual V-shaped nanostructures. Fig. 6.4(a) also shows the plasmonic modes excited in the proposed switch when VO_2 is in its metallic state. It can be seen that as VO_2 transforms from the semiconducting state to the metallic state, the plasmonic modes are blue-shifted and are significantly damped. The charge density profiles for the modes M1 and M2 for the case when VO_2 is in its metallic state are shown in Figs. 6.4(d, e). In addition, Figs. 6.4(h, i) show the E-field profiles for the proposed IVNS based switches with VO_2 in its metallic state. It must be noted from these E-field profiles that the plasmonic modes for the switch with VO_2 in its metallic state are heavily damped.

Fig. 6.5 shows the charge density profiles and the E-field profiles for the broadband plasmonic switch based on a periodic array of variable V-shaped nanostructures with six different arm lengths of VNSs (i.e., VVNS-140-120-100-80-60-40). Fig. 6.5(a) shows that with x-polarized light and with VO_2 in its semiconducting state, the reflectance spectrum of the switch exhibits three significant modes — two higher wavelength modes $M1_b$ and $M1_a$ and one lower wavelength mode

Table 6.1 Bandwidth and extinction ratio for different VVNS based plasmonic switches

Plasmonic switch	Multiwavelength Operation	Broadband Operation	
		Bandwidth at ER = 5 dB	Bandwidth at ER = 4 dB
VVNS-140-120	1320 nm (~ 12 dB) and 2670 nm (~ 15 dB)	-	-
VVNS-140-120-100	1320 nm (~ 11 dB) and 2570 nm (~ 14 dB)	-	-
VVNS-140-120-100-80	1320 nm (~ 9.5 dB) and 2500 nm (~ 11 dB)	-	-
VVNS-140-120-100-80-60	-	-	1570 nm
VVNS-140-120-100-80-60-40	-	1430 nm	1520 nm

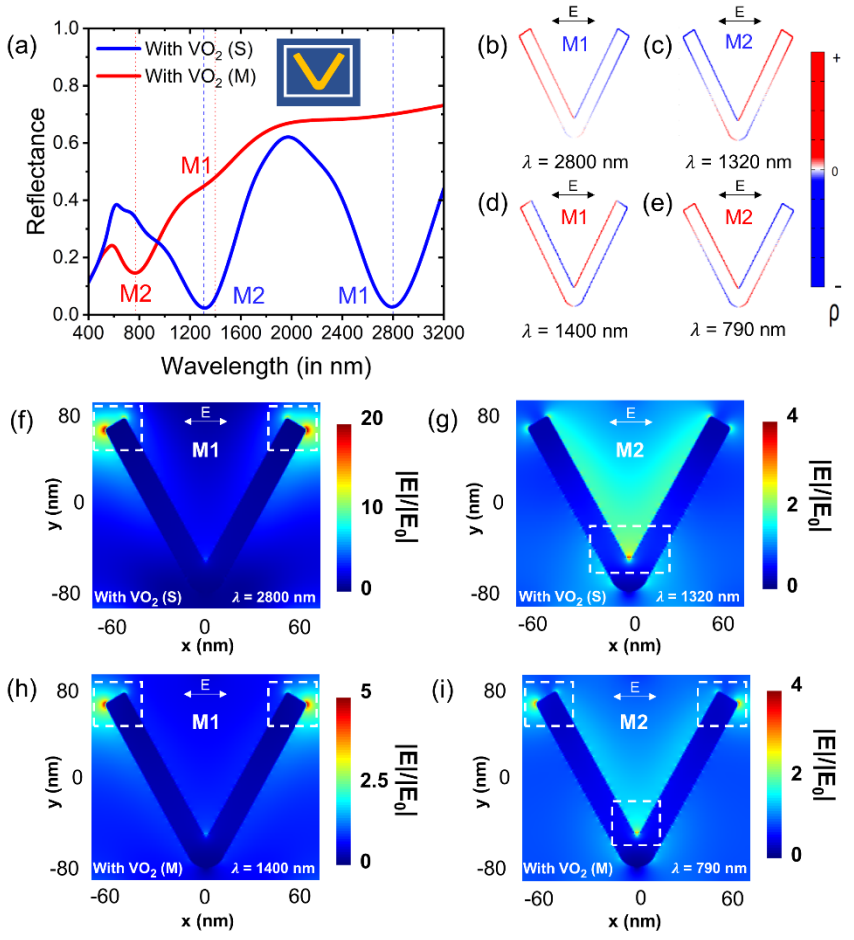

Fig. 6.4 (a) Reflectance spectra of a plasmonic switch based on a periodic array of identical V-shaped nanostructures with an arm length of 140 nm (i.e., IVNS-140) showing the modes M1 and M2 for the cases when VO_2 is in its semiconducting and metallic states. Charge density profiles for the plasmonic modes M1 and M2 of IVNS-140 based switch with VO_2 in its **(b, c)** semiconducting state, and **(d, e)** metallic state. E-field profiles for the plasmonic modes M1 and M2 of IVNS-140 based switch with VO_2 in its **(f, g)** semiconducting state, and **(h, i)** metallic state. The thickness of the VO_2 film (t), arm length of VNS (L), width of VNS (W), height of VNS (H), angle between two arms of VNS (θ), and gap (G) between adjacent VNSs is taken to be 100 nm, 140 nm, 20 nm, 50 nm, 60°, and 30 nm, respectively.

M2. Figs. 6.5(b-d) show the charge density profiles corresponding to these three plasmonic modes excited in the switch with VO_2 in its semiconducting state. In addition, Figs. 6.5(f-h) show the E-field profiles corresponding to these three modes. It can be seen from Fig. 6.5(f, g) that, for the higher wavelength plasmonic modes $M1_b$ and $M1_a$, the E-field is localized in the gaps between the adjacent VNSs. However, it must be noted that both these modes are geometry dependent plasmonic modes, and hence, the plasmon resonance wavelengths for the modes $M1_a$ and $M1_b$ are dependent on the arm lengths of the VNSs between which these modes are excited. Accordingly, it may be seen from Fig. 6.5(f) that at a wavelength of 2480 nm corresponding to mode $M1_b$, the E-field is localized between VNSs with higher arm lengths. However, Fig. 6.5(g) shows that for a wavelength of 1850 nm corresponding to mode $M1_a$, the E-field is localized between the adjacent VNSs of lower arm lengths. Fig. 6.5(h) shows that mode M1 leads to the localization of E-field between the VNSs of the lowest arm lengths, in addition to E-field localization in-between the arms of the VNSs. Fig. 6.5(a) also shows the modes of the plasmonic switch with VO_2 in its metallic state. With VO_2 in its metallic state, the switch exhibits only one mode, M2, for which the charge density profiles and the E-field profile are shown in Figs. 6.5(e, i), respectively.

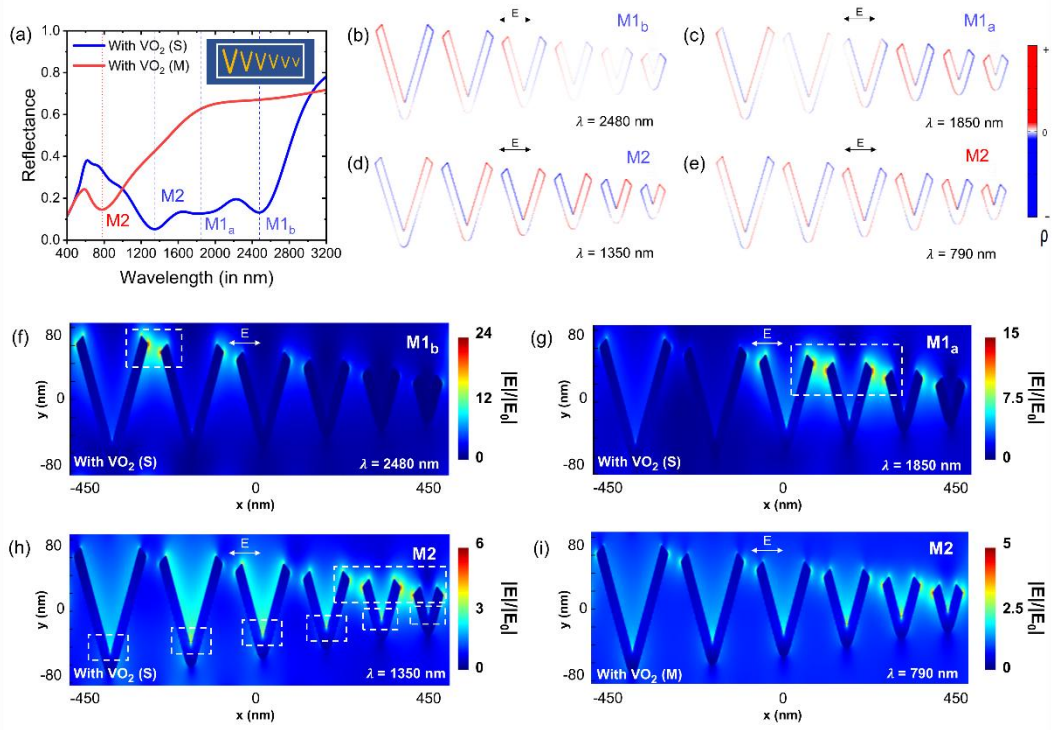

Fig. 6.5 (a) Reflectance spectra of a plasmonic switch based on a periodic array of variable V-shaped nanostructures with six different arm lengths (i.e., VVNS-140-120-100-80-60-40) showing the modes $M1_a$, $M1_b$ and M2 for the case when VO_2 is in its semiconducting state, and mode M2 when VO_2 is in its metallic state. Charge density profiles for the plasmonic modes **(b)** $M1_b$, **(c)** $M1_a$ and **(d)** M2 of the switch with VO_2 in its semiconducting state, and **(e)** M2 with VO_2 in its metallic state. E-field profiles for the plasmonic modes **(f)** $M1_b$, **(g)** $M1_a$ and **(h)** M2 of the switch with VO_2 in its semiconducting state, and **(i)** M2 with VO_2 in its metallic state. The thickness of the VO_2 film (t), width of VNSs (W), height of VNSs (H), angle between two arms of VNSs (θ), and gap (G) between adjacent VNSs is taken to be 100 nm, 20 nm, 50 nm, 60°, and 30 nm, respectively.

Fig. 6.6 shows the effect of varying the gap (G) between the two adjacent V-shaped nanostructures (VNSs) on the reflectance spectra and extinction ratio spectra of plasmonic switches based on IVNS-140 and on VVNS-140-120-100-80-60-40 when the thickness of VO_2 film (t), the width of VNS (W), the height of VNS (H), and the angle between two arms of VNS (θ) – are taken to be fixed as 100 nm, 20 nm, 50 nm, and 60°, respectively. The reflectance spectra, $R_S(\lambda)$ and $R_M(\lambda)$, for the switches with VO_2 in its semiconducting and metallic states are shown in Figs. 6.6(a, b). From Fig. 6.6(a), for the plasmonic switch based on IVNS-140, with VO_2 in its semiconducting state, it can be observed that the wavelengths corresponding to the plasmonic mode M1 and M2 undergo a red-shift and a blue-shift, respectively, as the gap between the adjacent VNSs is reduced. This can be attributed to the increased splitting between the hybrid modes M1 and M2, as the interaction between the adjacent VNSs increases on reducing the gap, G. It is also well known that, in case of coupled interactions between adjacent nanostructures, the splitting between the resultant modes becomes asymmetric as their separation decreases [33]. Thus, the higher energy (lower wavelength) mode M2 shifts downward in energy much faster as compared to the rate of upward shift in energy for the lower energy (high wavelength) mode M1. Further, it is already known from the previous discussion that the coupling of light into mode M1 primarily results in the localization of E-field between the adjacent VNSs, whereas coupling of light into mode M2 leads to the localization of E-field between the two arms of the VNS. Thus, on reducing the gap between the adjacent VNSs, the dipolar interaction between the adjacent VNSs increases, leading to a stronger plasmonic coupling and a red-shift in the plasmon resonance wavelength corresponding to mode M1 [34]. However, mode M2 experiences a near-negligible blue-shift as the gap between the two arms of the VNS remains unchanged. A similar behavior for both the modes can also be observed for the case when VO_2 is in its metallic state (See Fig. 6.6(b)). As the dips of the reflectance spectra, $R_S(\lambda)$, emerge out as peaks of the ER spectra, the wavelengths for the peak ER_{LW} and ER_{HW} exhibit a small blue-shift and significant red-shift, respectively, as the gap, G, is reduced from 40 nm to 10 nm (See Fig. 6.6(c)). Additionally, it must be noted from Fig. 6.6(c) that even at values of gaps as large as 40 nm between adjacent VNSs, which can be easily realized with state-of-the-art lithography techniques, the proposed multi-wavelength switch is able to demonstrate an extinction ratio of ~ 14 dB at two wavelengths of 1320 nm and 2700 nm.

For broadband operation, the reflectance spectra for the plasmonic switch based on VVNS-140-120-100-80-60-40 for the cases when VO_2 is in its semiconducting and metallic state are shown in Figs. 6.6(d, e), respectively. Fig. 6.6(d) shows that as the gap, G, between the adjacent VNSs is reduced, both the lower energy modes, $M1_b$ and $M1_a$, exhibit a significant red-shift of the plasmon resonance wavelength, whereas the higher energy mode M2 displays a slight blue-shift of the plasmon resonance wavelength. In addition, due to the increased interaction between the adjacent VNSs on reducing the gap, G, there is a significant redistribution of the amount of incident light coupled into the different plasmonic modes, with an increase in the plasmonic coupling of light into mode $M1_a$. Unlike the IVNS based multi-wavelength switches, in the case of VVNS based broadband switches, it can be observed from Fig. 6.6(f) that values of inter-VNS gap must be chosen such that there

is a near-equal coupling of incident light into all possible modes so that a true broadband-like characteristic in the ER spectra is obtained. For the demonstration of broadband switching, the inter-VNS gap of 30 nm was seen to exhibit a broadband behavior and hence was chosen for all the simulations carried out for this chapter.

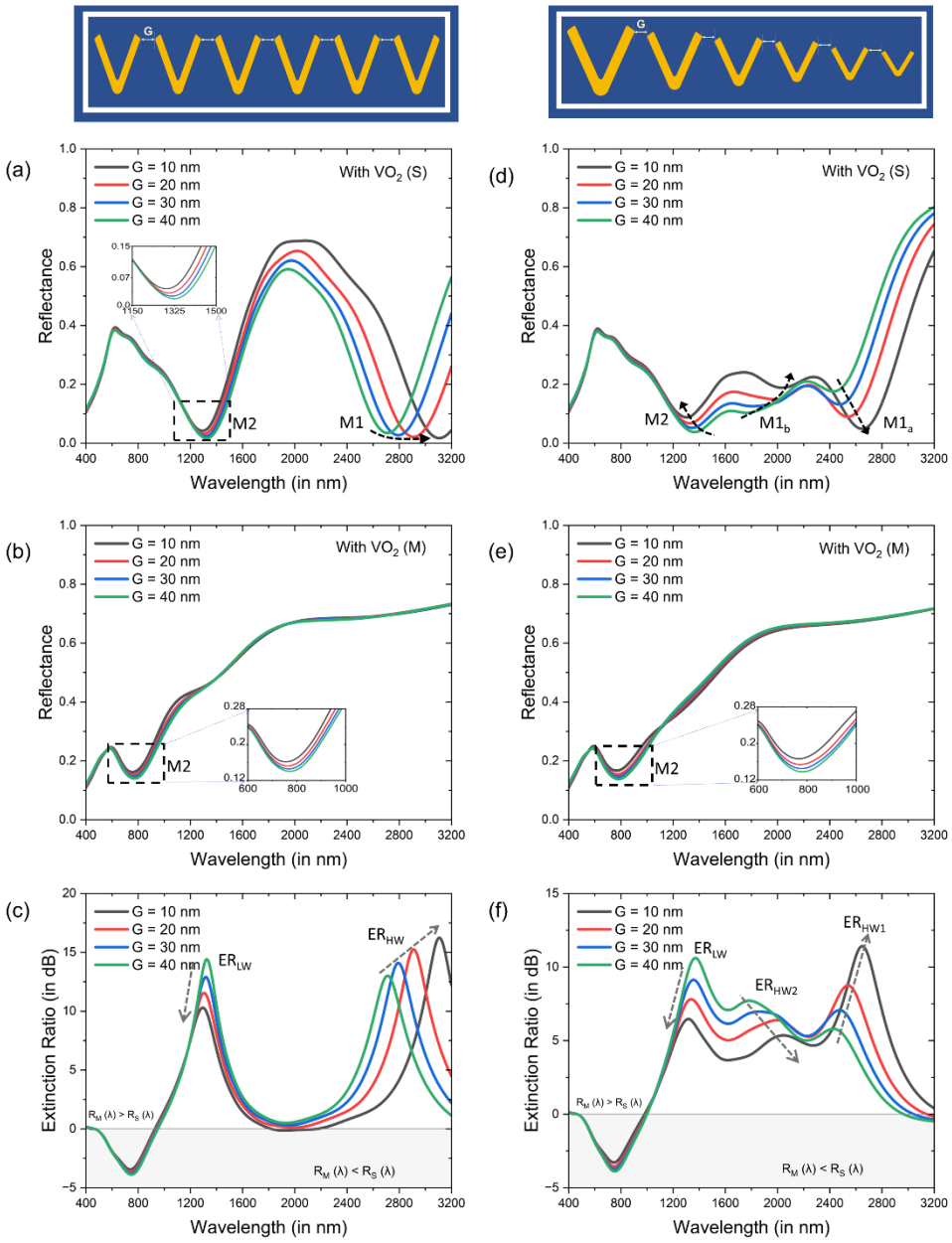

Fig. 6.6 Effect of varying the gap (G) between the two adjacent VNSs on the **(a)** reflectance spectra of IVNS-140 based switch with VO_2 in its semiconducting state, **(b)** reflectance spectra of IVNS-140 based switch with VO_2 in its metallic state, **(c)** extinction ratio spectra of IVNS-140, **(d)** reflectance spectra of VVNS-140-120-100-80-60-40 based switch with VO_2 in its semiconducting state, **(e)** reflectance spectra of VVNS-140-120-100-80-60-40 based switch with VO_2 in its metallic state, and **(f)** extinction ratio spectra of VVNS-140-120-100-80-60-40 based switch. The thickness of VO_2 film (t), width of VNSs (W), height of VNSs (H), and angle between two arms of VNSs (θ) is taken to be 100 nm, 20 nm, 50 nm, and 60°, respectively.

Fig. 6.7 shows the effect of varying the angle between the two arms of the V-shaped nanostructures (VNS) while keeping the inter-VNS gap, *G*, constant as 30 nm. The thickness of VO_2 film (*t*), the width of VNS (*W*), and the height of VNS (*H*) – are taken to be 100 nm, 20 nm, and 50 nm, respectively. It can be seen From Fig. 6.7(a) that for an IVNS based switch, with VO_2 in its semiconducting state, as the angle (θ) between the two arms of the VNS is increased, the plasmonic dip corresponding to mode M2 becomes weaker, which can be attributed to the reduced dipolar interaction between the two arms due to the increasing separation between them. The increasing separation between the two arms of the VNS also results in a blue-shift in the plasmon resonance wavelength for mode M2, similar to the electromagnetic behavior of a dimer of nanorods [34]. For the IVNS-140 based switch, this decreased coupling of incident light can also be seen in the E-field maps for mode M2 at the respective plasmon resonance wavelengths, for various values of angles, θ (See Fig. 6.7(b)). However, mode M1 exhibits an opposite behavior as angle, θ, is increased. Fig. 6.7(a) shows that the plasmonic dip corresponding to the coupling of incident light into mode M1 becomes stronger and exhibits a significant red-shift as the value of angle, θ, is increased. This suggests that the proportion of incident light coupled into plasmonic modes M1 and M2 is dependent on their relative efficiency of their excitation. A decrease in the efficiency of incident light coupling into mode M1 would, thus, imply an increase in the efficiency of light getting coupled into the plasmonic mode M2. The E-field profiles corresponding to mode M2 for the IVNS-140 with VO_2 in its semiconducting state are shown in Fig. 6.7(b) for different values of angles and show the increase in the light coupled into Mode M2 between the tips of the adjacent VNSs with an increase in the angle, θ. For the case when VO_2 switches to its metallic state, the reflectance spectra from the switch shows a decrease in the magnitude of the plasmonic dip corresponding to mode M2 along with a blue-shift in the plasmon resonance wavelength as the angle, θ, is increased (See Fig. 6.7(c)). The corresponding E-field profiles for the IVNS-140 with VO_2 in its metallic state are shown in Fig. 6.7(d). Mode M1 appears to be heavily damped in this case due to the oscillations of mobile electrons in the metallic state of VO_2. Fig. 6.7(e) shows the ER spectra for the IVNS-40 for the different values of angle, θ. In accordance with the EM behavior seen for the switch in case of the semiconducting and metallic states of VO_2, as the angle, θ, is increased, the peaks of the extinction ratio, ER_{LW} and ER_{HW} show a decreased strength with blue-shift in the plasmon resonance, and an increased strength with a red-shift in the plasmon resonance, respectively. Thus, for the IVNS based multi-wavelength switch, it can be concluded that the angle, θ, can be appropriately varied to tune the wavelengths of maximum ER and to control the trade-off between the magnitude of ER_{LW} and ER_{HW} that can be offered by the switch.

Figs. 6.7(f) shows the reflectance spectra for a VVNS-140-120-100-80-60-40 based switch, with VO_2 in its semiconducting state. It can be seen from Fig. 6.7(f) that mode M2 experiences a blue-shift in the plasmon resonance wavelength along with a decrease in the magnitude of its reflectance spectra dip, as the value of angle, θ, is increased, while modes $M1_b$ and $M1_a$ exhibit an opposite behavior similar to the case of the IVNS-140 based plasmonic switch explained earlier. The E-field profiles for the VVNS based plasmonic switch are shown in Fig. 6.7(g) for all 3 modes with the values of the angle, θ, being 30° and 75°. Figs. 7(h, i) show the effect of angle,

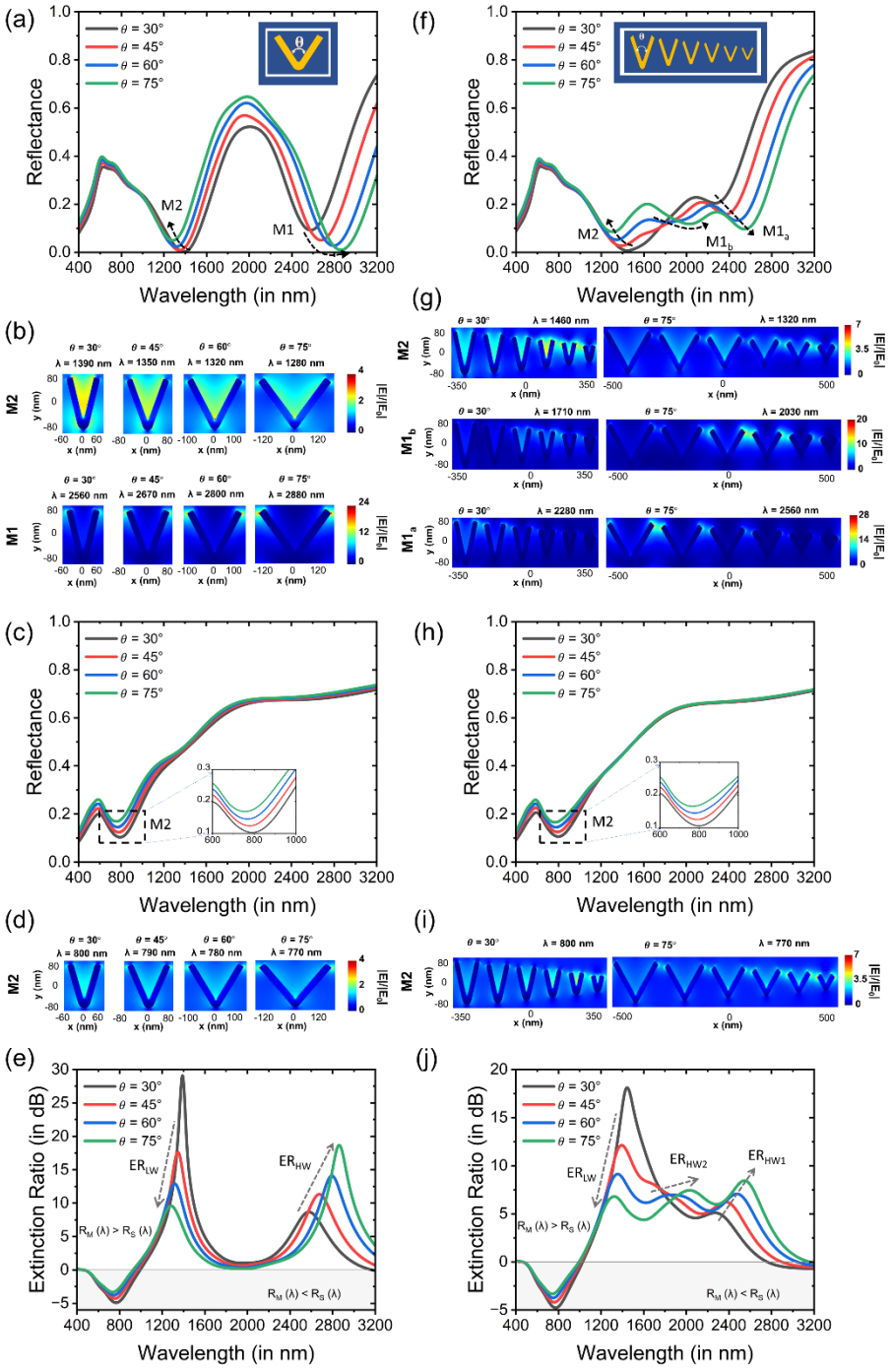

Fig. 6.7 Effect of varying the angle between two arms of VNS (θ) of an IVNS-140 based switch on the **(a)** Reflectance spectra and **(b)** E-field profiles for Mode M1 and M2, with VO_2 in its semiconducting state; **(c)** Reflectance spectra and **(d)** E-field profiles for Mode M2, with VO_2 in its metallic state; and **(e)** Extinction ratio spectra. Effect of varying the angle between two arms of VNS (θ) of a VVNS-140-120-100-80-60-40 based switch on the **(f)** Reflectance spectra and **(g)** E-field profiles for Mode $M1_a$, $M1_b$ and M2, with VO_2 in its semiconducting state; **(h)** Reflectance spectra and **(i)** E-field profiles for Mode M2, with VO_2 in its metallic state; and **(j)** Extinction ratio spectra. The thickness of VO_2 film (t), width of VNSs (W), height of VNSs (H), and gap (G) between adjacent VNSs is taken to be 100 nm, 20 nm, 50 nm, and 30 nm, respectively.

θ, on the reflectance spectra and the E-field profiles for the VVNS based switch for the case when VO_2 is in its metallic state. The ER spectra for the VVNS based switch for various values of angle, θ, is shown in Fig. 6.7(j). It can be observed that, as the angle, θ, is increased, the wavelength corresponding to ER_{LW} exhibits a blue-shift along with a decrease in the magnitude of ER_{LW}, whereas both ER_{HW1} and ER_{HW2} exhibit an increase in their magnitude along with a red-shift of their corresponding wavelengths. Therefore, for a broadband VVNS based switch, the variation in angle, θ, can be used to ensure the coupling of incident light nearly-equally into all possible plasmonic modes, to ensure a true broadband behavior of the plasmonic switch.

Fig. 6.8 shows the extinction ratio map showing the effect of varying the thickness of VO_2 film, *t*, on the extinction ratio spectra of IVNS-140 based switch (suitable for multi-wavelength switching) and VVNS-140-120-100-80-60-40 based switch (suitable for broadband switching). Fig. 6.8(a) shows the effect of varying the VO_2 layer thickness from 60 nm to 160 nm on the ER spectra for IVNS-140 based switch. It can be observed that the ER peak at the lower wavelength (ER_{LW}) exhibits a significant red-shift from 840 nm to 1760 nm on varying the thickness of VO_2 film from 60 nm to 160 nm. However, the ER peak at the higher wavelength (ER_{HW}) shows a lesser red-shift from 2650 nm to 3140 nm with large changes in the extinction ratio when the thickness of VO_2 film is varied from 60 nm to 160 nm. It must be noted that for a true multi-wavelength mode of operation, the ER at the two wavelengths of operation should be almost comparable to ensure the same switching performance at both wavelengths. For IVNS-140 based switch, a VO_2 layer thickness of 100 nm resulted in an almost equal ER ~ 14 dB at 1320 nm and 2800 nm. Hence, the optimal thickness of 100 nm was used throughout this work for all analyses. Figs. 6.9(a-c) show the detailed effect of thickness on the reflectance spectra and ER spectra for the IVNS-40 based switch, when VO_2 is in its semiconducting and metallic state, respectively.

Fig. 6.8(b) shows the extinction ratio map showing the effect of varying the VO_2 layer thickness from 60 nm to 160 nm on the ER spectra for VVNS-140-120-100-80-60-40 based switches. It can be observed that for VO_2 thicknesses lower than 80 nm, there is only one significant ER peak, and hence, the switch exhibits a single-wavelength mode of operation. However, as the VO_2 thickness is increased beyond 80 nm, multiple plasmonic peaks, as described in Fig. 6.3, emerge, leading to an overall broadband operation. However, for a true broadband operation, a near-similar ER should be achievable over the wavelength range of operation. Hence, it can be concluded from Fig. 6.8(b) that a VO_2 thickness between 100 nm to 120 nm should be employed where an ER > 5 dB is achievable over an ultra-wide wavelength range, i.e., wavelength range of 1430 nm with 100 nm VO_2 thickness, 1400 nm with 110 nm VO_2 thickness, and 1370 nm with 120 nm VO_2 thickness. Figs. 6.9(d-f) show the detailed effect of thickness on the reflectance spectra and ER spectra for the VVNS based switch, when VO_2 is in its semiconducting and metallic state, respectively.

It must be noted that the VO_2 thin films employed in this work to achieve the switching action are sensitive to the ambient environment. More specifically, VO_2 is known to gradually transform into its most thermos-dynamically stable phase, i.e.,

V_2O_5 or its hydroxides. This transformation leads to a significant decrease in the phase transition magnitude of these films [35]. Hence, for practical applications, to ensure environmental stability, the proposed switches can be coated with a transparent hydrophobic polymeric material such as polydimethylsiloxane (PDMS) [36-38]. The protective PDMS coating not only prevents the VO_2 film from oxidation and degradation on reaction with moisture, but also provides an enhanced switching performance. In addition to PDMS, thin films of hafnium dioxide (HfO_2) may also be employed to prevent degradation against humidity in the ambient environment [35]. HfO_2 is hydrophobic, has a low water vapor transmission rate, and possesses excellent mechanical properties.

As a proof of concept, an analysis of the effect of coating the proposed switch with a thick (~ 200 nm) PDMS layer is shown in Fig. 6.10. On coating with PDMS, the performance of the switch significantly improves for both the multi-wavelength and broadband switches, along with its increased environmental stability against degradation. It can be seen from Fig. 6.10 that the bandwidth of the VVNS-140-120-100-80-60-40 based plasmonic switch increases from 1430 nm to 2030 nm at an extinction ratio of 5 dB, when the switch is coated with a 200 nm PDMS layer. Moreover, all 3 extinction ratio peaks exhibit a significant rise in the extinction ratio.

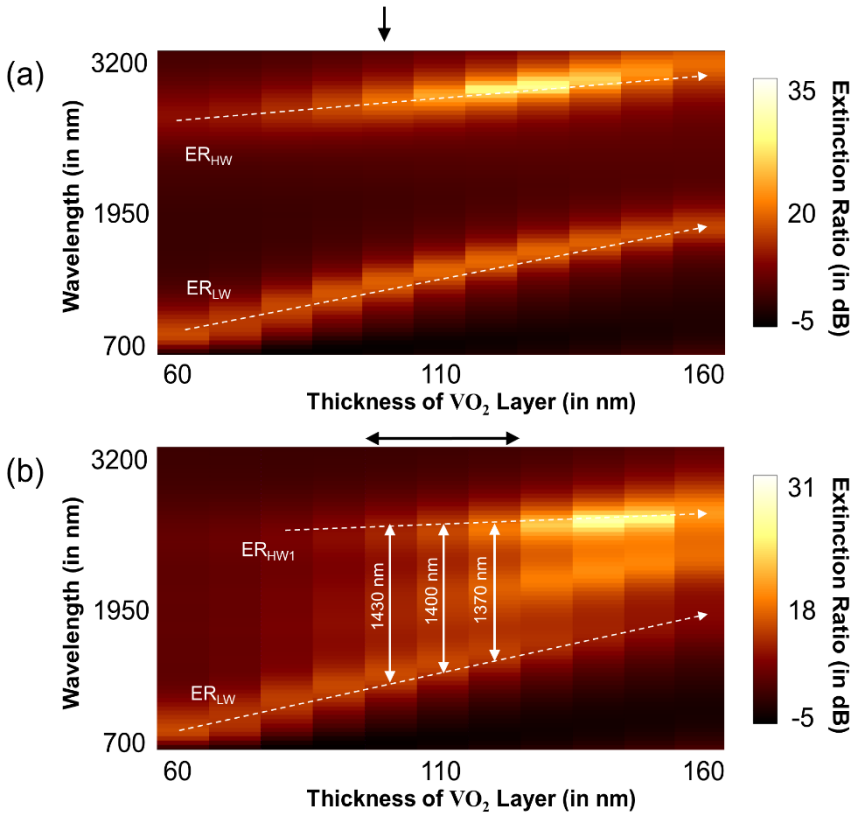

Fig. 6.8 Extinction ratio maps showing the effect of varying the thickness of the VO_2 film (t) on the extinction ratio spectra of **(a)** IVNS-140 based switch and **(b)** VVNS-140-120-100-80-60-40 based switch. The width of VNSs (W), height of VNSs (H), angle between two arms of VNSs (θ), and gap (G) between adjacent VNSs is taken to be 20 nm, 50 nm, 60°, and 30 nm, respectively.

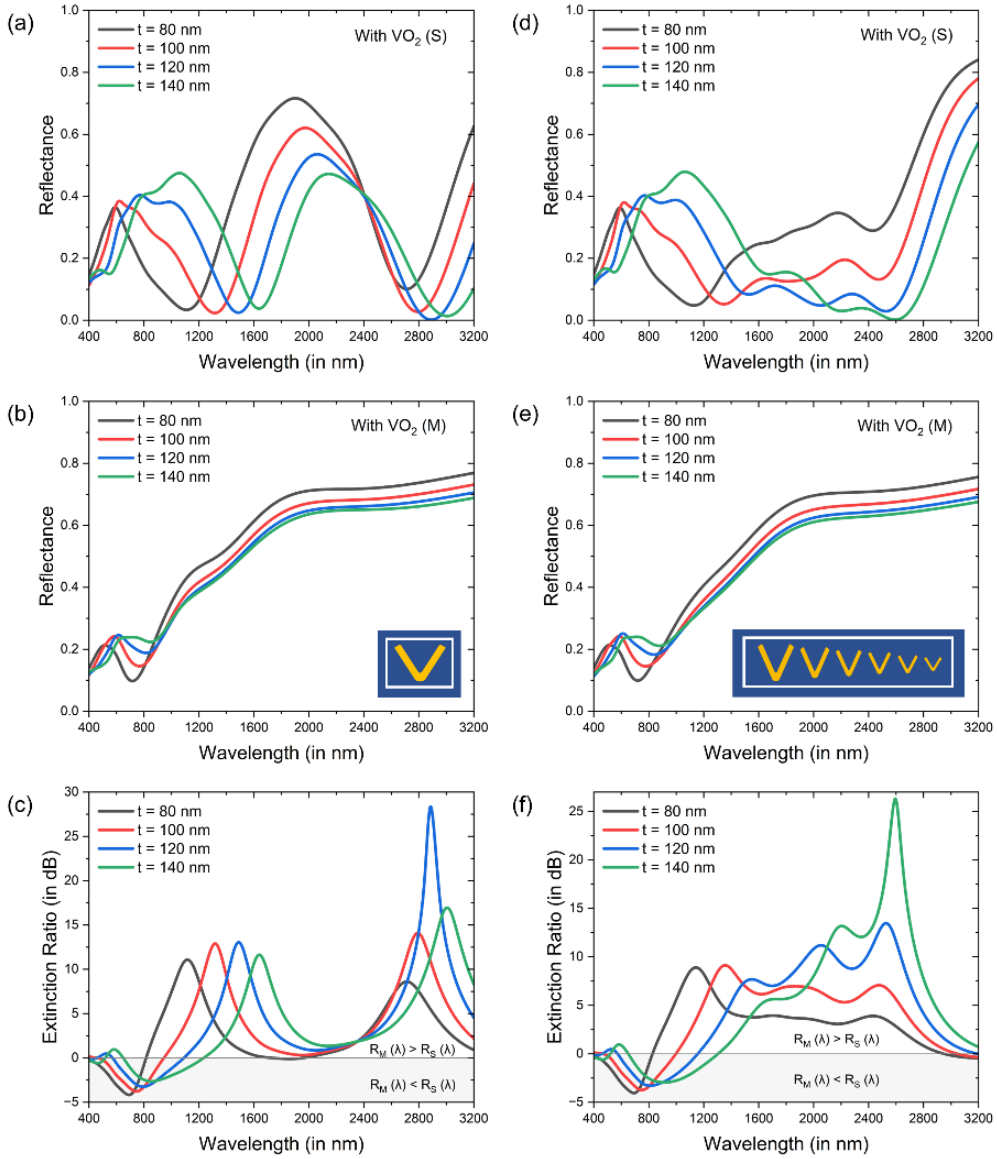

Fig. 6.9 Effect of varying the thickness of VO_2 layer (t) on the **(a)** reflectance spectra of IVNS-140 based switch with VO_2 in its semiconducting state, **(b)** reflectance spectra of IVNS-140 based switch with VO_2 in its metallic state, **(c)** extinction ratio spectra of IVNS-140 based switch, **(d)** reflectance spectra of VVNS-140-120-100-80-60-40 based switch with VO_2 in its semiconducting state, **(e)** reflectance spectra of VVNS-140-120-100-80-60-40 based switch with VO_2 in its metallic state, and **(f)** extinction ratio spectra of VVNS-140-120-100-80-60-40 based switch. The width of VNSs (W), height of VNSs (H), angle between two arms of VNSs (θ), and gap between the adjacent VNSs (G) is taken to be 20 nm, 50 nm, 60°, and 30 nm, respectively.

The effect of polarization of incident light on the reflectance spectra and extinction ratio spectra of the IVNS-140 and VVNS-140-120-100-80-60-40 based plasmonic switches is also analyzed by varying the angle of polarization, ϕ, from 0° to 90° as is shown in Fig. 6.11. Figs. 6.11(a, b) show the reflectance spectra of IVNS-140 based switches with VO_2 in its semiconducting state and metallic state, respectively. It can be observed from Fig. 6.11(a) that as the polarization of incident light is changed

from a longitudinally polarized light in x-direction to a transverse-polarized light in y-direction by varying the polarization angle, ϕ, from 0° to 90°, the number of significant plasmonic dips in the reflectance spectra are reduced from two – at 1320 nm and 2800 nm – to one – at 2000 nm. These plasmonic dips emerge as extinction ratio peaks in the ER spectra (See Fig. 6.11(c)), thus showing a shift from a multi-wavelength mode of operation to a single-wavelength mode of operation for the IVNS-140 based plasmonic switches along with a decrease in the extinction ratio from ~ 14 dB to ~ 8 dB. Similar behavior can also be observed from Figs. 6.11(d, f) for the VVNS-140-120-100-80-60-40 based switches where the broadband mode of operation changes to a single-wavelength mode of operation by varying the polarization angle, ϕ, from 0° to 90°. For x-polarized light, three plasmonic modes of VVNS-140-120-100-80-60-40 at 1350 nm, 1850 nm and 2480 nm can be seen for the case when VO_2 is in its semiconducting state, whereas a single plasmonic mode is observed at 1780 nm for y-polarized light. Thus, for the proposed plasmonic switches to work in the multi-wavelength and broadband mode of operation, the incident light was taken to be x-polarized, i.e., $\phi = 0°$, and transverse polarization was not employed.

Further, a polarization-independent design — a bidirectional VVNS (Bi-VVNS) based switch with variable VNSs in both x and y direction such that each VNS is rotated by 45° — has also been proposed. Fig. 6.12 shows the extinction ratio spectra of Bi-VVNS-140-120-100 based plasmonic switch for both the x-polarization and y-polarization. The thickness of VO_2 layer (t), width of VNSs (W), height of VNSs (H), angle between two arms of VNSs (θ), and gap between the adjacent VNSs (G) is taken to be 100 nm, 20 nm, 50 nm, 60°, and 40 nm, respectively. It can be observed from Fig. 6.12 that the Bi-VVNS-140-120-100 based switch works well for both the polarization states with a bandwidth of ~ 1400 nm spanning from wavelength of 1200 nm to 2600 nm but offers a limited ER of ~ 2.5 dB. Hence, it can be concluded that there is a trade-off between the peak ER achievable and the degree of polarization independence in the design of the proposed switches.

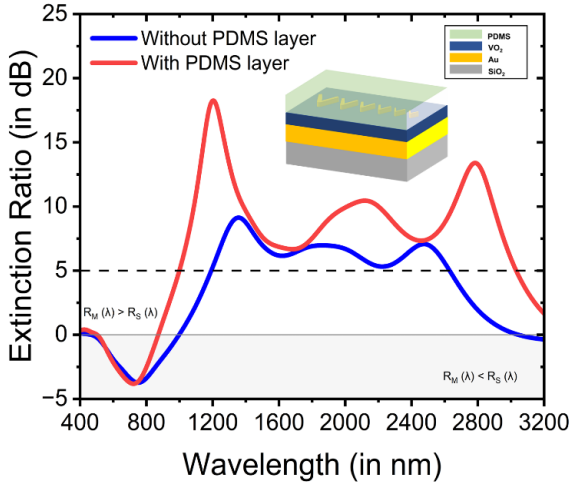

Fig. 6.10 Extinction ratio spectra of VVNS-140-120-100-80-60-40 based plasmonic switch with and without PDMS layer. The thickness of PDMS layer, thickness of VO_2 layer (t), width of VNSs (W), height of VNSs (H), angle between two arms of VNSs (θ), and gap between the adjacent VNSs (G) is taken to be 200 nm, 100 nm, 20 nm, 50 nm, 60°, and 30 nm, respectively.

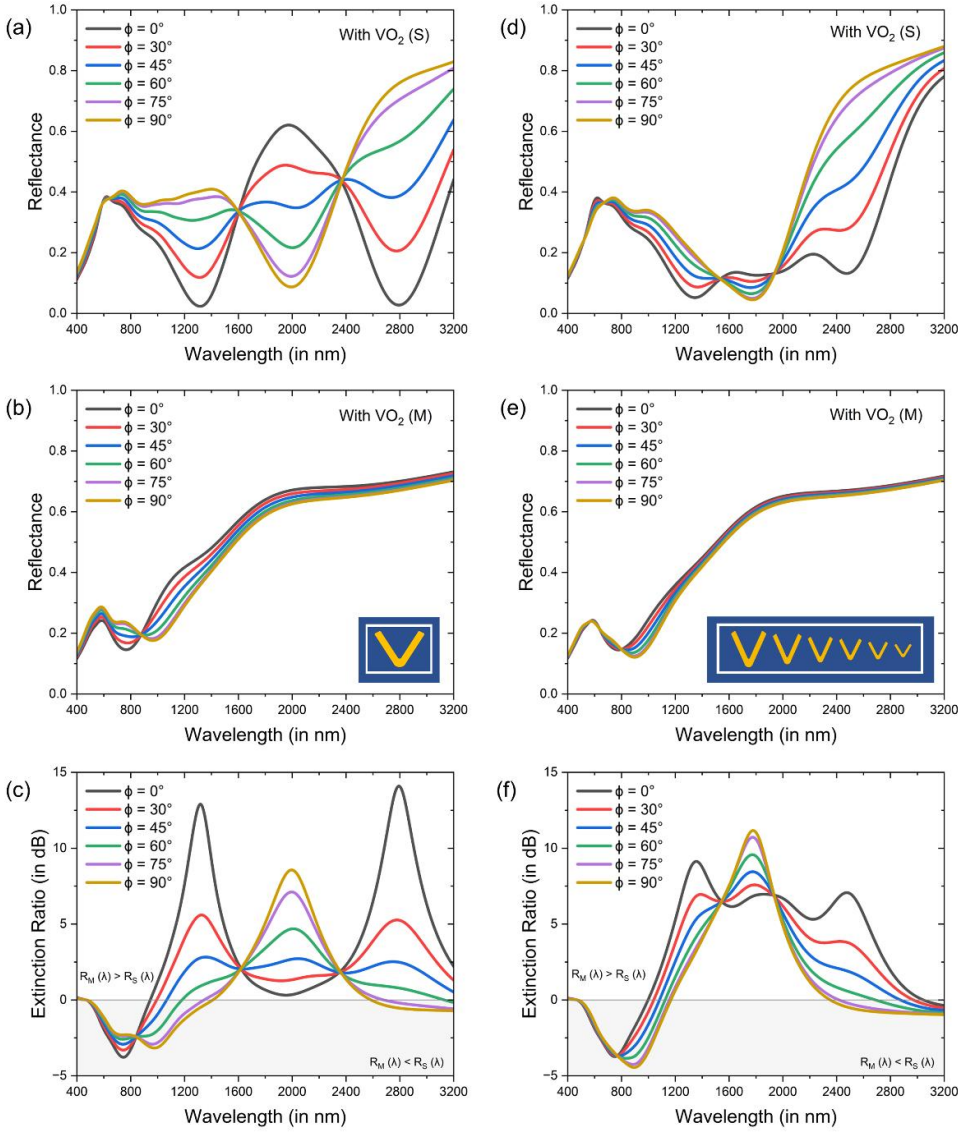

Fig. 6.11 Effect of varying the polarization angle (ϕ) of incident light on the **(a)** reflectance spectra of IVNS-140 based switch with VO_2 in its semiconducting state, **(b)** reflectance spectra of IVNS-140 based switch with VO_2 in its metallic state, **(c)** extinction ratio spectra of IVNS-140 based switch, **(d)** reflectance spectra of VVNS-140-120-100-80-60-40 based switch with VO_2 in its semiconducting state, **(e)** reflectance spectra of VVNS-140-120-100-80-60-40 based switch with VO_2 in its metallic state, and **(f)** extinction ratio spectra of VVNS-140-120-100-80-60-40 based switch. The thickness of VO_2 layer (t), width of VNSs (W), height of VNSs (H), angle between two arms of VNSs (θ), and gap between the adjacent VNSs (G) is taken to be 100 nm, 20 nm, 50 nm, 60°, and 30 nm, respectively.

Thus, the proposed IVNS and VVNS based plasmonic switches are capable of operating in the multi-wavelength and broadband mode of operation, respectively. A comparison between the multi-wavelength and broadband VO_2 based plasmonic switches proposed earlier and the current work is given in Table 6.2. Further, the geometrical parameters of the proposed switches can be varied to tune the wavelength range of operation and the ER achievable through these switches. Moreover, as these switches are based on VO_2, they can be potentially employed for

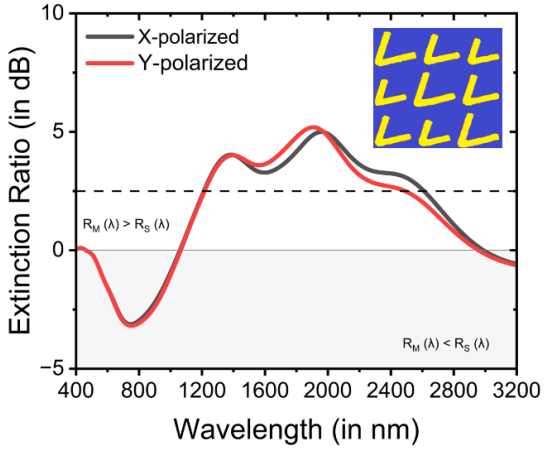

Fig. 6.12 Extinction ratio spectra of x-polarized and y-polarized 45° rotated Bi-VVNS-140-120-100 based plasmonic switch. The thickness of VO_2 layer (t), width of VNSs (W), height of VNSs (H), angle between two arms of VNSs (θ), and gap between the adjacent VNSs (G) is taken to be 100 nm, 20 nm, 50 nm, 60°, and 40 nm, respectively.

ultrafast multi-wavelength and broadband switching in applications such as optical networks. In the future, the performance of the proposed active plasmonic switch can be improved in terms of the highest ER achievable and the operational bandwidth by exploring additional designs. Further, broadband and multi-wavelength switches for the visible range of the spectrum (< 1000 nm) can be proposed with high extinction ratios, such that these switches could be employed for visible light communication. Moreover, multi-wavelength and broadband switching by employing other phase change materials in addition to VO_2 can also be explored for the visible, near-IR and mid-IR wavelength regimes.

6.5 Chapter Summary

Periodic arrays of V-shaped plasmonic nanostructures with identical arm lengths (IVNSs) and variable arm lengths (VVNSs) on VO_2 coated plasmonic substrates were proposed for multi-wavelength and broadband plasmonic switching, respectively. FDTD modelling of the IVNS based multi-wavelength plasmonic switches was carried out and an extinction ratio (ER) > 12 dB was demonstrated at two wavelengths in the near-IR wavelength range. Further, it was demonstrated that the wavelength of operation and the ER of these switches could be tuned by varying the geometrical parameters of these switches. In addition, broadband plasmonic switching was exhibited by employing periodic arrays of VNSs with variable arm lengths on top of a VO_2 coated plasmonic substrate. These switches, with six variable arm lengths in a unit cell of the periodic array, exhibited an ER > 5 dB over a wide wavelength range > 1400 nm spanning all optical communication bands, i.e., the O, E, S, C, L and U bands. Further, the effect of inter-VNS gap, the thickness of the VO_2 layer, and the angle between the arms of a VNS on the electromagnetic behavior of the plasmonic modes excited in these switches was exhaustively analyzed. It can be concluded that, for the proposed switches, as the anisotropy of the arm lengths of the VNSs in a unit cell of the periodic array placed on the VO_2 coated plasmonic substrate is increased, the operational mode of the switch progresses from being multi-wavelength to

broadband. In addition, as the switch progresses from being multi-wavelength to broadband, a trade-off is observed between the highest achievable ER and the operational wavelength range of the switch. The proposed switches have the potential to be employed in communication networks where ultrasmall and ultrafast switches with wide operational bandwidth are inevitable.

Table 6.2 Comparison of proposed IVNS and VVNS based work with previous works

Ref.	Brief Description of the Design	Band width	Highest ER*/ ΔOD#	Advantages	Potential Limitations
Joushaghani *et al.* [8]	Hybrid SPP-VO_2 waveguide switch	> 100 nm	ER ~ 20 dB	• Compact (micron-scale) • Low voltage (400 mV) operation • Integrated electric control	• Small operational bandwidth ~ 100 nm
Sun *et al.* [9]	Hybrid combination of aluminium nanoholes and VO_2	~ 650 nm	ER ~ 5 dB	• Operating wavelength range over 650 nm • Polarization-independent	• Operational bandwidth < 700 nm • Limited to the C, L and U band
Guo *et al.* [11]	Indium-tin oxide nanorod array (ITO-NRA) coated with VO_2	~ 250 nm	ΔOD ~ 0.2	• Sub-picosecond response time • Visible to mid-IR operation	• High power consumption
This work	Array of identical V-shaped nanostructures (IVNSs) and variable V-shaped nanostructures (VVNSs)	> 1400 nm	ER > 5 dB for broadband operation ER > 12 dB for multi-wavelength operation	• Multi-wavelength switching with high ER > 12 dB • Broadband switching with wide operational wavelength range (> 1400 nm) and moderate ER (> 5 dB) • Operational wavelength spanning the O, E, S, C, L and U bands	• ER < 5 dB for the polarization-independent design of the proposed switches

*ER: Extinction Ratio #ΔOD: Change in Optical Density

6.6 References

[1] Wuttig, M., Bhaskaran, H., and Taubner, T. "Phase-change materials for non-volatile photonic applications", *Nature Photonics*, 11, 465-476, 2017. https://doi.org/10.1038/nphoton.2017.126

[2] Yoo, H. *et al.* "Switching on versatility: Recent advances in switchable plasmonic nanostructures", *Small Science*, 3(10), 2300048, 2023. https://doi.org/10.1002/smsc.202300048

[3] Zhang, X., and Yang, J. "Ultrafast plasmonic optical switching structures and devices", *Frontiers in Physics*, 7, 190, 2019. https://doi.org/10.3389/fphy.2019.00190

[4] Kartalopoulos, S. V. *Free space optical networks for ultra-broad band services*. Wiley-IEEE Press, 2011. ISBN: 978-0-470-64775-2

[5] Davis, T. J., Gomez, D. E., and Roberts, A. "Plasmonic circuits for manipulating optical information", *Nanophotonics*, 6(3), 543-559, 2016. http://doi.org/10.1515/nanoph-2016-0131

[6] Rashidi, A., Entezar, S. R., and Hatef, A. "Tunable multispectral near-infrared absorption with a phase transition of VO_2 nanoparticles hybridized with 1D photonic crystals", *Nanotechnology*, 31(33), 335701, 2020. http://doi.org/10.1088/1361-6528/ab8e76

[7] Sharma, Y. *et al.* "Plasmonic switches based on arrays of plasmonic nanostructures surrounded by VO_2 thin films", *Quantum Sensing and Nano Electronics and Photonics XVI*, 109262S, 2019. https://doi.org/10.1117/12.2511206

[8] Joushaghani, A. *et al.* "Sub-volt broadband hybrid plasmonic-vanadium dioxide switches", *Applied Physics Letters*, 102(6), 061101, 2013. http://doi.org/10.1063/1.4790834

[9] Sun, M. *et al.* "A photonic switch based on a hybrid combination of metallic nanoholes and phase-change vanadium dioxide", *Scientific Reports*, 8, 11106, 2018. http://doi.org/10.1038/s41598-018-29476-6

[10] Mandal, P., Mohan, S., Sharma, S., and Goyat, M. S. "Broadband multi-resonant circular dichroism in metal-VO_2 hybrid dagger-like plasmonic structure for switching application", *Photonics and Nanostructures - Fundamentals and Applications*, 37, 100735, 2019. http://doi.org/10.1016/j.photonics.2019.100735

[11] Guo, P. *et al.* "Conformal coating of a phase change material on ordered plasmonic nanorod arrays for broadband all-optical switching", *ACS Nano*, 11(1), 693-701, 2016. http://doi.org/10.1021/acsnano.6b07042

[12] Chubich, D. A., Zvagelsky, R. D., Pisarenko, A. V., Zhukova, E. S., and Vitukhnovsky, A. G. "Optical properties of plasmonic nanoantennas based on arrays of interacting V-shaped structures in the mid-IR range", *Bulletin of the Lebedev Physics Institute*, 46(11), 344-347, 2019. https://doi.org/10.3103/S1068335619110046

[13] Jiao, J. *et al.* "Study on focusing properties of broadband range and oblique incidence on the basis of V-shaped nanoantenna", *Applied Physics A*, 122, 942, 2016. https://doi.org/10.1007/s00339-016-0449-1

[14] Stokes, N., Cortie, M. B., Davis, T. J., and McDonagh, A. M. "Plasmon resonances in V-shaped gold nanostructures", *Plasmonics*, 7, 235-243, 2012. https://doi.org/10.1007/s11468-011-9299-z

[15] Liaw, J. W., Huang, C. W., Huang, M. C., and Kuo, M. K. "Plasmon-enhanced optical bending and heating on V-shaped deformation of gold nanorod", *Applied Physics A*, 124, 17, 2018. https://doi.org/10.1007/s00339-017-1433-0

[16] Zhang, Y., and Zhang, Z. "Ultra-subwavelength and low loss in V-shaped hybrid plasmonic waveguide", *Plasmonics*, 12, 59-63, 2017. https://doi.org/10.1007/s11468-016-0228-z

[17] Li, J. *et al.* "Zigzag localized surface plasmon resonance wavelength shift of asymmetric V-shape Ag nanorods", *The Journal of Physical Chemistry C*, 122(30), 17400-17405, 2018. https://doi.org/10.1021/acs.jpcc.8b01786

[18] Wegkamp, D. *et al.* "Instantaneous band gap collapse in photoexcited monoclinic VO_2 due to photocarrier doping", *Physical Review Letters*, 113(21), 216401, 2014. https://doi.org/10.1103/PhysRevLett.113.216401

[19] Wall, S. *et al.* "Ultrafast changes in lattice symmetry probed by coherent phonons", *Nature Communications*, 3, 721, 2012. https://doi.org/10.1038/ncomms1719

[20] Xu, Z., Qin, G., Bernussi, A. A., and Fan, Z. "Electrothermally control of dynamic infrared switching of VO_2 thin film on FTO glass", *Journal of Alloys and Compounds*, 858, 157640, 2021. https://doi.org/10.1016/j.jallcom.2020.157640

[21] Kruger, B. A., Joushaghani, A., and Poon, J. K. S., "Design of electrically driven hybrid vanadium dioxide (VO_2) plasmonic switches", *Optics Express*, 20(21), 23598-23609, 2012. https://doi.org/10.1364/OE.20.023598

[22] Kasani, S., Zheng, P., Bright, J., and Wu, N. "Tunable visible-light surface plasmon resonance of molybdenum oxide thin films fabricated by E-beam evaporation", ACS Applied Electronic Materials, 1(11), 2389-2395, 2019. http://doi.org/10.1021/acsaelm.9b00555

[23] Liu, M., Li, X., Karuturi, S. K., Tok, A. I. Y., and Fan, H. J. "Atomic layer deposition for nanofabrication and interface engineering", *Nanoscale*, 4(5), 1522-1528, 2012. http://doi.org/10.1039/C2NR11875K

[24] Kim, D. H., and Kwok, H. S. "Pulsed laser deposition of VO_2 thin film", *Applied Physics Letters*, 65(25), 3188, 1994. http://doi.org/10.1063/1.112476

[25] Petti, L. *et al.* "A plasmonic nanostructure fabricated by electron beam lithography as a sensitive and highly homogeneous SERS substrate for bio-sensing applications", *Vibrational Spectroscopy*, 82, 22-30, 2016. http://doi.org/10.1016/j.vibspec.2015.11.007

[26] He, S., Tian, R., Wu, W., Li, W. D., and Wang, D. "Helium-ion-beam nanofabrication: Extreme processes and applications", *International Journal of Extreme Manufacturing*, 3(1), 012001, 2020. http://doi.org/10.1088/2631-7990/abc673

[27] Esashi, M., Kojima, A., Ikegami, N., Miyaguchi, H., and Koshida, N. "Development of massively parallel electron beam direct write lithography using active-matrix nanocrystalline-silicon electron emitter arrays", *Microsystems & Nanoengineering*, 1, 15029, 2015. https://doi.org/10.1038/micronano.2015.29

[28] Moon, S., Lee, S. Y., Choi, J., Kim, S. B., and Jeon, C. U. "Effects of lithographic parameters in massively parallel electron-beam systems", *Journal of Vacuum Science & Technology B*, 36(6), 06JA03, 2018. https://doi.org/10.1116/1.5048084

[29] Brandt, P. *et al.* "Alternative stitching method for massively parallel e-beam lithography", *Journal of Micro/Nanolithography, Microfabrication, and Microsystems*, 14(3), 031203, 2015. https://doi.org/10.1117/1.JMM.14.3.031203

[30] Higuchi, Y., Kanki, T., and Tanaka, H. "Joule-heat-driven high-efficiency electronic-phase switching in freestanding VO_2/TiO_2 nanowires", *Applied Physics Express*, 10(3), 033201, 2017. https://doi.org/10.7567/APEX.10.033201

[31] FDTD: 3D Electromagnetic Simulator, Lumerical Inc. [Online]. Available: https://www.ansys.com/en-in/products/optics/fdtd

[32] Novotny, L., and Hecht, B. *Principles of nano-optics*. Cambridge University Press, 2008. ISBN: 9780511794193. https://doi.org/10.1017/CBO9780511794193

[33] Dana, B. D. *et al.* "Hybrid plasmonic modes for enhanced refractive index sensing", *Advanced Sensor Research*, 2(12), 2300066, 2023. https://doi.org/10.1002/adsr.202300066

[34] Liu, M., and Chen, S. “Bright and dark plasmon resonance of Ag nanorod dimers”, *AIP Advances*, 13(12), 125023, 2023. https://doi.org/10.1063/5.0163797

[35] Chang, T. *et al.* “Mitigating deterioration of vanadium dioxide thermochromic films by interfacial encapsulation”, *Matter*, 1(3), 734-744, 2019. https://doi.org/10.1016/j.matt.2019.04.004

[36] Ayaz, R. M. A., and Mustafa, A. “Polydimethylsiloxane (PDMS) coated broadband tunable vanadium dioxide (VO_2) based linear optical cavity temperature sensor”, *Sensing and Imaging*, 25, 14, 2024. https://doi.org/10.1007/s11220-023-00453-2

[37] Gao, Z. *et al.* “A facile PDMS coating approach to room-temperature gas sensors with high humidity resistance and long-term stability”, *Sensors and Actuators B: Chemical*, 325, 128810, 2020. https://doi.org/10.1016/j.snb.2020.128810

[38] Yu, J. *et al.* “Water-durability and high-performance all-fiber humidity sensor using methyldiethanolamine-photopolymer-PDMS structure”, *Optics Express*, 31(25), 42637-42650, 2023. https://doi.org/10.1364/OE.509398

CHAPTER 7

FRACTALIZATION OF PENTAGON SHAPED PLASMONIC NANOANTENNAS FOR VO_2 BASED NEAR-FIELD SWITCHING APPLICATION

7.0 Chapter Overview

This chapter focuses on the design and modelling of fractal plasmonic nanoantennas based on fractalization of pentagon shaped nanostructures, with the objective of realizing efficient near-field switching using a vanadium dioxide (VO_2) film. Unlike plasmonic switches that rely on the modulation of far-field transmission or reflection characteristics, this work emphasizes the active manipulation of the near-field at the nanoscale – specifically, the electric field localized between the two arms of the nanoantenna. The switching mechanism is driven by the semiconductor-to-metal phase transition of VO_2, a well-known phase-change material. The fractalization to higher orders plays a crucial role in enhancing the redistribution of electromagnetic field such that a high intensity switching ratio (ISR) is realized at a wavelength of ~1500 nm. Finite Difference Time Domain (FDTD) analysis shows that an ISR as high as ~2300 could be achieved with the third order of the fractalized pentagon shaped nanoantenna at a wavelength of 1530 nm. The effect of the geometrical parameters like the length of the nanoantenna and the thickness of VO_2 layer on the ISR spectra are also studied for performance optimization and for tuning the high ISRs to various regions of the optical communication window.

7.1 Motivation

The VO_2 based plasmonic switches proposed by various researchers have been primarily designed for far-field switching. However, there have been limited reports of plasmonic active switching of the near-field of a plasmonic nanoantenna [1-3]. The control, switching and manipulation of the near-field of a plasmonic nanoantenna is particularly important for applications such as particle trapping and tweezing [4], Surface-Enhanced Raman Scattering (SERS) based sensors [5], design of vortex beams [6], non-linear optics [7], switchable lasing [8], and biosensing and molecular diagnostics [9]. Thus, this chapter focuses on the design and modelling of the VO_2 based plasmonic switches for near-field switching. These switches do not require any shaping or complex manipulation of the incident laser beam to achieve near-field switching and yet offer high ISRs of upto ~2300 with the third order of the fractalized pentagon shaped nanoantenna.

7.2 Introduction

One of the prominent applications of plasmonics is plasmonic nanoantennas (PNAs) – which can transfer the electromagnetic (EM) energy from the near-field to the far-field in its transmission mode and conversely in its reception mode

[10, 11]. Recently, many PNAs based on fractal nanostructures such as – Sierpinski triangles [12], Sierpinski carpet [13], Cayley tree [14], Koch fractal [15], Ternary tree [16] and others [17, 18] – have been proposed. Fractal is a geometrical shape which can be depicted by a foundational shape with an iterative transformation rule to achieve higher fractal features. The advantages of fractal variants of PNAs include – broadband spectral response [16], higher electromagnetic enhancement [13], tunability of plasmon resonance wavelength [14], and miniaturization of the antenna size [19]. Owing to such advantages, the fractal based PNAs become a suitable choice for designing active near-field plasmonic switches. However, there are limited reports of VO_2 based plasmonic near-field switches using fractal nanoantennas. For example, designs using dipole antennas, nanorods, or basic ring-rhombus geometries [1, 2] report ISR values typically ranging between 5 and 100. While the Sierpinski fractal contour-bowtie antenna could achieve an ISR of ~900 [20] there still remains scope for further improvement in terms of simpler geometries with higher ISR.

In this chapter, the active near-field switching is achieved by placing fractalized pentagon shaped PNAs on top of a gold coated silicon dioxide (SiO_2) substrate with VO_2 layer as a spacer between the nanoantenna and the substrate (See Fig. 7.1(a)). The PNA consists of two gold pentagon shaped segments arranged face-to-face with a narrow gap between them. The pentagon shape is selected for its symmetrical and compact geometry, which inherently supports strong plasmonic resonances. To enhance the electromagnetic field confinement and improve switching characteristics, the basic pentagon design is further modified through a fractalization process. The process begins with a solid pentagon (referred to as 1st order), and in each subsequent iteration, smaller pentagonal units are recursively embedded at a scaling ratio of 2/5, while maintaining self-similarity (See Fig. 7.1(a)). Fractal PNA upto 3rd order are considered with minimum feature size ~40 nm, thus making the fabrication feasible. Switching is achieved when the phase change material – VO_2 – changes from its tetragonal metallic phase (ON state) to monoclinic semiconductor phase (OFF state) on exposure to external heat, voltage, or optical stimulus (See Fig. 7.1(b)). The switching performance is measured in terms of near-field intensity switching ratio (ISR) – i.e., the ratio of intensity of ON state to the intensity of OFF state. It can be seen from Fig. 7.1(c) that the proposed plasmonic switches can achieve high ISR upto ~2300 at a wavelength of ~1500 nm. In addition to ultra-fast switching owing to VO_2, these near-field switches offer added advantages of passively tuning the wavelength of operation to any range of the spectrum by modifying the geometrical parameters of the nanostructures.

7.3 Numerical Methods

Finite Difference Time Domain (FDTD) based numerical analysis was carried out to calculate the electromagnetic fields in the switches proposed in this chapter by employing Ansys Lumerical FDTD Solver. For all the FDTD simulations, a 1 nm grid dimension was taken for all the directions (X, Y, and Z), while the source of the incident light was taken as a total field scattered field (TFSF) source with the spectral range being from 800 nm to 2200 nm. The linearly polarized light with incident electric-field (E_0) of 1 Vm^{-1} was incident normally from the top onto the nanostructures, with the electric-field aligned along the axis of the nanoantenna as

shown in Fig. 7.1(b). The electric-field enhancement at a point is calculated as the ratio of electric-field at the point (E) and the incident electric-field (E_0), while the near-field intensity enhancement is measured as $|E|^2/|E_0|^2$. In all the directions (X, Y, and Z), perfectly matched layer (PML) boundary conditions were employed for these simulations. Moreover, a rounding radius of 2 nm was considered in designing the pentagon shaped nanostructures to simulate practical fabrication constraints. In this chapter, a numerical analysis of various fractal orders of VO_2-based pentagon shaped fractal nanoantennas on near-field ISR is carried out first, which demonstrates that higher orders lead to higher near-field switching efficiency. Subsequently, the effect of geometrical parameters on the switching performance is also carried out.

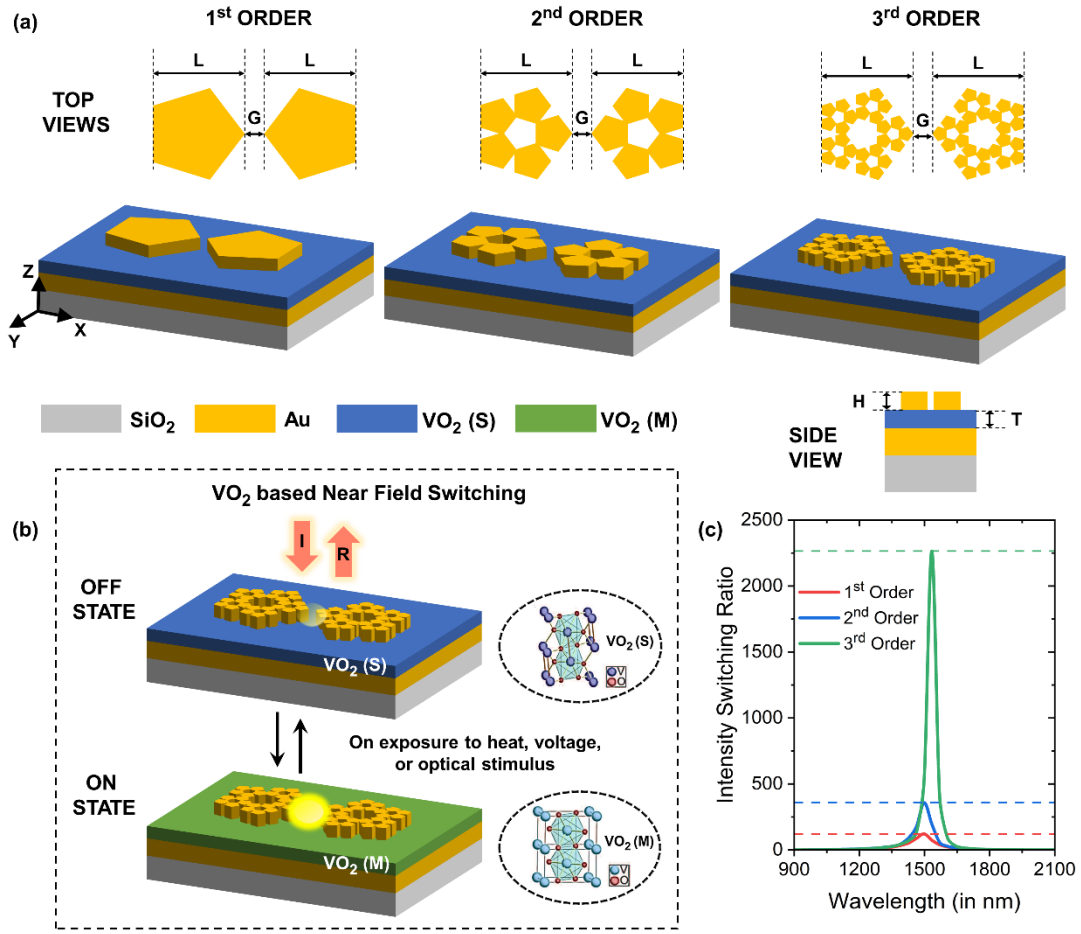

Fig. 7.1 (a) Schematics of 1st order, 2nd order, and 3rd order fractalized pentagon shaped plasmonic nanoantennas on gold-coated SiO_2 substrate with VO_2 layer as a spacer between the nanoantennas and the underlying substrate. The geometrical parameters like the length of pentagon segment '*L*', the height of pentagon segment '*H*', the gap between the two pentagon segments '*G*', and the thickness of VO_2 layer '*T*' are also shown. **(b)** Illustration of near-field switching mechanism based on the phase transformation of VO_2. **(c)** Intensity switching ratio spectra for all the three orders of the proposed plasmonic switches based on pentagon shaped fractal plasmonic nanoantennas.

7.4 Results and Discussion

The near-field switching performance of the proposed VO_2 based fractalized pentagon shaped nanoantennas is measured in terms of the intensity switching ratio (ISR), which is the ratio of the intensity enhancement obtained during the ON state of the switch (I_{ON}) when VO_2 is in its metallic state ($(|E|^2/|E_0|^2)_M$) to the intensity enhancement obtained during the OFF state of the switch (I_{OFF}) when VO_2 is in its semiconductor state ($(|E|^2/|E_0|^2)_S$) as shown in Eq. 7.1.

$$Near-field\ \ ISR = \frac{I_{ON}}{I_{OFF}} \tag{7.1}$$

Fig. 7.2 shows the effect of fractalization of pentagon shaped plasmonic nanoantennas from 1st order to 3rd order on the intensity enhancement ($|E|^2/|E_0|^2$) spectra of VO_2 (M) and VO_2 (S), and ISR (I_{ON}/ I_{OFF}) spectra of the proposed plasmonic switches. It can be observed from Figs. 7.2(a-c) that the dip in the intensity enhancement curve when VO_2 is in its semiconductor phase causes the plasmonic switching at a wavelength of ~1500 nm. As the order of fractalization is increased from 1st order to 2nd order, the ISR increases from ~120 to ~360 and is further increased to ~2300 when the fractal order increases to 3rd order. The increase in ISR is primarily attributed to the decrease in $(|E|^2/|E_0|^2)_S$ due to the redistribution of field and electromagnetic hotspot as fractal order is increased from 1 to 3. The electric field profiles shown in Figs. 7.2(d-f) clearly show that the plasmonic switch works in the ON state when VO_2 is in its metallic phase and OFF state when VO_2 is in its semiconductor phase. Moreover, the light is efficiently confined at the center of the two pentagon shaped segments for all the fractal orders, leading to high near-field switching efficiency.

Fig. 7.3 shows the effect of varying the length '*L*' of the pentagon segment of the proposed VO_2 based fractalized pentagon shaped nanoantennas. For the 1st order (See Figs. 7.3(a-c)), the plasmon resonance wavelength shows a slight red-shift when the length '*L*' is increased from 200 nm to 300 nm. This red-shift with an increase in the length '*L*' is expected due to a change in the dipolar polarizability of each nanoantenna with varying length and the dependence of the LSPR wavelength on the length of the nanoantenna [21]. In addition, the ISR first increases from ~40 to ~120 as the length '*L*' increase from 200 nm to 250 nm. However, it then decreases to ~90 when the length '*L*' is further increased to 300 nm. Similarly, for the 2nd order (See Figs. 7.3(d-f)), the plasmon resonance wavelength also shows a red-shift when the length '*L*' is increased from 200 nm to 300 nm. The ISR first increases from ~85 to ~470 as the length '*L*' increase from 200 nm to 275 nm. However, it then decreases to ~200 when the length '*L*' is further increased to 300 nm. For the 3rd order (See Figs. 7.3(g-i)), the plasmon resonance wavelength shows a red-shift when the length '*L*' is increased from 200 nm to 275 nm and then a slight blue-shift as the length '*L*' is further increased to 300 nm. The ISR first increases from ~500 to ~3200 as the length '*L*' increase from 200 nm to 225 nm. However, it then starts to decrease as the length '*L*' is increased further. Hence, it can be concluded that 250 nm is the optimal length of the pentagon segment of the nanoantenna.

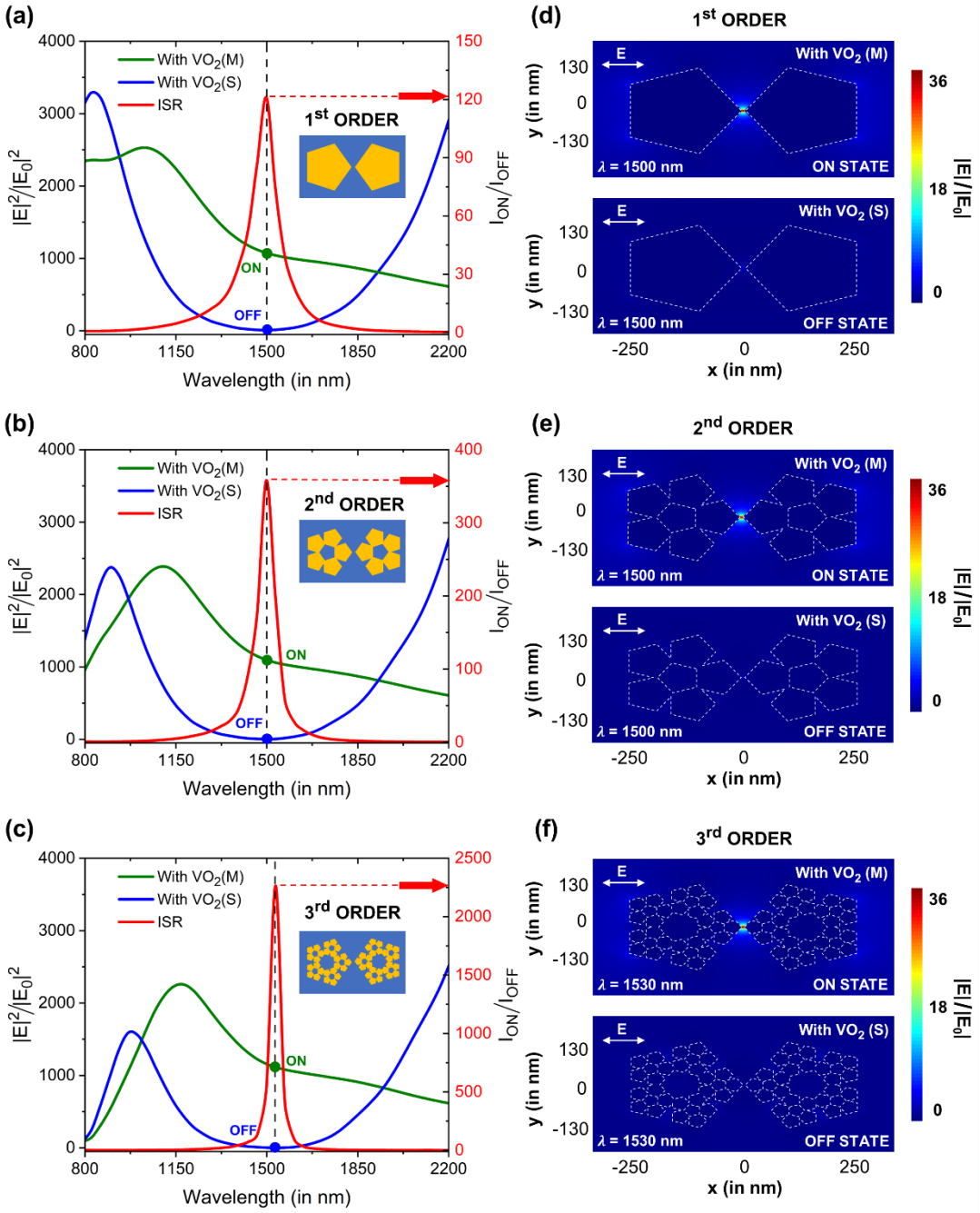

Fig. 7.2 Effect of fractalization of pentagon shaped plasmonic nanoantennas. Intensity enhancement spectra for VO_2 (M) and VO_2 (S), and ISR spectra of the plasmonic switches with pentagon shaped fractals for **(a)** 1st order, **(b)** 2nd order, and **(c)** 3rd order. Electric-field profiles of the plasmonic switches with pentagon shaped fractals for **(d)** 1st order, **(e)** 2nd order, and **(f)** 3rd order. The length of the pentagon segment '*L*', the height of the pentagon segment '*H*', the gap between the pentagon segments '*G*', and the thickness of VO_2 layer '*T*' are considered to be 250 nm, 150 nm, 5 nm, and 150 nm, respectively.

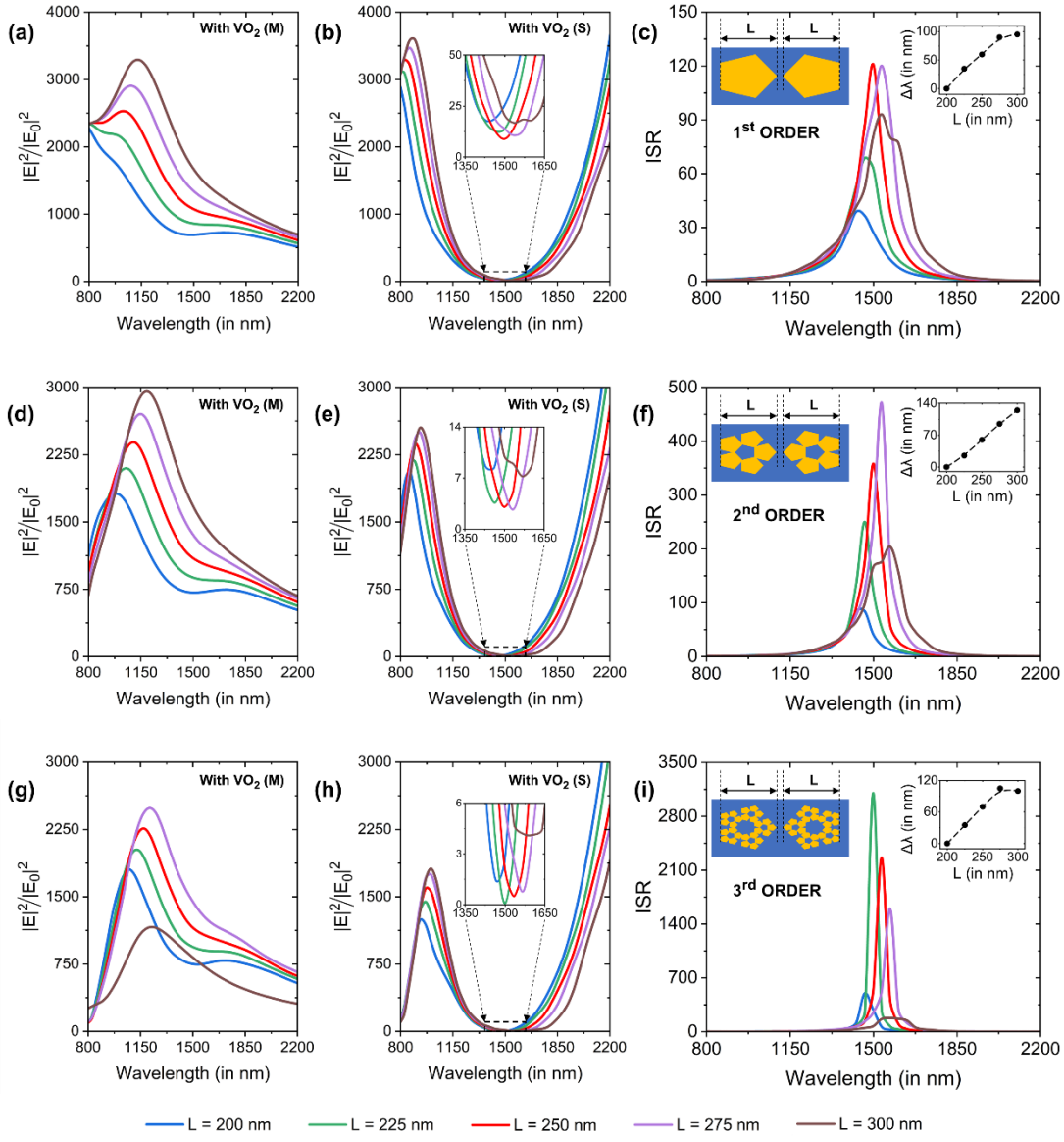

Fig. 7.3 Effect of varying the length '*L*' of the pentagon segment. Intensity enhancement spectra for **(a)** VO_2 (M) and **(b)** VO_2 (S), and **(c)** ISR spectra of the plasmonic switches with pentagon shaped fractals of 1st order. Intensity enhancement spectra for **(d)** VO_2 (M) and **(e)** VO_2 (S), and **(f)** ISR spectra of the plasmonic switches with pentagon shaped fractals of 2nd order. Intensity enhancement spectra for **(g)** VO_2 (M) and **(h)** VO_2 (S), and **(i)** ISR spectra of the plasmonic switches with pentagon shaped fractals of 3rd order. The plasmon resonance wavelength shift (Δλ) with increasing the length '*L*' from 200 nm to 300 nm is also shown in the insets of ISR spectra graphs. The height of the pentagon segment '*H*', the gap between the pentagon segments '*G*', and the thickness of VO_2 layer '*T*' are considered to be 150 nm, 5 nm, and 150 nm, respectively.

Fig. 7.4 shows the effect of varying the thickness of the VO_2 layer '*T*' from 125 nm to 175 nm on the intensity enhancement spectra for VO_2 (M) and VO_2 (S), and ISR spectra of the plasmonic switches for 1st, 2nd, and 3rd order fractalization of pentagon shaped nanoantennas. It can be observed from intensity enhancement spectra for VO_2 (M) shown in Figs. 7.4(a, d, g) that for all the three thicknesses of VO_2, i.e., *T* = 125 nm, 150 nm, and 175 nm, there is a red-shift in the plasmonic mode as the fractal order is increased from 1 to 3. A similar red-shift is observed in the intensity enhancement spectra for VO_2 (S) when the fractal order is increased from 1 to 3 as shown in Figs. 7.4(b, e, h). In addition, there is a decrease in $(|E|^2/|E_0|^2)_S$ due to the redistribution of field when the fractal order is increased from 1 to 3, leading to increase in the ISR values (See Figs. 7.4(c, f, i)). It can be observed from Fig. 7.4 that for all the values of '*T*', 3rd order fractal gives the best results. Moreover, the most optimal value of '*T*' is 150 nm as maximum ISR can be achieved with this thickness of VO_2 layer.

7.5 Chapter Summary

This chapter presented the design of plasmonic nanoantennas based on fractalized pentagon shaped geometries for efficient near-field switching using a VO_2 spacer layer. The fractalization process, applied up to the 3rd order, enhances field confinement and enables strong modulation of the localized electric field. Numerical analysis using FDTD simulations showed that increasing the fractal order significantly improves the ISR. The 1st, 2nd, and 3rd order designs achieved ISRs of ~120, ~360, and ~2300, respectively, at a wavelength of ~1500 nm. Parametric studies revealed that the nanoantenna length and VO_2 thickness critically influence switching performance. The optimal antenna length was found to be 250 nm, while a VO_2 thickness of 150 nm yielded the highest ISR. The results confirm that fractalization enhances near-field switching efficiency without requiring complex beam shaping, offering a promising route for compact and high-performance active plasmonic devices.

7.6 References

[1] Savaliya, P. B., Thomas, A., Dua, R., and Dhawan, A. "Tunable optical switching in the near-infrared spectral regime by employing plasmonic nanoantennas containing phase change materials", *Optics Express*, 25(20), 23755-23772, 2017. https://doi.org/10.1364/OE.25.023755

[2] Gupta, N., Savaliya, P. B., and Dhawan, A. "Plasmonic nanoantennas on VO_2 films for active switching of near-field intensity and radiation from nanoemitters", *Optics Express*, 28(19), 27476-27494, 2020. https://doi.org/10.1364/OE.391655

[3] Large, N., Abb, M., Aizpurua, J., and Muskens, O. L. "Photoconductively loaded plasmonic nanoantenna as building block for ultracompact optical switches", *Nano Letters*, 10(5), 1741–1746, 2010. https://doi.org/10.1021/nl1001636

[4] Erickson, D., Serey, X., Chen, Y. F., and Mandal, S. "Nanomanipulation using near field photonics", *Lab Chip*, 11(6), 995-1009, 2011. https://doi.org/10.1039/C0LC00482K

[5] Trugler, A. *et al.* "Near-field and SERS enhancement from rough plasmonic nanoparticles", *Physical Review B*, 89, 165409, 2014. https://doi.org/10.1103/PhysRevB.89.165409

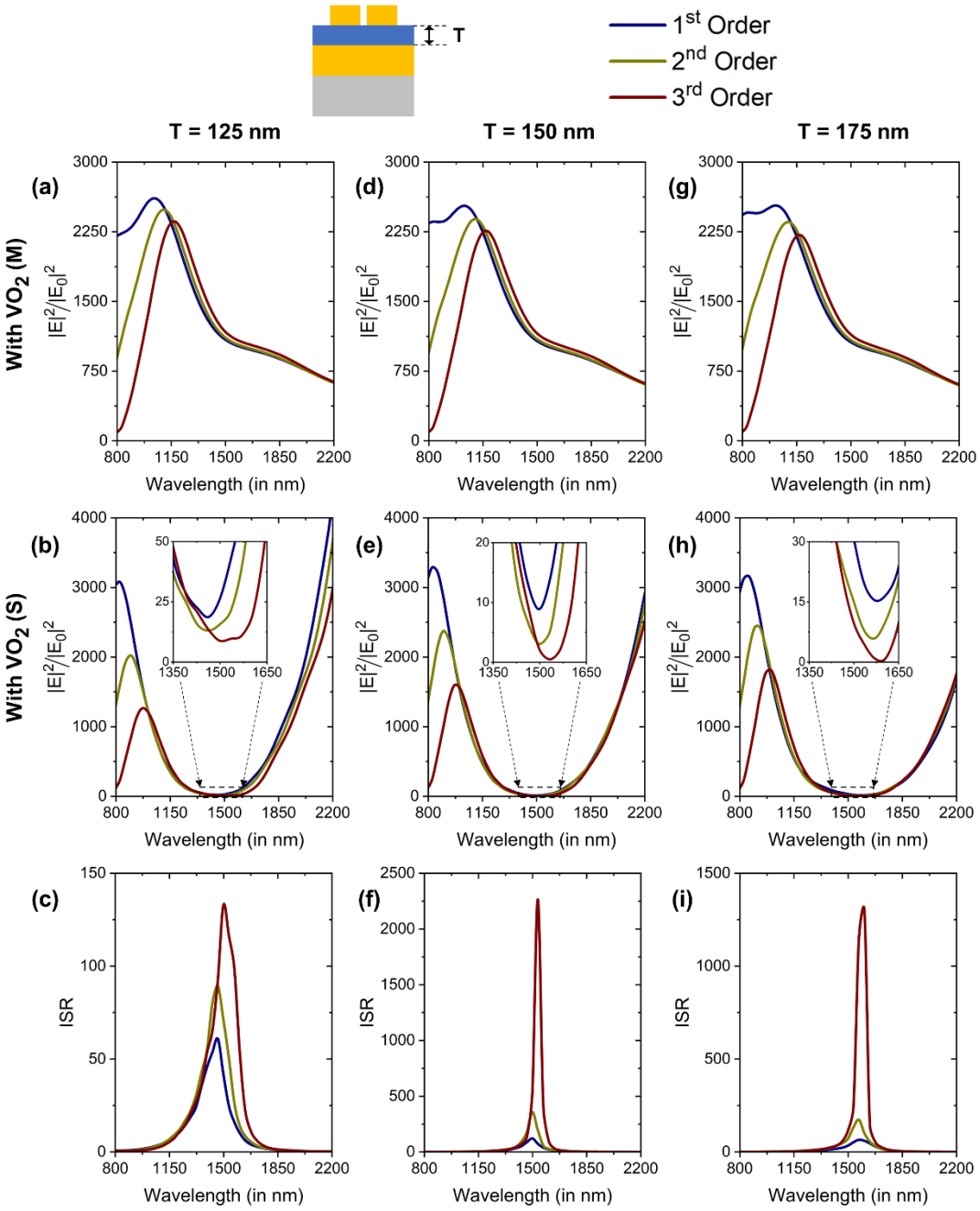

Fig. 7.4 Effect of varying the thickness of the VO_2 layer '*T*'. Intensity enhancement spectra for **(a)** VO_2 (M) and **(b)** VO_2 (S), and **(c)** ISR spectra of the plasmonic switches for 1st, 2nd, and 3rd order fractalization of pentagon shaped nanoantennas with T = 125 nm. Intensity enhancement spectra for **(d)** VO_2 (M) and **(e)** VO_2 (S), and **(f)** ISR spectra of the plasmonic switches for 1st, 2nd, and 3rd order fractalization of pentagon shaped nanoantennas with T = 150 nm. Intensity enhancement spectra for **(g)** VO_2 (M) and **(h)** VO_2 (S), and **(i)** ISR spectra of the plasmonic switches for 1st, 2nd, and 3rd order fractalization of pentagon shaped nanoantennas with T = 175 nm. The length of the pentagon segment '*L*', the height of the pentagon segment '*H*', and the gap between the pentagon segments '*G*' are considered to be 250 nm, 150 nm, and 5 nm, respectively.

[6] Zhang, Y., Liu, W., Gao, J., and Yang, X. “Generating focused 3D perfect vortex beams by plasmonic metasurfaces”, *Advanced Optical Materials*, 6(4), 1701228, 2018. https://doi.org/10.1002/adom.201701228

[7] Metzger, B., Hentschel, M., and Giessen, H. “Probing the near-field of second-harmonic light around plasmonic nanoantennas”, *Nano Letters*, 17(3), 1931-1937, 2017. https://doi.org/10.1021/acs.nanolett.6b05285

[8] Kohoutek, J. *et al.* “Integrated all-optical infrared switchable plasmonic quantum cascade laser”, *Nano Letters*, 12(5), 2537-2541, 2012. https://doi.org/10.1021/nl3007424

[9] Li, F. *et al.* “Exploring near-field sensing efficiency of complementary plasmonic metasurfaces for immunodetection of tumor markers”, Biosensors and Bioelectronics, 203, 114038, 2022. https://doi.org/10.1016/j.bios.2022.114038

[10] Giannini, V., Dominguez, A. I. F., Heck, S. C., and Maier, S. A. “Plasmonic nanoantennas: fundamentals and their use in controlling the radiative properties of nanoemitters”, *Chemical Reviews*, 111(6), 3888-912, 2011. https://doi.org/10.1021/cr1002672

[11] Habib, A., Zhu, X., Fong, S., and Yanik, A. A. “Active plasmonic nanoantenna: an emerging toolbox from photonics to neuroscience”, *Nanophotonics*, 9(12), 3805-3829, 2020. https://doi.org/10.1515/nanoph-2020-0275

[12] Bicket, I. C., Bellido, E. P., McRae, D. M., Labarthet, F. L., and Botton, G. A. “Carving plasmon modes in silver Sierpinski fractals”, *ACS Photonics*, 6(11), 2974-2984, 2019. https://doi.org/10.1021/acsphotonics.9b01179

[13] Nicola, F. D. *et al.* “Multiband plasmonic Sierpinski carpet fractal antennas”, *ACS Photonics*, 5(6), 2418-2425, 2018. https://doi.org/10.1021/acsphotonics.8b00186

[14] Gottheim, S., Zhang, H., Govorov, A. O., and Halas, N. J. “Fractal nanoparticle plasmonics: the Cayley tree”, *ACS Nano*, 9(3), 3284-3292, 2015. https://doi.org/10.1021/acsnano.5b00412

[15] Bellido, E. P. *et al.* “Self-similarity of plasmon edge modes on Koch fractal antennas”, *ACS Nano*, 11(11), 11240-11249, 2017. https://doi.org/10.1021/acsnano.7b05554

[16] Hegde, R. S., and Khoo, E. H. “Broadband optical response in ternary tree fractal plasmonic nanoantenna”, *Plasmonics*, 11, 465-473, 2016. https://doi.org/10.1007/s11468-015-0059-3

[17] Bicket, I. C., Bellido, E. P., McRae, D. M., Labarthet, F. L., and Botton, G. A. “Hierarchical plasmon resonances in fractal structures”, *ACS Photonics*, 7(5), 1246-1254, 2020. https://doi.org/10.1021/acsphotonics.0c00110

[18] Sederberg, S., and Elezzabi, A. Y. “Sierpinski fractal plasmonic antenna: a fractal abstraction of the plasmonic bowtie antenna”, *Optics Express*, 19(11), 10456-10461, 2011. https://doi.org/10.1364/OE.19.010456

[19] Cakmakyapan, S., Cinel, N. A., Cakmak, A. O., and Ozbay, E. “Validation of electromagnetic field enhancement in near-infrared through Sierpinski fractal nanoantennas”, *Optics Express*, 22(16), 19504-19512, 2014. https://doi.org/10.1364/OE.22.019504

[20] Sharma, Y., and Dhawan, A. “Active near-field plasmonic switches based on Sierpinski-fractal nanoantennas on VO_2 films”, *Journal of Optics*, 24(6), 065001, 2022. https://doi.org/10.1088/2040-8986/ac6208

[21] Khoshdel, V., and Saremi, M. S. “Plasmonic nano bow-tie arrays with enhanced LSPR refractive index sensing”, *Micro & Nano Letters*, 14(5), 566-571, 2019. https://doi.org/10.1049/mnl.2018.5588

CHAPTER 8

CONCLUSIONS, FUTURE SCOPE, AND SOCIAL IMPACT

8.0 Chapter Overview

This chapter concludes the thesis by summarizing the key findings and contributions arising from the design and analysis of vanadium dioxide (VO_2) based plasmonic switches. It presents a comparative evaluation of various switches developed for broadband, multi-wavelength, polarization-independent, and near-field applications, highlighting their relative advantages and performance outcomes. The chapter further outlines promising directions for future research aimed at enhancing device integration, performance, and applicability. Finally, it reflects on the broader societal implications of this work, emphasizing how such innovations in nanoscale photonics can contribute meaningfully to global challenges in healthcare, sustainability, education, and equitable access to technology.

8.1 Conclusions

This thesis provides a rigorous exploration of vanadium dioxide (VO_2) based plasmonic switches, encompassing a diverse range of device configurations for various operational regimes — namely broadband, multi-wavelength, polarization-independent, and near-field switching. VO_2, a phase change material, has been strategically selected due to its favorable characteristics such as near-room transition temperature, high endurance over repeated switching cycles, ultrafast response times (in the femtosecond to picosecond regime), and significant refractive index contrast between its semiconducting and metallic phases. These attributes have been instrumental in achieving compact and high-performance plasmonic switches.

The broadband switching functionality was achieved by using two principal designs — nanodisc-dimers with progressively increasing diameters (Discussed in Chapter 4), and V-shaped nanostructures with variable arm lengths (Discussed in Chapter 6). These configurations exploit plasmonic mode hybridization and dimensional variation to broaden the spectral response. The nanodisc-dimers array achieved broadband switching with extinction ratio (ER) of ~5 dB across 650 nm spectral range, covering C, L, and U bands. In comparison, the V-shaped nanostructures demonstrated a broadband extinction ratio (ER) > 5 dB over a bandwidth > 1400 nm, effectively spanning all major optical communication bands (O, E, S, C, L, and U), which has not been previously reported by any research group to the best of available knowledge. These designs provide tunability through geometrical parameter adjustment, making them suitable for applications demanding wideband spectral control.

Further innovation was demonstrated through the dual-wavelength and polarization-independent switch based on a combination of U and C shaped gold nanostructures (Discussed in Chapter 5). This design strategically exploited symmetry-breaking and introduced spatial offsets to achieve consistent performance across all

polarization angles. The switch exhibited high extinction ratios (~20 dB) simultaneously at 1560 nm and 2130 nm, irrespective of incident polarization angle. This is particularly advantageous in practical systems where light polarization may vary unpredictably, thereby eliminating the need for external polarizers. The multi-wavelength switching was also realized using periodic arrays of identical V-shaped nanostructures (Discussed in Chapter 6). This configuration exhibited strong, discrete switching at two specific wavelengths with extinction ratios > 12 dB. Such multi-wavelength behavior is crucial in wavelength division multiplexing (WDM) systems, where simultaneous operation at multiple channels is needed using a single compact component.

A comparative form of discussion on the performance of devices aiming at realizing the same functionality — broadband switching and multi-wavelength switching — has been added in Table 8.1 and Table 8.2, respectively.

From Table 8.2, it is evident that both the Nanodisc-Dimer (NDD) and Variable V-Shaped Nanostructure (VVNS) switches exhibit remarkable broadband switching capabilities enabled by the phase transition of VO_2. The NDD switch design achieves a compact, easily realizable structure with broadband modulation extending across the C, L, and U communication bands, making it suitable for integrated optical interconnects and broadband signal routing. In contrast, the VVNS switch configuration offers superior spectral coverage from the O to U bands, enabled by strong asymmetric plasmonic coupling between V-arms of varying lengths. This results in a broader and more tunable spectral response compared to the NDD geometry. Overall, both the switches effectively exploit VO_2-induced phase transition to realize broadband optical switching; however, the VVNS design provides higher bandwidth and flexibility, demonstrating its potential for next-generation reconfigurable broadband photonic systems.

Table 8.2 Comparative summary of proposed VO_2 based broadband plasmonic switches

Parameters	Nanodisc-Dimer (NDD) Switch	Variable V-Shaped Nanostructure (VVNS) Switch
Structural Design	Periodic gold nanodisc-dimers with increasing diameters on VO_2 layer at gold coated SiO_2 substrate	Periodic array of gold V-shaped nanostructures with variable arm lengths on VO_2 layer at gold coated SiO_2 substrate
Operating Wavelength Range	1460 nm to 2110 nm (C, L, and U bands)	1200 nm to 2630 nm (O, E, S, C, L, and U bands)
Extinction Ratio (ER)	5 dB across ~650 nm bandwidth	5 dB across ~1430 nm bandwidth
Key Plasmonic Mechanism	Mode hybridization between nanodiscs of varying diameters, generating overlapping resonances and broadband spectral response	Asymmetric plasmonic coupling between V-arms of unequal lengths, producing multiple hybridized resonances and extended spectral coverage
Primary Advantage	Simple geometry, broadband tunability, and ease of optimization	Extremely wide spectral coverage with geometric control over bandwidth

Table 8.3 Comparative summary of proposed VO_2 based multi-wavelength plasmonic switches

Parameters	Identical V-Shaped Nanostructure (IVNS) Switch	U–C Shaped Nanostructure Switch
Structural Design	Periodic array of identical gold V-shaped nanostructures on VO_2 layer at gold coated SiO_2 substrate	Periodic combination of U and C shaped gold nanostructures with spatial offset on VO_2 layer at gold coated SiO_2 substrate
Operating Wavelength	1320 nm and 2800 nm	1560 nm and 2130 nm
Extinction Ratio (ER)	~14 dB at both wavelengths	~20 dB at both wavelengths
Polarization Dependence	Polarization-dependent	Polarization-independent across all angles of incidence
Key Plasmonic Mechanism	Inter-particle coupling between identical V-shaped gaps forming hybridized dipole resonances at distinct wavelengths	Asymmetric mode coupling between U and C shaped nanorods, yielding two distinct and stable plasmonic resonances insensitive to polarization
Primary Advantage	High extinction ratio and multi-channel operation	High extinction ratio and polarization robustness with dual-wavelength response

As shown in Table 8.3, both the Identical V-Shaped Nanostructure (IVNS) and U-C Shaped Nanostructure switches effectively demonstrate multi-wavelength modulation through the phase transition of VO_2. The IVNS switch configuration exhibits strong dual-resonant behavior at 1320 nm and 2800 nm, driven by inter-particle coupling between identical V-shaped gaps. This results in high extinction ratios (~14 dB) at discrete wavelengths, making it well-suited for multi-channel or wavelength-division multiplexing (WDM) applications. In comparison, the U-C shaped switch achieves a higher extinction ratio (~20 dB) with polarization-independent operation at 1560 nm and 2130 nm due to asymmetric mode coupling between the U and C elements. This polarization robustness enhances its practical applicability in integrated photonic and optical logic systems, where polarization control is often challenging. Overall, both designs leverage the tunable optical properties of VO_2 to achieve efficient multi-wavelength modulation, with the U-C offset geometry offering superior extinction ratio and polarization stability, thereby representing a more versatile platform for compact, reconfigurable multi-band photonic switching devices.

While all the above designs operate in the far-field regime, this thesis also investigates near-field enhancement using VO_2-based plasmonic switches. Near-field devices enable highly localized electromagnetic field confinement and significantly enhanced field intensities — beneficial for applications such as single-molecule detection and nonlinear optical interactions. The pentagon shaped fractal nanoantennas (Discussed in Chapter 7) demonstrated high intensity switching ratios (ISR), reaching up to ~2300 for third order of the fractal geometry. The switching mechanism depends on the phase transition of VO_2, which modulates the localized electric-field intensities

between the two coupled pentagon shaped fractal segments. This design achieves extremely confined electromagnetic hotspots in the nanogap region, enabling near-field manipulation of light at sub-wavelength scales. Moreover, spectral tunability was demonstrated by altering geometrical parameters, making the switch adaptable for near-field optical applications such as surface-enhanced Raman spectroscopy (SERS), nanoscale sensing, optical tweezing, and non-linear optics.

Comparatively, the near-field switch offered superior spatial confinement and field enhancement but was optimized for localized operation, whereas the broadband and dual-wavelength designs excelled in far-field transmission modulation over extended spectral ranges. Thus, each proposed design serves distinct functional needs — near-field manipulation, wideband transmission control, or polarization-independent operation — providing a comprehensive solution for nanophotonic applications. This comprehensive investigation not only consolidates VO_2's position as a premier material for active nanophotonics but also paves a path forward for designing multifunctional switches essential to next-generation photonic circuits, optical interconnects, and integrated nanophotonic platforms.

8.2 Future Scope

This thesis presents a diverse suite of VO_2-based plasmonic switches optimized for both operational domains: far-field (broadband, multi-wavelength, and polarization-independent), and near-field plasmonic switching. While the presented designs offer significant advancements, several avenues remain open for future exploration as discussed below:

a) *Experimental realization and characterization*: Though the performance of the proposed switches has been studied through comprehensive FDTD simulations, experimental prototyping using advanced nanofabrication (EBL, PLD, He-ion milling) and optical characterization techniques is essential. Real-world testing of extinction ratios, switching speed, thermal stability, and endurance under operational stress would validate their practical viability.

b) *On-chip integration and CMOS compatibility*: Integration of these switches into CMOS-compatible platforms for lab-on-chip and photonic integrated circuit (PIC) applications remains a high-impact goal. Using transparent conductive oxides or hybrid plasmonic waveguides alongside VO_2 can bridge the gap between device-level innovation and system-level integration.

c) *Multifunctional switching*: Combining fractal nanoantennas with broadband or polarization-independent platforms may enable multi-domain switches capable of both near-field enhancement and spectral control.

d) *Multi-state and analog switching*: Most designs in this thesis are binary (ON/OFF). Exploring multi-level switching using inter-transition stages of VO_2 or analog control of transmission intensity could enable programmable photonic circuits, optical neural networks, or adaptive optics. It is because the insulator-metal transition (IMT) in VO_2 is not abrupt but occurs via intermediate inter-

transition stages involving mixed or metastable phases, such as M2 (Monoclinic 2) and T (Triclinic), resulting from a decoupling between the structural and electronic transitions. These transient states exhibit coexisting semiconducting and metallic characteristics, offering tunable optical and electronic responses that are advantageous for controllable plasmonic switching.

e) *Thermal management and power optimization*: The development of low-power or passive triggering mechanisms (e.g., via ambient temperature gradients or solar illumination) for VO_2 switching would reduce energy overheads, particularly in high-density photonic circuits.

8.3 Social Impact

The plasmonic switches proposed in this thesis, though developed within a scientific and engineering framework, hold profound implications for broader societal well-being. Their compactness, energy efficiency, and functional versatility offer solutions to real-world challenges that affect communities at large by bridging the digital divide. As global connectivity becomes essential for education, employment, and governance, there is a growing need for affordable, high-speed communication infrastructure — especially in underserved rural or remote areas. The development of ultra-compact, low-power plasmonic switches can contribute to the miniaturization and cost reduction of optical communication equipment, making broadband access more widely available and equitable. In addition, with rising global energy demands, reducing power consumption in digital infrastructure is an urgent priority. VO_2 based plasmonic switches operate with minimal energy and offer passive switching capabilities at near-room temperatures. Their deployment can help lower the energy footprint of data centers and communication networks, contributing to global climate and sustainability goals.

In summary, while this thesis advances the field of nanophotonics, its broader value lies in the potential to enhance quality of life, reduce inequality, support sustainable development, and enable accessible technologies. By aligning scientific innovation with social relevance, this work contributes meaningfully to a more connected, healthier, and equitable world.

APPENDIX – I

DISPERSION MODELS

The dielectric functions of dispersive materials like metals are modelled using different theoretical models [I.1], which approximate the optical properties of the metals in a given frequency range. In this section, some of these classical models are discussed.

I.1 Drude Model

This is one of the simplest models proposed by Paul Drude in 1900 [I.2]. It assumes that a metal is a free gas and is a combination of free electrons with a background of immobile positive ions. In addition, there is no binding force between the electrons and the nucleus or the positive ions. The dispersion and background absorption due to inter-band transitions can be modelled by using this model. The equation of motion for the electrons under the effect of an external harmonically oscillating driving force, $E = E_0 e^{-j\omega t}$, can be written as follows [I.2, I.3]:

$$m\ddot{x} + m\gamma\dot{x} = -eE_0 e^{-j\omega t} \tag{I.1}$$

where, 'm' is the mass of the free electron, 'γ' is the damping factor, and 'e' is the charge of an electron.

In the Drude model, the electron is affected by two simultaneous forces [I.2, I.3]:

a) The acceleration force ($m\ddot{x}$) which is exerted on the electron by the driving electric field
b) A damping force ($m\gamma\dot{x}$) which is exerted on the electron due to collisions like the electron-electron interaction and the lattice interaction

On solving for the dielectric permittivity, $\varepsilon(\omega)$, the following relation is obtained:

$$\varepsilon(\omega) = 1 - \frac{\omega_p^2}{\omega^2 + i\gamma\omega} \tag{I.2}$$

where, $\omega_p = \sqrt{\frac{Ne^2}{m\varepsilon_0}}$ is the plasma frequency, 'N' is number of electrons per unit volume of the material, and 'ε_0' is the free space permittivity.

Since, $\varepsilon(\omega) = \varepsilon_r(\omega) + i\varepsilon_i(\omega)$, the real and imaginary parts can be separated as follows:

$$\varepsilon_r(\omega) = 1 - \frac{\omega_p^2}{\omega^2 + \gamma^2} \tag{I.3}$$

and

$$\varepsilon_i(\omega) = \frac{\omega_p^2 \gamma}{\omega(\omega^2 + \gamma^2)} \tag{I.4}$$

I.2 Lorentz Model

This model assumes that the material is made up of bound electrons, i.e., the electrons are bound to the nucleus and thus oscillate around their equilibrium central positions, thus generating a spring or restoring force ($m{\omega_0}^2 x$) in addition to the damping force discussed in the last section [I.4]. The equation of motion for such an electron under the influence of an external oscillating field, $E = E_0 e^{-j\omega t}$, can be written as follows [I.4]:

$$m\ddot{x} + m\gamma\dot{x} + m{\omega_0}^2 x = -eE_0 e^{-j\omega t} \tag{I.5}$$

In the above Eq. I.5, 'ω_0' is the natural frequency of oscillation for the system, 'm' is the mass of the free electron, 'e' is the charge on the electron and 'γ' is the damping factor.

The inter-band transitions can be captured completely in the expression for the dielectric constant using the Lorentz model and can be written as:

$$\varepsilon(\omega) = 1 + \frac{\omega_p^2}{{\omega_0}^2 - \omega^2 - i\gamma\omega} \tag{I.6}$$

Since, $\varepsilon(\omega) = \varepsilon_r(\omega) + i\varepsilon_i(\omega)$, the real and imaginary parts can be separated as follows:

$$\varepsilon_r(\omega) = 1 + \frac{\omega_p^2({\omega_0}^2 - \omega^2)}{({\omega_0}^2 - \omega^2)^2 + \gamma^2\omega^2} \tag{I.7}$$

and

$$\varepsilon_i(\omega) = \frac{\omega_p^2 \gamma\omega}{({\omega_0}^2 - \omega^2)^2 + \gamma^2\omega^2} \tag{I.8}$$

If multiple Lorentz-type oscillators are considered, the dielectric function for the material becomes:

$$\varepsilon(\omega) = 1 + \sum_j \frac{\omega_{pj}^2}{{\omega_{0j}}^2 - \omega^2 - i\gamma_j\omega} \tag{I.9}$$

where, 'j' is the number of oscillators with frequency 'ω_{0j}'.

I.3 Lorentz-Drude Model

The Lorentz-Drude model captures the aspects of both models discussed above, i.e., the inter-band and the intra-band transitions [I.5]. According to this model, the dielectric constant can be expressed as:

$$\varepsilon(\omega) = 1 - \frac{\omega_{pD}^2}{\omega^2 + i\gamma\omega} + \sum_j \frac{f_j \omega_{pLj}^2}{{\omega_0}_j{}^2 - \omega^2 - i\gamma_j\omega} \tag{I.10}$$

where, 'f_j' is the strength of the Lorentz oscillators, 'ω_{pL}' is the plasma frequency, 'ω_0' is the natural frequency of oscillation for the system, 'γ' is the damping factor, and $\omega_{pD} = \sqrt{f_0 \omega_{pL}}$.

I.4 References

[I.1] Hulse, C., and Knoesen, A. "Dispersive models for the finite-difference time-domain method: Design, analysis, and implementation", *The Journal of the Optical Society of America A*, 11(6), 1802-1811, 1994. https://doi.org/10.1364/JOSAA.11.001802

[I.2] Drude, P. "Zur elektronentheorie der metalle", *Annalen der Physik*, 306(3), 566-613, 1900. https://doi.org/10.1002/andp.19003060312

[I.3] Vial, A., Grimault, A. S., Macías, D., Barchiesi, D., and de La Chapelle, M. L. "Improved analytical fit of gold dispersion: Application to the modeling of extinction spectra with a finite-difference time-domain method", *Physical Review B*, 71(8), 085416, 2005. https://doi.org/10.1103/PhysRevB.71.085416

[I.4] Tompkins, H., and Irene, E. A. *Handbook of Ellipsometry*. William Andrew, 2005. ISBN: 978-0-8155-1499-2

[I.5] Shibayama, J., Ando, R., Nomura, A., Yamauchi, J., and Nakano, H. "Simple trapezoidal recursive convolution technique for the frequency-dependent FDTD analysis of a Drude-Lorentz model", *IEEE Photonics Technology Letters*, 21(2), 100-102, 2009. https://doi.org/10.1109/LPT.2008.2009003

APPENDIX – II

DIELECTRIC CONSTANTS OF MATERIALS

II.1 Dielectric constants of metals used for the FDTD Simulations

The calculation and subsequent fitting of the dielectric constants for metallic VO_2, semiconductor VO_2, and gold employed in designing the plasmonic switches proposed in this thesis is based on the Lorentz-Drude Model [II.1-II.3] as follows:

$$\varepsilon(\omega) = \varepsilon_\infty + \sum_{k=1}^{6} \frac{\Delta\varepsilon_k}{-\alpha_k\omega^2 - b_k(i\omega) + c_k} \tag{II.1}$$

Here, '$\varepsilon(\omega)$' is the frequency-dependent complex dielectric constant of the material, with '$n(\omega)$' and '$k(\omega)$' representing the frequency-dependent real and imaginary parts of the refractive index of the material. The first term 'ε_∞' is a constant contributing to the real part of the dielectric constant due to high-frequency electronic transitions while the second term is the sum of Lorentz oscillators describing lattice vibrations and the inter-band transitions of bound electrons, along with the Drude free-electron contributions.

The calculation and subsequent fitting of the dielectric constants for metallic VO_2, semiconductor VO_2, and gold employed in this thesis was done such that:

The values of the material constants for metallic VO_2 were taken as: ε_∞: 3.95; $\Delta\varepsilon_1$: 284.7835992; $\Delta\varepsilon_2$: 34.49365809; $\Delta\varepsilon_3$: 195.7081155; $\Delta\varepsilon_4$: 323.4583261; $\Delta\varepsilon_5$: 570.5996093; $\Delta\varepsilon_6$: 0; α_1: 1; α_2: 1; α_3: 1; α_4: 1; α_5: 1; α_6: 0; b_1: 3.344700147; b_2: 7.914574094; b_3: 13.79232715; b_4: 18.34111935; b_5: 24.4771238; b_6: 0; c_1: 0; c_2: 18.99430511; c_3: 201.3457979; c_4: 311.0176212; c_5: 543.4281993; c_6:0 [II.2].

The values of the material constants for semiconductor VO_2 were taken as: ε_∞: 4.26; $\Delta\varepsilon_1$: 21.10833326; $\Delta\varepsilon_2$: 20.57271235; $\Delta\varepsilon_3$: 27.9097635; $\Delta\varepsilon_4$: 104.1014275; $\Delta\varepsilon_5$: 411.6548635; $\Delta\varepsilon_6$: 384.8646853; α_1: 1; α_2: 1; α_3: 1; α_4: 1; α_5: 1; α_6: 1; b_1: 4.083574816; b_2: 3.122733683; b_3: 3.671568571; b_4: 7.469830329; b_5: 23.27526155; b_6: 20.19793471; c_1: 26.7194092; c_2: 43.40234673; c_3: 57.78418944; c_4: 194.2190812; c_5: 312.807647; c_6: 363.0798918 [II.2].

The values of the constants for gold were taken as: ε_∞: 1; $\Delta\varepsilon_1$: 1589.516; $\Delta\varepsilon_2$: 50.19525; $\Delta\varepsilon_3$: 20.91469; $\Delta\varepsilon_4$: 148.4943; $\Delta\varepsilon_5$: 1256.973; $\Delta\varepsilon_6$: 9169; α_1: 1; α_2: 1; α_3: 1; α_4: 1; α_5: 1; α_6: 1; b_1: 0.268419; b_2: 1.220548; b_3: 1.747258; b_4: 4.406129; b_5: 12.63; b_6: 11.21284; c_1: 0; c_2: 4.417455; c_3: 17.66982; c_4: 226.0978; c_5: 475.1387; c_6: 4550.765 [II.3].

The wavelength dependence of real and imaginary parts of the dielectric permittivity 'ε' for metallic VO_2, semiconductor VO_2, and gold is plotted in Fig. II.1(a-c).

All switches employed in this thesis have been effectively modelled as nanostructures placed on top of a substrate with an effective dielectric permittivity 'ε_{eff}'. As a thick gold layer is present on top of the SiO_2 layer, the substrate under the proposed nanostructures can be treated equivalent to a layer of VO_2 on top of a gold substrate. The effective medium constants can then be modelled using an effective medium approximation. For this analysis, the well-known Bruggeman's effective medium approximation [II.4] has been used to model the effective dielectric permittivity of the resulting substrate using the following equations:

$$f_{VO_2(S)}\left(\frac{\varepsilon_{VO_2(S)} - \varepsilon_{eff}}{\varepsilon_{VO_2(S)} + 2\varepsilon_{eff}}\right) + \left(1 - f_{VO_2(S)}\right)\left(\frac{\varepsilon_{Au} - \varepsilon_{eff}}{\varepsilon_{Au} + \varepsilon_{eff}}\right) = 0 \quad ; \quad with\ VO_2\ (S) \tag{II.2}$$

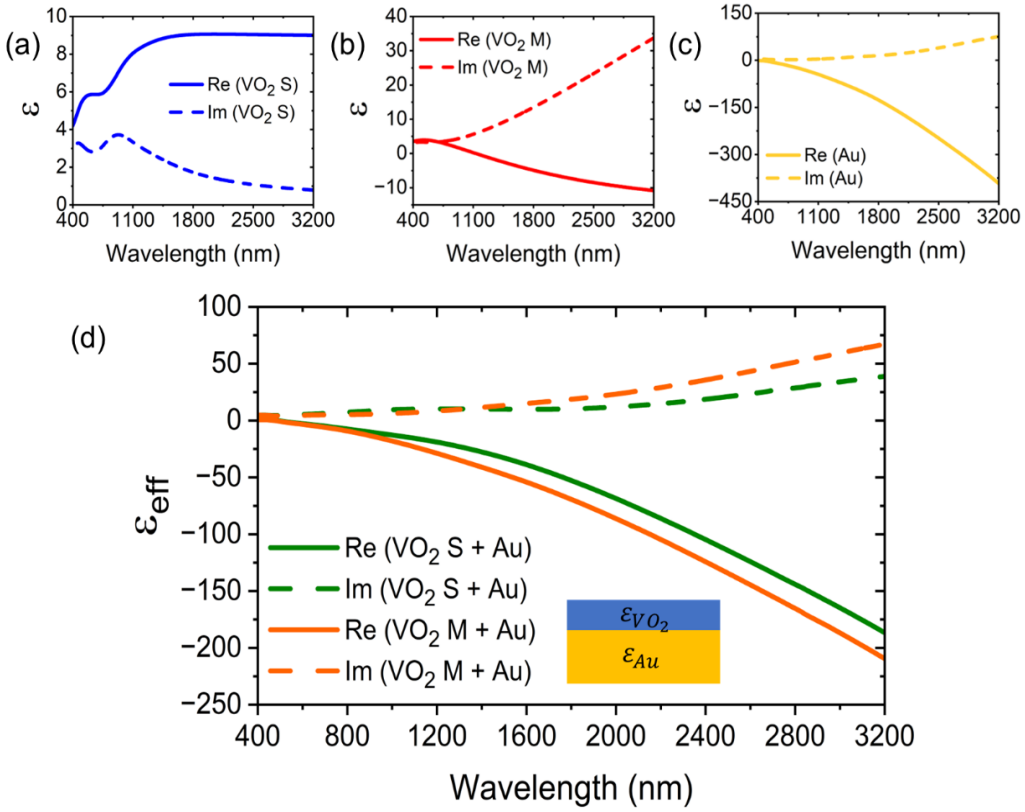

Fig. II.1 Wavelength dependence of real and imaginary parts of the dielectric permittivity 'ε' for **(a)** metallic VO_2, **(b)** semiconductor VO_2, and **(c)** gold. **(d)** Dielectric constants for the effective medium with VO_2(S)-Au and VO_2(M)-Au.

$$f_{VO_2(M)}\left(\frac{\varepsilon_{VO_2(M)} - \varepsilon_{eff}}{\varepsilon_{VO_2(M)} + 2\varepsilon_{eff}}\right) + \left(1 - f_{VO_2(M)}\right)\left(\frac{\varepsilon_{Au} - \varepsilon_{eff}}{\varepsilon_{Au} + \varepsilon_{eff}}\right) = 0 \quad ; \qquad with\ VO_2\ (M) \tag{II.3}$$

where, $\varepsilon_{VO_2(S)}$, $\varepsilon_{VO_2(M)}$, ε_{Au} and ε_{eff} are the wavelength-dependent dielectric permittivities of VO_2 (S), VO_2 (M), gold and the modelled effective medium, respectively. The filling factor ($f_{VO_2(M)}$ or $f_{VO_2(S)}$) corresponds to the volume fraction of the VO_2 film. If the VO_2 layer thickness and the Au layer thickness are taken as 100 nm and 200 nm, the dielectric permittivity for the effective medium with VO_2(S)-Au and VO_2(M)-Au are shown in Fig. II.1(d).

II.2 References

[II.1] Taflove, A., and Hagness, S. C. *Computational electrodynamics: The finite-difference time-domain method*. Artech House, 2005.

[II.2] Verleur, H. W., Barker, A. S., and Berglund, C. N. "Optical Properties of VO_2 between 0.25 and 5 eV", *Physical Review*, 172(3), 788, 1968. https://doi.org/10.1103/PhysRev.172.788

[II.3] Palik, E. D. *Handbook of Optical Constants of Solids*. Academic Press, 1998.

[II.4] Niklasson, G. A., Granqvist, C. G., and Hunderi, O. "Effective medium models for the optical properties of inhomogeneous materials", *Applied Optics*, 20, 26-30, 1981. https://doi.org/10.1364/AO.20.000026

DELHI TECHNOLOGICAL UNIVERSITY

(Formerly Delhi College of Engineering)
Shahbad Daulatpur, Main Bawana Road, Delhi-110042, India

PLAGIARISM VERIFICATION

Title of the Thesis: Design and modelling of nanophotonic devices

Total Pages: 180

Name of the Scholar: Kirti Dalal

Supervisor: Dr. Yashna Sharma

Department: Electronics and Communication Engineering

This is to report that the above thesis was scanned for similarity detection. Process and outcome are given below:

Software used: Turnitin

Submission ID: trn:oid:::27535:124298335

Similarity Index: 10%

Total Word Count: 69,451

Date: 31st October 2025

Candidate's Signature

Signature of Supervisor

BRIEF PROFILE

Ms. Kirti Dalal is a Ph.D. Scholar in the Department of Electronics and Communication Engineering, Delhi Technological University, Delhi, India. She received her M. Tech. degree in Digital Communication from Ambedkar Institute of Advanced Communication Technologies and Research, Guru Gobind Singh Indraprastha University, Delhi, India in the year 2020 and B. Tech. degree in Electronics and Communications Engineering from G. B. Pant Govt. Engineering College, Guru Gobind Singh Indraprastha University, Delhi, India in the year 2018.

Her major research interests include design and modelling of nanophotonic devices, plasmonic switches, and optical communication.

ORCID ID: https://orcid.org/0000-0002-3778-641X

Google Scholar: https://scholar.google.com/citations?hl=en&user=AH2ExD0AAAAJ

LinkedIn: https://linkedin.com/in/kirtidalal